

# **A Multifaceted Approach to Preserve Effective Antibiotics Utilizing Antibiotic Susceptibility Testing, Antimicrobial Coatings or Glycomimetic Adjuvants**

## **Dissertation**

der Mathematisch-Naturwissenschaftlichen Fakultät  
der Eberhard Karls Universität Tübingen  
zur Erlangung des Grades eines  
Doktors der Naturwissenschaften  
(Dr. rer. nat.)

vorgelegt von  
Oliver Riester  
aus Villingen-Schwenningen

Tübingen  
2024

Gedruckt mit Genehmigung der Mathematisch-Naturwissenschaftlichen Fakultät der Eberhard Karls Universität Tübingen.

Tag der mündlichen Qualifikation:	20.06.2024
Dekan:	Prof. Dr. Thilo Stehle
1. Berichterstatter:	Prof. Dr. Hans-Peter Deigner
2. Berichterstatter:	Prof. Dr. Stefan Laufer
3. Berichterstatter:	Prof. Dr. Jean-Francois Stumbé

## List of Abbreviations

<b>AB</b>	Antibiotics
<b>AFM</b>	Atomic force microscopy
<b>AMR</b>	Antimicrobial resistance
<b>AMR-P</b>	Antimicrobial resistant pathogen
<b>AST</b>	Antibiotic susceptibility testing
<b>BSI</b>	Bloodstream infections
<b>CFU</b>	Colony forming units
<b>CSP</b>	Carbasugar precursors
<b>dLAMP</b>	Digital loop-mediated isothermal amplification
<b>DPV</b>	Differential pulse voltammetry
<b>EIS</b>	Electrochemical impedance spectroscopy
<b>EUCAST</b>	European Committee on Antimicrobial Susceptibility Testing
<b>EPS</b>	Extracellular polymeric substance
<b>iPRISM</b>	Intensity-based phase-shift reflectometric interference spectroscopic measurements
<b>LRI</b>	Lower respiratory tract infections
<b>MRSA</b>	Multidrug-resistant <i>Staphylococcus aureus</i>
<b>NAP</b>	National antimicrobial action plans
<b>PEEK</b>	Polyether ether ketone
<b>QS</b>	Quorum sensing
<b>WGS</b>	Whole genome sequencing
<b>WHO</b>	World Health Organization



## Acknowledgements

The production of this thesis, as well as the experiments described in it were performed between 2020 and 2024 in the group of Prof. Dr. Hans-Peter Deigner at the Institute of Precision Medicine, Furtwangen University.

I would like to express my sincere gratitude to Prof. Dr. Hans-Peter Deigner for giving me the opportunity to be part of his group and for making this work possible in the first place. Thank you for your invaluable guidance, support, encouragement and especially the freedom to explore my own ideas, hypotheses and approaches during this work. I greatly appreciate the many discussions and joyful conversations we had and have. Your expertise, constructive feedback, unwavering commitment and trust you have placed in me have been decisive in shaping this dissertation, particularly during the unique time of the pandemic.

I would also like to thank Prof. Dr. Stefan Laufer for his supervision of this work, his time and commitment and the trust he has placed in me.

Furthermore, I would like to thank the entire working group for the wonderful atmosphere and constructive cooperation. A special thanks goes to Dr. Lars Kaiser, Helga Weinschrott and Andreas Krames for the discussions, scientific input and encouragement during the experiments creating an excellent environment inside and outside the lab. Gratitude goes to Dr. Max Borgolte for the fruitful collaboration around the projects of antibacterial coatings. In addition, particular gratitude goes to Prof. Magnus Schmidt for the excellent discussions, fruitful collaboration and NMR analysis as well as Pia Burkhartsmaier and Yuna Gurung for synthesis of the carbasugar precursors.

I would also like to thank my friends, especially Max Waldhauer, for their support and distraction after stressful days.

Finally, I want to express my heartfelt thanks to my whole family for their constant love, encouragement, patience and interest in my work. My parents, who supported me in every situation that life confronted me. My two brothers, who have always supported me and reminded me that good food is the most important thing in life. And last but not least, my cat Kratos, who contributed to the writing of this thesis by taking a nap on the keyboard. Thank you all for being part of my life and for giving me the privilege of being part of yours.

# Contents

<b>Zusammenfassung</b>	<b>ix</b>
<b>Abstract</b>	<b>xi</b>
<b>List of Publications</b>	<b>xii</b>
<b>1 Introduction</b>	<b>1</b>
1.1 The Antibiotic Crisis . . . . .	1
1.2 Antimicrobial Susceptibility Testing (AST) . . . . .	4
1.3 Non-traditional Antimicrobials and Resensitization Strategies . . . . .	8
1.3.1 Coatings . . . . .	10
1.3.2 Resensitization . . . . .	10
<b>2 Objectives</b>	<b>13</b>
2.1 Antibiotic Susceptibility Testing (AST) for Responsible and Effective Use of Antibiotics to Minimize New Resistances . . . . .	13
2.2 Chitosan as a Natural Antimicrobial Material for Novel Coatings . . . . .	14
2.3 Glycomimetic Adjuvants: Carbasugar-precursors as Biofilm Inhibitors and Resensitization Approach . . . . .	14
<b>3 Results and Discussion</b>	<b>15</b>
3.1 Antibiotic Susceptibility Testing (AST) . . . . .	15
3.1.1 Direct 3D Printed Biocompatible Microfluidics: Assessment of Human Mesenchymal Stem Cell Differentiation and Cytotoxic Drug Screening in a Dynamic Culture System . . . . .	15
3.1.2 Rapid Phenotypic Antibiotics Susceptibility Analysis by a 3D Printed Prototype . . . . .	34
3.2 Antimicrobial Coatings Related to Chitosan . . . . .	47
3.2.1 Methacryloyl-GlcNAc Derivatives Copolymerized with Dimethacry- lamide as a Novel Antibacterial and Biocompatible Coating . . . . .	47
3.2.2 Synthesis of a biocompatible benzophenone-substituted chitosan hydrogel as novel coating for PEEK with extraordinary strong an- tibacterial and anti-biofilm properties . . . . .	72

---

3.3 Glycomimetic Adjuvants: Carbasugar-precursors . . . . .	88
3.3.1 Synergy of R-(–)carvone and cyclohexenone-based carbasugar precursors with antibiotics to enhance antibiotic potency and inhibit biofilm formation . . . . .	88
<b>4 Summary and Outlook</b>	<b>102</b>
<b>Bibliography</b>	<b>106</b>
<b>List of Figures</b>	<b>119</b>
<b>A Appendix</b>	<b>120</b>
A.1 Supporting Material for Chapter 3.1 . . . . .	120
A.1.1 Supporting Material: Direct 3D Printed Biocompatible Microfluidics: Assessment of Human Mesenchymal Stem Cell Differentiation and Cytotoxic Drug Screening in a Dynamic Culture System	120
A.1.2 Supporting Material: Rapid Phenotypic Antibiotics Susceptibility Analysis by a 3D Printed Prototype . . . . .	130
A.2 Supporting Material for Chapter 3.2 . . . . .	151
A.2.1 Supporting Material: Methacryloyl-GlcNAc Derivatives Copolymerized with Dimethacrylamide as a Novel Antibacterial and Biocompatible Coating . . . . .	151
A.2.2 Supporting Material: Synthesis of a biocompatible benzophenone-substituted chitosan hydrogel as novel coating for PEEK with extraordinary strong antibacterial and anti-biofilm properties . . . . .	157
A.3 Supporting Material for Chapter 3.3 . . . . .	166
A.3.1 Supporting Material: Synergy of R-(–)carvone and cyclohexenone-based carbasugar precursors with antibiotics to enhance antibiotic potency and inhibit biofilm formation . . . . .	166



# Zusammenfassung

Der aktuelle Trend zunehmender Antibiotikaresistenzen und abnehmender Anzahl wirksamer Antibiotika wird zu einer Gefahr für das Gesundheitssystem, da er den medizinischen Fortschritt bei der Behandlung von Infektionen revidieren könnte. Das Problem wird nicht nur von der Weltgesundheitsorganisation, sondern auch in einer Vielzahl von nationalen Aktionsplänen adressiert. Die vorliegende Dissertation befasst sich mit Ansätzen, die dazu beitragen können, den derzeitigen Trend umzukehren, und gliedert sich in drei Abschnitte, deren Ergebnisse in Publikationen vorgestellt werden.

Im ersten Abschnitt wird ein schneller, phänotypischer Antibiotika-Empfindlichkeitstest vorgestellt, dessen Ergebnisse Voraussetzung für einen verantwortungsvollen und effektiven Einsatz von zugelassenen Antibiotika sind. Ein besonderes Augenmerk lag auf Infektionen der Blutbahn und der Zeitspanne von der Probenahme bis zum Ergebnis, die bei den derzeitigen klinischen Standardverfahren mehrere Tage beträgt. Der entwickelte Test ermöglicht es, diese Zeit auf 5-10 Stunden zu verkürzen, so dass die Verabreichung von Breitbandantibiotika auf die Initialdosis reduziert werden kann. Im zweiten Abschnitt wurden antibakterielle und biofilmhemmende Beschichtungen mit Chitosan als Vorbild synthetisiert und für eine mögliche Anwendung im Bereich der Wundheilung oder Implantatbeschichtung charakterisiert. Dieser lokale therapeutische Ansatz ermöglicht eine effizientere Behandlung und schont die Antibiotikareserven, indem er den Einsatz von systemischen Antibiotika reduziert oder sogar überflüssig macht. Im dritten Abschnitt wurden Glycomimetika auf ihre Eignung zur ergänzenden und unterstützenden Therapie untersucht. Die untersuchten Carbazucker-Vorstufen zeigten ein deutliches Potential in den Bereichen Biofilm-Inhibition und bakterielle Resensibilisierung. Eigenschaften, die vor allem bei der Behandlung chronischer Wunden auf deutliche Fortschritte hoffen lassen. Für die klinische Anwendung müssten die getesteten Glycomimetika jedoch noch weiter optimiert werden.

Die bearbeiteten Bereiche tragen dazu bei, wirksame Antibiotika im Gesundheitssystem zu erhalten und die Entwicklung von neuen Resistenzen zu verlangsamen. Synergieeffekte dieser Ansätze in Kombination mit anderen und zukünftiger Forschungsarbeiten besitzen das Potential dem vorhandenen Trend zunehmender Antibiotikaresistenzen und abnehmender wirksamer Antibiotika umzukehren. Die zunehmende Umsetzung der in vielen länderspezifischen "One Health"-Konzepten zum Ausdruck gebrachten Absicht, Maßnahmen zur gezielten Antibiotikagabe anzuwenden, gibt Anlass zu Optimismus für die zukünftige Behandlung bakterieller Infektionen.



# Abstract

The current trend of increasing antibiotic resistance and the decreasing number of effective antibiotics is becoming an ongoing risk for the healthcare system, as it could reverse medical progress in the treatment of infections. Therefore, the issue is not only addressed by the World Health Organization (WHO), but also in a variety of national action plans. This dissertation examines various approaches that can help to reverse the current trend and is divided into three sections, the results of which are presented in publications.

The first section, which comprises the main part of the thesis, demonstrates a rapid, phenotypic antibiotic susceptibility test, the results of which are a prerequisite for the responsible and effective use of approved antibiotics, so that they retain their efficacy in the long term. Particular attention was given to bloodstream infections and the time from sampling to result, which is several days with current standard clinical procedures. The developed test reduces this time to 5-10 hours, allowing the administration of broad-spectrum antibiotics to be reduced to the initial dose.

In the second section, antibacterial and biofilm-inhibiting coatings were synthesized using chitosan as a model and characterized for possible application in the field of wound healing or implant coating. This local therapeutic approach enables more efficient treatment and conserves existing antibiotics by reducing or even eliminating the need for systemic antibiotics.

In the third section, glycomimetics were examined for their suitability as adjuvants. The evaluated carbasugar precursors showed considerable potential in the areas of biofilm inhibition and bacterial resensitization, properties that give hope for significant progress in the treatment of chronic wounds in particular. For clinical application, however, the tested glycomimetics would need to be further optimized, both in terms of effectiveness and the specificity of the target with a known mechanism.

Each of the sections investigated contributes to maintaining effective antibiotics in the healthcare system and slowing the emergence of new resistances. The synergistic effects of these approaches in combination with the ones of other and future scientific studies have the potential to reverse the existing trend of rising antibiotic resistance and dwindling number of effective antibiotics. The increasing implementation of the intention expressed in many country-specific "One Health" concepts to apply measures for the targeted and effective administration of antibiotics gives cause for optimism for the future treatment of bacterial infections.

# List of Publications

## Original Articles, included in this work:

### Chapter 3.1:

- Riester, O.; Laufer, S.; Deigner, H.-P. *Direct 3D Printed Biocompatible Microfluidics: Assessment of Human Mesenchymal Stem Cell Differentiation and Cytotoxic Drug Screening in a Dynamic Culture System*. *Journal of Nanobiotechnology* **2022**, 20 (1), 540. <https://doi.org/10.1186/s12951-022-01737-7>.
- Riester, O.; Kaiser, L.; Laufer, S.; Deigner, H.-P. *Rapid Phenotypic Antibiotics Susceptibility Analysis by a 3D Printed Prototype*. *Adv. Sci.* **2024**, 2308806. <https://doi.org/10.1002/adv.202308806>.

### Chapter 3.2:

- Borgolte, M.; Riester, O.; Kacerova, T.; Rentschler, S.; Schmidt, M. S.; Jacksch, S.; Egert, M.; Laufer, S.; Csuk, R.; Deigner, H. P. *Methacryloyl-GlcnaC Derivatives Copolymerized with Dimethacrylamide as a Novel Antibacterial and Biocompatible Coating*. *Pharmaceutics* **2021**, 13 (10), 1–24. <https://doi.org/10.3390/pharmaceutics13101647>.
- Borgolte, M.; Riester, O.; Quint, I.; Blendinger, F.; Bucher, V.; Laufer, S.; Csuk, R.; Scotti, L.; Deigner, H. P. *Synthesis of a Biocompatible Benzophenone-Substituted Chitosan Hydrogel as Novel Coating for PEEK with Extraordinary Strong Antibacterial and Anti-Biofilm Properties*. *Materials Today Chemistry* **2022**, 26, 101176. <https://doi.org/10.1016/j.mtchem.2022.101176>.

### Chapter 3.3:

- Riester, O.; Burkhardtmaier, P.; Gurung, Y.; Laufer, S.; Deigner, H. P.; Schmidt, M. S. *Synergy of R-(–)Carvone and Cyclohexenone-Based Carbasugar Precursors with Antibiotics to Enhance Antibiotic Potency and Inhibit Biofilm Formation*. *Scientific Reports* **2022**, 12 (1), 1–13. <https://doi.org/10.1038/s41598-022-22807-8>.

---

**Further publications, including reviews, which are not or not directly included in this work:**

- Riester, O.; Borgolte, M.; Csuk, R.; Deigner, H. P. *Challenges in Bone Tissue Regeneration: Stem Cell Therapy, Biofunctionality and Antimicrobial Properties of Novel Materials and Its Evolution*. International Journal of Molecular Sciences **2021**, 22 (1), 1–25. <https://doi.org/10.3390/ijms22010192>.
- El-Kurdi, S.; Abu Thaher, B.; Wahedy, K.; Schollmeyer, D.; Nopper, L.; Riester, O.; Deigner, H. *Efficient Synthesis and X-Ray Structure of [1,2,4]Triazolo[4,3-a]Pyridines via Oxidative Cyclization Using N-Chlorosuccinimide (NCS)*. Crystals **2021**, 11 (10), 1156. <https://doi.org/10.3390/cryst11101156>.
- Liu, S.; Cheng, L.; Liu, Y.; Zhang, H.; Song, Y.; Park, J. H.; Dashnyam, K.; Lee, J. H.; Khalak, F. A. H.; Riester, O.; Shi, Z.; Ostrovidov, S.; Kaji, H.; Deigner, H. P.; Pedraz, J. L.; Knowles, J. C.; Hu, Q.; Kim, H. W.; Ramalingam, M. *3D Bioprinting Tissue Analogs: Current Development and Translational Implications*. Journal of Tissue Engineering **2023**, 14. <https://doi.org/10.1177/20417314231187113>.



# 1 Introduction

## 1.1 The Antibiotic Crisis

Antimicrobial resistance (AMR) is a pervasive challenge in today's healthcare system and poses a serious threat to human health. The World Health Organization (WHO) has classified it as one of the "urgent health challenges for the next decade" and drew attention to the rising number of deaths caused by antibiotic-resistant pathogens [1]. According to data from 2019, infections with antimicrobial resistant pathogens (AMR-Ps) are responsible for an alarming number of deaths worldwide: around 4.95 million (64 per 100,000) deaths are associated with AMR-Ps and 1.27 million (16.4 per 100,000) deaths are directly attributable to infections with AMR-Ps [2]. The WHO predicts that the number of deaths caused by AMR-Ps could rise to up to 10 million per year worldwide by 2050 if no action is taken [3]. Mestrovic et al. [4] stated in their study on the European region (including Central Asia) that developed countries, especially those with implemented national antimicrobial action plans (NAP), fare better. In Sweden, the country with the lowest mortality rate by AMR-Ps in the European region, only 11.8 deaths per 100 000 people are associated and 2.5 deaths per 100,000 people are directly attributable to infections with AMR-Ps. This is considerably lower than the average for the European region, with 541,000 (58.1 per 100,000) deaths associated and 133,000 (14.3 per 100,000) deaths directly attributable to infections with AMR-Ps. Around 78.8% of all deaths caused by AMR-Ps are due to either lower respiratory tract infections (LRI), bloodstream infections (BSI) or intra-abdominal infections, with LRI and BSI accounting for the majority of infection syndromes [2]. Most NAP aim to optimize the use of antimicrobials in human and animal health [5]. This is also reflected in the EU's proclaimed prevention strategy: "Reduce the overall use of antibiotics in humans by 20%" and "At least 65% of the total antibiotics used in humans should be used effectively" [6]. Examining national efforts, France, through the law No. 2014-1170 of 13 October 2014 on the future of agriculture, food and forestry (Article 49) [7], has demonstrated a commitment to reducing critical antibiotics by 25% until 2016, which was achieved according to the report: "Between 2014 and 2016, a decrease of 75% for fluoroquinolones and 81% for last generation cephalosporins was observed, largely fulfilling the objective established by the law in 2014" [8]. In 2021, the WHO reported that 163 countries had already participated in the survey on the implementation of the Global Action Plan on addressing AMRs [9], 122 of which had already implemented a NAP in 2022 according to the study by Charani et al. [10]. Although the importance of the issue has increased significantly worldwide and appropriate measures have been introduced, trends indicate that the overall global consumption of antibiotics will continue to increase, as in the treatment of children with lower respiratory tract infections, for example, an

increase by 46% has been observed between 2000 and 2018 [11]. In food-producing animals, in turn, an increase by 8% between 2020 and 2030 has been predicted [12]. Increased usage will inevitably lead to further development of resistance [13, 14], resulting in the spread of resistant pathogens, which in turn increases the chance of ineffective antibiotics being prescribed. As a result, the treatment is not effective and further antibiotics are prescribed - a vicious circle, as shown in Figure 1.1 - which progressively reduces the number of antibiotics that are still effective.

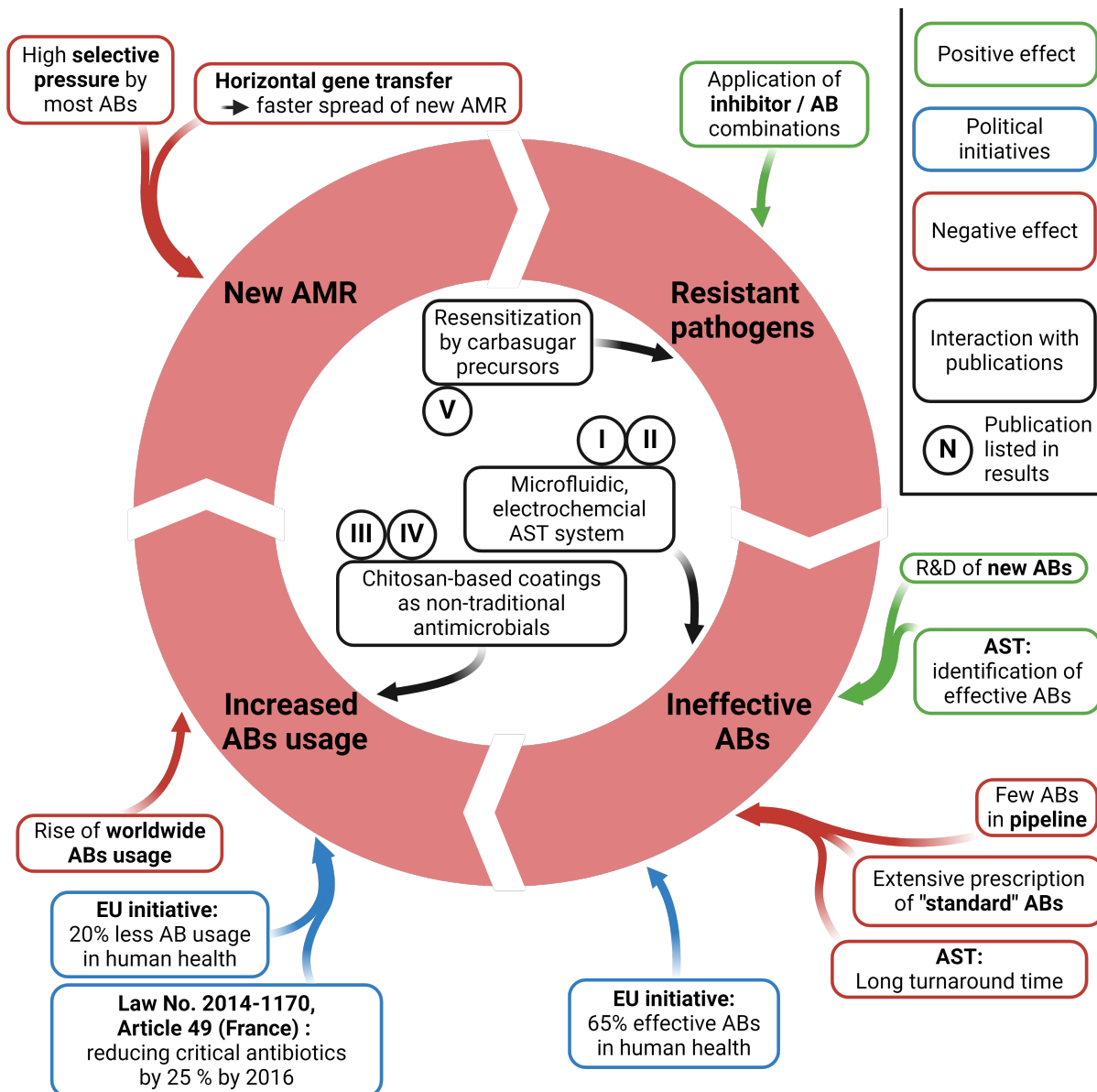


Figure 1.1: Vicious cycle of antimicrobial resistance (AMR) leading to the use of more antibiotics (ABs) and decrease of still effective critical ABs. Examples of policy initiatives, positive and negative effects and the interaction of the publications listed in the results on the cycle are presented. Figure created with biorender.com.

---

This circumstance could be safely neglected as long as sufficient new antibiotics were available and continuously new ones were developed to ensure the availability of effective antibiotics. Unfortunately, this is not the case, with only 32 new antibiotics currently in clinical trials targeting WHO priority pathogens [15]. Furthermore, only a small percentage ultimately receive approval, with just 5 new antibiotics (226 total new drugs) approved by the FDA between 2018 and 2022, compared to 16 (95 total new drugs) between 1983 and 1987 [16]. The decline in approved antibiotics, both in absolute numbers and relative to all drugs, combined with the identification of resistant pathogens often in less than one year after approval [17, 18], highlights the discrepancy between the clinical trial pipeline and clinical need. It is therefore crucial that these antibiotics are used responsibly to significantly extend the time until resistances emerge and safeguard the efficacy of these life-saving medications.

## 1.2 Antimicrobial Susceptibility Testing (AST)

An important tool in this context is the widespread use of antimicrobial susceptibility testing (AST), which allows existing antibiotics to be used much more efficiently while improving treatment outcomes and avoiding unnecessary side effects from the administration of ineffective antibiotics. The current approach for determining effective antibiotics involves a preliminary culture (e.g., blood culture for bloodstream infections (BSI)) and the subsequent AST using a disk diffusion test or automated methods. In order to start treatment without delay, especially in severe cases, broad-spectrum antibiotics are initially administered until the results of the AST are available. Using current clinical methods for BSI, the turnaround time from specimen collection to result is 28 hours at best, but usually 48 hours or more [19–21]. Yet, a rapid test of 8 hours would be desirable, limiting usage of broad-spectrum antibiotics to the first administration, as the decision on antibiotics for the second administration should be based on the AST [22, 23]. Short turnaround times are strived for in any diagnostic test, but in the case of AST, they are fundamentally important. Every hour earlier switched to targeted antibiotic therapy improves clinical outcomes [24–26], especially in patients with septic shock, where survival rates decrease by 7.6% for every hour of delay [27]. Given the fact, that the time to result has such a profound impact, both on the emergence of new resistance by reducing overall consumption of broad-spectrum antibiotics and on therapeutic outcomes by allowing earlier initiation of targeted antibiotic therapy, the scientific community has focused on developing new methods to reduce it. These methods can be classified into two categories, genotypic and phenotypic, with the phenotypic AST category comprising tests that detect the direct effect of the antibiotic on the pathogen, while the genotypic methods detect the presence of genes required for resistance [28].

It is important to note that, depending on the infection syndrome, a preculture may be required prior to AST, e.g., a blood culture for BSI, yet in many studies only the time for AST after preculture is stated, which can distort the actual time from patient to result. Genotypic AST, particularly based on whole genome sequencing (WGS) has attracted a lot of attention, as it was assumed to eliminate the need for high bacterial concentrations and thus pre-culture, resulting in a significantly shorter turnaround time. However, most current studies are still based on isolated pure cultures and therefore require a pre-culture [29]. In addition, WGS has shown the potential to remove the biggest challenge to genotypic AST so far - exclusion of AMRs due to the targeted approach - as genotypic AST was previously almost exclusively based on PCR [30–34] or microarrays [35, 36]. The technological improvements and greater accessibility of WGS have, therefore, significantly increased the power of genotypic AST, as the whole genome can be compared with databases for resistance and it is no longer necessary to decide in advance on the sequences or genes to be analyzed, which has been demonstrated in scientific studies using next-generation sequencing, e.g., nanopore sequencing [37–39] or

Illumina sequencing [40–42]. Due to the theoretical advantages of WGS - e.g., untargeted and without preculture - genotypic AST is envisioned as a new standard to replace the classical phenotypic AST prevalent in clinics, but to date these advantages remain entirely or partially theoretical and still need to be translated into practice in addition to cost, high-throughput and interpretative issues [43]. Technological advances of WGS substantially increased the potential of genotypic AST, while at the same time shifting the focus to the next challenge: the database. In order to detect the resistance genes, they must first be known and included in the database, such that matching the sequencing data with the database can identify them. However, this challenge appears to be manageable, even if it involves a considerable degree of effort and will require continuous updating of the database in the form of an ongoing process to incorporate newly discovered resistance genes. The fact that unknown resistance genes cannot be detected using this method is also only an issue in the initial phase of newly emerged resistances if the database is continuously maintained and unknown resistance mechanisms are systematically analyzed. However, the approach to solving this challenge is based on overcoming an even more fundamental issue, the existence of a single, unified database. This was also emphasized in the evaluation of WGS as an AST tool by European Committee on Antimicrobial Susceptibility Testing (EUCAST) in 2017, alongside the need for the database to support the various systems and bioinformatic tools available [29]. Consequently, the EUCAST report concluded that "for most bacterial species there is currently insufficient evidence to support the use of WGS-inferred AST to guide clinical decision making." [29]. The statement of the EUCAST report is further supported, for example, by a study by Rebelo et al. [44] comparing 500 bacterial isolates from Danish clinical microbiology laboratories using WGS (Illumina NextSeq, genotypic) and standard microdilution in broth (phenotypic). When comparing the results of both methods, Rebelo et al. found agreement in 91.7% of all cases (pathogen-antibiotic combinations). In 6.2%, no resistance was detected using microdilution in broth, whereas resistance was detected using WGS. The resistance genes were therefore present in these pathogens, but did not cause resistance, e.g., as a result of insufficient expression levels [45, 46]. Although these cases should be avoided in the future as they falsely exclude antibiotics that are still effective and consequently limit the choice of the most appropriate antibiotic for treatment, there is no direct harm to the patient as long as other effective antibiotics have been identified that can be administered. The remaining 2.1%, on the other hand, have the potential to negatively influence the treatment outcome, as these cases did not show resistance detected by WGS, although phenotypic resistance was present. Considering that these 2.1% of overall cases examined correspond to 26.4% of all phenotypically detected resistances, demonstrating that almost one in four resistances were not detected by WGS, highlights the current unsuitability of WGS as an AST tool for clinical decision making without phenotypic verification [22].

For the foreseeable future, phenotypic AST tests will therefore be irreplaceable as a standard for clinical decision-making, although this may change, as noted in the EUCAST report, once the

above-mentioned shortcomings of genotypic AST are addressed and genotypic AST provides comparable results and lower costs.

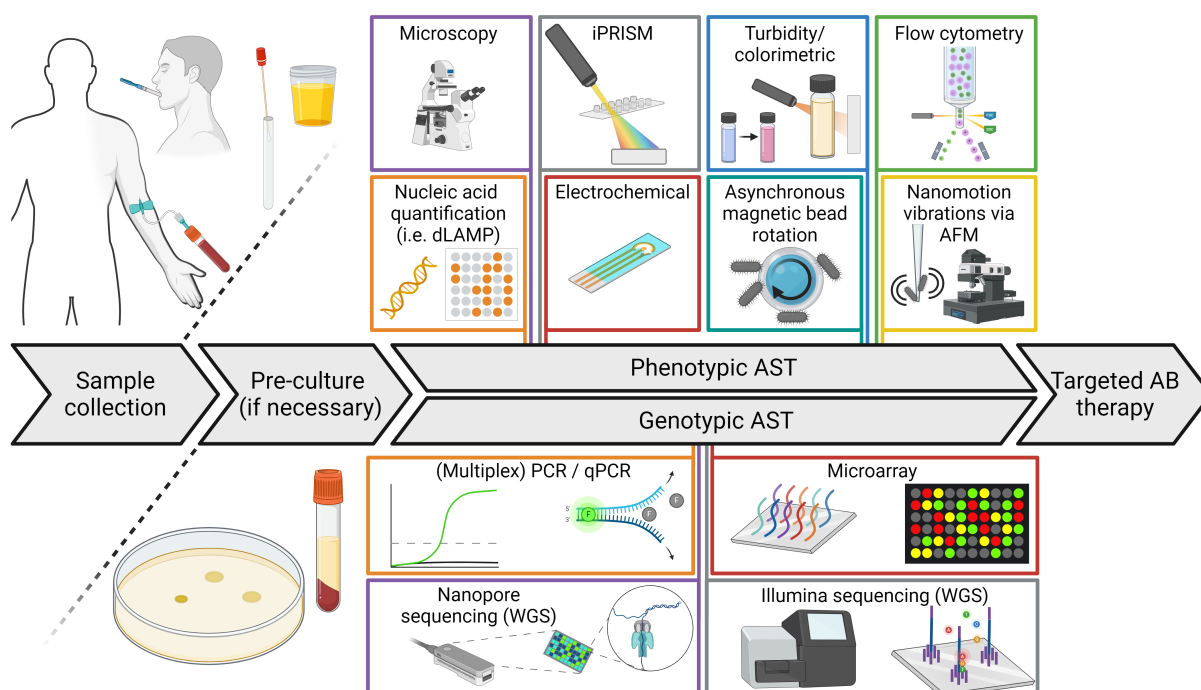


*Figure 1.2:* Workflow from sample collection until targeted antibiotic (AB) therapy. A generalized overview of several phenotypic [47–65] and genotypic [30–42] approaches for antimicrobial susceptibility testing (AST) methods is illustrated. Figure created with biorender.com.

The currently best option to improve AST is thereby to reduce the turnaround time of phenotypic ASTs and replace the current “gold standard” with novel methods surpassing it. Numerous approaches, including different methods and their combinations, have been presented in the scientific literature to shorten the turnaround time required for phenotypic AST, as illustrated in Figure 1.2. Examples include: microscopic detection of growth [47–49], colorimetric detection [59], fluorescence [60, 61], extracellular ATP by luminescence [62], flow cytometry [64], intensity-based phase-shift reflectometric interference spectroscopic measurements (iPRISM) [51], quantification of DNA [50], antibody-modified magnetic nanoparticles [63], vibrations by bacterial nanomotion [65], electrochemical measurement methods such as differential pulsed voltammetry (DPV) [52–55], cyclic voltammetry [56] or electrochemical impedance spectroscopy (EIS) [57, 58].

Most approaches focus on the AST itself and demonstrate significant time savings compared to current standards, but often neglect the steps between patient sampling and AST. These approaches start with samples in growth medium or urine with a high concentration of bacteria,

available only in special cases such as urinary tract infections with bacteria, but otherwise require pre-culture to achieve the initial bacterial concentrations necessary for the method. Considering that pre-culture and logistics currently take up a large part of the time from sample collection to result, greater attention should be paid on reducing or eliminating them. This applies in particular to lower respiratory tract infections (LRI) or bloodstream infections (BSI), which have very low bacterial concentrations (LRI: sputum  $> 10^4$  CFU/ml [66, 67]; BSI: serum  $< 10^3$  CFU/ml [68, 69]) and limit the possible direct-from-sample AST approaches due to viscosity and interference of present biomolecules. However, BSI and LRI are the two most common infectious syndromes associated with AMR-P and are responsible for the majority of deaths attributable to AMR-P [2]. Future phenotypic AST systems should, therefore, be compatible with samples associated with these infectious syndromes and also explicitly consider the time required for precultures.

## 1.3 Non-traditional Antimicrobials and Resensitization Strategies

Various resistance mechanisms against antimicrobials are known, as reviewed in detail by Smith et al. [70] or Darby et al. [71]; such as target modification and protection [72, 73], target repair and compensation [74, 75], agent modification or inactivation [76], restriction of membrane permeability [16], efflux pumps [77] or biofilm formation [78, 79]. The difficulty in tackling them is that resistance is subject to constant change and adapts quickly on a global level to the circumstances or antimicrobial strategies applied, e.g., through selective pressure, high mutation rates or horizontal gene transfer [80–82]. Despite the fact that the use of AST is an important, if not the most important instrument in the fight against AMR, it does not completely prevent the development of resistance, but only considerably slow it down, even if antibiotics are used appropriately [83, 84]. It, therefore, can be assumed that resistances will still be present in the future, and some of the future AMR mechanisms do not even exist today. In order to continue to have sufficient effective antibiotics available, it is imperative that new antimicrobial agents and strategies are developed or bacteria are resensitized to existing antibiotics. Traditional, or conventional, antibiotics refers to antibiotics by the paradigm of the first discovered antibiotics, which comprises nearly all of the currently used antibiotics, most of them are small molecules targeting physiological processes and prevent a specific, vital action, leading ultimately to bacterial death [16, 85]. Non-traditional antibiotics, on the other hand, refer to the broader category of all strategies and approaches that do not fit into the traditional category [86, 16]. Figure 1.3 provides an overview of antimicrobial agents, AMR mechanisms and resensitization approaches. Most non-traditional antimicrobials follow one of the following principles [87–91]; first, a reduced selection pressure, e.g., by supporting the host immune system or by reducing virulence factors. Second, an interaction with more fundamental principles, e.g., physical mechanisms such as the membrane integrity that affect multiple targets, or third, adaptive strategies that can easily cope with new resistances and evolve with them, e.g., bacteriophages. As previously mentioned, the number of newly developed antibiotics is low by historical standards and there are no signs of a trend reversal. The low number of newly approved antibiotics combined with increasing resistance has probably led to a paradigm shift in antibiotic treatment, which now aims to extend the time until antibiotics become ineffective instead of counteracting the emergence of resistance by developing more and more antibiotics. In addition to the use of AST, supplementing conventional antibiotic therapies with non-traditional antibiotics is, therefore, an advantageous approach, as the development of ever new conventional antibiotics only to discover resistance to them after a few months to years of clinical use seems rather unattractive and inefficient [17, 18]. It is likely that future antibacterial strategies will be based on a combination of several components which act mutually complementary, each in their most effective way.

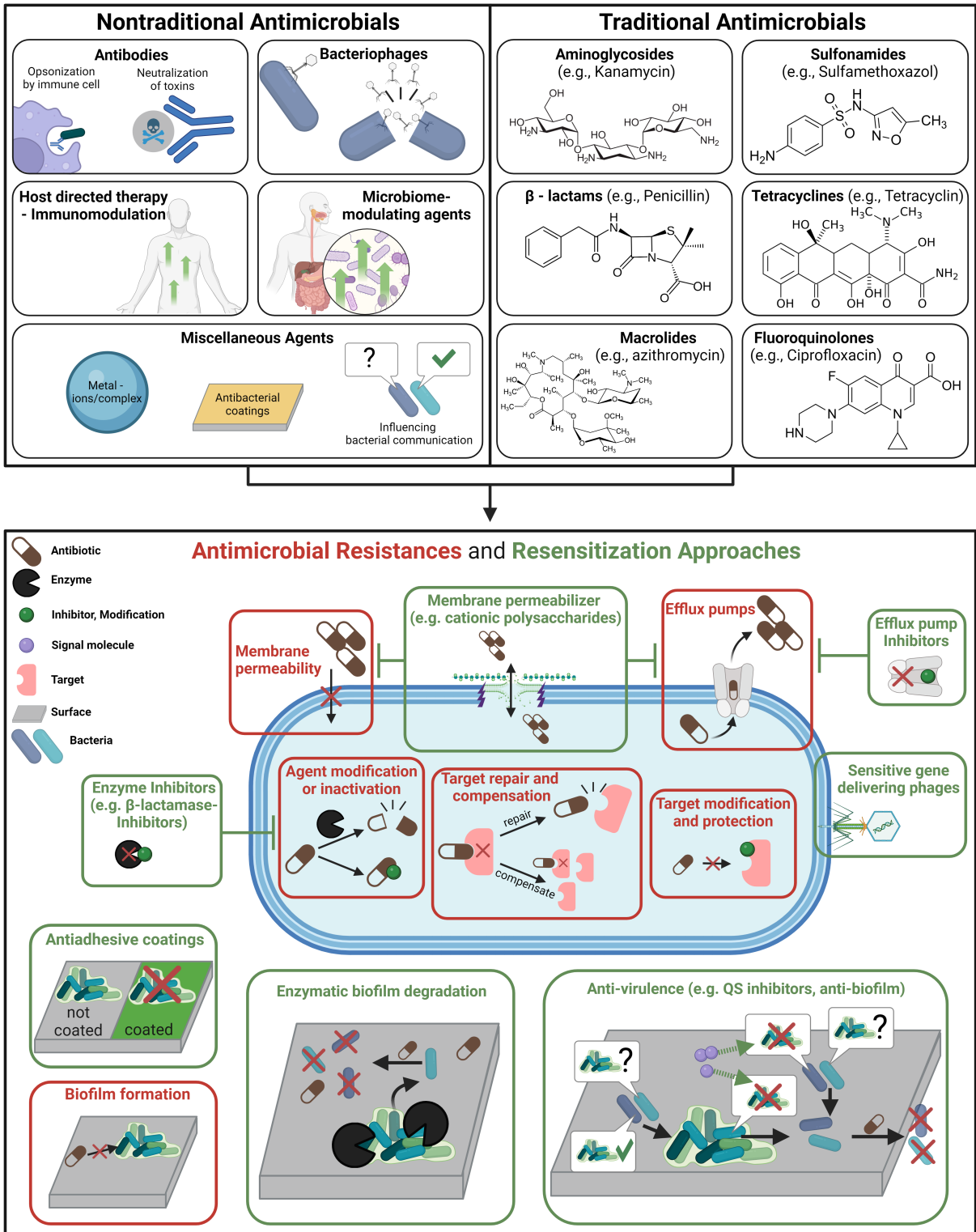


Figure 1.3: Generalized overview of most prominent traditional [92, 93] and non-traditional [94] antimicrobials, antimicrobial resistances and resensitization approaches. Figure created with biorender.com.

### 1.3.1 Coatings

One example, which is already being used in clinical practice in certain variants, is the use of antimicrobial coatings on implants, supplementing conventional systemic antibiotics and significantly reducing post-operative implant-related infections [95, 96]. Post-operative implant-related infections directly influence the success chance of the surgery, as an infection results in immunological host response, thereby increasing the likelihood of implant rejection, ultimately leading to implant failure [97]. Silver ions, nanoparticles, iodine or linked antibiotics are currently on the market as antibacterial implant coatings, while hydrophilic surfaces, superhydrophobic surfaces, anti-adhesive polymers, nanopatterned surfaces, enzyme- and biofilm-disrupting agents or chitosan derivatives are still in preclinical stages [98]. Surface modifications by physical or chemical modification in the form of coatings are particularly suitable for use on medical implants to prevent post-operative infections, as they are locally effective, can be applied to large surfaces and do not affect the mechanical properties of the implant [99]. By incorporating antibiotics directly into the coating, which are released over time, side effects can be drastically reduced as the systemic concentration is lower and the antibiotics are more effective due to a higher concentration at the implant site. Ideally, the coating and conventional antibiotics complement each other in one system and the use of systemic antibiotics becomes obsolete [100]. Another approach utilizing the properties of coatings aims at increased adhesion and proliferation of host cells to prevent rejection of the implant and thus improve tissue integration and biocompatibility, a process that the coatings can support through specific proliferative and adherent effects [101, 102]. This underlines the potential of coatings, especially for implants, as they can shift the probability of surface colonization to the advantage of the host cells by improving the host's regenerative capacity in combination with bactericidal activity.

### 1.3.2 Resensitization

Resensitization of AMR-*Ps* to antibiotics via inhibitors or adjuvants is another strategy that contributes to the continued availability of effective antibiotics as it is, by definition - Cambridge Dictionary: "to make someone sensitive to (= aware of or affected by) something again" [103] - the opposite of resistance emergence. In this context, the strategy of antibiotic adjuvants can help to increase the availability of effective antibiotics in a more cost-effective way than the continuous development of new antibiotics [104]. Nevertheless, the impact is probably in the short term, as resensitization by adjuvants is subject to the same challenge as the antibiotics themselves: It promotes the development of resistance due to the selective pressure of the antibiotic-adjuvant combination on the bacterial population [105]. Similar to antibiotics, it is, therefore, likely that resensitization strategies with high selective pressure or directed only at a specific target will become ineffective quickly, whereas strategies based on a more fundamental

principle that induce less selective pressure (e.g., anti-virulence or quorum sensing [106, 107]) should have a lower probability of developing resistance.

Various strategies to resensitize AMR-*P*s are described in the scientific literature, and those approved for clinical use are mainly inhibitors of  $\beta$ -lactamases (e.g., clavulanic acid, sulbactam, tazobactam, avibactam, varborbactam and relebactam) [108, 109]. This is not surprising, as with the introduction and clinical success of the first traditional antibiotic, the  $\beta$ -lactam antibiotic penicillin G, research and development of new antibiotics focused on its derivatives, resulting in many antibiotics with the common structural feature of the  $\beta$ -lactam ring [110]. As a result, between 2004 and 2014, 65.24% of all antibiotics prescribed in the United States were from the  $\beta$ -lactam class [111]. Since resistance to  $\beta$ -lactam antibiotics mainly occurs in the form of enzymes, the  $\beta$ -lactamases, and the use of antibiotics of the  $\beta$ -lactam class is widespread, it is obvious that the majority of interest for inhibitors also relates to these [112]. One example is the study by Tehrani et al. [113] describing the use of commonly used small molecule carboxylic acid derivatives to inhibit metallo- $\beta$ -lactamases. Other studies focused on the use of drugs already approved for other applications, such as auronofin [114], an antirheumatic drug, showing synergistic effects in combination with carbapenem and colistin by displacement of Zn(II) cofactors necessary for resistance, or disulfiram [104], an alcohol-abuse drug, restoring the susceptibility of AMR-*P*s to carbapenem and colistin. Approaches that are not based on the inhibition of enzymes have also been described, for instance Mu et al. [115] described cationic polysaccharides damaging the inner and outer membrane of bacteria and affecting efflux pumps, resulting in resensitization of multidrug-resistant bacteria to rifampicin. Another study achieved resensitization utilizing dominant sensitive gene delivering phages [116].

The study of bacterial behavior has led to the discovery of underlying mechanisms and systems that can be exploited by new strategies to target the virulence factors responsible for AMR or pathogenesis. Virulence factors are considered to be bacterial properties that have a pathogenic effect, with biofilm formation currently being one of the most important virulence factors responsible for AMR [117]. Restricted access at the molecular level through a combination of diffusion barriers across the extracellular matrix, efflux pumps and antimicrobial-destroying enzymes in conjunction with gene transfer and biofilm-integrated persister cells as AMR mechanisms significantly limits treatment once the biofilm has formed [118]. The resensitization and prevention of biofilm associated AMR results in three different treatment approaches [119]; first, prevention of biofilm formation at an early stage by inhibiting the adhesion of bacteria to surfaces. Second, disrupting an existing biofilm and third, interfering with bacterial response regulators affecting the quorum sensing system. Depending on the circumstances and application, all three approaches have their advantages and are more or less suitable. Biofilm prevention is particularly relevant in the form of coatings on indwelling medical devices, as it can pre-emptively and locally prevent the formation of biofilms on high-risk surfaces. When the

biofilm is already present on a surface, treatment with matrix degrading enzymes is one option. Two examples of enzymes described in the literature for this purpose are Dispersin B and DNase I. Dispersin B hydrolyzes the glycosidic bonds of  $\beta$ -1,6-N-acetyl-D-glucosamine [120] and endonuclease DNase I inhibits early biofilm formation by cleaving phosphodiester bonds adjacent to pyrimidines [121, 122].

Influencing the quorum sensing (QS) system is one of the more recent approaches to combat AMR, as "we are beginning to understand the links between QS and bacterial sociality" [123]. Nevertheless, using the bacteria's own communication system to disperse biofilm and decrease virulence appears to be more favorable in terms of practicability and probability of resistance emergence than combating each biofilm-associated resistance mechanism individually. The most prominent signaling molecules that play a role in the quorum sensing system include N-acylhomoserine lactone (Gram-negative pathogens), autoinducing peptides (Gram-positive bacteria) and autoinducer-2 [124, 125]. Several compounds have been identified to interfere with the QS system and have shown promising results to inhibit biofilm formation and disperse biofilms; furanones [126, 127], 2-aminoimidazole compounds [128] or N-Acyl Cyclopentylamides [129] are some examples.

This dissertation addresses several projects in these areas, the objectives of which are described in more detail in the next chapter.

## 2 Objectives

The balance between the emergence of new AMRs and the amount of available and effective antimicrobial agents is constantly changing. Over the last decades, the number of new AMRs has outweighed the number of new antibiotics, leading to obvious challenges in hospitals and medical treatment worldwide. Since the emergence and spread of new AMRs results from the selective pressure of antibiotics, new resistances will emerge as long as antibiotics are used. Consequently, as long as humans utilize antibiotics, they will continue to be confronted with new resistances against them. To shift this balance in favor of human beings, the development of new antibiotics, including new therapeutic approaches, must therefore go hand in hand with the responsible and effective use of antibiotics to minimize new resistances. The aim of this dissertation is to investigate different approaches for this purpose.

### **2.1 Antibiotic Susceptibility Testing (AST) for Responsible and Effective Use of Antibiotics to Minimize New Resistances**

A fundamental prerequisite for the responsible use of antibiotics is the ability to identify which antibiotics are effective and which are not. This project's objective was to develop a rapid electrochemical AST system, which is easy to use and produces results after around 8 hours directly from serum. Therefore, the possibilities of 3D printing for the production of microfluidic prototypes on a laboratory scale were created first. An important part of this work was to find out which material is suitable for biological applications, as it must be suitable for printing microfluidic structures, as well as being water-resistant and non-toxic. The second part of the project was the development of a 3D-printed prototype for a rapid, electrochemical, phenotypic AST, which was achieved by combining the established 3D printing process with electrochemical measurement methods and computational analysis. The AST was demonstrated for 4 clinically relevant pathogens of bloodstream infection using artificially spiked plasma with realistic bacterial concentrations as samples and showed results 5 to 10 hours after sampling.

## **2.2 Chitosan as a Natural Antimicrobial Material for Novel Coatings**

The prevention of microbial infections by prophylactic administration of antibiotics is a standard procedure for implant surgery in order to significantly reduce the risk of implant failure [130]. Initial local infections, that can arise from surgical wounds or contaminated implant surfaces, offer the opportunity to treat the infection locally without the need for high doses of systemic antibiotics, reducing the overall used amount of antibiotics and the associated side effects. Antibacterial or anti-adhesive coatings in particular are suitable for this challenge as they are locally effective, prevent biofilm formation, can be applied to the implant prior to surgery and also have the potential to improve host cell attachment to accelerate regeneration if desired. The project focused on the use of chitosan, a natural antibacterial material, or its derivatives as inspiration for biocompatible coatings. The coatings were evaluated for their suitability when applied to polymer surfaces, in particular polyether ether ketone (PEEK), their antimicrobial and antibiofilm properties and their biocompatibility.

## **2.3 Glycomimetic Adjuvants: Carbasugar-precursors as Biofilm Inhibitors and Resensitization Approach**

Glycomimetics are another resensitization approach with enormous potential but also challenges. The underlying idea is that glycomimetics are similar to natural carbohydrates but with different biological properties, thereby can act as inhibitors or signaling molecules without contributing as a energy source to bacterial growth, as they show enhanced chemical and enzymatic stability [131]. The variety of substrates that can be mimicked in theory makes it possible to influence any process in microbes involving carbohydrates, with the distinct advantage of their chemical and enzymatic stability, allowing effective concentrations to be present over longer periods. The biggest challenge, however, is that it is difficult to predict the actual mechanism of action of the glycomimetic, as it can influence several enzymatic reactions, metabolic pathways and signaling pathways, so that for applications the effect is often simply determined experimentally without knowing the exact mechanism. In this project, the effect of synthesized carbasugar-precursors on human cells and bacteria was evaluated by assessing their cytotoxicity, biofilm inhibiting and antimicrobial properties with the aim of applying these molecules as antibiotic adjuvants appropriate for their effects.

# 3 Results and Discussion

## 3.1 Antibiotic Susceptibility Testing (AST)

### 3.1.1 Direct 3D Printed Biocompatible Microfluidics: Assessment of Human Mesenchymal Stem Cell Differentiation and Cytotoxic Drug Screening in a Dynamic Culture System

#### Own contribution to the article

The authors' contribution to this publication was as follows. The conceptualization of the study was performed by Prof. Deigner and the author of this thesis. All experiments were planned, performed and evaluated by the author of this thesis. Prof. Deigner was responsible for funding acquisition and shared the supervision of the work with Prof. Laufer. Writing of the original draft with visualizations was carried out by the author of this thesis with constructive input from Prof. Deigner. All authors reviewed, edited and approved the manuscript.

Reprinted with permission from the Authors. Journal of Nanobiotechnology published by BioMed Central Ltd. (Part of Springer Nature). Copyright © 2022, The Author(s). This article is an open access article distributed under a Creative Commons Attribution 4.0 International License (<http://creativecommons.org/licenses/by/4.0/>).

**Riester, O.; Laufer, S.; Deigner, H.-P. Direct 3D Printed Biocompatible Microfluidics: Assessment of Human Mesenchymal Stem Cell Differentiation and Cytotoxic Drug Screening in a Dynamic Culture System. Journal of Nanobiotechnology 2022, 20 (1), 540. <https://doi.org/10.1186/s12951-022-01737-7>.**

RESEARCH

Open Access



# Direct 3D printed biocompatible microfluidics: assessment of human mesenchymal stem cell differentiation and cytotoxic drug screening in a dynamic culture system

Oliver Riester<sup>1,2</sup>, Stefan Laufer<sup>2,3</sup> and Hans-Peter Deigner<sup>1,4,5\*</sup>

## Abstract

**Background:** In vivo-mimicking conditions are critical in in vitro cell analysis to obtain clinically relevant results. The required conditions, comparable to those prevalent in nature, can be provided by microfluidic dynamic cell cultures. Microfluidics can be used to fabricate and test the functionality and biocompatibility of newly developed nanosystems or to apply micro- and nanoelectromechanical systems embedded in a microfluidic system. However, the use of microfluidic systems is often hampered by their accessibility, acquisition cost, or customization, especially for scientists whose primary research focus is not microfluidics.

**Results:** Here we present a method for 3D printing that can be applied without special prior knowledge and sophisticated equipment to produce various ready-to-use microfluidic components with a size of 100 µm. Compared to other available methods, 3D printing using fused deposition modeling (FDM) offers several advantages, such as time-reduction and avoidance of sophisticated equipment (e.g., photolithography), as well as excellent biocompatibility and avoidance of toxic, leaching chemicals or post-processing (e.g., stereolithography). We further demonstrate the ease of use of the method for two relevant applications: a cytotoxicity screening system and an osteoblastic differentiation assay. To our knowledge, this is the first time an application including treatment, long-term cell culture and analysis on one chip has been demonstrated in a directly 3D-printed microfluidic chip.

**Conclusion:** The direct 3D printing method is tested and validated for various microfluidic components that can be combined on a chip depending on the specific requirements of the experiment. The ease of use and production opens up the potential of microfluidics to a wide range of users, especially in biomedical research. Our demonstration of its use as a cytotoxicity screening system and as an assay for osteoblastic differentiation shows the methods potential in the development of novel biomedical applications. With the presented method, we aim to disseminate microfluidics as a standard method in biomedical research, thus improving the reproducibility and transferability of results to clinical applications.

\*Correspondence: [dei@hs-furtwangen.de](mailto:dei@hs-furtwangen.de)

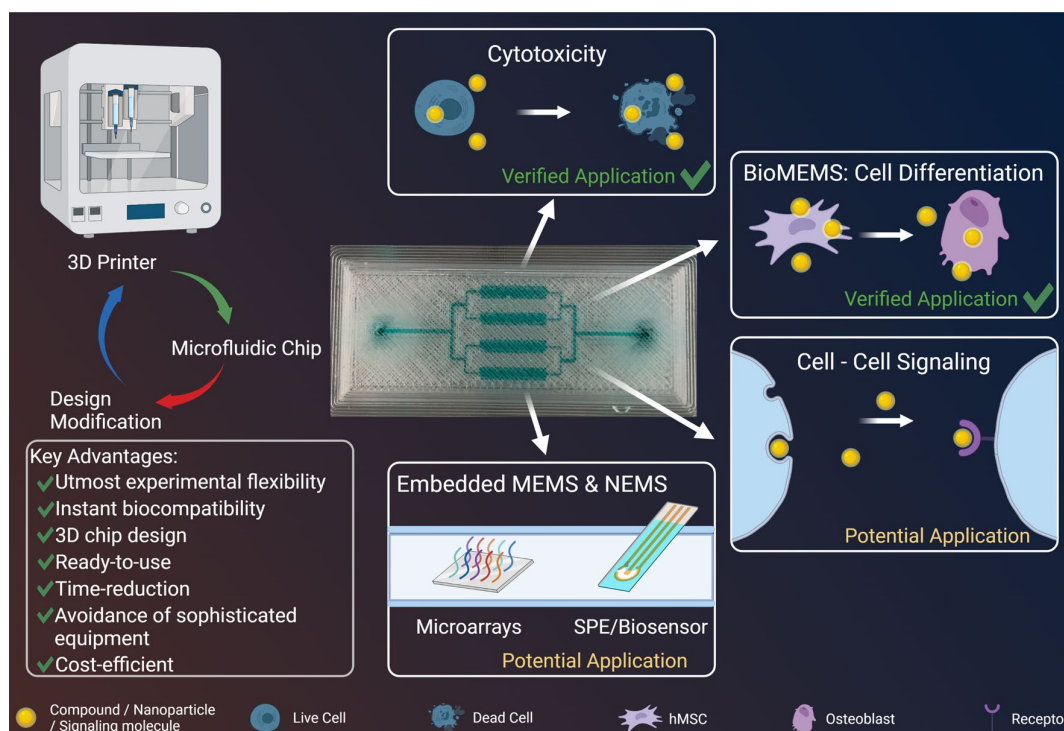
<sup>1</sup> Institute of Precision Medicine, Furtwangen University, Jakob-Kienzle-Strasse 17, 78054 Villingen-Schwenningen, Germany  
Full list of author information is available at the end of the article



© The Author(s) 2022. **Open Access** This article is licensed under a Creative Commons Attribution 4.0 International License, which permits use, sharing, adaptation, distribution and reproduction in any medium or format, as long as you give appropriate credit to the original author(s) and the source, provide a link to the Creative Commons licence, and indicate if changes were made. The images or other third party material in this article are included in the article's Creative Commons licence, unless indicated otherwise in a credit line to the material. If material is not included in the article's Creative Commons licence and your intended use is not permitted by statutory regulation or exceeds the permitted use, you will need to obtain permission directly from the copyright holder. To view a copy of this licence, visit <http://creativecommons.org/licenses/by/4.0/>. The Creative Commons Public Domain Dedication waiver (<http://creativecommons.org/publicdomain/zero/1.0/>) applies to the data made available in this article, unless otherwise stated in a credit line to the data.

**Keywords:** Microfluidic, Direct 3D printed, Drug screening system, Stem cell differentiation, Microfluidic long-term cell culture, Ready-to-use, Biocompatible

### Graphical Abstract



### Background

The ability of stem cells to differentiate into specialized cell types is considered one of the most promising ways to replace damaged tissue or even entire organs, and to provide effective treatments for numerous diseases [1, 2]. However, despite major research efforts in this field over the past decades, the application of stem cell therapies beyond clinical trials still faces several practical challenges, including stem cell origin, isolation, expansion, stability and efficient protocols for targeted differentiation [3, 4]. The systems investigated are becoming increasingly complex, particularly in the fields of system- and cell biology, wherein many systems interact and are often not fully understood [5–8]. These problems led to the development of high-throughput methods as well as the software necessary to create, treat and analyze the large numbers of test samples [9–11]. Stem cell differentiation is one of these complex processes influenced by a variety of extrinsic and intrinsic interactions [12–14]. In targeted stem cell differentiation, not only single molecules or mechanisms, but a multitude of extrinsic and

intrinsic interacting systems are crucial in ultimately determining the lineage of differentiation. Microfluidic systems help in targeted differentiation, analysis and cultivation of stem cells by creating realistic microenvironments or by improving the predictability of biological assays. According to Ertl et al., microfluidic devices offer many advantages “to overcome most of the challenges associated with stem cell identification, expansion and differentiation, with the greatest advantage being that lab-on-a-chip technology allows for the precise regulation of culturing conditions, while simultaneously monitoring relevant parameters using embedded sensory systems” [15]. Microfluidic applications range from the production of nanomaterials and chemical reactions to biosensors, diagnostic systems and high-throughput screening systems [16–22]. The characteristics of a microfluidic system with laminar flow and short diffusion paths optimize these applications in many aspects, for example by enabling users to manipulate liquids in a targeted manner and achieve near-ideal mixing ratios without additional energy input. Microfluidic devices have

shown promising results in life sciences, such as decreased consumption of expensive and limited materials, or the establishment of manipulable dynamic culture systems superior to static cell culture systems [23–26]. However, one factor in particular has made these systems difficult to obtain for many researchers and therefore rarely used: experiments or applications often require customized devices, thus hindering standardized commercial manufacturing [27]. Consequently, many applications are limited by the standardized chips available on the market, which are often simply designed to be suitable for as many applications as possible. For more demanding applications, users must either have equipment for in-house production or rely on custom-made chips [28, 29]. Both options are often costly, thus discouraging many users. On-site production is preferable solely because it eliminates delivery times, thus allowing for immediate adjustments and improvements, particularly in prototype production. The current standard procedures for the creation of individualized microfluidic devices are indirect casting processes, photolithography or e-beam lithography; these labor- and equipment-intensive methods require extensive manual work [30, 31]. Soft lithography is another method for producing micro- and nanostructures that is more cost-effective than photolithography, because it no longer requires a clean room. However, the costs still prevent widespread use, and the method remains labor intensive [32, 33]. Another disadvantage of these techniques is that they can only be used to produce 2D chip designs, and even here they require experienced personnel, as several layers have to be joined manually. Nevertheless, these methods remain in use because they have achieved the best accuracy to date and have produced structures on the scale of several nanometers [30]. In contrast, micropaper-based analytical devices ( $\mu$ PADs) are very well suited when high accuracy at nanometer and micrometer scale is not required. The idea underlying  $\mu$ PADs is to make microfluidic systems ready for mass production of simple and rapid diagnostic tests. The low accuracy and the generation of only 2D chips is sufficient for many applications but limits the design of more advanced chips [34]. Given the aforementioned methods, the production of complex 3D microfluidic chips is not a trivial challenge. 3D printing emerged as an alternative method for the production of microfluidics. Commercially available 3D printers currently have sufficient accuracy to print channel widths of several hundred micrometers, as a result of intensive development in recent decades [35, 36]. Several 3D printing technologies are available, such as inkjet printing [37], stereolithography (SLA) [38], digital light processing [31] and fused deposition modeling (FDM) [39]. FDM is the most widely used 3D printing technology, owing to

its simplicity: only the polymer filament is needed as a resource in the process, in contrast to other printing technologies in which the polymers are dissolved in a solution or are present as a resin and polymerize in the process [35, 40]. FDM 3D printers are popular not only because of their ease of use but also because they do not require additional substances such as photoinitiators, which are often toxic and leak from devices over time [41]. In addition, a wide range of polymers can be purchased, thereby avoiding limitations in material selection. For the production of microfluidic chips by 3D printing, two production options are available: indirect production [42], in which a negative form is printed for a casting process, and direct production, in which the computer-aided design (CAD) model is converted directly to the microfluidic chip. Indirect production, as shown by He et al. [43], results in highly transparent and biocompatible chips suitable for cell culture and analytical assays. However, they are limited by two factors: first, the minimum component size is determined by the width of the printable line. Second, the printed negative mold must be stable and elastic enough not to be deformed during casting. This is particularly challenging for large and complex 3D structures connected by small channels. In contrast, directly printed chips do not have any stability problems of a negative mold, but have lower material transparency depending on the manufacturing process, which hampers optical measurements and observations. Bressan et al. [44] created a mixture of both fabrication methods by inserting a prefabricated transparent window made of poly (methyl methacrylate) (PMMA) into a chip printed from poly (lactic acid) (PLA). Thus, the problem of transparency was solved, but replaced by a vulnerability at the interface of the two materials, leading to leakage. A different approach to achieve the necessary transparency is to optimize the printing parameters, as shown for example by Tothill et al. for PLA [45]. However, these parameters are material-specific and must therefore be investigated once for the respective polymer before application. Most previous studies on direct FDM 3D printing either show simple applications with only one component on a chip and channel sizes in the millifluidic range, or focus on the achievable accuracy without showing suitability for biological applications [37, 46]. In this study, we therefore demonstrate the fabrication of biocompatible microfluidic chips with structures of 100  $\mu$ m and smaller using three relevant polymers and that experiments from preparation to cell culture and analysis can be performed on a single chip by combining multiple components. We studied the polymers—PLA, PMMA and polycarbonate (PC)—which are frequently used in the field of microfluidics and cover a wide range of applications with their advantages and characteristics, as

listed in Table 1. PLA, for example, is particularly suitable for prototype construction or the generation of vascular scaffolds [47], owing to its simple handling, good availability and high accuracy. PMMA, in contrast, has excellent biocompatibility and modifiability with different chemical groups [48–50]. The third polymer, PC, has high mechanical stability, as well as temperature resistance and chemical stability against acids [51], and is ideal for applications with high temperatures up to 140 °C [52]. Here, we demonstrated the generation of microfluidic chips by using the mentioned polymers, without a need for additional support materials. In the device generation, we used the direct 3D printing principle, as shown in Fig. 1, which allowed us to generate ready-to-use microfluidic devices from the CAD model with just several clicks. In this context, we demonstrate the fabrication of 3D chip designs and widely used microfluidic structures, as well as their application in microfluidic cytotoxicity and stem cell differentiation assays.

## Results

### Resolution of direct 3D printed microfluidic channels

The direct FDM 3D printing of microfluidic devices is influenced by various parameters including the accuracy of the printer step motors, the printer head nozzle

diameter, the environmental temperature and even the humidity. In this study, four parameters were optimized for each polymer: printing temperature ( $\vartheta$ ), printing speed ( $v$ ), layer height ( $h$ ) and fan speed ( $fan$ ). Each parameter is directly involved in the printing process and has a significant influence on the obtained dimensions of printed structures [37, 69, 70]. It was observed that  $\vartheta$  and  $v$  had the strongest effect on the printing results (Additional file 1: Fig. S1–S15), while layer height and fan speed had a lesser influence. The former ( $h$ ) showed an effect, particularly at low Z-resolution, because the structure must be sliced as an integer multiple of the layer height. Layer heights of 200  $\mu\text{m}$  resulted in the loss of structures below 200  $\mu\text{m}$  in the Z-direction or were sliced as if they were 200  $\mu\text{m}$  structures. Very low layer heights, such as 25  $\mu\text{m}$ , resulted in good slicing, but the printed layers were not uniform because the print head smudged the newly applied material. Layers of 100  $\mu\text{m}$  provided a good compromise between both effects and were therefore used in further printing tests. The optimized parameters for the three tested polymers PLA, PMMA and PC are listed in Table 2. By applying the listed parameters, channel widths of 100  $\mu\text{m}$  and channel heights of 300  $\mu\text{m}$  were reproducibly generated, as shown in Fig. 2. The low standard deviations (Fig. 2) obtained

**Table 1** Characteristics and possible applications of poly (lactic acid) (PLA), poly (methyl methacrylate) (PMMA) and polycarbonate (PC) in the generation of microfluidic devices

Polymer	Characteristics	Possible applications
PLA	Advantage: <ul style="list-style-type: none"> <li>• Easy to use</li> <li>• Recyclable</li> <li>• Transparent</li> <li>• Low auto-fluorescence [53]</li> <li>• No absorption of small molecules [53]</li> </ul> Disadvantage: <ul style="list-style-type: none"> <li>• Hydroscopic material – swelling in water</li> <li>• Lactic acid as degradation product</li> <li>• Can show cytotoxic effects</li> </ul>	Prototype design Organ on-chip [53] Cell culture [53] Incorporation of Microelectrodes [54]
PMMA	Advantage: <ul style="list-style-type: none"> <li>• Transparent</li> <li>• Biocompatible [48, 49]</li> <li>• Surface modification [50]</li> <li>• Heat resistant up to 90 °C [55]</li> <li>• Impermeable to air [56]</li> <li>• UV-resistant</li> <li>• Resistant to many acids, bases, alcohols, oils and fats [57]</li> </ul> Disadvantage: <ul style="list-style-type: none"> <li>• Not resistant to many organic solvents</li> </ul>	PCR-on-chip [50] Lab-on-chip [58–60] DNA/Protein analysis [61, 62] Electrochemical detection [54, 63] Colorimetric assays Assembling of micro and nanoparticles [44, 64]
PC	Advantage: <ul style="list-style-type: none"> <li>• Transparent</li> <li>• Heat resistant up to 140 °C [52]</li> <li>• Acid resistance [51]</li> <li>• Naturally hydrophilic surface [65]</li> <li>• Surface modification [66]</li> </ul> Disadvantage: <ul style="list-style-type: none"> <li>• Sensitive during printing process: environmental conditions</li> <li>• Poor adhesion properties during the printing process</li> </ul>	Electrochemical detection [54, 67] Lab-on-chip [60, 67] PCR-on-chip [65, 68] Biomedical studies [68] Droplet generation [65]

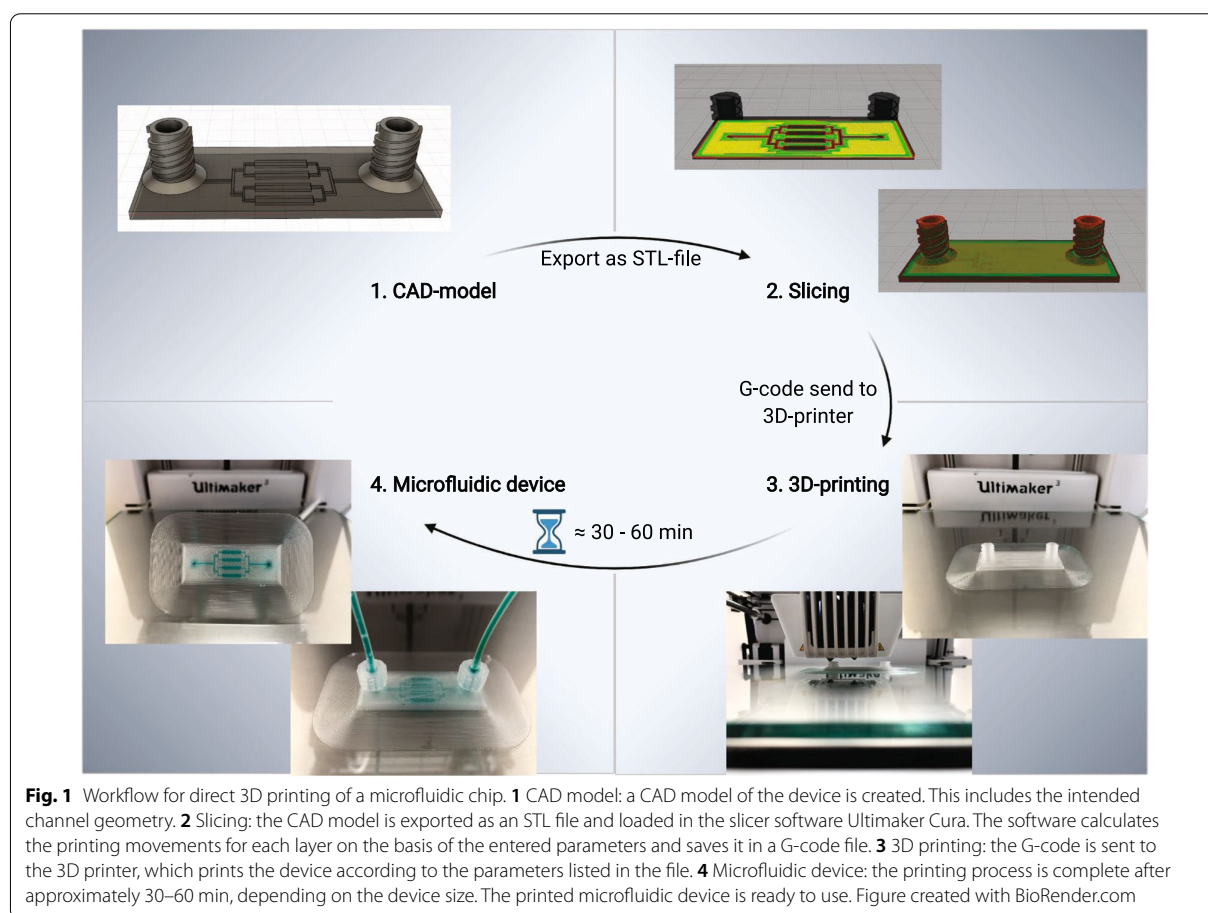


**Table 2** Optimized printing parameters for the generation of microfluidic devices with an Ultimaker 3 FDM 3D printer and Ultimaker Cura Slicer Software

Polymer	Printing temperature [°C]	Printing speed [mm s <sup>-1</sup> ]	Layer height [mm]	Fan speed [%]
PLA	190	70	0.1	50
PMMA	245	70	0.1	50
PC	240	80	0.1	0

across three different devices indicate good and consistent device to device performance. The polymers PLA and PMMA showed the best correlations between the CAD model and the obtained channel widths (Additional file 1: Fig. S16–S18), with only occasional significant differences between them. PC, on the other hand, mostly resulted in significantly smaller channels than specified, especially for channel widths of 500  $\mu\text{m}$  (X:  $400 \pm 28 \mu\text{m}$ ; Y:  $452 \pm 22 \mu\text{m}$ ) and 1000  $\mu\text{m}$  (X:  $826 \pm 22 \mu\text{m}$ ; Y:

$946 \pm 35 \mu\text{m}$ ). Printing channels with a width of 50  $\mu\text{m}$  was also possible, but they occasionally merged and required post-processed manual verification of permeability (Additional file 1: Fig. S13). Therefore, they were excluded from the data shown.

### 3D microfluidic structures

It is beneficial to perform all steps of an experiment (preparation/treatment, cultivation, analysis) on one chip in order to achieve additional benefits for biomedical applications. Therefore, it is preferred to produce and combine several components and structures on one chip, resulting in customized chip designs. However, the production of customized devices is often time-consuming and expensive [71]. Thus, 3D printing enables new devices to be designed and adapted in a time-efficient, cost-efficient and customized manner. The practicality and advantages of 3D printed microfluidic systems was demonstrated by creating and testing three microfluidic chip designs. The generated chips are shown in Fig. 3. First, a chip with two intersecting serpentine channels

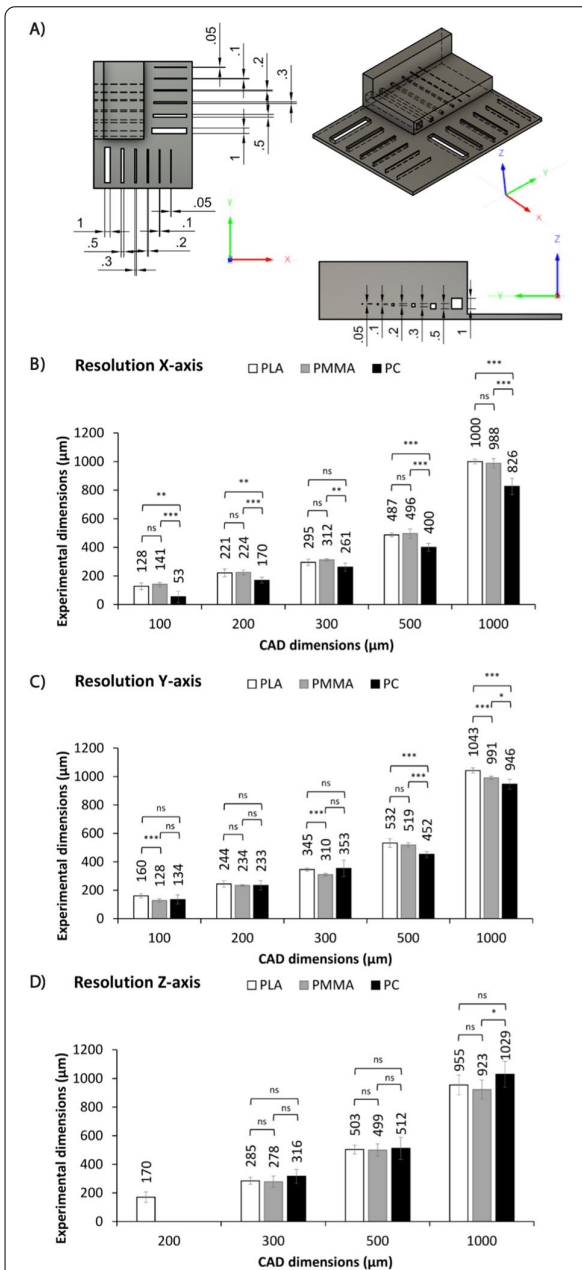


**Fig. 2** Measurement of widths and heights of FDM printed microchannels. The printed test objects were compared with the CAD model to evaluate the achievable resolutions for poly (lactic acid) (PLA), poly (methyl methacrylate) (PMMA) and polycarbonate (PC). **A** CAD model of the test device. Dimensions are in mm. **B** Resolution of channel widths along the X-axis of the 3D printer. Dimensions are in µm. **C** Resolutions of channel width along the Y-axis of the 3D printer. Dimensions are in µm. **D** Resolution of channel height along the Z-axis of the 3D printer. Dimensions are in µm. Values are shown as mean  $\pm$  SD of 3 devices, 3 measurements per device. Statistical significance was analyzed with Two-way ANOVA and Tukey post-hoc test (n s, not significant; \* $p < 0.05$ ; \*\* $p < 0.01$ ; \*\*\* $p < 0.001$ )

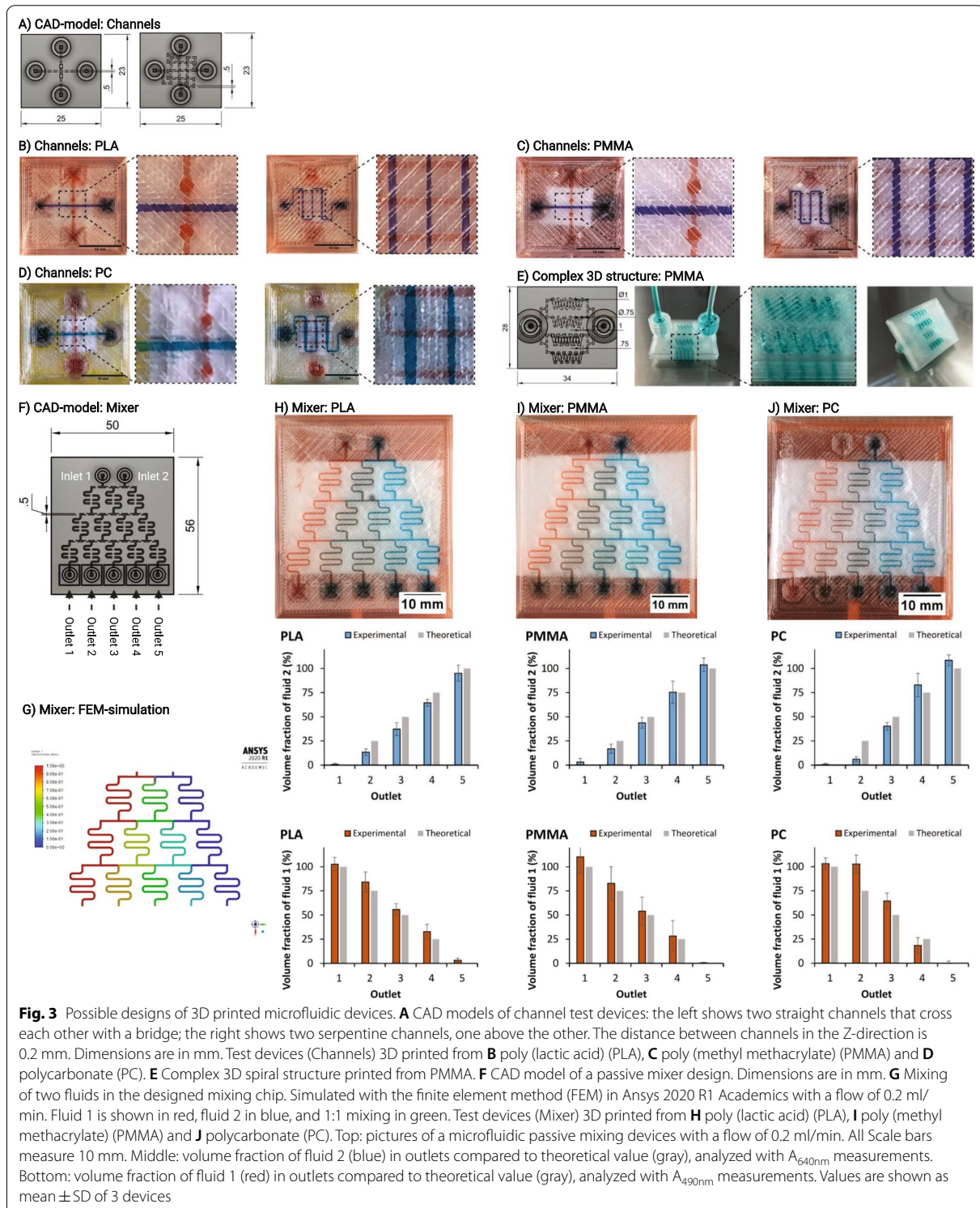
with a spacing in the Z-direction of 0.2 mm was printed. Multiple layers of channels were successfully created on top of each other without leakage, separated by only two printed polymer layers in between. This design is advantageous because several channel structures can be stacked on top of each other, reducing the device's size. The second chip generated consisted of two straight channels crossing each other with a bridge, demonstrating the feasibility of printing channels not only in the X- and Y-directions, but also in the Z-direction for all three polymers tested. This ability facilitates chip planning and the connection of channels, which need not be arranged next to each other as in 2D chip designs. The third chip design (Fig. 3E) shows a 3D spiral structure as an example of more complex structures, that are difficult to produce using traditional methods. This third chip design was printed with PLA, PMMA and PC (only PMMA shown), with PC causing channel closure and PLA and PMMA showing comparable results.

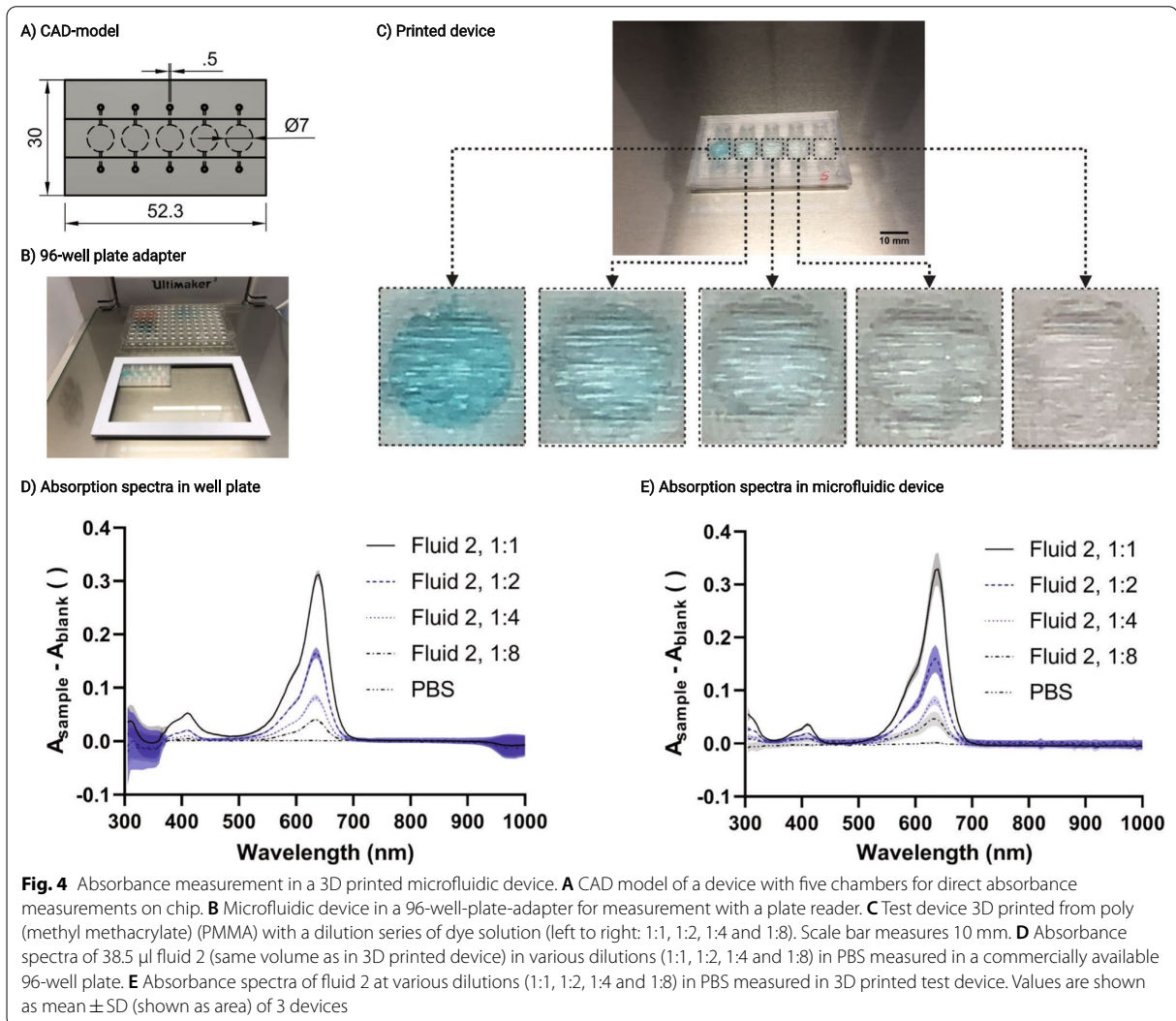
#### Microfluidic concentration-gradient generator

A frequently used component in the preparation/treatment steps of microfluidic experiments are gradient generators. The passive mixer shown in Fig. 3F) was 3D printed from PLA, PMMA and PC with the parameters in Table 2. The absorbance of fluids eluted from test devices at outlets 1 to 5 was measured at 490 nm and 640 nm to calculate the fluid fraction of fluid 1 and fluid 2 for each device separately, as shown in Fig. 3H–J). The devices printed from PLA and PMMA showed good correlation between the theoretically expected volume fractions and the experimental volume fractions. With a maximum relative deviation of 9% compared with the theoretical value, PMMA showed better correlation than the PLA device, with a maximum relative deviation of 15%. As observed in the experiments for the achieved resolution, the devices printed from PC appeared to underperform, thus resulting in a maximum relative deviation of 21% with respect to the theoretically expected values. This could particularly be observed in outlets 2 and 4, which show nearly the same volume fractions as outlets 1 and 5, respectively.

#### Absorbance measurement on chip

Direct measurement of absorbance in the microfluidic chip does not require elution, avoiding some of the disadvantages of external measurement, such as dilution or solubility problems. It also simplifies chip design and experimental setup because the entire experiment can be performed on one chip. As shown in Fig. 4, the transparency of the printed device is suitable to perform absorbance measurements with quality comparable to that of commercially available 96-well plates. The

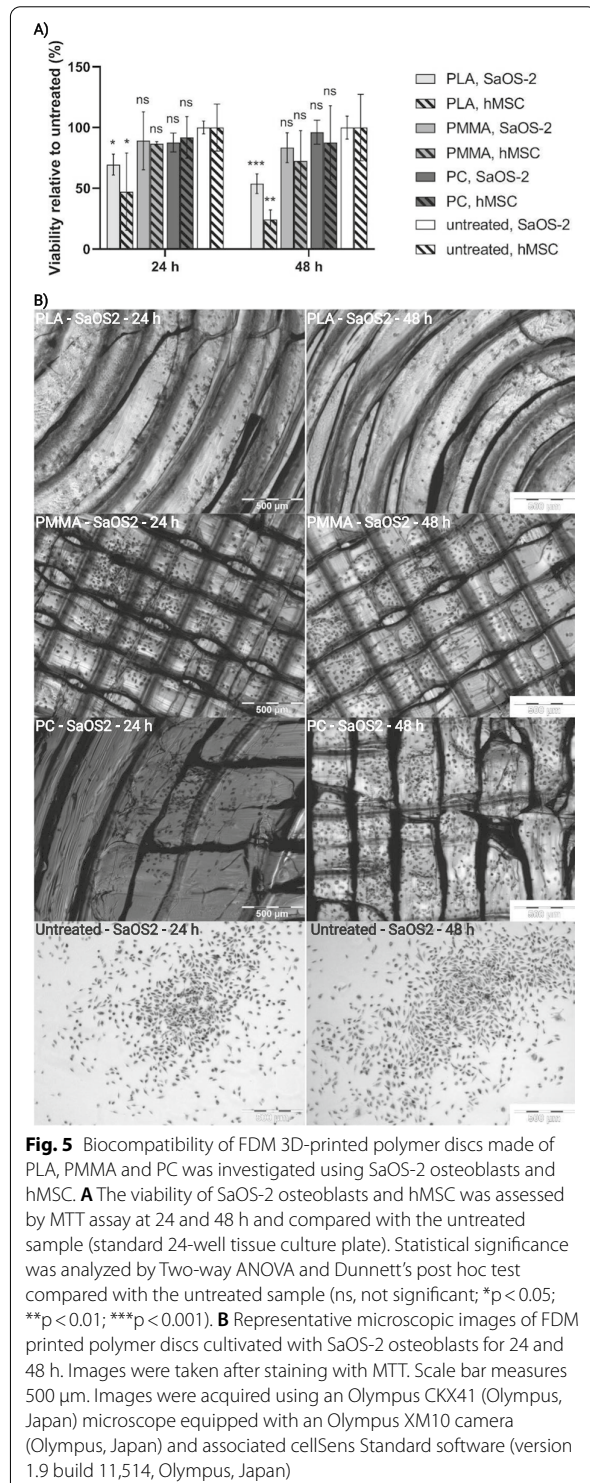




slightly higher standard deviation (SD) of the absorbance measurements (Fig. 4E) in the printed chips (SD of  $A_{640\text{nm}; \text{fluid 2, 1:1}}$  to  $A_{640\text{nm}; \text{PBS}}$ : 0.0225; 0.0172; 0.0056; 0.0095; 0.0014) compared to the 96-well plate (SD of  $A_{640\text{nm}; \text{fluid 2, 1:1}}$  to  $A_{640\text{nm}; \text{PBS}}$ : 0.0070; 0.0079; 0.0045; 0.0019; 0.0012) is likely a result of light scattering at the line-patterned surface. This line-patterned surface topology (Fig. 4C) originates from the manufacturing process of FDM 3D printing and can be improved by post-treatment, for example with solvents. The transparency of the printed microfluidics is sufficient not only to measure absorbances, but also to observe and analyze living cells inside the chip with a microscope (Fig. 6D).

#### Biocompatibility of chip material

For application in biomedical test systems, a biocompatible, non-leaching and non-toxic material is essential for the success of the experiment which disqualifies most commercially available SLA resins [72, 73]. For cell cultures on chip, it is particularly important that no cytotoxic effects occur in direct contact with the material over a period of several days. Therefore, the viability of SaOS-2 osteoblasts and human mesenchymal stem cells (hMSCs) cultured in direct contact with FDM 3D-printed discs made of PLA, PMMA, and PC was investigated. It was observed that the polymers PMMA and PC showed no significant difference in viability to the corresponding cells cultured in tissue culture wells (Fig. 5) after 24 and 48 h. Furthermore, no



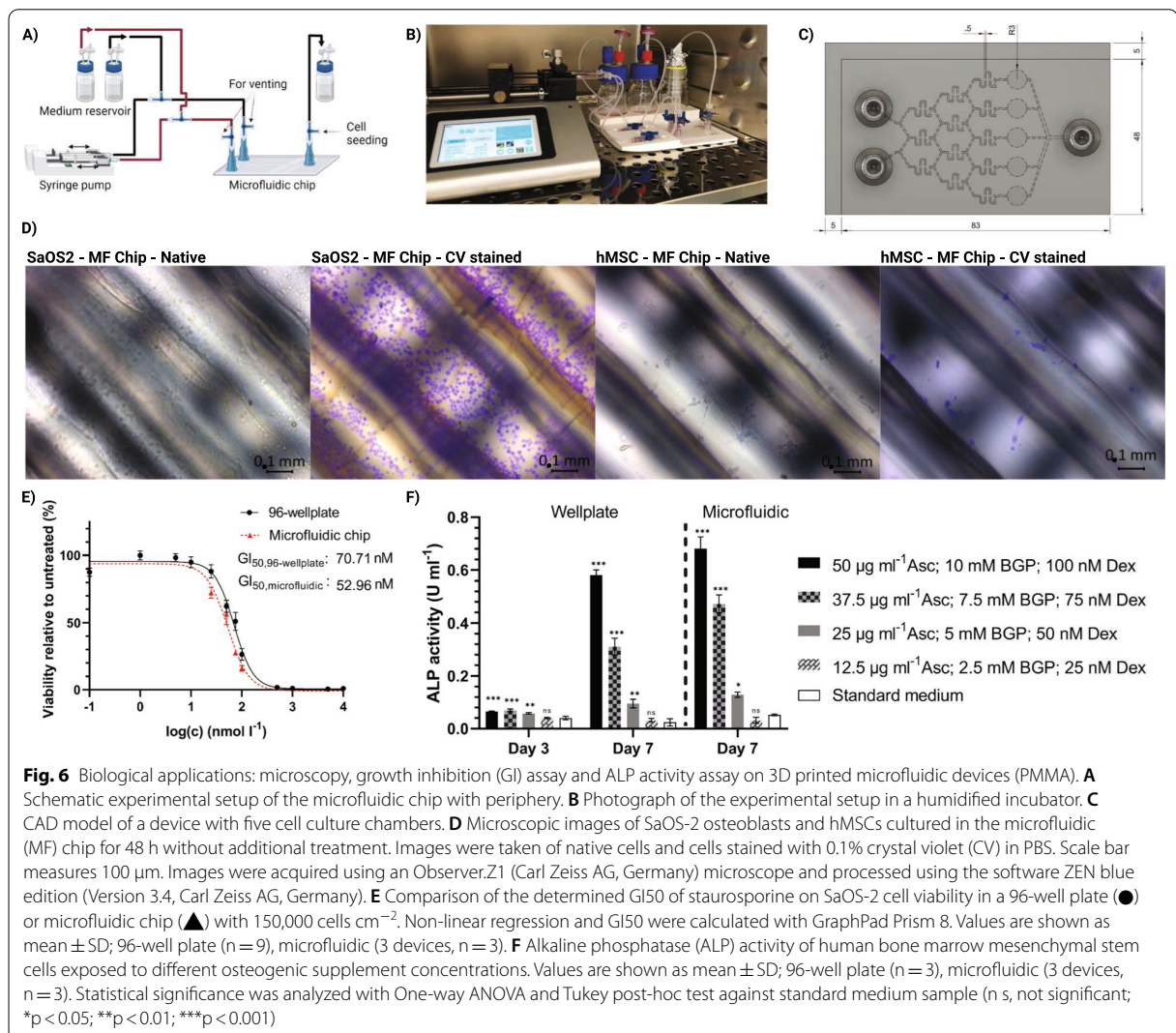
major morphological changes were detected compared to cells cultured under standard conditions, as shown for the SaOS-2 osteoblasts in Fig. 5B and for the hMSCs in Additional file 1: Fig. S19. The viability of both cell types (SaOS-2 osteoblasts and hMSCs) decreased significantly after being cultured on PLA discs for 24 h. This trend continued for the 48-h samples, resulting in a  $46.2 \pm 6.6\%$  decrease in SaOS-2 osteoblast viability and a  $75.6 \pm 6.4\%$  decrease in hMSC viability compared with the respective controls.

#### Drug screening system: microfluidic cytotoxicity assay

As a first relevant application, we demonstrate a validated cytotoxic screening system that combines a chemical concentration gradient with cell culture chambers and analytics in one chip. Assessment of the half maximal growth-inhibitory concentration ( $GI_{50}$ ) of toxic reagents in a microfluidic chip device resulted in higher reproducibility and accuracy, and less reagent consumption than manual assessment. The superiority of direct 3D printed microfluidic chips was demonstrated by analyzing the  $GI_{50}$  value of the potent cytotoxic drug staurosporine ( $GI_{50}$  of  $13.6 - 105.6 \text{ nmol l}^{-1}$ , depending on the cell line [74]) on the cell viability of SaOS-2 osteoblasts (Fig. 6E). The calculated  $GI_{50}$  values of  $52.96 \pm 2.43 \text{ nmol l}^{-1}$  in the microfluidic chip and  $70.71 \pm 4.92 \text{ nmol l}^{-1}$  in the 96-well plate confirmed the improved reproducibility and accuracy expected from the use of microfluidics for cytotoxicity assays.

#### Microfluidic ALP activity assay as an early marker of osteogenic differentiation

As a second relevant application, we demonstrate a validated differentiation system for hMSCs. On the basis of an alkaline phosphatase (ALP) activity assay, a simple microfluidic chip for the cultivation, differentiation and analysis of mesenchymal stem cells into their osteogenic lineage (Fig. 6) was designed. Different concentrations of the osteogenic supplement consisting of ascorbic acid (Asc),  $\beta$  glycerophosphate (BGP) and dexamethasone (Dex) were tested in the microfluidic device and compared to the results obtained via standard cell culture. As shown in Fig. 6F), after 3 days of cultivation, only minor yet significant differences in ALP activity (well plate, standard cell culture) were observed when cells were treated with osteogenic supplement compared with standard medium. On day 7, however, the ALP activity (well plate, standard cell culture) increased substantially in response to the adjusted concentration of osteogenic



supplement. The highest concentration of osteogenic supplement ( $50 \mu\text{g ml}^{-1}$  Asc, 10 mM BGP and 100 nM Dex) resulted in high ALP activity ( $0.58 \text{ U ml}^{-1}$ ), whereas with decreasing concentration, the ALP activity ( $0.58$ ;  $0.31$ ;  $0.1$ ;  $0.03$ ;  $0.02 \text{ U ml}^{-1}$ ) also decreased. For the lowest tested concentration ( $12.5 \mu\text{g ml}^{-1}$  Asc, 2.5 mM BGP and 25 nM Dex) no significant difference with respect to standard medium without osteogenic supplement was observed. A similar trend was observed for the microfluidic device at day 7, with slightly higher ALP activity ( $0.68$ ;  $0.47$ ;  $0.13$ ;  $0.03$ ;  $0.05 \text{ U ml}^{-1}$ ) than with standard cell culture conditions.

## Discussion

Using a commercial available FDM 3D printer and polymers, we present a method to efficiently manufacture microfluidic chips for biomedical applications. The method presented is cost- and labor-efficient, needs little prior knowledge, avoids toxic or leaching chemicals, allows easy adaptation of the chip to the specific challenges of the experiment and produces ready-to-use as well as long-term biocompatible microfluidics. In addition, a 3D chip design can be produced, offering new possibilities compared to traditional manufacturing methods that can only create 2D chip designs.

The observed difference between printed test objects and the CAD model for the achieved resolution (Fig. 2) can partially be explained by the accuracy of the printer's step motors, which the manufacturer indicates is  $\pm 12.5 \mu\text{m}$  [75]. In addition, the printing process itself can explain the deviation. During the printing process, the polymer melts in the print head and is extruded through the nozzle. Subsequently, the polymer cools and becomes solid again, forming a unit with the surrounding material. A short cooling time is crucial to achieving high resolution, because as long as the polymer is in its fluid state, external forces such as gravity or vibrations alter its final position in the object. This phenomenon has been observed particularly for PC, which requires cooling fan deactivation and a high  $\theta$  during the printing process; otherwise the polymer leaving the nozzle does not attach to the previously printed layer. This problem can be remedied by using a closed print chamber with controlled ambient temperature by raising the temperature of the previously printed layers [76]. Consequently, the adhesion of the subsequent layer is improved and the cooling fan can be activated to dissipate the heat emitted by the print-head. Since we wanted to demonstrate the feasibility of producing microfluidic devices using a commercially available FDM 3D printer without any customizations, we did not test a heated print chamber in this study. The effects of this phenomenon can be clearly observed in chips made from PC (Fig. 3). The corners of the channels were narrower than those in the CAD model, and the straight channels between them had a slightly oval shape. This had a particularly strong impact on the performance of the mixer design, where slight fluctuations in the channel widths decreased or increased the hydrodynamic resistance ( $R_H$ );  $R_H$  is anti-proportional to the circular channel radius ( $r$ ) and increases with channel length ( $L$ ) and dynamic viscosity ( $\mu$ ), as shown in Eq. 1 [77]. Thus, channels with a greater diameter show less hydrodynamic resistance, which results in higher flow rates ( $Q$ ) (Eq. 2), since the pressure difference ( $\Delta p$ ) remains constant. Consequently, fluctuations in  $Q$  observed at each channel branch ultimately influence the volume fractions at the chips' outlets.

$$R_H = \frac{8\mu L}{\pi r^4} \quad (1)$$

$$\Delta p = Q * R_H \quad (2)$$

As listed in Table 1, the polymers tested have different advantages and disadvantages and find different applications accordingly. It is worth mentioning that PLA is hydroscopic and the dimensions of the channels may change over time due to swelling when used in contact

with water. Especially at very low flow rates, such as in a long-term cell culture, the change in channel dimensions or the lactic acid released by the degradation can have a negative effect on the experiment. Furthermore, swelling itself can also lead to differences between the effective concentration ( $c_{\text{eff}}$ ) and the set concentrations ( $c_{\text{set}}$ ). For this reason, we would recommend PLA for the development of "quick and dirty" prototypes or for experiments with a short duration, since the printing properties are excellent and the effects mentioned above are mainly seen in longer experiments. In longer experiments, PMMA would be more suitable as a chip material, as it does not have the problems mentioned for PLA, but at the same time has very good printing properties and biocompatibility. With PC, on the other hand, the inaccuracy during the printing process must be taken into account if a heatable printing chamber is not available. Nevertheless, PC is recommended for experiments requiring higher temperatures than  $90 \text{ }^\circ\text{C}$ , such as PCR applications, especially if the chip has only one channel, as it is form-stable even at temperatures up to  $140 \text{ }^\circ\text{C}$ . It should also be mentioned that when solvents are used, care should be taken to ensure that they do not attack the polymer in question.

Additionally, our observations confirm the advantages of FDM 3D printing for biomedical applications, substantially by a wide range of commercially available long-term biocompatible materials. Zhu et al. [78] tested several materials printed with FDM, Multi-Jet Modelling, and SLA and observed high toxicity for several species, except for the samples printed with FDM. This was one of the reasons why we decided against SLA 3D printing and in favor of FDM 3D printing, despite the better resolution of SLA [79]. The biocompatibility of PMMA and PC, as reported in the literature [48, 49, 80], can be confirmed by the results obtained in this study. In contrast, more ambivalent findings are described in the literature for PLA. For example, Li et al. [81] and Silva et al. [82] observed good biocompatibility, while Lee et al. [80] reported inflammatory responses to PLA scaffolds and Majidi et al. [83] observed a reduction in viability of L929 fibroblast cells by almost 50% after 72 h, although they attributed this to reduced cell attachment and not a toxic effect. In agreement with the results of Majidi et al., we observed a decrease in cell viability for PLA, which can also be attributed to either decreased cell adhesion or a toxic effect. In any case, the tested PLA is not suitable for use in microfluidic devices with biological applications without further treatment. The PLA used is of technical grade and contains different additives depending on the manufacturer, so it may vary from manufacturer to manufacturer. This shows that it is necessary and useful to test polymers for cytotoxicity before their application in

biological systems, thus avoiding side effects or misleading results.

Based on the properties (print resolution, optical transparency, and biocompatibility) of the polymers tested, we selected PMMA as the polymer of choice for the subsequent microfluidic devices with biomedical applications. We observed better performance for the microfluidic chips than the 96-well plate experiments, both for the cytotoxic screening system and the osteogenic differentiation system. The observed lower  $GI_{50}$  for the microfluidic cytotoxic screening system compared with the 96-well plate could be due to two effects: first, the concentration settings in the microfluidic chip might have been more accurate than manual pipetting, and consequently, the lower scatter in the measurement data decreased the likelihood of statistical outliers being included in the calculation. Second, the dynamic cultivation in the microfluidic system might have ensured constant and uniformly distributed concentrations in the cultivation chambers, such that  $c_{\text{set}}$  corresponded to  $c_{\text{eff}}$  within the cells. In contrast, lower concentrations might have occurred locally in the static system of a 96-well plate, thus resulting in a lower  $c_{\text{eff}}$ . Another advantage of the microfluidic system is its faster preparation time, particularly when the same assay is performed several times, for example, in a routine analysis or a high-throughput experiment.

The better performance of the microfluidic assay for osteogenic differentiation was reflected in increased ALP activity and demonstrated the importance of in vivo-mimicking conditions. This might have been a result of synergistic effects of the shear stress, which is constantly present in the dynamic culture system of the microfluidic device [84] and is known to have a positive effect on osteogenic differentiation of mesenchymal stem cells [85–88]. With this simple microfluidic chip, the osteogenic effect of supplements at different concentrations was successfully confirmed after 7 days of cultivation without the need for extensive manual work. Furthermore, the chip in combination with the ALP activity assay could be used to analyze the osteogenic effects of several other chemicals or could be combined with other colorimetric assays or fluorescent probes to analyze different cellular functions. Both applications can be further improved by adding additional chambers to the chip design, which can reduce concentration intervals or cover a wider concentration range. In addition, testing combinations of several compounds should be possible by creating a 3D gradient generator that can accommodate four or even more inlets.

## Conclusions

In summary, microfluidic methods offer many advantages over current standard methods, especially in dynamic cell culture systems, but are partially limited in their biocompatibility, availability and adaptability. To provide a solution to this problem, we present the use of a conventional, unmodified 3D printer for the cost-efficient and rapid production of customizable and biocompatible microfluidic chips. We demonstrated the suitability of 3D printing for reproducible production of 100  $\mu\text{m}$  channel structures for 2D and 3D chip structures and layouts. In addition, we demonstrated the applicability and superiority of self-printed microfluidic chips in cell culture, both in assessing cytotoxicity, and in inducing and analyzing stem cell differentiation in dynamic culture systems. The chips presented have the advantages that all steps of an experiment (preparation/treatment, cultivation, analysis) are performed on one chip and can be easily adapted to the specific challenges of the experimental design. This can be realized, for example, by increasing the number of cell culture chambers for higher data density, integrating sensor systems into the chip design, adding new inlets for feeding additional chemicals, or using a different chip material for surface modification or temperature optimization.

## Materials and methods

Chips were printed with an Ultimaker 3 (Ultimaker, Netherlands) FDM 3D printer with a 0.4 mm nozzle head using 2.85 mm polymer filaments purchased from filamentworld.com (Germany). Polymers were purchased in transparent forms: PLA-transparent (PLA300XCLR), PMMA-transparent (PMM300XCLR) and PC-transparent (PCA300XCLR). To validate and apply the created microfluidic devices, we used a Legato 111 (KD Scientific, United States of America) syringe pump. The test fluids were a mixture of water and food coloring (Ruf, Germany) purchased from a local store. Blue solution (fluid 2) was adjusted to an  $A_{640\text{nm}}$  of 1, and red solution (fluid 1) was adjusted to match the viscosity of the blue solution, thus resulting in an  $A_{490\text{nm}}$  of 0.45. Absorbance measurements were performed with a TECAN infinite M200 PRO (TECAN, Switzerland) plate reader. SaOS-2 human osteogenic sarcoma cells (ACC 243, DSMZ) were cultured in McCoy's 5A medium supplemented with 10% fetal calf serum, penicillin at 100 U  $\text{ml}^{-1}$  and streptomycin at 100 U  $\text{ml}^{-1}$ . Human bone marrow derived mesenchymal stem cells (hMSC) were cultured in stem cell expansion medium SCM015 supplemented with penicillin at 100 U  $\text{ml}^{-1}$  and streptomycin at 100 U  $\text{ml}^{-1}$ . Chemicals and cell culture media were purchased from Sigma Aldrich, Germany, unless stated otherwise.

### Fabrication of devices

An overview of the manufacturing process of microfluidic chips with a 3D printer is shown in Fig. 1. First, a CAD model was created in Autodesk Fusion 360 (Autodesk, USA). The model included the structures contained in the finished chip, such as channel structures, reaction chambers and tube connections. Then the CAD model was exported as an STL file and uploaded to the open source slicer software Cura (Version 4.6.1, Ultimaker, Netherlands). In this step, users can change various parameters affecting the printing process. By adjusting these parameters to the polymer used or the structures to be printed, the printing results can be improved. After the CAD model is sliced according to the entered parameters, the software saves the information in a G-code file that is sent to the 3D printer. After 30 to 60 min, depending on the chip size, the printing process is complete, and the device can be removed from the print bed. It can be used immediately or further modified for complex applications. The Cura files with the adjusted slicing parameters for the three listed polymers are provided in the Additional file 2.

### Resolution assessment of direct 3D printed microfluidic channels

Test specimens with channels in the X-, Y- and Z-directions were printed to study the influence of different parameters on the print resolution. The parameters analyzed were printing temperature ( $\vartheta$ ), printing speed ( $v$ ), layer height ( $h$ ) and fan speed ( $fan$ ). Images of the channels in the X-, Y- and Z-directions were taken from the printed test device by using an Olympus CKX41 (Olympus, Japan) microscope with a mounted Olympus XM10 camera (Olympus, Japan) and the associated software cellSens Standard (Version 1.9 Build 11,514, Olympus, Japan). Subsequently, the achieved channel widths and heights were calculated with imageJ (Version 1.52a, National Institutes of Health, USA) and compared with the given values of the CAD model. In addition, a visual inspection was performed after injection of liquid into the channels to ensure that they were not blocked.

### 3D microfluidic structures

Microfluidic devices were fabricated for each of the three polymers (PLA, PMMA and PC). Chips were tested for leakage and functionality by injection of test liquids. Several chip components were generated, which can be arranged and combined on a chip depending on the application. Three chips were designed, containing structures of varying complexity. The first was a chip with two intersecting serpentine channels with a spacing in the Z-direction of 0.2 mm. This chip demonstrated the printability of multiple structures on top of each other in one device without leakage. The second was a chip with two straight channels crossing each other with a bridge, which demonstrated the generation of channels not only in the X- and Y-directions, but also in the Z-direction. The third was a chip containing spirals of different diameters and cross-section geometries, which are representative of the implementation of complex 3D structures in the chip design.

### Microfluidic gradient generator

Microfluidic mixer components are used in many microfluidic chips. These structures are primarily used to mix multiple liquid streams but can also be used to create a concentration gradient across different liquid streams with the correct arrangement of microfluidic channels. The gradient generator chip that we fabricated included two inlets, five outlets and all channels of the same sizes, thus resulting in the theoretical volume fractions listed in Table 3. The theoretical fluid compositions at the outlets were verified by injecting two solutions, red solution (fluid 1) and blue solution (fluid 2), into the microfluidic devices with a Legato 111 (KD Scientific, Germany) syringe pump. Each inlet was adjusted to a flow of  $0.2 \text{ ml min}^{-1}$ . After equilibrium was reached, images of the chip were collected, and the outlets were emptied. A  $100 \mu\text{l}$  volume of each of the fluids collected from the outlets was transferred to a 96-well plate, and the absorbance at 640 nm and 490 nm was measured with a plate reader. The proportion of blue and red fluid was calculated according to a linear calibration curve.

**Table 3** Theoretical volume fractions of fluids entering or leaving the passive microfluidic mixer

	Inlet 1	Inlet 2	Outlet 1	Outlet 2	Outlet 3	Outlet 4	Outlet 5
Theoretical volume fraction of fluid 1 ( $\varphi_{fluid1}$ ) <sup>a</sup>	1	0	1	0.75	0.5	0.25	0
Theoretical volume fraction of fluid 2 ( $\varphi_{fluid2}$ ) <sup>b</sup>	0	1	0	0.25	0.5	0.75	1

<sup>a</sup> red solution (fluid 1)

<sup>b</sup> blue solution (fluid 2)

#### Absorbance measurement on chip

A microfluidic chip with five round chambers (diameter = 7 mm, height = 1 mm) was generated. The 96-well plate format was chosen to allow the chip to be measured in a standard plate reader. For this purpose, the chip was plugged into a 3D printed adapter and measured analogously to a conventional 96-well plate. First, every chamber was filled with PBS, and the absorbance spectra were measured as the offset value. Afterward, PBS was replaced by a dilution series of test solutions (1:1, 1:2, 1:4 and 1:8 of fluid 2 in PBS). The absorbance spectra were measured and compared with the absorbance spectra in a conventional 96-well plate.

#### Biocompatibility of chip material

Biocompatibility analyses were performed with SaOS-2 human osteogenic sarcoma cells and hMSC in direct contact with the polymers PLA, PMMA and PC. 3D-printed polymer discs ( $r = 6.5$  mm,  $h = 0.2$  mm) were seeded with 50,000 cells each and cell viability was assessed after 24 and 48 h by 3-(4,5-dimethylthiazol-2-yl)-2,5-diphenyltetrazolium bromide (MTT) assay. Briefly, polymer discs were placed in a 24-well plate and a cell suspension containing  $5 \times 10^6$  cells  $\text{ml}^{-1}$  was prepared (hMSCs were used at passage 2). 10  $\mu\text{l}$  of the cell suspension was dispersed on the polymer discs and incubated at 37 °C and 5%  $\text{CO}_2$ . After 30 min, 50  $\mu\text{l}$  of medium was carefully added to prevent drying, and after another 3.5 h, 500  $\mu\text{l}$  of medium was added. The medium was replaced by 500  $\mu\text{l}$  MTT solution (MTT at 1  $\text{mg ml}^{-1}$  in medium) at cultivation times of 24 or 48 h and samples were incubated for 2 h. Afterwards, polymer discs were washed 2 times with 500  $\mu\text{l}$  PBS and transferred to a new well. Formazan crystals were dissolved by adding 500  $\mu\text{l}$  of DMSO and quantified in triplicate at 100  $\mu\text{l}$  at 570 nm in a plate reader. Cell viability was calculated as the ratio of absorbance between cells cultured on polymer discs and cells cultured in a tissue culture well.

#### Microfluidic cytotoxicity assay

SaOS-2 human osteogenic sarcoma cells were used to determine the half maximal growth-inhibitory concentration ( $\text{GI}_{50}$ ) of staurosporine (APEX-BIO Technology LLC, USA). Cells were seeded on the microfluidic chip at a density of 150,000 cells  $\text{cm}^{-2}$  after the chip had been filled with sterile PBS. The seeding process was performed as follows: the cell chamber was filled with cell suspension via the chip outlet using a pipette. The filling was stopped as soon as the cell chamber was completely filled to ensure that no cells adhered in the channels of the upstream. The fill level was visually determined by the color difference between cell suspension (red) and sterile

PBS (transparent). Before treatment with staurosporine at 0, 25, 50, 75 and 100  $\text{nmol l}^{-1}$ , cells were allowed to attach to the cell culture chambers for 4 h. Excess cells adhering in the downstream channels are partially flushed out of the system by the applied flow of the experiment. Treatment was performed with a flow rate of 0.008  $\text{ml h}^{-1}$  per cell culture chamber by injection of culture medium (inlet 1; 0.02  $\text{ml h}^{-1}$ ) and staurosporine at 100  $\text{nmol l}^{-1}$  in culture medium (inlet 2; 0.02  $\text{ml h}^{-1}$ ). In addition, SaOS-2 cells (150,000 cells  $\text{cm}^{-2}$ ) were treated with 100  $\mu\text{l}$  medium supplemented with staurosporine at 0, 1, 5, 10, 25, 50, 75, 100, 500, 1,000, 5,000 and 10,000  $\text{nmol l}^{-1}$  in 96-well culture plates by manual pipetting. Afterwards, the cells were incubated in a humidified incubator at 37 °C and 5%  $\text{CO}_2$  for 24 h before cell viability was assessed with MTT assay. First, the medium was replaced with 100  $\mu\text{l}$  MTT solution (MTT at 1  $\text{mg ml}^{-1}$  in medium) and incubated for 2 h. Subsequently, the MTT solution was removed, and 100  $\mu\text{l}$  10 (w/v)% sodium dodecyl sulfate in phosphate-buffered saline (PBS) was added and incubated for another 4 h. The absorbance was measured at 570 nm directly in the chip and the 96-well plate by using a plate reader. Cell viability was calculated as the ratio of absorbance between the samples with and without staurosporine treatment. MTT assays were repeated three times, each time with a new device, and the  $\text{GI}_{50}$  value was calculated with GraphPad Prism 8 (GraphPad Software, USA).

#### Microfluidic ALP activity assay as an early marker of osteogenic differentiation

Alkaline phosphatase (ALP) activity was assessed in a microfluidic chip as an early marker of the osteogenic differentiation of hMSCs. Cells were cultured in stem cell expansion medium SCM015 (Sigma Aldrich, Germany) supplemented with penicillin at 100  $\text{U ml}^{-1}$ , streptomycin at 100  $\text{U ml}^{-1}$  and different concentrations of osteogenic supplement (Asc, BGP and Dex) that has been shown in the literature to induce osteogenic differentiation [89, 90]. At passage three, hMSCs were seeded at a density of 150,000 cells  $\text{cm}^{-2}$  in the microfluidic chip as well as in a 96-well culture plate, as previously described, and treated with osteogenic supplement for 7 days in a humidified incubator at 37 °C and 5%  $\text{CO}_2$ . Dilution of the osteogenic supplement stock (Asc at 500  $\mu\text{g ml}^{-1}$  (Carl Roth, Germany), BGP at 100  $\text{mmol l}^{-1}$  (Carl Roth, Germany) and Dex at 1  $\mu\text{mol l}^{-1}$ ) was performed in medium, thus resulting in 10, 7.5, 5 and 2.5 (v/v)% stock concentrations for the 96-well plate. SCM015 without osteogenic supplement was used as a control. The microfluidic chip was injected with SCM015 and 10 (v/v)% stock concentrations, each at one inlet, thus

resulting in theoretical concentrations of 10, 7.5, 5, 2.5 and 0 (v/v)% stock concentrations in the cell chambers. ALP activity was assessed with an Alkaline Phosphatase Diethanolamine Activity Kit (AP0100, Sigma Aldrich, Germany) according to the manufacturer's instructions with modifications. Briefly, after cultivation, the medium was replaced with 100  $\mu$ l reaction solution consisting of 98  $\mu$ l reaction buffer (included in the kit) with 1(v/v)% Triton X-100 and 2  $\mu$ l  $0.67 \text{ mol l}^{-1}$  p-nitrophenyl phosphate (included in the kit). The absorbance was measured every 30 s for 300 s at 405 nm directly in the chip or the 96-well plate with a plate reader. The average linear rate ( $A_{405\text{nm}} \text{ min}^{-1}$ ) was used to calculate the ALP activity according to a calibration curve.

#### Numeric simulation of fluidic behavior in microfluidic chips

Numeric simulation was performed with the finite element method (FEM) to verify the observed mixing ratios in the designed microfluidic chips. For this purpose, a system consisting of two phases of water was defined. Boundary conditions for the inlets were set according to the experiments. The outlet boundary condition was set to a pressure outlet with a gauge pressure of 0 Pa. The simulation was performed with ANSYS 2020 R1 Academic (ANSYS Inc., United States of America) by using the simplec algorithm. The volume fractions of both phases were calculated and displayed along the longitudinal section.

#### Supplementary Information

The online version contains supplementary material available at <https://doi.org/10.1186/s12951-022-01737-7>.

**Additional file 1: Figure S1.** Obtained dimensions of the 3D printed poly (lactic acid) (PLA) test device for various printing temperatures. Remaining parameters were kept constant at  $v = 30 \text{ mm/s}$ ,  $h = 50 \mu\text{m}$  and  $\text{fan} = 100\%$ . Results are shown for the X-, Y- and Z-axis separately. Values shown as mean  $\pm$  standard deviation of 3 devices. **Figure S2.** Obtained dimensions of the 3D printed poly (methyl methacrylate) (PMMA) test device for various printing temperatures. Remaining parameters were kept constant at  $v = 50 \text{ mm/s}$ ,  $h = 100 \mu\text{m}$  and  $\text{fan} = 50\%$ . Results are shown for the X-, Y- and Z-axis separately. Values shown as mean  $\pm$  standard deviation of 3 devices. **Figure S3.** Obtained dimensions of the 3D printed polycarbonate (PC) test device for various printing temperatures. Remaining parameters were kept constant at  $v = 50 \text{ mm/s}$ ,  $h = 100 \mu\text{m}$  and  $\text{fan} = 0\%$ . Results are shown for the X-, Y- and Z-axis separately. Values shown as mean  $\pm$  standard deviation of 3 devices. **Figure S4.** Obtained dimensions of the 3D printed poly (lactic acid) (PLA) test device for various printing speeds. Remaining parameters were kept constant at  $\theta = 190^\circ\text{C}$ ,  $h = 50 \mu\text{m}$  and  $\text{fan} = 100\%$ . Results are shown for the X-, Y- and Z-axis separately. Values shown as mean  $\pm$  standard deviation of 3 devices. **Figure S5.** Obtained dimensions of the 3D printed poly (methyl methacrylate) (PMMA) test device for various printing speeds. Remaining parameters were kept constant at  $\theta = 245^\circ\text{C}$ ,  $h = 100 \mu\text{m}$  and  $\text{fan} = 50\%$ . Results are shown for the X-, Y- and Z-axis separately. Values shown as mean  $\pm$  standard deviation of 3 devices. **Figure S6.** Obtained dimensions of the 3D printed polycarbonate (PC) test device for various printing speeds. Remaining parameters were kept constant at  $\theta = 240^\circ\text{C}$ ,  $h = 100 \mu\text{m}$  and  $\text{fan} = 0\%$ . Results are shown for the X-, Y- and Z-axis separately. Values shown as mean  $\pm$  standard deviation of 3 devices. **Figure S7.** Obtained dimensions of the

3D printed poly (lactic acid) (PLA) test device for various layer heights. Remaining parameters were kept constant at  $\theta = 190^\circ\text{C}$ ,  $v = 70 \text{ mm/s}$  and  $\text{fan} = 100\%$ . Results are shown for the X-, Y- and Z-axis separately. Values shown as mean  $\pm$  standard deviation of 3 devices. **Figure S8.** Obtained dimensions of the 3D printed poly (methyl methacrylate) (PMMA) test device for various layer heights. Remaining parameters were kept constant at  $\theta = 245^\circ\text{C}$ ,  $v = 70 \text{ mm/s}$  and  $\text{fan} = 50\%$ . Results are shown for the X-, Y- and Z-axis separately. Values shown as mean  $\pm$  standard deviation of 3 devices. **Figure S9.** Obtained dimensions of the 3D printed polycarbonate (PC) test device for various layer heights. Remaining parameters were kept constant at  $\theta = 240^\circ\text{C}$ ,  $v = 80 \text{ mm/s}$  and  $\text{fan} = 0\%$ . Results are shown for the X-, Y- and Z-axis separately. Values shown as mean  $\pm$  standard deviation of 3 devices. **Figure S10.** Obtained dimensions of the 3D printed poly (lactic acid) (PLA) test device for various fan speeds. Remaining parameters were kept constant at  $\theta = 190^\circ\text{C}$ ,  $v = 70 \text{ mm/s}$  and  $h = 100 \mu\text{m}$ . Results are shown for the X-, Y- and Z-axis separately. Values shown as mean  $\pm$  standard deviation of 3 devices. **Figure S11.** Obtained dimensions of the 3D printed poly (methyl methacrylate) (PMMA) test device for various fan speeds. Remaining parameters were kept constant at  $\theta = 245^\circ\text{C}$ ,  $v = 70 \text{ mm/s}$  and  $h = 100 \mu\text{m}$ . Results are shown for the X-, Y- and Z-axis separately. Values shown as mean  $\pm$  standard deviation of 3 devices. **Figure S12.** Obtained dimensions of the 3D printed polycarbonate (PC) test device for various fan speeds. Remaining parameters were kept constant at  $\theta = 240^\circ\text{C}$ ,  $v = 80 \text{ mm/s}$  and  $h = 100 \mu\text{m}$ . Results are shown for the X-, Y- and Z-axis separately. Values shown as mean  $\pm$  standard deviation of 3 devices. **Figure S13.** Representative microscopic images of FDM printed micro channels in a poly (lactic acid) (PLA) test device. Analysis performed with "imageJ" (Version 1.52a, National Institutes of Health, USA). Scale bar measures 200  $\mu\text{m}$ . **Figure S14.** Representative microscopic images of FDM printed micro channels in a poly (methyl methacrylate) (PMMA) test device. Analysis performed with "imageJ" (Version 1.52a, National Institutes of Health, USA). Scale bar measures 200  $\mu\text{m}$ . **Figure S15.** Representative microscopic images of FDM printed micro channels in a PC test device. Analysis performed with "imageJ" (Version 1.52a, National Institutes of Health, USA). Scale bar measures 200  $\mu\text{m}$ . **Figure S16.** Relative deviation between experimental dimensions and CAD dimensions in X-direction. **Figure S17.** Relative deviation between experimental dimensions and CAD dimensions in X-direction. **Figure S18.** Relative deviation between experimental dimensions and CAD dimensions in X-direction. **Figure S19.** Representative microscopic images of FDM printed polymer discs cultivated with human mesenchymal stem cells (hMSC) for 24 and 48 hours. Viability of hMSC cultivated on PLA, PMMA and PC discs was analyzed with MTT assay and compared to untreated hMSCs cultivated in a standard tissue culture 24-well plate. Images were taken after staining with MTT. Scale bar measures 500  $\mu\text{m}$ .

**Additional file 2.** PLA.curaprofile contains the optimized slicing parameters for the polymer PLA, which can be imported into the slicing program Cura. PMMA.curaprofile contains the optimized slicing parameters for the polymer PMMA, which can be imported into the slicing program Cura. PC.curaprofile contains the optimized slicing parameters for the polymer PC, which can be imported into the slicing program Cura.

#### Acknowledgements

The authors thank Lars Kaiser for support and helpful advice, as well as K. R. and Maxim for their encouragement and D. S. B. for continual input.

#### Author contributions

Conceptualization: HPD; data curation: OR; formal analysis: OR; funding acquisition: HPD; investigation: OR; methodology: OR; resources: HPD, SL; supervision: HPD, SL; visualization: OR; writing—original draft: OR; writing—review and editing: HPD, SL, OR. All authors read and approved the final manuscript.

#### Funding

Open Access funding enabled and organized by Projekt DEAL. The authors are grateful for funding of this work provided by the project "TriMaBone—Trinationale Forschungsinitiative: 3D-Druck Materialien für resorbierbare Knochen-implantate" (Europäischer Fonds für regionale Entwicklung—EFRE) in the program "Interreg VOberrhein" (ref: 5115/3.17) and for partial support by "CoHMed MS-Tox Test" (FKZ:13FH5E01IA; BMBF) and WMP (FKZ: 13FH197PX;

BMBF). We acknowledge support for the Article Processing Charge from the DFG (German Research Foundation, 491454339).

#### Availability of data and materials

All data generated or analysed during this study are included in this published article [and its Additional information files].

#### Declarations

#### Ethics approval and consent to participate

Not applicable.

#### Consent for publication

Not applicable.

#### Competing interests

The authors declare that they have no competing interests.

#### Author details

<sup>1</sup>Institute of Precision Medicine, Furtwangen University, Jakob-Kienzle-Strasse 17, 78054 Villingen-Schwenningen, Germany. <sup>2</sup>Institute of Pharmaceutical Sciences, Department of Pharmacy and Biochemistry, Eberhard-Karls-University Tuebingen, Auf Der Morgenstelle 8, 72076 Tuebingen, Germany. <sup>3</sup>Tuebingen Center for Academic Drug Discovery & Development (TüCAD2), 72076 Tuebingen, Germany. <sup>4</sup>Faculty of Science, Eberhard-Karls-University Tuebingen, Auf Der Morgenstelle 8, 72076 Tuebingen, Germany. <sup>5</sup>EXIM Department, Fraunhofer Institute IZI (Leipzig), Schillingallee 68, 18057 Rostock, Germany.

Received: 22 March 2022 Accepted: 2 December 2022

Published online: 27 December 2022

#### References

- Leberfinger AN, Ravnicek DJ, Dhawan A, Ozbolat IT. Concise review: bioprinting of stem cells for transplantable tissue fabrication. *Stem Cells Transl Med.* 2017;6:1940–8. <https://doi.org/10.1002/sctm.17-0148>.
- Yamanaka S. Pluripotent stem cell-based cell therapy—promise and challenges. *Cell Stem Cell.* 2020;27:523–31.
- Aly RM. Current state of stem cell-based therapies: an overview. *Stem Cell Investig.* 2020;7:8–8.
- Saha K, Jaenisch R. Technical Challenges in Using Human Induced Pluripotent Stem Cells to Model Disease. *Cell Stem Cell.* 2009;5:584–95.
- Hartwell LH, Hopfield JJ, Leibler S, Murray AW. From molecular to modular cell biology. *Nature.* 1999;402:C47–52.
- Lauffenburger DA. Cell signaling pathways as control modules: complexity for simplicity? *Proc Natl Acad Sci.* 2000;97:5031–3. <https://doi.org/10.1073/pnas.97.10.5031>.
- Zeng Z, Miao N, Sun T. Revealing cellular and molecular complexity of the central nervous system using single cell sequencing. *Stem Cell Res Ther.* 2018;9:234. <https://doi.org/10.1186/s13287-018-0985-z>.
- Kakkar A, Traverso G, Farokhzad OC, Weissleder R, Langer R. Evolution of macromolecular complexity in drug delivery systems. *Nat Rev Chem.* 2017;1:0063.
- Hook AL, Anderson DG, Langer R, Williams P, Davies MC, Alexander MR. High throughput methods applied in biomaterial development and discovery. *Biomaterials.* 2010;31:187–98. <https://doi.org/10.1016/j.biomaterials.2009.09.037>.
- Kim HD, Lee EA, Choi YH, An YH, Koh RH, Kim SL, et al. High throughput approaches for controlled stem cell differentiation. *Acta Biomater.* 2016;34:21–9.
- Fernandes TG, Diogo MM, Clark DS, Dordick JS, Cabral JMS. High-throughput cellular microarray platforms: applications in drug discovery, toxicology and stem cell research. *Trends Biotechnol.* 2009;27:342–9.
- Park JW, Fu S, Huang B, Xu R-H. Alternative splicing in mesenchymal stem cell differentiation. *Stem Cells.* 2020. <https://doi.org/10.1002/stem.3248>.
- Xia P, Wang X, Qu Y, Lin Q, Cheng K, Gao M, et al. TGF- $\beta$ 1-induced chondrogenesis of bone marrow mesenchymal stem cells is promoted by low-intensity pulsed ultrasound through the integrin-mTOR signaling pathway. *Stem Cell Res Ther.* 2017;8:281. <https://doi.org/10.1186/s13287-017-0733-9>.
- George S, Hamblin MR, Abrahamse H. Differentiation of mesenchymal stem cells to neuroglia: in the context of cell signalling. *Stem Cell Rev Rep.* 2019;15:814–26. <https://doi.org/10.1007/s12015-019-09917-z>.
- Ertl P, Sticker D, Charwat V, Kasper C, Lepperding G. Lab-on-a-chip technologies for stem cell analysis. *Trends Biotechnol.* 2014;32:245–53.
- Song Y, Hormes J, Kumar CSSR. Microfluidic synthesis of nanomaterials. *Small.* 2008;4:698–711. <https://doi.org/10.1002/sml.200701029>.
- Zhao X, Bian F, Sun L, Cai L, Li L, Zhao Y. Microfluidic generation of nanomaterials for biomedical applications. *Small.* 2020;16:1–19.
- Elvira KS, i Solvas XC, Wootton RCR, DeMello AJ. The past, present and potential for microfluidic reactor technology in chemical synthesis. *Nat Chem.* 2013;5:905–15.
- Liao Z, Wang J, Zhang P, Zhang Y, Miao Y, Gao S, et al. Recent advances in microfluidic chip integrated electronic biosensors for multiplexed detection. *Biosens Bioelectron.* 2018;121:272–80.
- Padash M, Enz C, Carrara S. Microfluidics by additive manufacturing for wearable biosensors: a review. *Sensors.* 2020;20:4236.
- Yang K, Park HJ, Han S, Lee J, Ko E, Kim J, et al. Recapitulation of in vivo-like paracrine signals of human mesenchymal stem cells for functional neuronal differentiation of human neural stem cells in a 3D microfluidic system. *Biomaterials.* 2015;63:177–88. <https://doi.org/10.1016/j.biomaterials.2015.06.011>.
- Du G, Fang Q, den Toonder JMJ. Microfluidics for cell-based high throughput screening platforms—A review. *Anal Chim Acta.* 2016;903:36–50. <https://doi.org/10.1016/j.aca.2015.11.023>.
- Giridharan V, Yun Y, Hajdu P, Conforti L, Collins B, Jang Y, et al. Microfluidic platforms for evaluation of nanobiomaterials: A review. *J Nanomater.* 2012;2012:14.
- Lee JM, Zhang M, Yeong W. Characterization and evaluation of 3D printed microfluidic chip for cell processing. *Microfluid Nanofluidics.* 2016;20:1–15.
- Hayes CJ, Dalton TM. Microfluidic droplet-based PCR instrumentation for high-throughput gene expression profiling and biomarker discovery. *Biomol Detect Quantif.* 2015;4:22–32. <https://doi.org/10.1016/j.bdq.2015.04.003>.
- Bellmann J, Goswami RY, Girardo S, Rein N, Hosseinzadeh Z, Hicks MR, et al. A customizable microfluidic platform for medium-throughput modeling of neuromuscular circuits. *Biomaterials.* 2019;225:119537. <https://doi.org/10.1016/j.biomaterials.2019.119537>.
- Ko E, Tran V-K, Son SE, Hur W, Choi H, Seong GH. Characterization of Au@PtNP/GO nanozyme and its application to electrochemical microfluidic devices for quantification of hydrogen peroxide. *Sensors Actuators B Chem.* 2019;294:166–76.
- Naskar S, Kumaran V, Markandeya YS, Mehta B, Basu B. Neurogenesis-on-Chip: Electric field modulated transdifferentiation of human mesenchymal stem cell and mouse muscle precursor cell coculture. *Biomaterials.* 2020;226:119522. <https://doi.org/10.1016/j.biomaterials.2019.119522>.
- Gutierrez E, Groisman A. Quantitative measurements of the strength of adhesion of human neutrophils to a substratum in a microfluidic device. *Anal Chem.* 2007;79:2249–58. <https://doi.org/10.1021/ac061703n>.
- Qin D, Xia Y, Whitesides GM. Soft lithography for micro- and nanoscale patterning. *Nat Protoc.* 2010;5:491–502.
- Mohamed MGA, Kumar H, Wang Z, Martin N, Mills B, Kim K. Rapid and inexpensive fabrication of multi-depth microfluidic device using high-resolution LCD stereolithographic 3D printing. *J Manuf Mater Process.* 2019;3:1–11.
- Mukherjee P, Nebuloni F, Gao H, Zhou J, Papautsky I. Rapid prototyping of soft lithography masters for microfluidic devices using dry film photore-sist in a non-cleanroom setting. *Micromachines.* 2019;10:192.
- Iwai K, Shih KC, Lin X, Brubaker TA, Sochol RD, Lin L. Finger-powered microfluidic systems using multilayer soft lithography and injection molding processes. *Lab Chip.* 2014;14:3790.
- Nilghaz A, Guan L, Tan W, Shen W. Advances of paper-based microfluidics for diagnostics—the original motivation and current status. *ACS Sensors.* 2016;1:1382–93. <https://doi.org/10.1021/acssensors.6b00578>.
- Moreno-Rivas O, Hernández-Velázquez D, Piazza V, Marquez S. Rapid prototyping of microfluidic devices by SL 3D printing and their biocompatibility study for cell culturing. *Mater Today Proc.* 2019;13:436–45. <https://doi.org/10.1016/j.matpr.2019.03.189>.

36. Lee J-Y, An J, Chua CK. Fundamentals and applications of 3D printing for novel materials. *Appl Mater Today*. 2017;7:120–33.
37. Waheed S, Cabot JM, Macdonald NP, Lewis T, Guijt RM, Paull B, et al. 3D printed microfluidic devices: enablers and barriers. *Lab Chip R Soc Chem*. 2016;16:1993–2013.
38. Vasilescu SA, Bazaz SR, Jin D, Shimoni O, Warkiani ME. 3D printing enables the rapid prototyping of modular microfluidic devices for particle conjugation. *Appl Mater Today*. 2020;20:100726. <https://doi.org/10.1016/j.apmt.2020.100726>.
39. Melocchi A, Parietti F, Maroni A, Foppoli A, Gazzaniga A, Zema L. Hot-melt extruded filaments based on pharmaceutical grade polymers for 3D printing by fused deposition modeling. *Int J Pharm*. 2016;509:255–63. <https://doi.org/10.1016/j.ijpharm.2016.05.036>.
40. Zhou Z, Ruiz Cantu L, Chen X, Alexander MR, Roberts CJ, Hague R, et al. High-throughput characterization of fluid properties to predict droplet ejection for three-dimensional inkjet printing formulations. *Addit Manuf*. 2019;29:100792. <https://doi.org/10.1016/j.addma.2019.100792>.
41. Salentijn GJ, Oomen PE, Grajewski M, Verpoorte E. Fused deposition modeling 3D printing for (Bio)analytical device fabrication: procedures, materials, and applications. *Anal Chem*. 2017;89:7053–61.
42. Hwang Y, Paydar OH, Candler RN. 3D printed molds for non-planar PDMS microfluidic channels. *Sens Actuators A Phys*. 2015;226:137–42. <https://doi.org/10.1016/j.sna.2015.02.028>.
43. He Y, Qiu J, Fu J, Zhang J, Ren Y, Liu A. Printing 3D microfluidic chips with a 3D sugar printer. *Microfluid Nanofluidics*. 2015;19:447–56. <https://doi.org/10.1007/s10404-015-1571-7>.
44. Bressan LP, Robles-Najar J, Adamo CB, Quero RF, Costa BMC, de Jesus DP, et al. 3D-printed microfluidic device for the synthesis of silver and gold nanoparticles. *Microchem J*. 2019;146:1083–9. <https://doi.org/10.1016/j.microc.2019.02.043>.
45. Tothill AM, Partridge M, James SW, Tatam RP. Fabrication and optimisation of a fused filament 3D-printed microfluidic platform. *J Micromech Microeng*. 2017;27:035018.
46. Beauchamp MJ, Nordin GP, Woolley AT. Moving from millifluidic to truly microfluidic sub-100- $\mu\text{m}$  cross-section 3D printed devices. *Anal Bioanal Chem*. 2017;409:4311–9. <https://doi.org/10.1007/s00216-017-0398-3>.
47. Kabirian F, Ditekowski B, Zamanian A, Heying R, Mozafari M. An innovative approach towards 3D-printed scaffolds for the next generation of tissue-engineered vascular grafts. *Mater Today Proc*. 2018;5:15586–94.
48. Gautam R, Singh RD, Sharma V, Siddhartha R, Chand P, Kumar R. Biocompatibility of polymethylmethacrylate resins used in dentistry. *J Biomed Mater Res Part B Appl Biomater*. 2012;100B:1444–50. <https://doi.org/10.1002/jbm.b.32673>.
49. Lye KW, Tideman H, Wolke JCG, Merckx MAW, Chin FKC, Jansen JA. Biocompatibility and bone formation with porous modified PMMA in normal and irradiated mandibular tissue. *Clin Oral Implants Res*. 2013;24:100–9. <https://doi.org/10.1111/j.1600-0501.2011.02388.x>.
50. Chen Y, Zhang L, Chen G. Fabrication, modification, and application of poly(methyl methacrylate) microfluidic chips. *Electrophoresis*. 2008;29:1801–14. <https://doi.org/10.1002/elps.200700552>.
51. Hermanson NJ, Crittenden PA, Novak LR, Woods RA. Chemical resistance of polycarbonate. Amsterdam: Elsevier; 1998. p. 117–22.
52. Shamim N, Koh YP, Simon SL, McKenna GB. Glass transition temperature of thin polycarbonate films measured by flash differential scanning calorimetry. *J Polym Sci Part B Polym Phys*. 2014;52:1462–8. <https://doi.org/10.1002/polb.23583>.
53. Ongaro AE, Di Giuseppe D, Kermanizadeh A, Miguez Crespo A, Mencatini A, Ghibelli L, et al. Polylactic is a sustainable, low absorption, low autofluorescence alternative to other plastics for microfluidic and organ-on-chip applications. *Anal Chem*. 2020;92:6693–701. <https://doi.org/10.1021/acs.analchem.0c00651>.
54. Sochol RD, Sweet E, Glick CC, Wu S-Y, Yang C, Restaino M, et al. 3D printed microfluidics and microelectronics. *Microelectron Eng*. 2018;189:52–68.
55. Sibeko MA, Saladino ML, Luyt AS, Caponetti E. Morphology and properties of poly(methyl methacrylate) (PMMA) filled with mesoporous silica (MCM-41) prepared by melt compounding. *J Mater Sci*. 2016;51:3957–70. <https://doi.org/10.1007/s10853-015-9714-5>.
56. Yavuz C, Oliaei SNB, Cetin B, Yesil-Celiktas O. Sterilization of PMMA microfluidic chips by various techniques and investigation of material characteristics. *J Supercrit Fluids*. 2016;107:114–21.
57. Ali U, Karim KJBA, Buang NA. A review of the properties and applications of poly (methyl methacrylate) (PMMA). *Polym Rev*. 2015;55:678–705. <https://doi.org/10.1080/15583724.2015.1031377>.
58. Trotta G, Volpe A, Ancona A, Fassi I. Flexible micro manufacturing platform for the fabrication of PMMA microfluidic devices. *J Manuf Process*. 2018;35:107–17.
59. Tomazelli Coltro WK, Cheng CM, Carrilho E, de Jesus DP. Recent advances in low-cost microfluidic platforms for diagnostic applications. *Electrophoresis*. 2014;35:2309–24. <https://doi.org/10.1002/elps.201400006>.
60. Guo J, Yu Y, Cai L, Wang Y, Shi K, Shang L, et al. Microfluidics for flexible electronics. *Mater Today*. 2021. <https://doi.org/10.1016/j.mattod.2020.08.017>.
61. Sabourin D, Petersen J, Snakenborg D, Brivio M, Gudnadson H, Wolff A, et al. Microfluidic DNA microarrays in PMMA chips: streamlined fabrication via simultaneous DNA immobilization and bonding activation by brief UV exposure. *Biomed Microdevices*. 2010;12:673–81. <https://doi.org/10.1007/s10544-010-9420-7>.
62. Battle KN, Jackson JM, Witek MA, Hupert ML, Hunsucker SA, Armistead PM, et al. Solid-phase extraction and purification of membrane proteins using a UV-modified PMMA microfluidic bioaffinity  $\mu\text{SPE}$  device. *Analyst*. 2014;139:1355–63.
63. Wongkaew N, He P, Kurth V, Surareungchai W, Baumner AJ. Multi-channel PMMA microfluidic biosensor with integrated IDUAs for electrochemical detection. *Anal Bioanal Chem*. 2013;405:5965–74. <https://doi.org/10.1007/s00216-013-7020-0>.
64. Yeh CH, Zhao Q, Lee SJ, Lin YC. Using a T-junction microfluidic chip for monodisperse calcium alginate microparticles and encapsulation of nanoparticles. *Sens Actuators A Phys*. 2009;151:231–6.
65. Su S, Jing G, Zhang M, Liu B, Zhu X, Wang B, et al. One-step bonding and hydrophobic surface modification method for rapid fabrication of polycarbonate-based droplet microfluidic chips. *Sens Actuators B Chem*. 2019;282:60–8.
66. Jia Y, Asahara H, Hsu Y-I, Asoh T-A, Uyama H. Surface modification of polycarbonate using the light-activated chlorine dioxide radical. *Appl Surf Sci*. 2020;530:147202.
67. Wang Y, He Q, Dong Y, Chen H. In-channel modification of biosensor electrodes integrated on a polycarbonate microfluidic chip for micro flow-injection amperometric determination of glucose. *Sens Actuators B Chem*. 2010;145:553–60.
68. Ogończyk D, Węgrzyn J, Jankowski P, Dąbrowski B, Garstecki P. Bonding of microfluidic devices fabricated in polycarbonate. *Lab Chip*. 2010;10:1324.
69. Romanov V, Samuel R, Chaharlang M, Jafek AR, Frost A, Gale BK. FDM 3D printing of high-pressure, heat-resistant, transparent microfluidic devices. *Anal Chem*. 2018;90:10450–6.
70. Guo T, Holzberg TR, Lim CG, Gao F, Gargava A, Trachtenberg JE, et al. 3D printing PLGA: a quantitative examination of the effects of polymer composition and printing parameters on print resolution. *Biofabrication*. 2017;9:024101.
71. Wang L, Kodzius R, Yi X, Li S, Hui YS, Wen W. Prototyping chips in minutes: direct laser plotting (DLP) of functional microfluidic structures. *Sens Actuators B Chem*. 2012;168:214–22. <https://doi.org/10.1016/j.snb.2012.04.011>.
72. Macdonald NP, Zhu F, Hall CJ, Rebound J, Crosier PS, Patton EE, et al. Assessment of biocompatibility of 3D printed photopolymers using zebrafish embryo toxicity assays. *Lab Chip*. 2016;16:291–7.
73. Piironen K, Haapala M, Talman V, Järvinen P, Sikanen T. Cell adhesion and proliferation on common 3D printing materials used in stereolithography of microfluidic devices. *Lab Chip*. 2020;20:2372–82.
74. Correa H, Aristizabal F, Duque C, Kerr R. Cytotoxic and antimicrobial activity of pseudo-pterostins and seco-pseudo-pterostins isolated from the octocoral *Pseudopterogorgia elisabethae* of San Andrés and Providencia islands (Southwest Caribbean Sea). *Mar Drugs*. 2011;9:334–44.
75. Ultimaker. Ultimaker 3 manual (En) v1.4. p. 1–60. 2017. <https://ultimaker.com/en/products/ultimaker-3>. Accessed 28 Jan 2021.
76. Park SJ, Lee JE, Lee HB, Park J, Lee N-K, Son Y, et al. 3D printing of bio-based polycarbonate and its potential applications in ecofriendly indoor manufacturing. *Addit Manuf*. 2020;31:100974.
77. Stone HA. Introduction to fluid dynamics for microfluidic flows. In: Lee H, Westervelt RM, Ham D (eds) *CMOS Biotechnology. Series on Integrated Circuits and Systems*. Springer, Boston, MA. 2007. [https://doi.org/10.1007/978-0-387-68913-5\\_2](https://doi.org/10.1007/978-0-387-68913-5_2).

78. Zhu F, Friedrich T, Nugegoda D, Kaslin J, Wlodkowic D. Assessment of the biocompatibility of three-dimensional-printed polymers using multispecies toxicity tests. *Biomicrofluidics*. 2015;9:061103. <https://doi.org/10.1063/1.4939031>.
79. Sanchez Noriega JL, Chartrand NA, Valdoz JC, Cribbs CG, Jacobs DA, Poulson D, et al. Spatially and optically tailored 3D printing for highly miniaturized and integrated microfluidics. *Nat Commun*. 2021;12:5509.
80. Lee SJ, Choi JS, Park KS, Khang G, Lee YM, Lee HB. Response of MG63 osteoblast-like cells onto polycarbonate membrane surfaces with different micropore sizes. *Biomaterials*. 2004;25:4699–707.
81. Li RY, Liu ZG, Liu HQ, Chen L, Liu JF, Pan YH. Evaluation of biocompatibility and toxicity of biodegradable poly (DL-lactic acid) films. *Am J Transl Res*. 2015;7:1357–70.
82. da Silva D, Kaduri M, Poley M, Adir O, Krinsky N, Shainsky-Roitman J, et al. Biocompatibility, biodegradation and excretion of polylactic acid (PLA) in medical implants and theranostic systems. *Chem Eng J*. 2018;340:9–14. <https://doi.org/10.1016/j.cej.2018.01.010>.
83. Joz Majidi H, Babaei A, Kazemi-Pasarvi S, Arab-Bafrani Z, Amiri M. Tuning polylactic acid scaffolds for tissue engineering purposes by incorporating graphene oxide-chitosan nano-hybrids. *Polym Adv Technol*. 2021;32:1654–66.
84. Lim KT, Hexiu J, Kim J, Seonwoo H, Choung P-H, Chung JH. Synergistic effects of orbital shear stress on in vitro growth and osteogenic differentiation of human alveolar bone-derived mesenchymal stem cells. *Biomed Res Int*. 2014;2014:1–18.
85. Castillo AB, Jacobs CR. Mesenchymal stem cell mechanobiology. *Curr Osteoporos Rep*. 2010;8:98–104. <https://doi.org/10.1007/s11914-010-0015-2>.
86. Bjerre L, Bunger CE, Kassem M, Mygind T. Flow perfusion culture of human mesenchymal stem cells on silicate-substituted tricalcium phosphate scaffolds. *Biomaterials*. 2008;29:2616–27.
87. Stiehler M, Bunger C, Baatrup A, Lind M, Kassem M, Mygind T. Effect of dynamic 3-D culture on proliferation, distribution, and osteogenic differentiation of human mesenchymal stem cells. *J Biomed Mater Res Part A*. 2008. <https://doi.org/10.1002/jbm.a.31967>.
88. Babaliari E, Petekidis G, ChatziniKolaidou M. A precisely flow-controlled microfluidic system for enhanced pre-osteoblastic cell response for bone tissue engineering. *Bioengineering*. 2018;5:66.
89. Hong D, Chen HX, Xue Y, Li DM, Wan XC, Ge R, et al. Osteoblastogenic effects of dexamethasone through upregulation of TAZ expression in rat mesenchymal stem cells. *J Steroid Biochem Mol Biol*. 2009;116:86–92.
90. Langenbach F, Handschel J. Effects of dexamethasone, ascorbic acid and  $\beta$ -glycerophosphate on the osteogenic differentiation of stem cells in vitro. *Stem Cell Res Ther*. 2013;4:1.

### Publisher's Note

Springer Nature remains neutral with regard to jurisdictional claims in published maps and institutional affiliations.

Ready to submit your research? Choose BMC and benefit from:

- fast, convenient online submission
- thorough peer review by experienced researchers in your field
- rapid publication on acceptance
- support for research data, including large and complex data types
- gold Open Access which fosters wider collaboration and increased citations
- maximum visibility for your research: over 100M website views per year

At BMC, research is always in progress.

Learn more [biomedcentral.com/submissions](https://biomedcentral.com/submissions)



### **3.1.2 Rapid Phenotypic Antibiotics Susceptibility Analysis by a 3D Printed Prototype**

#### **Own contribution to the article**

The authors' contribution to this publication was as follows. The conceptualization of the study was performed by Prof. Deigner and the author of this thesis with the support of Dr. Kaiser and Prof. Laufer. All experiments were planned, performed and evaluated by the author of this thesis, including the writing of the Python script for the data analysis of the electrochemical measurements. Dr. Kaiser and Prof. Deigner were responsible for funding acquisition. The supervision of the work was performed by Prof. Laufer and Prof. Deigner. Writing of the original draft with visualizations was carried out by the author of this thesis with the support of Prof. Deigner. All authors reviewed, edited and approved the manuscript.

Reprinted with permission from the Authors. Copyright © 2024 The Authors. Advanced Science published by Wiley-VCH GmbH. This article is an open access article distributed under a Creative Commons Attribution 4.0 International License (<http://creativecommons.org/licenses/by/4.0/>).

**Riester, O.; Kaiser, L.; Laufer, S.; Deigner, H.-P. Rapid Phenotypic Antibiotics Susceptibility Analysis by a 3D Printed Prototype. Adv. Sci. 2024. <https://doi.org/10.1002/adv.202308806>.**



## RESEARCH ARTICLE

ADVANCED  
SCIENCE

www.advancedscience.com

# Rapid Phenotypic Antibiotics Susceptibility Analysis by a 3D Printed Prototype

*Oliver Riester, Lars Kaiser, Stefan Laufer, and Hans-Peter Deigner\**

One of the most important public health concerns is the increase in antibiotic-resistant pathogens and corresponding treatment of associated infections. Addressing this challenge requires more efficient use of antibiotics, achievable by the use of evidence-based, effective antibiotics identified by antibiotic susceptibility testing (AST). However, the current standard method of phenotypic AST used for this purpose requires 48 h or more from sample collection to result. Until results are available, broad-spectrum antibiotics are used to avoid delaying treatment. The turnaround time must therefore be shortened in order for the results to be available before the second administration of antibiotics. The phenotypic electrochemical AST method presented here identifies effective antibiotics within 5–10 h after sampling. Spiked serum samples, including polymicrobial samples, with clinically relevant pathogens and respective concentrations commonly found in bloodstream infections (*Escherichia coli*, *Staphylococcus aureus*, *Klebsiella pneumoniae*, and *Pseudomonas aeruginosa*) are used. Direct loading of the test with diluted serum eliminates the need for a pre-culture, as required by existing methods. Furthermore, by combining several electrochemical measurement procedures with computational analysis, allowing the method to be used both online and offline, the AST achieves a sensitivity of 94.44% and a specificity of 95.83% considering each replicate individually.

a growing health problem worldwide that could lead to 10 million deaths per year by 2050, if no action is taken.<sup>[1]</sup> As of 2019, infections with AR pathogens were responsible for a worrying number of deaths worldwide, accounting for ≈4.95 million (64 per 100 000) deaths associated with AR pathogens and 1.27 million (16.4 per 100 000) deaths directly attributable to infections with AR pathogens.<sup>[2]</sup> In particular, the fact that pathogens resistant to new antibiotics are often detected in clinics within a year after their approval,<sup>[3]</sup> as well as the correlation between excessive use and the development of new resistances,<sup>[4]</sup> highlights the necessity of responsible and restrictive use of antibiotics. Although the causal relationship between excessive antibiotic use and the emergence of resistance has been acknowledged for some time, antibiotic use is increasing rather than decreasing,<sup>[5,6]</sup> particularly in the veterinary sector, where estimated antimicrobial consumption is projected to increase by 8% between 2020 and 2030, based on current trends.<sup>[7]</sup> In addition to reducing the likelihood of new resistances emerging, the targeted use of antibiotics with confirmed efficacy has the advantage of improving treatment outcomes.<sup>[8,9]</sup> However, in order to use the most appropriate and effective antibiotic, one must first

## 1. Introduction

Treating infections caused by antibiotic-resistant (AR) pathogens displays an increasing challenge and is, according to the WHO,

targeted use of antibiotics with confirmed efficacy has the advantage of improving treatment outcomes.<sup>[8,9]</sup> However, in order to use the most appropriate and effective antibiotic, one must first

O. Riester, L. Kaiser, H.-P. Deigner  
Institute of Precision Medicine  
Furtwangen University  
Jakob-Kienzle-Strasse 17, 78054 Villingen-Schwenningen, Germany  
E-mail: [deigner@gmx.de](mailto:deigner@gmx.de)

O. Riester, S. Laufer  
Institute of Pharmaceutical Sciences  
Department of Pharmacy and Biochemistry  
Eberhard-Karls-University Tuebingen  
Auf der Morgenstelle 8, 72076 Tuebingen, Germany

S. Laufer  
Tuebingen Center for Academic Drug Discovery & Development  
(TüCAD2)  
72076 Tuebingen, Germany

S. Laufer  
IFIT Cluster of Excellence EXC 2180 'Image-Guided and Functionally  
Instructed Tumor Therapies'  
University of Tuebingen  
72076 Tuebingen, Germany

H.-P. Deigner  
Faculty of Science  
Eberhard-Karls-University Tuebingen  
Auf der Morgenstelle 8, 72076 Tuebingen, Germany

H.-P. Deigner  
EXIM Department  
Fraunhofer Institute IZI (Leipzig)  
Schillingallee 68, 18057 Rostock, Germany

The ORCID identification number(s) for the author(s) of this article can be found under <https://doi.org/10.1002/advs.202308806>

© 2024 The Authors. Advanced Science published by Wiley-VCH GmbH. This is an open access article under the terms of the [Creative Commons Attribution](#) License, which permits use, distribution and reproduction in any medium, provided the original work is properly cited.

DOI: 10.1002/advs.202308806

know which is effective against the pathogen present, thus requiring antimicrobial susceptibility testing (AST). The current state of the art involves blood culture as the first step, followed by isolation of pathogens and finally AST.<sup>[10]</sup> As a result, the turnaround time from sample collection to AST result is typically 48 h or more, with blood culture and isolation of potential pathogens taking 24 to 48 h and the actual AST taking 16 to 24 h for gold standard methods or 4 to 8 h for automated methods.<sup>[10,11]</sup> However, it would be desirable to obtain an AST result within 8 h or less after sample collection in order to be able to administer a proven effective antibiotic to the patient after the initial antibiotic administration. For this reason, a wide variety of technologies and processes are being tested and further developed to determine their suitability for meeting the desired turnaround time while maintaining the same quality as the current gold standard.

AST are classified in two categories: phenotypic and genotypic. Phenotypic approaches, the current gold standard, study the effect of an administered antibiotic on a bacterial population by measuring its metabolic activity or bacterial growth and thus detect the direct effect of the antibiotic. Genotypic approaches, on the other hand, do not detect the direct effect of the antibiotic, rather they test for the presence of genes that are required for resistance. This approach has the advantage that, in theory, there is no need for prior cultivation, although this still represents a challenge in practice.<sup>[12]</sup> Shifman et al.<sup>[13]</sup> used a reverse-transcriptase polymerase chain reaction (RT-PCR) to quantify RNA markers of *Yersinia pestis* accountable for ARs. They were able to determine the minimum inhibitory concentration of doxycycline within 7 h after positive blood culture, a significant advantage over the CLSI standard of 24 h, especially for *Yersinia pestis*, whose slow *ex vivo* growth was specifically pointed out by the authors. A disadvantage of PCR-based methods is that the primers targeting the resistance gene must be chosen specifically in advance. This problem can be addressed by whole genome sequencing (WGS) approaches, which are becoming increasingly attractive as next-generation sequencing advances. For example, using nanopore metagenomics, Charalampous et al.<sup>[14]</sup> demonstrated that it is possible to detect the pathogen and the resistance genes of a bacterial lower respiratory tract infection within 6 h. Nevertheless, the European Committee on Antimicrobial Susceptibility Testing (EUCAST) stated in 2017 that the available evidence for WGS as an AST tool is either insufficient or nonexistent and therefore inappropriate for clinical decision making.<sup>[12]</sup> They also pointed out the urgent need for a single database of all known resistance genes/mutations to facilitate comparison between different systems and bioinformatic tools. These statements are also supported by a study from Rebelo et al.<sup>[15]</sup> in which they compared 500 bacterial isolates from Danish clinical microbiology laboratories tested with WGS (Illumina NextSeq, genotypic) and standard broth microdilution (phenotypic). Concordance was observed in 91.7 % of all cases, with the remaining 8.3 % divided as follows: 6.2 % were phenotypically susceptible isolate-antimicrobial combinations that possessed resistance genes but did not exhibit effective resistance, and 2.1 % had phenotypic resistances that were not detected by WGS, representing 26.4 % of all phenotypic resistances present that were not detected by WGS. This highlights that, given the current state of the art, genotypic tests, particularly WGS-based tests, often require phenotypic verifi-

cation to provide clinically relevant conclusions.<sup>[16]</sup> Therefore, phenotypic AST tests will remain irreplaceable as the standard for the foreseeable future, making it vital to reduce their turnaround time.

To shorten the turnaround time of phenotypic AST, it is particularly helpful to avoid the upstream blood culture, thus requiring tests to be loaded directly with the patient sample or a dilution thereof and the bacterial concentrations present therein. The majority of AR-associated deaths are caused by lower respiratory or bloodstream infections<sup>[2]</sup> and sputum or serum specimens contain approximately  $>10^4$ <sup>[17,18]</sup> or  $<10^3$  CFU/ml,<sup>[19,20]</sup> respectively. Thus, an appropriate detection method should be able to provide results ideally within the first 8 h of testing under these starting conditions. A variety of detection methods have been described in the literature for rapid phenotypic AST, such as detection by fluorescence,<sup>[21,22]</sup> luminescent measurement of extracellular ATP,<sup>[23]</sup> microscopic detection of cell growth,<sup>[24]</sup> antibody-modified magnetic nanoparticles,<sup>[25]</sup> electrochemical measurements by differential pulsed voltammetry (DPV)<sup>[26–28]</sup> or electrochemical impedance spectroscopy (EIS).<sup>[29]</sup>

However, most of them were demonstrated only in buffer, growth medium, or artificial urine, and often at high initial concentrations of  $10^5$  CFU/ml or more, requiring prior incubation. Some methods also destroy the sample during the measurement, e.g. by lysing the bacteria, which leads to an increased number of samples if a time course and no endpoint determination is to be recorded.

Herein, we demonstrate a 3D-printed phenotypic rapid AST system based on a combination of DPV and EIS measurements. To our knowledge, this study is the first demonstration of a rapid AST system that provides results from spiked serum samples at 1000 CFU/ml in  $<10$  h after sample collection (Figure 1). The approach combines EIS measurements with DPV measurements of Resazurin, which is metabolized by living bacteria to resorufin.<sup>[30]</sup> The assay was tested for seven clinically relevant bacterial strains with different resistance profiles to kanamycin and oxytetracycline, which were selected as example antibiotics due to their widespread resistance<sup>[31,32]</sup> and their correspondence with the resistance/susceptibility profile of the bacterial strains used. Included were most common pathogens of bloodstream infections, such as *Escherichia coli* (*E. coli*), *Staphylococcus aureus* (*S. aureus*), *Klebsiella pneumoniae* (*K. pneumoniae*), and *Pseudomonas aeruginosa* (*P. aeruginosa*).<sup>[33]</sup> Furthermore, it was demonstrated that the 3D-printed system can be scaled up to multiple chambers and can also be complemented with a suitable microfluidic channel system to ensure user-friendly loading.

## 2. Results and Discussion

### 2.1. Combining 3D Printed Microfluidic Device Designs with Embedded SPEs

The devices were designed such that commercial screen-printed electrodes (SPEs) could be embedded within the test system. By combining the SPEs with a 3D-printed microfluidic device, a closed system was developed, minimizing evaporation and allowing test intervals of more than 16 h. Several designs were created

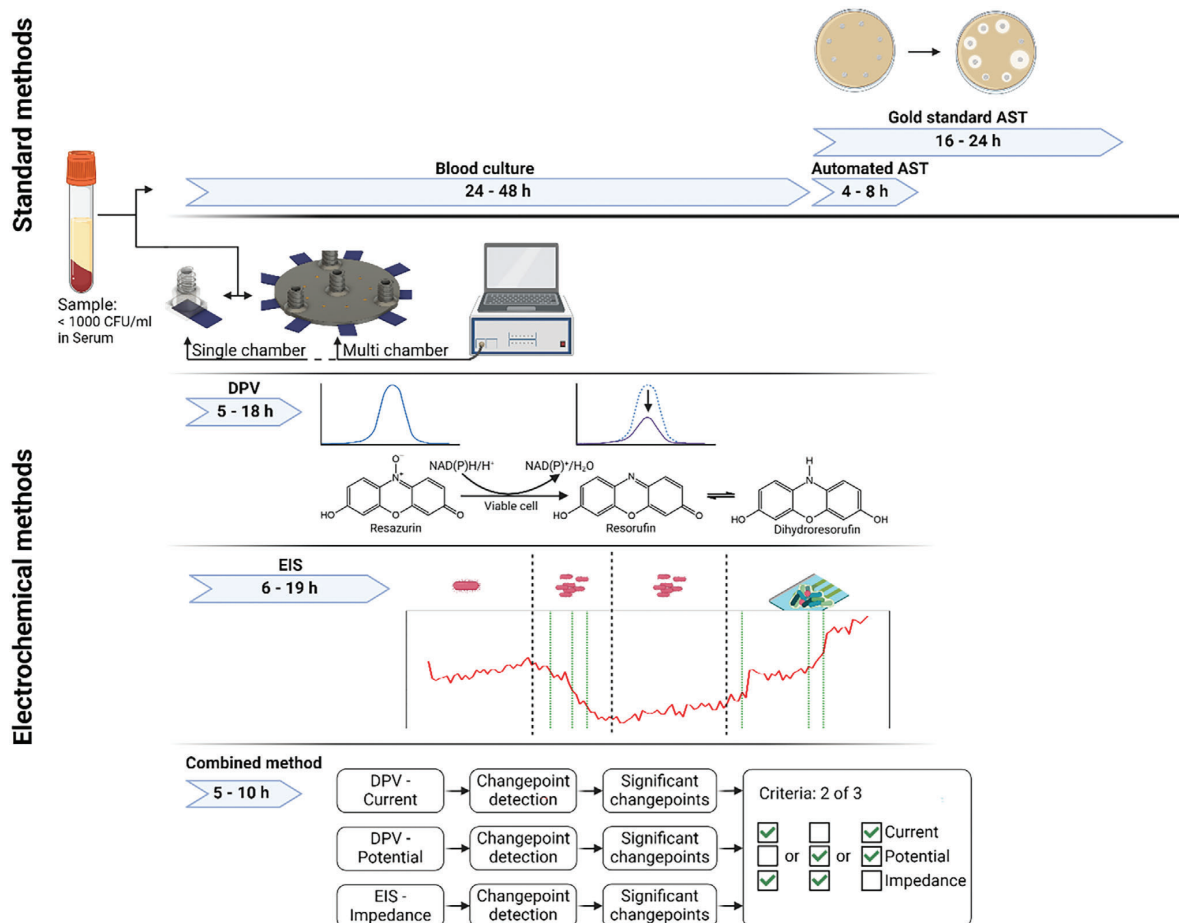


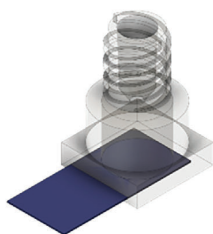
**Figure 1.** Overview of AST with respective time intervals using standard methods or the here demonstrated electrochemical methods. The rapid AST platform in a 3D printed microfluidic device can be used as a single chamber or a multi-chamber version. Measurement of antimicrobial susceptibility is based on electrochemical impedance spectroscopy (EIS) and the metabolic reduction of resazurin to resorufin analyzed by differential pulse voltammetry (DPV).

that demonstrate the flexibility of the concept to meet application requirements. For example, devices were developed for anaerobic and aerobic culture conditions in single and multi-chamber versions (Figure 2). The anaerobic and multi-chamber devices were only tested for tightness and ease of filling in order to provide a proof of concept (Figure S1, Supporting Information). AST experiments were performed in single-chamber aerobic devices (Figure 2A,B), with multiple devices being measured in parallel. The designs can be further adapted to suit the desired test conditions and the number of antibiotics or concentrations to be tested. For example, the multi-chamber version can be adapted to an aerobic design by removing the vent channels (Figure 2D, shown in red) and replacing the top layer of the chambers with a gas permeable membrane.

## 2.2. Antibiotic Susceptibility Test by Agar Diffusion Assay – Gold Standard

To enable a comparison of the newly developed method with the current gold standard, the used strain-antibiotic combinations were evaluated using the agar diffusion test, displayed in Figure 3. The test was performed as reference AST with 21 strain-antibiotic combinations, including 7 untreated, 7 treated with kanamycin, and 7 treated with oxytetracycline. The reference test demonstrated growth in all 7 untreated samples, resistance in 6 combinations, and susceptibility in 8 combinations. The observed resistances were mostly consistent with data available in the Bacdiv library.<sup>[34]</sup> The only differences were observed for the *P. aeruginosa* strains, as *P. aeruginosa* (DSM

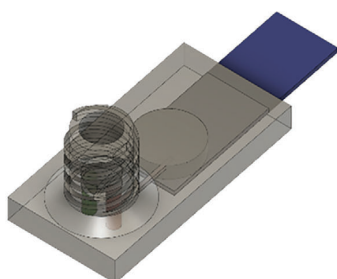
A) CAD model: aerobic test device



B) Aerobic test device with cap



C) CAD model: anaerobic test device



D) CAD model: multichamber test device

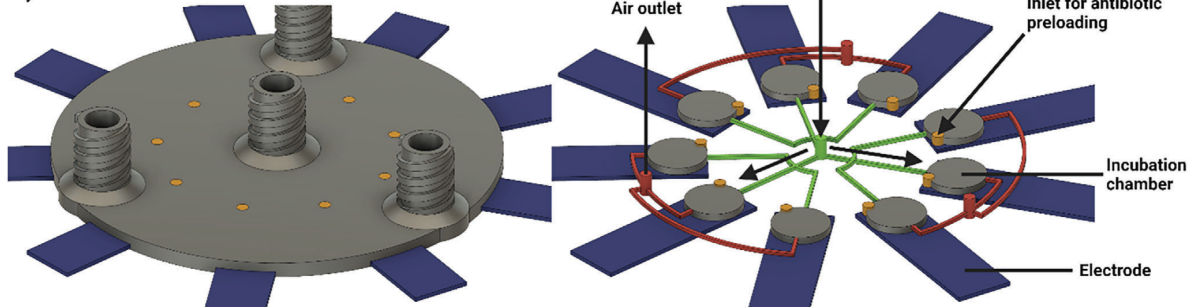


**Figure 2.** 3D printed device designs. 3D-printed devices with integrated SPEs were fabricated from PMMA in various designs. A) CAD model of aerobic design with headspace for oxygen exchange. B) Image of aerobic test device with implemented IS-C electrode and sealed with Luer lock cap. CAD model of C) single-chamber and D) multi-chamber versions of the anaerobic design with respective microfluidic distribution structures. Shown are microfluidic structures for filling with sample (green), venting air present (red), and preloading antibiotics (orange). Arrows indicate flow direction during sample loading. For images of the 3D-printed anaerobic and multi-chamber designs, the reader is referred the supplementary materials.

102273) should be sensitive to tetracycline (no entry for oxytetracycline) according to the library, which was not observed for oxytetracycline, chemically similar to tetracycline. In addition, *P. aeruginosa* (DSM 25123) is not listed as resistant in the library, but showed resistance or high tolerance to oxytetracycline. These differences may also be due to differences in the concentrations tested, as they were chosen to be comparable to the ones used in the electrochemical experiments.

### 2.3. Antibiotic Susceptibility Test by Electrochemical Detection

Phenotypic AST using electrochemical methods for the detection of bacterial growth have several advantages, especially when com-

pared to fluorescence measurements, such as comparable sensitivity and selectivity, low cost, low power requirements, multiple measurement methods, and compatibility with microfabrication technology.<sup>[35]</sup> In particular the possibility to combine several measurement methods in one device and perform them simultaneously for one sample offers immense potential. In the following, the detection of bacterial growth (or the absence when susceptible to antibiotic) for clinically relevant bacterial strains in spiked plasma samples using DPV and EIS in combination with computational analysis is demonstrated. Representative plots for multi-resistant *Staphylococcus aureus* (MRSA, DSM 28766) are shown as examples in **Figures 4** and **5**. MRSA was selected as an example strain as it shows resistance to kanamycin and sensitivity to oxytetracycline. For representative plots of further tested

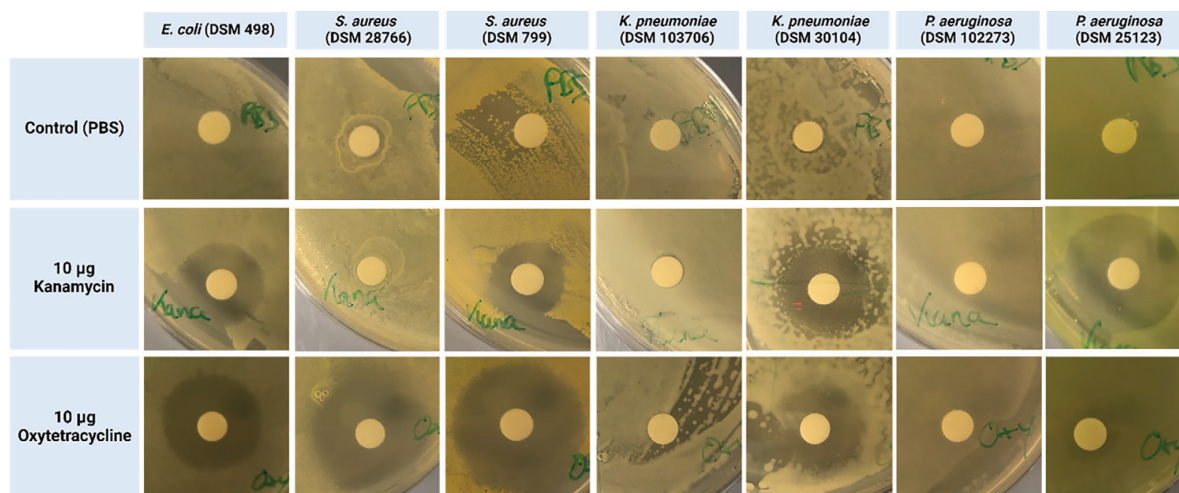


**Figure 3.** Antibiotic susceptibility test by agar diffusion test. Indicated bacterial strains are tested for susceptibility to the antibiotics kanamycin and oxytetracycline at concentrations of 10  $\mu\text{g}$  per disc. Susceptibility to antibiotics is indicated by the formation of an inhibition zone surrounding the discs. PBS was included as control.

bacterial strains (*E. coli* (DSM 498); *S. aureus* (DSM 799); *K. pneumoniae* (DSM 103706); *K. pneumoniae* (DSM 30104); *P. aeruginosa* (DSM 102273); *P. aeruginosa* (DSM 25123)) the reader is referred to Figures S2–S8 (Supporting Information). The ASTs performance (sensitivity, specificity, positive predictive value (PPV), and negative predictive value (NPV)) was evaluated using the agar diffusion assay (Figure 3) as reference. Furthermore, the turnaround time for detection of growth was analyzed using each method individually or in combination (Table S1, Supporting Information; Figures 4 and 5). The electrochemical antibiotic susceptibility test was performed 68 times, including five control samples without bacteria and the same strain-antibiotic combinations as for the agar diffusion assay, each with three independent replicates.

### 2.3.1. Differential Pulsed Voltammetry (DPV)

The use of DPV for the measurement of resazurin metabolization is already described in the literature.<sup>[27,28]</sup> However, to our knowledge, the method has never been demonstrated in plasma or serum samples with realistic bacterial concentrations suitable for bloodstream infection. Diluted samples of spiked serum (1000 CFU/ml) were tested with an Italsens-Carbon (IS-C) SPE, resulting in 250 CFU/ml in 25/75% FCS/LB. It was observed that the current was unstable in the first 3 to 4 h and the absolute initial values varied from device to device at the same initial resazurin concentration (Figure 4A). The observed increase in current ( $I$ ) during the first 3 to 4 h was likely the result of protein adsorption and equilibration of the reference electrode caused by wetting effects and was observed for all bacterial strains and controls. However, the effect did not influence the measurement, as within the first few hours the growth of the bacteria is still too low to be detected. In addition, it was shown (Figure S12, Supporting Information), that this effect can be reduced by pre-wetting the

electrodes in advance. Although the initial current increase did not interfere with the measurement itself, pre-equilibrium values were excluded and the analysis was performed with the first derivative, as the increase was always detected as a change point by the detection algorithm.

The analysis of the first derivative has two advantages in this respect: first, the offset of the individual instruments becomes less influential and second, the signal change, which serves as evidence of bacterial growth, becomes more comparable for different samples. The first derivative of  $I$  can assume both positive and negative values as a result of bacterial growth. Negative values (e.g., Figure 4A: *S. aureus* – No antibiotic between 10 and 14 h) can be interpreted as a decrease in resazurin concentration due to its metabolization, as shown in Figures S9 and S10 (Supporting Information) for different resazurin concentrations. Positive values (e.g., Figure 4A: *S. aureus* – No antibiotic between 6 and 9 h), on the other hand, can be explained by a decrease in pH as described by Cakir et al.,<sup>[30]</sup> e.g., as a result of accumulated metabolites during bacterial growth. The presence of additional protons increases the measured current of the 2-electron transfer reaction from resazurin to resorufin and the potential of the peak maximum in the course of the experiment, leading to an initial increase in the current until the effect is superimposed by the decrease in the resazurin concentration. The decrease in current in samples with bacterial growth is therefore not solely due to the decrease in resazurin concentration, but also partly due to the aforementioned peak shift, as the evaluation was carried out constantly at  $-0.3$  V, even if the potential of the peak maximum had shifted. In addition to the current intensity, however, the peak shift can also be used as a parameter for determining bacterial growth.

Bioinformatic analysis via current intensity using change point detection resulted in growth detection after  $4.89 \pm 0.21$  h up to 13.17 h, depending on the strain-antibiotic combination (Figure 4B). In some cases, growth was also delayed by the

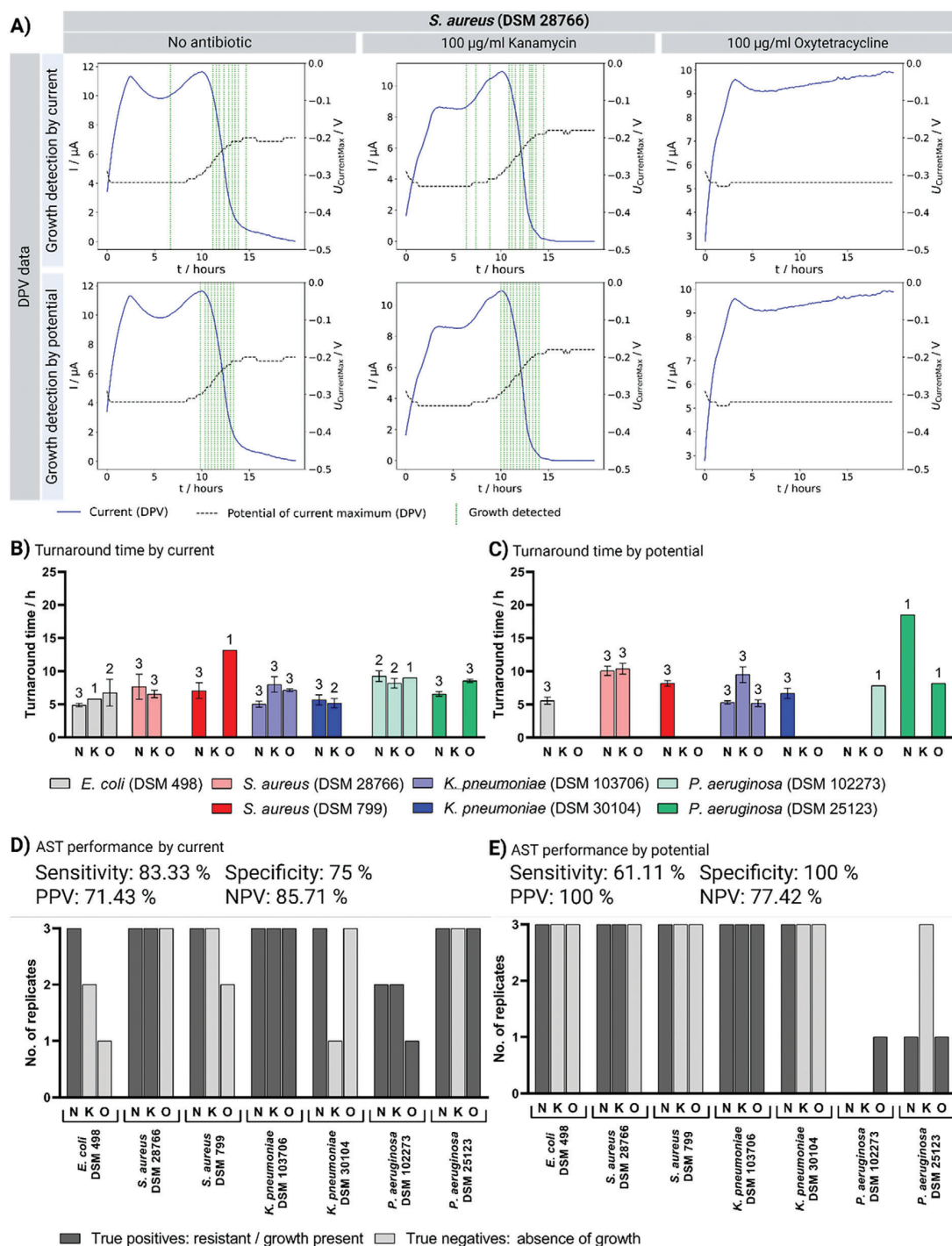


**Figure 4.** Electrochemical measurement and bioinformatic analysis of antibiotic susceptibility by DPV. Bacterial growth of pathogens (1000 CFU/ml in serum corresponding to 50 CFU/measuring chamber) with 100  $\mu\text{g ml}^{-1}$  kanamycin (K), 100  $\mu\text{g ml}^{-1}$  oxytetracycline (O), or without antibiotic (N) detected by differential pulsed voltammetry (DPV) via current intensity or potential shift. A) Representative replicates for DPV measurement of MRSA (DSM 28766) with growth detected by current or potential. Turnaround time (mean  $\pm$  SD) until growth was detected by B) current or C) potential. Number above bars indicates replicates that detected growth ( $n = 3$ , independent devices). Performance of AST by D) current or E) potential compared to agar diffusion assay (Figure 3) with true positives (resistant to treatment/exhibits growth) and true negatives (susceptible to treatment/exhibits no growth).

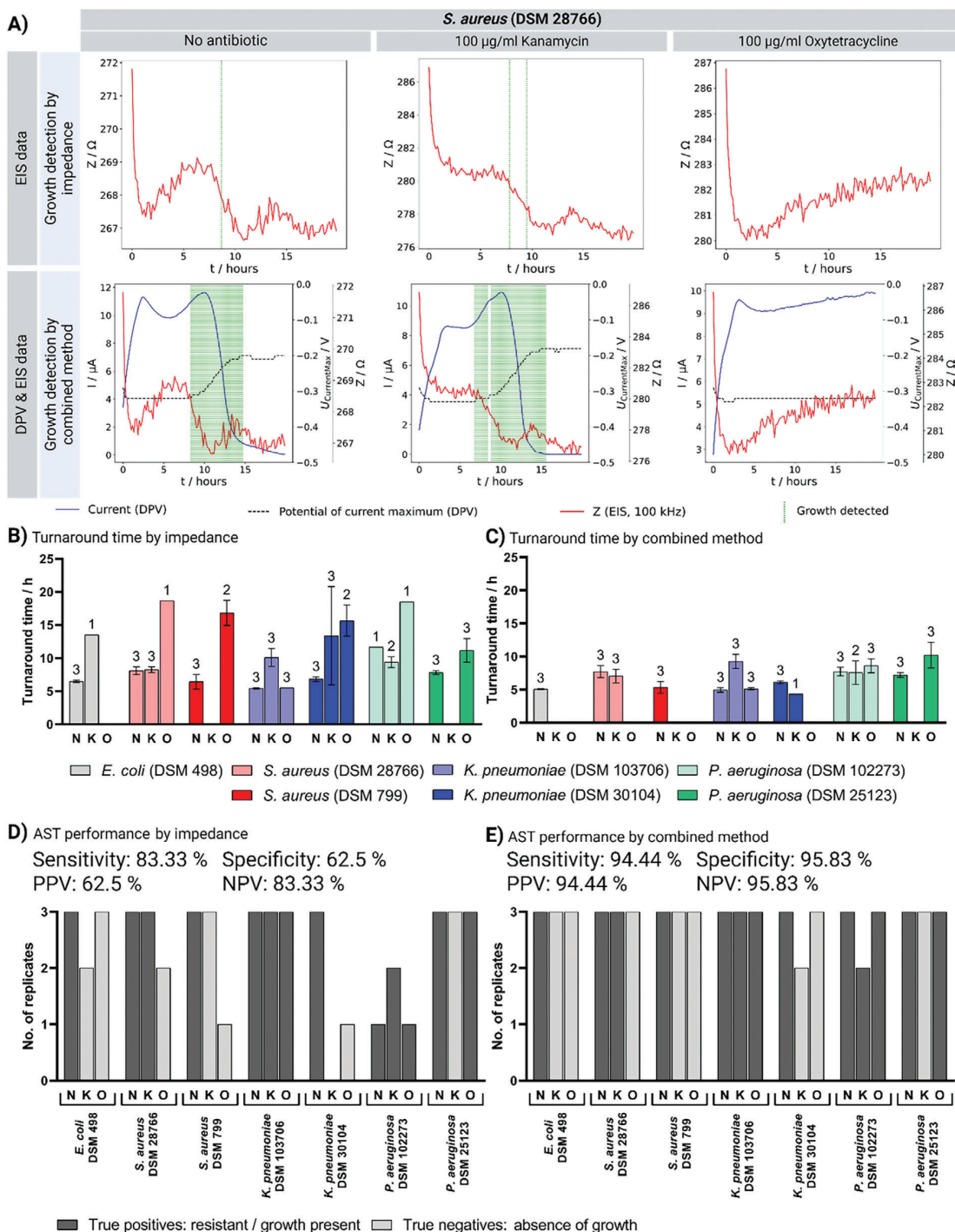


**Figure 5.** Electrochemical measurement and bioinformatic analysis of antibiotic susceptibility by EIS or combined method. Bacterial growth of pathogens (1000 CFU/ml in serum corresponding to 50 CFU/measuring chamber) with  $100 \mu\text{g ml}^{-1}$  kanamycin (K),  $100 \mu\text{g ml}^{-1}$  oxytetracycline (O), or without antibiotic (N) detected by electrochemical impedance spectroscopy (EIS) or a combined method of EIS and DPV. A) Representative replicates for EIS and DPV measurement of MRSA (DSM 28766) with growth detected by impedance or combined method. Turnaround time (mean  $\pm$  SD) until growth was detected by B) impedance or C) combined method. Number above bars indicates replicates that detected growth ( $n = 3$ , independent devices). Performance of AST by D) impedance or E) combined method compared to agar diffusion assay (Figure 3) with true positives (resistant to treatment/exhibits growth) and true negatives (susceptible to treatment/exhibits no growth).

addition of antibiotics, e.g. when *K. pneumoniae* (DSM 107306) was tested for susceptibility to kanamycin (Figure 4B,C; Figure S5, Supporting Information), indicating a partial effect of the antibiotic but not sufficient to completely stop growth. In the 42 tests performed excluding controls, analysis via current intensity detected 21 (15 true positives, 6 false positives) resistant and 21 (18 true negatives, 3 false negatives) sensitive strain-antibiotic combinations, resulting in a sensitivity of 83.33% and a specificity of 75% (Figure 4D). When using the peak maximum potential as a parameter for change point detection, growth was detected between  $5.17 \pm 0.41$  h and 18.5 h (Figure 4C), and thus slower than detection via current. Analysis via potential resulted in the detection of 11 (11 true positives, 0 false positives) resistances and 31 (24 true negatives, 7 false negatives) susceptibilities, resulting in a lower sensitivity of 61.11% but a higher specificity of 100% (Figure 4E).

### 2.3.2. Electrochemical Impedance Spectroscopy (EIS)

In order to improve the performance of the electrochemical AST and to detect slowly metabolizing or biofilm-forming pathogens, the DPV method was supplemented by EIS, a method that can be performed with the same experimental setup. The principle of the EIS measurement method for bacterial growth can produce both increasing and decreasing curve patterns for measured impedance over time, which are explained in the literature as follows: an increase in impedance is due to a decrease in accessible electrode surface area as a result of a bacterial layer on the surface (e.g., biofilm formation), whose cell membranes act as an insulating layer, decreasing the accessible area for electron transfer.<sup>[36]</sup>

The effect of impedance reduction is described, for example, by Asami et al.,<sup>[37]</sup> stating that living bacteria with intact cell membranes behave like electrical capacitors in solution. By increasing in numbers, the bacteria increase the capacitive characteristics of the dielectric and thereby influence the measured capacitance ( $C$ ) and impedance ( $Z$ ). According to equation 1, where  $i$  is the imaginary unit and  $\omega$  the angular frequency, an increase in  $C$  results in a decrease of  $Z$ .

$$Z = \frac{1}{i\omega C} \quad (1)$$

The frequency of the alternating current applied during the EIS measurement also determines which components or properties, such as cell size, cell membrane, or periplasmic space, have an influence on the measurement signal.<sup>[38,39]</sup> In theory, the effects described result in various plausible signal changes. However, for all seven strains tested it became apparent that they caused a reduction in impedance during growth, which indicates planktonic growth according to the second effect. For some antibiotic-strain combinations (e.g., oxytetracycline – *K. pneumoniae*, Figure S5, Supporting Information), a subsequent increase in impedance is observed after a longer test period, possibly indicating the formation of a biofilm on the electrode according to the first effect. Using impedance ( $Z$ ) at 100 kHz as a parameter for bioinformatic analysis to detect bacterial growth resulted in turnaround times ranging from  $5.44 \pm 0.08$  h up to 18.67 h, depending on the pathogen. Thereby, 24 (15 true positives, 9 false positives) resistant and 18 (15 true negatives, 3

false negatives) sensitive strain-antibiotic combinations were detected, which results in a sensitivity of 83.33% and a specificity of 62.5%.

### 2.3.3. Analysis by Combined Method

As previously demonstrated, growth detection based solely on current, potential, or impedance parameters have their advantages and disadvantages. For example, detection via current showed the fastest turnaround times, but only mediocre sensitivity (83.33%) and specificity (75%), as well as low signal changes in pathogens with slow metabolism such as *P. aeruginosa* (Figures S7 and S8, Supporting Information). For pathogens with slow metabolism, detection by impedance was advantageous as the measurement principle is not based on metabolic activity. However, the specificity was significantly lower with 62.5%, while it was 100% for detection via potential. In order to use the advantages of all parameters and measurement principles and thus compensate for their disadvantages, a combined analysis was performed using all parameters. The combination of different electrochemical measurement methods benefits the AST assay by incorporating all favorable signal changes and cross-checking the results obtained by the different parameters. This results in a reduction of false positives and false negatives, thus increasing the sensitivity and selectivity of the test. Using the combined method (significant change point for 2 of 3 parameters over the last hour), 94.44% sensitivity and 95.83% selectivity were achieved at turnaround times of  $4.94 \pm 0.28$  to  $10.22 \pm 1.59$  h, based on a reduction in the number of false negatives and false positives to 1 out of 42 tests, respectively. The method is therefore suitable for identifying an effective antibiotic within 8–24 h after sampling and significantly reduces the 28–72 h typically required by standard methods.

## 3. Conclusion

In summary, an approach for efficient and reliable antibiotic susceptibility testing is presented, which is already close to a prototype with clinical utility. It demonstrates the combination of different electrochemical measurement methods in a device that benefits from 3D-printed microfluidic devices and leads to reproducible and rapid results, even for clinically problematic pathogens. The AST enables treatment of patients with evidence-based, effective antibiotics, improving treatment outcomes while conserving available reserve antibiotics by reducing future antibiotic resistance. The assay presented here was used to detect resistance to kanamycin and oxytetracycline in seven strains, including *E. coli* and two strains each of *S. aureus*, *K. pneumoniae*, and *P. aeruginosa* with different resistance profiles. Bacterial growth (or lack thereof) was detected after  $4.94 \pm 0.28$  to  $10.22 \pm 1.59$  h under realistic conditions of a bloodstream infection, resulting in the resistance profile for each sample. For each individual replicate, a sensitivity of 94.44% and a specificity of 95.83% was obtained, or 100% for both when the majority outcome of each triplicate was considered. The time saving is achieved in particular by cultivating the bacteria (blood culture requires 24–48 h by default) and the actual AST (4–24 h by default) in a single step. Compared to other AST systems (Table 1), the turnaround time was

**Table 1.** Comparison of the demonstrated phenotypic AST system with commercial (Vitek2 and BD Phoenix) and experimental systems.

AST system	This study	Vitek2 [40]	BD Phoenix [40]	Hannah et al. [41]	Balteskin et al. [24]	Azizi et al. [22]
Measurement principle	Electrochemical (DPV, EIS)	Turbidity	Colorimetric redox indicator	Electrochemical (EIS)	Microscopy	Fluorescence
Sample origin	Serum	Respiratory, blood, eye	Respiratory, blood, eye	Growth medium	Urine or growth medium	Growth medium
Preculture needed?	Direct	Preculture 18–24 h	Preculture 18–24 h	Preculture overnight (12–18 h)	Preculture 2 h	Preculture overnight (12 h)
Sample preparation	Dilute 1/4 with growth medium	"McFarland standard of 0.5 to 0.63 in 0.45% sodium chloride"	"25 $\mu$ l was transferred to AST broth to obtain a final inoculum density of $\approx 5 \times 10^5$ CFU/ml"	"Bacteria from the overnight cultures were directly pipetted onto the gels on the electrode surface"	During chip loading, bacteria are trapped in the channels.	Chip pre-treatment: 30 min in water to saturate and thus reduce evaporation.
Bacteria in prepared sample [CFU/ml]	<250	$\approx 1.5 \times 10^8$	$5 \times 10^5$	$10^7$	$>10^4$	$10^7$
Turnaround time (ex. preculture) [h]	5–10 (5–10)	27.8–33.8 (9.8)	30.1–36.1 (12.1)	13–19 ( $\approx 1$ )	>2.5 (>0.5)	13–15 (1–3)
Challenges remaining						
Demonstrated for complex samples	Yes	Yes	Yes	No	No	No
Hands-on time	Low	average	average	Low	High	Low
Demonstrated for several pathogens	Yes	Yes	Yes	No	Yes (mainly for <i>E. coli</i> )	Yes
Sophisticated equipment required / Point of care possible	No / Yes	Yes / No	Yes / No	No / Yes	Yes / No	No / Yes
Scalability for high throughput applications	Good	Good	Good	Good	Poor	Good
Method-specific challenges		Long preculture	Long preculture	Evaporation restricts longer measurements	Channel size has to match bacteria: high variability results for <i>K. pneumonia</i> and <i>S. saprophyticus</i>	

significantly reduced, allowing an effective antibiotic to be identified at the time of the second antibiotic administration, thereby significantly improving the treatment outcome. Furthermore, the use of broad-spectrum antibiotics and the total amount of administered antibiotics can be reduced, thus limiting the emergence of further resistances. It was also pointed out that the assay has the potential to be used in multi-chamber systems with an appropriate microfluidic distribution structure for easy filling. This would not only allow the serum sample to be tested for different antibiotics simultaneously and in principle for polymicrobial infections (Figures S13 and S14, Supporting Information), but also allow the minimum inhibitory concentration of the antibiotic in question to be determined by testing different concentrations of antibiotics (Figure S15, Supporting Information). The authors also note that the electrodes used are unmodified, commercially available electrodes that could be exchanged for optimized electrodes with higher sensitivity to further improve the turnaround time and robustness of the test system. The properties of the electrodes, such as the material of the working and reference electrodes or modifications of the surface, as well as the properties of the medium have an influence on the respective measurement

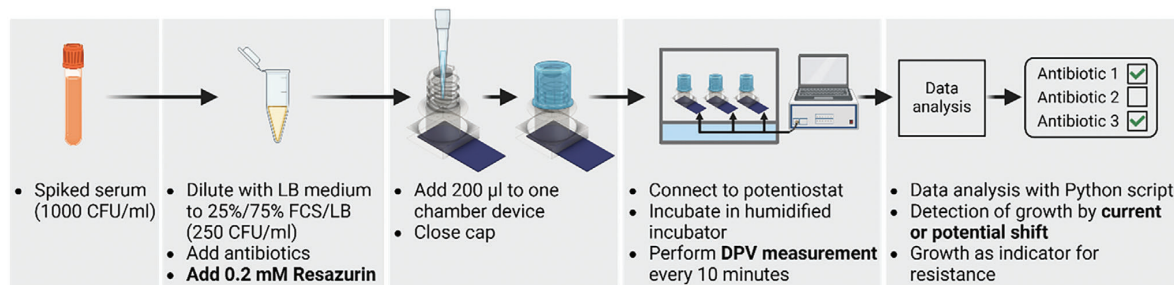
results, thereby a direct transfer of the results and parameters to be analyzed to systems with other electrodes should be validated individually in each case.

#### 4. Experimental Section

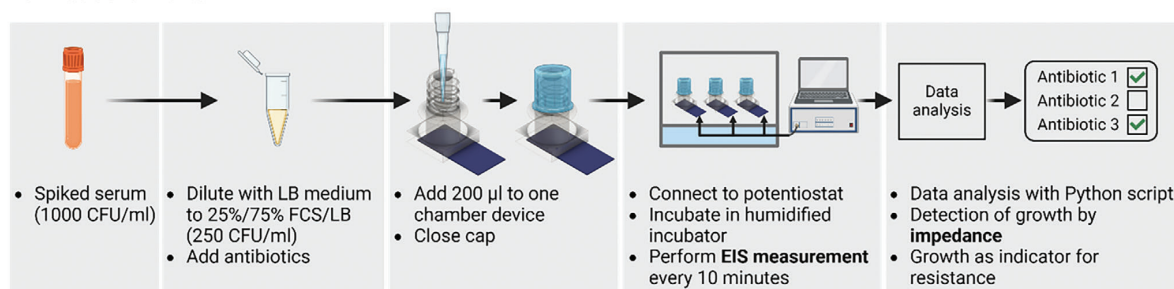
Two Screen printed electrodes (SPEs) were preevaluated for suitability as application in the 3D printed device. The electrodes were purchased from PalmSens (PalmSens BV, Houten, Netherlands). First an Italsens IS-C SPE with graphite working and counter electrode, and a silver pseudo reference electrode, and second a BVT-AC1 with gold working and counter electrode with a Ag/AgCl reference electrode. LB medium (Lennox) and LB-Agar (Luria/Miller) were purchased from Carl Roth (Carl Roth GmbH + Co. KG, Karlsruhe, Germany). Fetal calf serum (FCS), oxytetracycline hydrochloride, and kanamycin sulfate were purchased from Sigma Aldrich (Sigma-Aldrich Chemie GmbH, Taufkirchen, Germany). Resazurin was purchased from VWR (VWR International GmbH, Darmstadt, Germany). A Minitron (Infors HT, Bottmingen, Switzerland) was used as an incubator.

**Device Fabrication:** Prototype devices were fabricated as previously described.<sup>[42]</sup> Briefly, a CAD model was created in Autodesk Fusion 360 (Autodesk, United States) and processed in the slicer software Ulti-

## DPV measurement:



## EIS measurement:



## Combined method (DPV &amp; EIS):

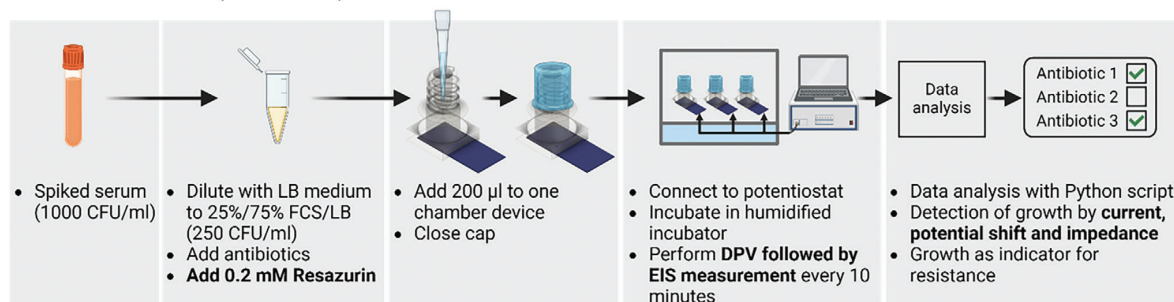


**Figure 6.** Workflow for the electrochemical AST method with the 3D printed prototype. Workflows from spiked serum are shown for combined method (DPV & EIS) and for performing as separate measurements. Differences between workflows are highlighted in bold letters.

maker Cura (Version 4.6.1, Ultimaker, Netherlands). Prototype devices were printed with an Ultimaker 3 (Ultimaker, Netherlands) FDM 3D printer with a 0.4 mm nozzle head using the polymer PMMA-transparent (PMM300XCLR) purchased from filamentworld.com (Germany). As general parameters, a printing temperature of 245 °C, printing speed of 70 mm s<sup>-1</sup>, layer height of 0.1 mm, and fan speed at 50% was used. The printing process was paused at the appropriate layer (modification of the G-code by post-processing scripts available by default) to insert the SPEs and continued afterward. As SPEs, commercially available Italsens IS-C SPEs were used for the antibiotic susceptibility test experiments. To ensure a firm bond between the electrode strip backing material and the already solidified 3D print, a small drop of superglue was applied before insertion of the electrode, ensuring that the glue adhered only to the bottom of the electrode backing material. After fabrication, the devices were sterilized under a sterile work bench with UV light for 30 min from each side and closed with a sterile luer-lock cap.

**Bacteria Culture:** Cultures of *Escherichia coli* (DSM 498), multidrug-resistant *Staphylococcus aureus* (MRSA, DSM 28766), susceptible *S. aureus* (DSM 799), *Klebsiella pneumoniae* (DSM 103706), *K. pneumoniae* (DSM

30104), *Pseudomonas aeruginosa* (DSM 102273), and *P. aeruginosa* (DSM 25123) were cultured overnight in LB medium at 37 °C and 100 rpm before being used to prepare spiked serum samples. For each experiment, a new cryo-vial was thawed and cultured. Strains were purchased from the Leibniz Institute DSMZ-Deutsche Sammlung von Mikroorganismen und Zellkulturen GmbH (Braunschweig, Germany) and stored at -80 °C in glycerol stocks.

**Antibiotic Susceptibility Test by Agar Diffusion Assay:** The agar diffusion assay was performed for the tested bacterial strains with the antibiotics kanamycin and oxytetracycline in order to confirm the resistances listed in the online library bacdive.<sup>[34]</sup> A bacterial solution with an OD<sub>600</sub> of 0.025 in LB media was created from an overnight culture and 100 µl was evenly distributed on a standard microbial petridish with LB agar. Sterile filter paper discs were soaked with 10 µl (1 mg ml<sup>-1</sup>) antibiotic solution in PBS, resulting in 10 µg antibiotic per disc and placed on agar ≈5 min after the inoculation. After 15 min, the petridishes were turned upside down and placed in an incubator with 37 °C. After 24 h the plates were analyzed and pictures of the inhibition zones around the antibiotic soaked discs were taken.

**Antibiotic Susceptibility Test – Differential Pulsed Voltammetry:** Resazurin concentration, which decreased as a result of active metabolism, was measured by the electrochemical method of DPV, as illustrated in Figure 6. Sterile 3D printed prototypes were prepared with IS-C SPEs, as previously described. Serum was spiked with an overnight bacterial culture to 1000 CFU/ml, corresponding to a bloodstream infection of 1000 CFU/ml, and diluted with LB medium to 25%/75% FCS/LB (results in 250 CFU/ml). After 0.2 mM Resazurin and the antibiotic were added, 200  $\mu$ l were pipetted into the device ( $t = 0$  h). The device was closed and the sensor was connected to the potentiostat PalmSens 4. The connected device was then incubated in a humidified incubator at 37 °C without shaking and the amount of metabolized resazurin was evaluated with DPV ( $E_{\text{begin}} = -0.8$  V;  $E_{\text{end}} = 0.0$  V;  $E_{\text{pulse}} = 0.05$  V;  $t_{\text{pulse}} = 0.01$  s; Scan rate = 0.05 V/s) every 10 min over 20 h. Measurements were performed with the PalmSens4 (PalmSens BV, Houten, Netherlands) potentiostat and the Software PSTrace (Version 5.9.2317, PalmSens BV, Netherlands).

**Antibiotic Susceptibility Test – Electrochemical Impedance Spectroscopy:** The experimental setup for EIS measurement (Figure 6) was similar to the one described above for DPV measurements, except that resazurin was not required. Instead of the DPV protocol, the EIS measurement protocol at frequencies of  $10^5$ ,  $10^4$ ,  $10^3$ ,  $10^2$ ,  $10$ , and  $1$  Hz with an  $E_{\text{dc}} = 0.3$  V and  $E_{\text{ac}} = 0.01$  V was applied using the PalmSens4 and the Software PSTrace.

**Antibiotic Susceptibility Test – Combined Method (DPV & EIS):** For the combined method, both measurements (DPV & EIS) were necessary. They did not require a separate experimental setup and can thereby be performed in parallel on one device. The initial preparation (Figure 6) was identical to the one for the DPV measurement, only the measurement differs. The measurements for DPV and EIS were performed sequentially with the parameters described above, as the protocol for DPV was performed first and after a 10 s pause the protocol for EIS was performed.

**Bioinformatic & Statistical Analysis:** Electrochemical data were recorded using PSTrace and exported for further analysis using a Python script (version 3.11.3). The three most promising parameters were used for bioinformatics analysis. For the DPV measurement, these were first, the current ( $I$ ) at  $-0.3$  V, which was related to the resazurin concentration, and second, the potential ( $U$ ) of the peak maximum, which shifted to a more positive potential as pH decreased. The third parameter was the impedance ( $Z$ ) at 100 kHz of the EIS measurement. The detection of bacterial growth in the acquired time series was performed by change point detection (Pruned Exact Linear Time (PELT) algorithm) using the ruptures package version 1.1.7 [43] and significance detection by the SciPy package version 1.10.1.[44] Potential values for detecting the Peakshift were used without prior adjustments. For  $I$  and  $Z$ , only values after reaching equilibrium, determined according to Dalheim et al.,[45] were used. In addition, the change point detection method for detecting growth by current was performed on the first derivative of  $I$ . Each change point was then analyzed for significant differences between the first derivative of the time series values used for change point detection and the corresponding control without bacterial growth. Only change points with significant differences (paired  $t$ -test,  $p < 0.05$  was considered as significant) to 4 out of 5 independent control samples were considered as significant change points and displayed in plots as growth detected. Evaluation of a combination of parameters was performed by calculating a score ranging from 0 to 3, which increased by 1 for each significant change point of a parameter at the analysis timepoint and 1 h before. The score was restricted to a maximum increase of 1 by each parameter, with a score of 2 or more indicating growth detected. Plots were created using the package matplotlib.

The performance of the AST method compared to the AST method using the agar diffusion test was calculated according to Equations (2)–(5), whereby the presence of a resistance to the tested antibiotic was defined as a positive condition. The number of positive (P) and negative (N) conditions were determined according to the results of the agar diffusion test. True positives (TP) and true negatives (TN) were test results of the AST method to be evaluated that indicate the presence or absence of resistance in accordance with the agar diffusion test. False positive (FP) and false negative (FN), on the other hand, were test results of the AST method to

be evaluated that indicated the presence or absence of resistance contrary to the results of the agar diffusion test.

$$\text{Sensitivity} = \frac{TP}{T} \quad (2)$$

$$\text{Specificity} = \frac{TN}{N} \quad (3)$$

$$\text{Positive predictive value (PPV)} = \frac{TP}{TP + FP} \quad (4)$$

$$\text{Negative predictive value (NPV)} = \frac{TN}{TN + FN} \quad (5)$$

## Supporting Information

Supporting Information is available from the Wiley Online Library or from the author.

## Acknowledgements

This work was supported in part by Steinbeis Center for Personalized Medicine (StZ 1789). Support from the Federal Ministry of Science, Research, and Art of Baden-Württemberg (grant no: 32–7545.20/4/59) is greatly acknowledged. The authors thank Andreas Krames for support and helpful advice. Figures were created with biorender.com.

Open access funding enabled and organized by Projekt DEAL.

## Conflict of Interest

O.R. and H.P.D. are inventors on a patent application (DPMA Deutsches Patent- und Markenamt DRN: 2023082213530700DE) that covers the electrochemical AST system.

## Author Contributions

O.R., L.K., S.L., and H.P.D. conceptualized the idea of the study. O.R. designed methodology; contributed to software development; and performed formal analysis, investigation, data curation, and visualization. L.K. and H.P.D. performed funding acquisition. S.L. and H.P.D. performed supervision. O.R. and H.P.D. wrote original draft. O.R., L.K., S.L., and H.P.D. wrote, reviewed, and edited the final manuscript.

## Data Availability Statement

The data that support the findings of this study are available from the corresponding author upon reasonable request.

## Keywords

3D printer, antibiotic resistances, antibiotic susceptibility testing, no preculture, phenotypic, screen printed electrodes

Received: November 16, 2023

Revised: January 31, 2024

Published online:

[1] G. Humphreys, F. Fleck, *Bull. World Health Organ.* **2016**, *94*, 638.

[2] C. J. L. Murray, K. S. Ikuta, F. Sharara, L. Swetschinski, G. R. Aguilar, A. Gray, C. Han, C. Bisignano, P. Rao, E. Wool, S. C. Johnson, A. J. Browne, M. G. Chipeta, F. Fell, S. Hackett, G. Haines-Woodhouse, B. H. Kashef Hamadani, E. A. P. Kumaran, B. McManigal, S. Achalapong, R. Agarwal, S. Akech, S. Albertson, J. Amuasi, J. Andrews, A. Aravkin, E. Ashley, F.-X. Babin, F. Bailey, S. Baker, et al., *Lancet* **2022**, *399*, 629.

- [3] Centers for Disease Control and Prevention, "Antibiotic Resistance Threats in the United States, 2019", <https://www.cdc.gov/drugresistance/biggest-threats.html>, (accessed: June, 2023).
- [4] A. Chokshi, Z. Sifri, D. Cennimo, H. Hornig, *J. Global Infect. Dis.* **2019**, *11*, 36.
- [5] A. J. Browne, M. G. Chipeta, G. Haines-Woodhouse, E. P. A. Kumaran, B. H. K. Hamadani, S. Zarara, N. J. Henry, A. Deshpande, R. C. Reiner, N. P. J. Day, A. D. Lopez, S. Dunachie, C. E. Moore, A. Stergachis, S. I. Hay, C. Dolecek, *Lancet Planet. Health* **2021**, *5*, e893.
- [6] E. Y. Klein, M. Milkowska-Shibata, K. K. Tseng, M. Sharland, S. Gandra, C. Pulcini, R. Laxminarayan, *Lancet Infect. Dis.* **2021**, *21*, 107.
- [7] R. Mulchandani, Y. Wang, M. Gilbert, T. P. Van Boeckel, *PLOS Glob. Public Health* **2023**, *3*, e0001305.
- [8] C. I. Kang, S. H. Kim, H. B. Kim, S. W. Park, Y. J. Choe, M. D. Oh, E. C. Kim, K. W. Choe, *Clin. Infect. Dis.* **2003**, *37*, 745.
- [9] H. Li, M. Morowitz, N. Thomas, P. K. Wong, *SLAS Technol.* **2019**, *24*, 603.
- [10] A. Vasala, V. P. Hytönen, O. H. Laitinen, *Front. Cell. Infect. Microbiol.* **2020**, *10*, 308.
- [11] M. P. Weinstein, *Performance Standards for Antimicrobial Susceptibility Testing*, Clinical And Laboratory Standards Institute, Wayne, Pennsylvania **2019**.
- [12] M. J. Ellington, O. Ekelund, F. M. Aarestrup, R. Canton, M. Doumith, C. Giske, H. Grundman, H. Hasman, M. T. G. Holden, K. L. Hopkins, J. Iredell, G. Kahlmeter, C. U. Köser, A. MacGowan, D. Mevius, M. Mulvey, T. Naas, T. Peto, J. M. Rolain, Samuelsen, N. Woodford, *Clin. Microbiol. Infect.* **2017**, *23*, 2.
- [13] O. Shifman, I. Steinberger-Levy, R. Aloni-Grinstein, D. Gur, M. Aftalion, I. Ron, E. Mamroud, R. Ber, S. Rotem, *Front. Microbiol.* **2019**, *10*, 754.
- [14] T. Charalampous, G. L. Kay, H. Richardson, A. Aydin, R. Baldan, C. Jeanes, D. Rae, S. Grundy, D. J. Turner, J. Wain, R. M. Leggett, D. M. Livermore, J. O'Grady, *Nat. Biotechnol.* **2019**, *37*, 783.
- [15] A. R. Rebelo, V. Bortolaia, P. Leekitcharoenphon, D. S. Hansen, H. L. Nielsen, S. Ellermann-Eriksen, M. Kemp, B. L. Røder, N. Frimodt-Møller, T. S. Søndergaard, J. E. Coia, C. Østergaard, H. Westh, F. M. Aarestrup, *Front. Microbiol.* **2022**, *13*, 804627.
- [16] A. van Belkum, T. T. Bachmann, G. Lüdke, J. G. Lisby, G. Kahlmeter, A. Mohess, K. Becker, J. P. Hays, N. Woodford, K. Mitsakakis, J. Moran-Gilad, J. Vila, H. Peter, J. H. Rex, W. M. Dunne, *Nat. Rev. Microbiol.* **2019**, *17*, 51.
- [17] L. Ø. Andersen, H. V. Olesen, A. H. Spannow, S. L. M. Rubak, *BMC Pulm. Med.* **2022**, *22*, 198.
- [18] K. M. Hare, K. Grimwood, A. J. Leach, H. Smith-Vaughan, P. J. Torzillo, P. S. Morris, A. B. Chang, *J. Pediatrics* **2010**, *157*, 1001.
- [19] P. Yagupsky, F. S. Nolte, *Clin. Microbiol. Rev.* **1990**, *3*, 269.
- [20] A. K. Boardman, J. Campbell, H. Wirz, A. Sharon, A. F. Sauer-Budge, *PLoS One* **2015**, *10*, e0116837.
- [21] W. Lei, K. Demir, J. Overhage, M. Grunze, T. Schwartz, P. A. Levkin, *Adv. Biosyst.* **2020**, *4*, 2000073.
- [22] M. Azizi, M. Zaferani, B. Dogan, S. Zhang, K. W. Simpson, A. Abbaspourrad, *Anal. Chem.* **2018**, *90*, 14137.
- [23] J. Ihssen, N. Jovanovic, T. Sirec, U. Spitz, *PLoS One* **2021**, *16*, e0244200.
- [24] Ö. Baltekin, A. Boucharin, E. Tano, D. I. Andersson, J. Elf, *Proc. Natl. Acad. Sci. USA* **2017**, *114*, 9170.
- [25] I. Sinn, P. Kinnunen, T. Albertson, B. H. McNaughton, D. W. Newton, M. A. Burns, R. Kopelman, *Lab Chip* **2011**, *11*, 2604.
- [26] C. R. Nemr, S. J. Smith, W. Liu, A. H. Mepharm, R. M. Mohamadi, M. Labib, S. O. Kelley, *Anal. Chem.* **2019**, *91*, 2847.
- [27] B. Crane, J. P. Hughes, S. J. Rowley Neale, M. Rashid, P. E. Linton, C. E. Banks, K. J. Shaw, *Analyst* **2021**, *146*, 5574.
- [28] J. D. Besant, E. H. Sargent, S. O. Kelley, *Lab Chip* **2015**, *15*, 2799.
- [29] S. Hannah, A. Dobra, P. Lasserre, E. O. Blair, D. Alcorn, P. A. Hoskisson, D. K. Corrigan, *Biosensors* **2020**, *10*, 153.
- [30] S. Çakir, E. Y. Arslan, *Chem. Pap.* **2010**, *64*, 386.
- [31] S. Virdis, C. Scarano, F. Cossu, V. Spanu, C. Spanu, E. P. L. De Santis, *Vet. Med. Int.* **2010**, *2010*, 517060.
- [32] J. Hyde, C. Gorham, D. E. Brackney, B. Steven, *PLoS One* **2019**, *14*, e0218907.
- [33] D. J. Diekema, P. R. Hsueh, R. E. Mendes, M. A. Pfaller, K. V. Rolston, H. S. Sader, R. N. Jones, *Antimicrob. Agents Chemother.* **2019**, *63*, 10.
- [34] Leibniz-Institut DSMZ-Deutsche Sammlung von Mikroorganismen und Zellkulturen GmbH, "BacDive | The Bacterial Diversity Metadatabase", <https://bacdive.dsmz.de/>, (accessed: June, 2023).
- [35] V. N. Goral, N. V. Zaytseva, A. J. Baeumner, *Lab Chip* **2006**, *6*, 414.
- [36] A. L. Furst, M. B. Francis, *Chem. Rev.* **2019**, *119*, 700.
- [37] K. Asami, *J. Non-Cryst. Solids* **2002**, *305*, 268.
- [38] C. H. Clausen, M. Dimaki, C. V. Bertelsen, G. E. Skands, R. Rodriguez-Trujillo, J. D. Thomsen, W. E. Svendsen, *Sensors* **2018**, *18*, 3496.
- [39] D. C. Spencer, T. F. Paton, K. T. Mulrone, T. J. J. Inglis, J. M. Sutton, H. Morgan, *Nat. Commun.* **2020**, *11*, 5328.
- [40] S. A. Mittman, R. C. Huard, P. Della-Latta, S. Whittier, *J. Clin. Microbiol.* **2009**, *47*, 3557.
- [41] S. Hannah, E. Addington, D. Alcorn, W. Shu, P. A. Hoskisson, D. K. Corrigan, *Biosens. Bioelectron.* **2019**, *145*, 111696.
- [42] O. Riestler, S. Laufer, H.-P. Deigner, *J. Nanobiotechnol.* **2022**, *20*, 540.
- [43] C. Truong, L. Oudre, N. Vayatis, *Signal Process.* **2020**, *167*, 107299.
- [44] P. Virtanen, R. Gommers, T. E. Oliphant, M. Haberland, T. Reddy, D. Cournapeau, E. Burovski, P. Peterson, W. Weckesser, J. Bright, S. J. van der Walt, M. Brett, J. Wilson, K. J. Millman, N. Mayorov, A. R. J. Nelson, E. Jones, R. Kern, E. Larson, C. J. Carey, İ. Polat, Y. Feng, E. W. Moore, J. VanderPlas, D. Laxalde, J. Perktold, R. Cimrman, I. Henriksen, E. A. Quintero, C. R. Harris, et al., *Nat. Methods* **2020**, *17*, 261.
- [45] Ø. Ø. Dalheim, S. Steen, *J. Ocean Eng. Sci.* **2020**, *5*, 333.

## 3.2 Antimicrobial Coatings Related to Chitosan

### 3.2.1 Methacryloyl-GlcNAc Derivatives Copolymerized with Dimethacrylamide as a Novel Antibacterial and Biocompatible Coating

#### Own contribution to the article

The authors' contribution to this publication was as follows. The conceptualization of the study was carried out by Prof. Deigner. Chemical synthesis of functional monomers was performed by Dr. Borgolte and Ms. Kacerova. The preparation of polymer coatings, FT-IR spectra, NMR characterization and biocompatibility studies (cytotoxicity) was carried out by Dr. Borgolte. Scanning electron microscope (SEM) and atomic force microscope (AFM) images were prepared and acquired by Dr. Blendinger. Microbiological tests, including the antibacterial effect of the coatings, biofilm formation and live/dead staining were performed and visualized by the author of this thesis, except the antibacterial assay by CFU, which was performed by Dr. Jacksch. Prof. Deigner was responsible for the acquisition of funding. Project administration was performed by Ms. Rentschler. The supervision of the work was carried out by Prof. Csuk, Prof. Laufer and Prof. Deigner. Writing of the original draft with visualizations was carried out by Dr. Borgolte and the author of this thesis with support from Prof. Deigner. All authors reviewed, edited and approved the manuscript.

Reprinted with permission from the Authors. Copyright © 2021 by the authors. Licensee MDPI, Basel, Switzerland. This article is an open access article distributed under the terms and conditions of the Creative Commons Attribution (CC BY) license (<http://creativecommons.org/licenses/by/4.0/>).

**Borgolte, M.; Riester, O.; Kacerova, T.; Rentschler, S.; Schmidt, M. S.; Jacksch, S.; Egert, M.; Laufer, S.; Csuk, R.; Deigner, H. P. Methacryloyl-GlcNAc Derivatives Copolymerized with Dimethacrylamide as a Novel Antibacterial and Biocompatible Coating. *Pharmaceutics* 2021, 13 (10), 1–24.  
<https://doi.org/10.3390/pharmaceutics13101647>.**



Article

# Methacryloyl-GlcNAc Derivatives Copolymerized with Dimethacrylamide as a Novel Antibacterial and Biocompatible Coating

Max Borgolte <sup>1,2</sup>, Oliver Riester <sup>1,3,4</sup>, Tereza Kacerova <sup>5,6</sup>, Simone Rentschler <sup>1,3</sup>, Magnus S. Schmidt <sup>1</sup>, Susanne Jacksch <sup>1</sup>, Markus Egert <sup>1</sup>, Stefan Laufer <sup>3,4</sup>, René Csuk <sup>2</sup> and Hans-Peter Deigner <sup>1,4,7,\*</sup>

- <sup>1</sup> Institute of Precision Medicine, Furtwangen University, Jakob-Kienzle Str. 17, 78054 Villingen-Schwenningen, Germany; Max.Borgolte@hs-furtwangen.de (M.B.); Oliver.Riester@hs-furtwangen.de (O.R.); S.Rentschler@hs-furtwangen.de (S.R.); Magnus.Schmidt@hs-furtwangen.de (M.S.S.); Susanne.Jacksch@hs-furtwangen.de (S.J.); Markus.Egert@hs-furtwangen.de (M.E.)
- <sup>2</sup> Department of Organic Chemistry, Martin-Luther University Halle-Wittenberg, Kurt-Mothes Str. 2, 06120 Halle (Saale), Germany; Rene.csuk@chemie.uni-halle.de
- <sup>3</sup> Department of Pharmaceutical and Medicinal Chemistry, Institute of Pharmaceutical Sciences, Eberhard Karls University Tuebingen, Auf der Morgenstelle 8, 72076 Tuebingen, Germany; Stefan.laufer@uni-tuebingen.de
- <sup>4</sup> Faculty of Science, Eberhard Karls University Tuebingen, Auf der Morgenstelle 8, 72076 Tuebingen, Germany
- <sup>5</sup> Department of Chemistry, Czech University of Life Sciences, Kamýcká 129, 16500 Prague, Czech Republic; tereza.kacerova.18@ucl.ac.uk
- <sup>6</sup> Department of Chemistry, University College London, London WC1H 0AJ, UK
- <sup>7</sup> EXIM Department, Fraunhofer Institute IZI (Leipzig), Schillingallee 68, 18057 Rostock, Germany
- \* Correspondence: dei@hs-furtwangen.de



**Citation:** Borgolte, M.; Riester, O.; Kacerova, T.; Rentschler, S.; Schmidt, M.S.; Jacksch, S.; Egert, M.; Laufer, S.; Csuk, R.; Deigner, H.-P. Methacryloyl-GlcNAc Derivatives Copolymerized with Dimethacrylamide as a Novel Antibacterial and Biocompatible Coating. *Pharmaceutics* **2021**, *13*, 1647. <https://doi.org/10.3390/pharmaceutics13101647>

Academic Editors: Ewa Klodzińska; and Marek Konop

Received: 3 August 2021

Accepted: 2 October 2021

Published: 9 October 2021

**Publisher's Note:** MDPI stays neutral with regard to jurisdictional claims in published maps and institutional affiliations.



**Copyright:** © 2021 by the authors. Licensee MDPI, Basel, Switzerland. This article is an open access article distributed under the terms and conditions of the Creative Commons Attribution (CC BY) license (<https://creativecommons.org/licenses/by/4.0/>).

**Abstract:** Improving medical implants with functional polymer coatings is an effective way to further improve the level of medical care. Antibacterial and biofilm-preventing properties are particularly desirable in the area of wound healing, since there is a generally high risk of infection, often with a chronic course in the case of biofilm formation. To prevent this we here report a polymeric design of polymer-bound *N*-acetyl-glucosamine-oligoethylene glycol residues that mimic a cationic, antibacterial, and biocompatible chitosan surface. The combination of easy to use, crosslinkable, thin, potentially 3D-printable polymethacrylate layering with antibacterial and biocompatible functional components will be particularly advantageous in the medical field to support a wide range of implants as well as wound dressings. Different polymers containing a *N*-acetylglucosamine-methacryloyl residue with oligoethylene glycol linkers and a methacryloyl benzophenone crosslinker were synthesized by free radical polymerization. The functional monomers and corresponding polymers were characterized by <sup>1</sup>H, <sup>13</sup>C NMR, and infrared (IR) spectroscopy. The polymers showed no cytotoxic or antiadhesive effects on fibroblasts as demonstrated by extract and direct contact cell culture methods. Biofilm formation was reduced by up to 70% and antibacterial growth by 1.2 log, particularly for the 5% GlcNAc-4EG polymer, as observed for *Escherichia coli* and *Staphylococcus aureus* as clinically relevant Gram-negative and Gram-positive model pathogens.

**Keywords:** carbohydrates; glycosides; antibacterial; antibiofilm; MRSA; *E. coli*; biocompatible

## 1. Introduction

Bacterial wound infections are a major health problem, comparable to infections subsequent to surgical procedures, especially when a biofilm is formed significantly reducing the susceptibility of bacteria to antibiotics [1–3]. In combination with the increasing number of reported multidrug-resistant pathogens, antibiotic resistant bacterial infections are a clinical problem that will become even more acute in the future [4]. An implant or scaffold has to be functional for fibroblast or stem cells adhesion to ensure proper resorption of

the implant into the surrounding tissue. This functionalization promotes adhesion often unspecifically for all cells and organisms, including bacteria, leading to a “race to the surface” [5,6], whereby the patient’s cells and bacteria compete to adhere to an implant’s surface. The critical time window for this competition between body tissue and bacteria has been determined to be the first 6 h after implantation, while a single bacteria can form a biofilm within 24 h [7]. After 48–96 h, the biofilm becomes resistant to therapeutic treatment as the formed matrix renders the encapsulated bacteria less susceptible to host defense mechanisms and antibiotic therapy [8–12]. Conventionally, antibiotic prophylaxis is used in both implant surgery and traumatic wound care to reduce the likelihood of bacterial infections [13,14]. However, the problem of increasing multidrug-resistant bacteria, particularly in clinical settings, has led to a re-evaluation of the extensive use of antibiotics [15,16]. To some degree, reducing the usage of systemic antibiotics can prevent the emergence of new multidrug-resistant pathogens. In order to prevent infections even with reduced administration of antibiotics, other antimicrobial mechanisms must also be applied, such as antimicrobial modification of surfaces or addition of nanoparticles [17–19].

Cationic polymers have been widely described in articles and reviews with regard to their antibacterial properties and use in self-disinfecting surfaces; most contain a quaternary ammonium group or alkyl pyridinium group as the functional component [20–25]. The mechanism of action of these cationic polymers in solution is well described by the Shai-Matsuzaki-Huang (SMH) model [26–28]. The antibacterial action of surfaces coated with cationic polymers is thought to follow a similar mechanism through polymeric brushes [21,29–33], but some publications describe a simple monolayer of cationic groups as being antibacterial as well [34]. Murata et al. propose a mechanism driven mainly by surface charge instead of insertion of cationic polymer brushes into the bacterial cell wall, following an SMH-like mechanism [20]. The exact mechanism of the antibacterial effect of cationic polymers requires further discussion and clarification.

Chitosan is a cationic polymeric aminoglycan, consisting of *N*-acetylglucosamine (GlcNAc) and glucosamine repeating units; it is used in tissue engineering applications such as bone tissue engineering [35–37], stem cell encapsulation [38–40], and wound dressing [41,42]. The polymer is thought to exhibit its antibacterial properties through a cationic mechanism via glucosamine’s amino group by disrupting the outer and inner bacterial cell membrane [43–45] and has been shown to mediate biofilm formation of *Actinobacillus pleuromoniae* [46]. The corresponding monomer, GlcNAc, has been shown to prevent biofilm formation by *Escherichia coli* [47]. Because of its insolubility in water and organic solvents, except ionic liquids, chitosan has been used in several polymeric modifications to combine its proliferative and antibacterial properties with the mechanical stiffness of other polymers, taking advantage of different synthetic polymers or nanoparticles, rendering it useful for biomedical applications [48].

Another group of antimicrobial compounds is the 1,2,3-triazoles, which exhibit antibacterial activity mainly through formation of hydrogen bonds of the triazole ring with other moieties, forming a cationic surface and possibly leading to an SMH-like antibacterial mechanism [49]. These 1,2,3-triazoles can easily be introduced by Huisgen 1,3-dipolar cycloaddition of an azide and alkyne, without the need for complicated workup procedures or toxic and expensive reagents, making it suitable for polymer modifications [50,51]. Several polymers modified in this way are listed in a library of (1,2,3-triazol-1-yl)quinazolin-4-ones and have shown antibacterial properties against Gram-positive and Gram-negative bacteria [52,53]. In addition, a library of 1,2,3-triazol-sucrose derivatives showed antifungal and antibacterial properties while maintaining low cytotoxicity against non-tumor cell lines [54–56].

An additional approach is the design of antiadhesive surfaces to prevent colonization of implant surfaces. Pandiyarajan et al. [57] described a surface-attached hydrogel network, consisting of poly-dimethacrylamide copolymerized with methacryloyl benzophenone (MBP), that had antiadhesive properties against proteins and blood platelets. Surface anchoring was accomplished via photoactive UV crosslinking of the benzophenone moi-

ety [57]. The benzophenone undergoes a UV-induced, radical C–H insertion reaction, as reviewed by Prucker et al. [58] rendering it suitable for functionalization of polymeric surfaces to obtain stable, covalently attached hydrogel networks [58]. To the best of our knowledge, there is no description of combining the antimicrobial properties of a cationic GlcNAc residue with an antiadhesive, UV-crosslinkable acrylamide hydrogel in order to reduce microbial contamination of implant surfaces in the literature.

In this study, we combined the previously described approaches that resulted in a surface-bound poly-dimethacrylamide methyl (PDMAM) network with UV-induced anchoring via benzophenone, combining it with a GlcNAc residue containing a triazole and a distinct linker to the PDMAM network backbone. We thereby mimicked an antimicrobial chitosan surface while taking advantage of the antiadhesive PDMAM hydrogel as base layer. The hydrogel network can be easily obtained via solvent casting of the polymer solution, followed by UV crosslinking. We investigated the effect of the combinatorial approach of triazole functional groups and chitosan-mimicking surfaces on the antimicrobial, antibiofilm, and biocompatible properties of such coatings.

## 2. Experimental Section

### 2.1. Chemical Synthesis and Characterization

#### 2.1.1. General Methods

TLC was carried out on Silica Gel 60 F254 (Merck KGaA, Darmstadt, Germany, layer thickness 0.2 mm) with detection by UV light (254 nm) or by charring with 1% KMnO<sub>4</sub> in 1N NaOH. Flash column chromatography (FC) was performed on M&N Silica Gel 60 (0.063–0.200 mm, MACHEREY-NAGEL GmbH, Düren, Germany). <sup>1</sup>H NMR and <sup>13</sup>C NMR spectra were recorded on a Bruker Avance I 200, Bruker Avance II 400 (Bruker Corporation, Billerica, MA, USA), or Varian Unity 500 (Varian, Palo Alto, CA, USA) spectrometer. Chemical shifts are reported in parts per million relative to solvent signals (CDCl<sub>3</sub>: δH = 7.26 ppm, δC = 77.0 ppm; DMSO-d<sub>6</sub>: δH = 2.49 ppm, δC = 39.7 ppm; CD<sub>3</sub>OD: δH = 4.78 ppm, δC = 49.3 ppm). Signals were assigned by first-order analysis, and assignments were supported, where feasible, by 2-dimensional <sup>1</sup>H, <sup>1</sup>H and <sup>1</sup>H, <sup>13</sup>C correlation spectroscopy. Coupling constants are reported in hertz. Chemicals and reagents were purchased from Acros Organics (Geel, Belgium), Sigma-Aldrich (Munich, Germany), Carl Roth (Karlsruhe, Germany), ABCR (Karlsruhe, Germany), or MCAT (Donaueschingen, Germany) and were used without further purification.

#### 2.1.2. Synthesis of Azido Linkers 2, 4, 5, 6

Azido linkers were synthesized according to a procedure published by Mahou and Wandrey [59], following a cascade of sequential tosylation and NaN<sub>3</sub> substitution steps. For diethylene glycol linker 2, 2-(2-chloro-ethoxy)-ethanol was chosen as the starting material instead of the tosylated diethylene glycol residue, according to another published procedure [60].

#### 2.1.3. General Tosylation Procedure

Tosylation was carried out according to a literature report [59]. The corresponding linker (1 eq) and *p*-toluenesulfonyl chloride (1.1 eq) were dissolved in dichloromethane (DCM) at 0 °C and NEt<sub>3</sub> (2 eq) was added. After stirring for 2 h, the ice bath was removed and the mixture stirred overnight at room temperature. Washing twice with water and once with brine, followed by evaporation of the solvent, yielded the tosylated linker as a yellowish oil.

#### 2.1.4. Chain Prolongment of Azido Linkers via Tosylate 5, 6

Chain prolongment was carried out according to the literature [59]. Tosylated azido linker 4 (1 eq) and NaH (1.1 eq) were suspended in water-free tetrahydrofuran (THF) under Ar atmosphere. After stirring for 30 min at room temperature, diethylene glycol for product 5 or 1,8-octanediol for product 6 (5 eq) was added dropwise to the mixture. After

stirring for 48 h under reflux, H<sub>2</sub>O was added, the solvent evaporated, and the aqueous layer extracted 3× with DCM Washing 2× with NaOH, followed by evaporation of the solvent and column chromatography (ethyl acetate/methanol 19:1, R<sub>f</sub> = 0.4), yielded the pure products **5** and **6** as yellowish oils.

#### 8-(2-[2-[2-(2-Azido-ethoxy)-ethoxy]-ethoxy]-ethoxy)-octan-1-ol **6**

Yield: 71%

<sup>1</sup>H-NMR (CDCl<sub>3</sub>, 400 MHz): 3.71–3.63 (m, 14H, O–CH<sub>2</sub>), 3.59 (dt, *J* = 4.5, 1.2 Hz, 2H, O–CH<sub>2</sub>), 3.46 (t, *J* = 6.8 Hz, 2H, O–CH<sub>2</sub>), 3.40 (t, *J* = 5.1 Hz, 2H, N<sub>3</sub>–CH<sub>2</sub>), 1.57 (dt, *J* = 13.2, 6.5 Hz, 4H, CH<sub>2</sub>), 1.40–1.29 (m, *J* = 17.9 Hz, 8H, CH<sub>2</sub>).

<sup>13</sup>C-NMR (CDCl<sub>3</sub>, 100 MHz): 71.48 (O–CH<sub>2</sub>), 70.72 (O–CH<sub>2</sub>), 70.70 (O–CH<sub>2</sub>), 70.65 (O–CH<sub>2</sub>), 70.61 (O–CH<sub>2</sub>), 70.08 (O–CH<sub>2</sub>), 70.04 (O–CH<sub>2</sub>), 63.01 (O–CH<sub>2</sub>), 50.70 (N<sub>3</sub>–CH<sub>2</sub>), 32.77 (CH<sub>2</sub>), 29.60 (CH<sub>2</sub>), 29.39 (CH<sub>2</sub>), 29.33 (CH<sub>2</sub>), 26.00 (CH<sub>2</sub>), 25.66 (CH<sub>2</sub>).

#### 2.1.5. General Procedure for the Synthesis of Azidomethacrylates **7–10**

Azido methacrylates were synthesized as published [61]. Briefly, azido linker (1 eq) and NEt<sub>3</sub> (1.3 eq) were dissolved in water-free DCM in a sealed Schlenk flask under Ar atmosphere cooled in an ice bath to 0 °C. Methacryloyl chloride (1.2 eq) was added dropwise to the mixture. The solution was allowed to warm to room temperature and stirred at room temperature overnight. Washing with 1M H<sub>2</sub>SO<sub>4</sub> (3×, equal volume to solvent) followed by drying over Na<sub>2</sub>SO<sub>4</sub> and evaporation of the solvent yielded the crude product. Further purification by column chromatography (ethyl acetate/hexane 1:10) yielded the pure products.

#### 2-Methyl-acrylic acid 2-(2-azido-ethoxy)-ethyl ester **7**

Yield: 81%

<sup>1</sup>H-NMR (CDCl<sub>3</sub>, 400 MHz): 6.17 (s, 1H, CH<sub>2</sub>), 5.60 (s, 1H, CH<sub>2</sub>), 4.34 (t, *J* = 4.7 Hz, 2H, O–CH<sub>2</sub>), 3.78 (t, *J* = 4.7, 2H, O–CH<sub>2</sub>), 3.71 (t, *J* = 5.0, 2H, O–CH<sub>2</sub>), 3.40 (t, *J* = 4.9, 2H, CH<sub>2</sub>–N<sub>3</sub>), 1.98 (s, 3H, CH<sub>3</sub>).

<sup>13</sup>C-NMR (CDCl<sub>3</sub>, 100 MHz): 167.3 (C=O), 136.1 [C(CH<sub>3</sub>)(CH<sub>2</sub>)], 125.9 (C=CH<sub>2</sub>), 70.1 (O–CH<sub>2</sub>), 69.2 (O–CH<sub>2</sub>), 63.7 (O–CH<sub>2</sub>), 50.7 (N<sub>3</sub>–CH<sub>2</sub>), 18.3 (CH<sub>3</sub>).

#### 2-Methyl-acrylic acid 2-[2-[2-(2-azido-ethoxy)-ethoxy]-ethoxy]-ethyl ester **8**

Yield: 71%

<sup>1</sup>H-NMR (CDCl<sub>3</sub>, 400 MHz): 6.16 (s, 1H, CH<sub>2</sub>), 5.60 (s, 1H, CH<sub>2</sub>), 5.33 (t, *J* = 4.9 Hz, 2H, O–CH<sub>2</sub>), 3.77 (t, *J* = 3.8 Hz, 2H, O–CH<sub>2</sub>), 3.70 (s, 10H, O–CH<sub>2</sub>), 3.41 (t, *J* = 5.0 Hz, 2H, CH<sub>2</sub>–N<sub>3</sub>), 1.97 (s, 3H, CH<sub>3</sub>).

<sup>13</sup>C-NMR (CDCl<sub>3</sub>, 100 MHz): 136.2 [C(CH<sub>3</sub>)(CH<sub>2</sub>)], 125.8 (C=CH<sub>2</sub>), 70.8 (O–CH<sub>2</sub>), 70.1 (O–CH<sub>2</sub>), 69.2 (O–CH<sub>2</sub>), 63.8 (O–CH<sub>2</sub>), 50.7 (N<sub>3</sub>–CH<sub>2</sub>), 18.3 (CH<sub>3</sub>).

#### 2-Methyl-acrylic acid 2-[2-[2-[2-(2-azido-ethoxy)-ethoxy]-ethoxy]-ethoxy]-ethyl ester **9**

Yield: 55%

<sup>1</sup>H-NMR (CDCl<sub>3</sub>, 400 MHz): 6.17 (s, 1H, CH<sub>2</sub>), 5.60 (s, 1H, CH<sub>2</sub>), 4.34 (t, *J* = 4.7 Hz, 2H, O–CH<sub>2</sub>), 3.78 (t, *J* = 4.7, 2H, O–CH<sub>2</sub>), 3.71 (t, *J* = 5.0, 2H, O–CH<sub>2</sub>), 3.40 (t, *J* = 4.9, 2H, CH<sub>2</sub>–N<sub>3</sub>), 1.98 (s, 3H, CH<sub>3</sub>).

<sup>13</sup>C-NMR (CDCl<sub>3</sub>, 100 MHz): 167.4 (C=O), 136.2 [C(CH<sub>3</sub>)(CH<sub>2</sub>)], 125.7 (C=CH<sub>2</sub>), 70.7 (O–CH<sub>2</sub>), 70.6 (O–CH<sub>2</sub>), 70.0 (O–CH<sub>2</sub>), 69.2 (O–CH<sub>2</sub>), 63.9 (O–CH<sub>2</sub>), 50.7 (N<sub>3</sub>–CH<sub>2</sub>), 18.3 (CH<sub>3</sub>).

#### 2-Methyl-acrylic acid 8-(2-[2-[2-(2-azido-ethoxy)-ethoxy]-ethoxy]-ethoxy)-octyl ester **10**

Yield: 66%

<sup>1</sup>H-NMR (CDCl<sub>3</sub>, 400 MHz): 6.11 (s, 1H, CH<sub>2</sub>), 5.56 (s, 1H, CH<sub>2</sub>), 4.15 (t, *J* = 6.7 Hz, 2H, O–CH<sub>2</sub>), 3.72–3.64 (m, 14H, O–CH<sub>2</sub>), 3.62–3.57 (m, 2H, O–CH<sub>2</sub>), 3.46 (t, *J* = 6.8 Hz, 2H,

O-CH<sub>2</sub>), 3.41 (t, *J* = 5.1 Hz, 2H, N<sub>3</sub>-CH<sub>2</sub>), 1.96 (s, 2H, O-CH<sub>2</sub>), 1.73–1.64 (m, 2H, O-CH<sub>2</sub>), 1.62–1.57 (m, 2H, O-CH<sub>2</sub>), 1.44–1.26 (m, 8H, O-CH<sub>2</sub>).

<sup>13</sup>C-NMR (CDCl<sub>3</sub>, 100 MHz): 167.56 (C=O), 136.55 [C(CH<sub>3</sub>)(CH<sub>2</sub>)], 125.16 (C=CH<sub>2</sub>), 71.48 (O-CH<sub>2</sub>), 70.72 (O-CH<sub>2</sub>), 70.70 (O-CH<sub>2</sub>), 70.65 (O-CH<sub>2</sub>), 70.64 (O-CH<sub>2</sub>), 70.62 (O-CH<sub>2</sub>), 70.08 (O-CH<sub>2</sub>), 70.05 (O-CH<sub>2</sub>), 64.80 (O-CH<sub>2</sub>), 50.70 (N<sub>3</sub>-CH<sub>2</sub>), 29.61 (CH<sub>2</sub>), 29.36 (CH<sub>2</sub>), 29.21 (CH<sub>2</sub>), 28.60 (CH<sub>2</sub>), 26.02 (CH<sub>2</sub>), 25.93 (CH<sub>2</sub>), 18.34 (CH<sub>3</sub>).

### 2.1.6. General Procedure for Click Reaction of Azidomethacrylates with **13**

The click reaction was carried out under optimized conditions according to Schmidt et al. 2014 [62]. Azido methacrylate (1 eq) and propargyl GlcNAc **13** (1 eq) were dissolved in a mixture of dichloromethane/methanol/water (10:10:3). Then, CuSO<sub>4</sub> (0.04 eq), tris(benzyltriazolylmethyl)amine (TBTA) (0.01 eq), and sodium ascorbate (0.22 eq) were added, and the mixture was heated to reflux for 1 h. After cooldown and adding water, the solution was extracted 3 times with dichloromethane, the organic layer dried over Na<sub>2</sub>SO<sub>4</sub>, and the solvent evaporated in vacuum. Column chromatography yielded the products as yellowish oil.

2-Methyl-acrylic acid 2-[2-[4-(3-acetylamino-4,5-dihydroxy-6-hydroxymethyl-tetrahydro-pyran-2-yloxymethyl)-[1,2,3]triazol-1-yl]-ethoxy]-ethyl ester **11a**

Yield: 75%

<sup>1</sup>H-NMR (CDCl<sub>3</sub>, 400 MHz): 7.67 (s, 1H, Ar-H), 6.03 (s, 1H, CH<sub>2</sub>), 5.84 (s, 1H, H-1), 5.54 (s, 1H, CH<sub>2</sub>), 5.16 (t, *J* = 9.2 Hz, 1H, H-3), 5.04 (t, *J* = 9.4 Hz, 1H, H-4), 4.83–4.75 (m, 3H, O-CH<sub>2</sub> + H-2), 4.49 (s, 2H, O-CH<sub>2</sub>), 4.24–4.19 (m, 2H, O-CH<sub>2</sub>), 4.07 (dd, *J* = 16.3, 9.5 Hz, 1H, H-6), 3.92 (s, 1H, H-6), 3.82 (s, 2H, O-CH<sub>2</sub>), 3.68–3.65 (m, 1H, H-5), 3.63 (t, *J* = 4.7 Hz, 2H, O-CH<sub>2</sub>), 2.03 (s, 3H, C(O)CH<sub>3</sub>), 1.96 (s, 3H, C(O)CH<sub>3</sub>), 1.95 (s, 3H, C(O)CH<sub>3</sub>), 1.87 (s, 3H, C(O)CH<sub>3</sub>), 1.79 (s, 3H, CH<sub>3</sub>).

2-Methyl-acrylic acid 2-[2-(2-[2-[4-(4,5-diacetoxy-6-acetoxymethyl-3-acetylamino-tetrahydro-pyran-2-yloxymethyl)-[1,2,3]triazol-1-yl]-ethoxy]-ethoxy)-ethoxy]-ethyl ester **11b**

Yield: 63%

<sup>1</sup>H-NMR (CDCl<sub>3</sub>, 400 MHz): 7.58 (s, 1H, Ar-H), 5.96 (s, 1H, CH<sub>2</sub>), 5.71 (d, *J* = 8.5 Hz, 1H, H-1), 5.42 (s, 1H, CH<sub>2</sub>), 5.05 (t, *J* = 9.9 Hz, 1H, H-3), 4.95 (t, *J* = 9.6 Hz, 1H, H-4), 4.78 (d, *J* = 12.3 Hz, 1H, H-2), 4.68 (dd, *J* = 23.6, 10.5 Hz, 2H, O-CH<sub>2</sub>-Ar), 4.39 (t, *J* = 4.7 Hz, 2H, O-CH<sub>2</sub>), 4.17–4.10 (m, 3H, O-CH<sub>2</sub> + H-6), 3.99 (dd, *J* = 12.4, 2.1 Hz, 1H, H-6), 3.82 (dd, *J* = 18.0, 8.5 Hz, 1H, H-5), 3.72 (t, *J* = 5.0 Hz, 2H, O-CH<sub>2</sub>), 3.60–3.57 (m, 2H, O-CH<sub>2</sub>), 3.53–3.45 (m, 10H, O-CH<sub>2</sub>), 1.94 [s, 2H, C(O)CH<sub>3</sub>], 1.87 [s, 3H, C(O)CH<sub>3</sub>], 1.86 [s, 3H, C(O)CH<sub>3</sub>], 1.79 [s, 3H, C(O)CH<sub>3</sub>], 1.69 (s, 3H, CH<sub>3</sub>).

2-Methyl-acrylic acid

2-(2-[2-[2-(2-[2-[4-(3-acetylamino-4,5-dihydroxy-6-hydroxymethyl-tetrahydro-pyran-2-yloxymethyl)-[1,2,3]triazol-1-yl]-ethoxy]-ethoxy)-ethoxy]-ethoxy)-ethoxy)-ethyl ester **11c**

Yield: 56%

<sup>1</sup>H-NMR (CDCl<sub>3</sub>, 400 MHz): 7.76 (s, 1H, Ar-H), 6.12 (s, 1H, CH<sub>2</sub>), 6.05 (d, *J* = 8.4 Hz, 1H, H-1), 5.57 (d, *J* = 1.6 Hz, 1H, CH<sub>2</sub>), 5.23 (t, *J* = 9.9 Hz, 1H, H-3), 5.09 (t, *J* = 9.6 Hz, 1H, H-4), 4.94 (d, *J* = 12.6 Hz, 1H, H-2), 4.84 (dd, *J* = 33.4, 10.4 Hz, 2H, O-CH<sub>2</sub>-Ar), 4.54 (t, *J* = 4.8 Hz, 2H, O-CH<sub>2</sub>), 4.32–4.23 (m, 3H, O-CH<sub>2</sub> + H-6), 4.14 (dd, *J* = 12.4, 2.1 Hz, 1H, H-6), 3.87 (t, *J* = 5.0 Hz, 2H, O-CH<sub>2</sub>), 3.77–3.71 (m, 3H, O-CH<sub>2</sub> + H-5), 3.68–3.59 (m, 20H, O-CH<sub>2</sub>), 2.09 (s, 3H, C(O)CH<sub>3</sub>), 2.02 (s, 3H, C(O)CH<sub>3</sub>), 2.01 (s, 3H, C(O)CH<sub>3</sub>), 1.94 (s, 3H, C(O)CH<sub>3</sub>), 1.85 (s, 3H, CH<sub>3</sub>).

**2-Methyl-acrylic acid****8-[2-[2-(2-[2-(4-(4,5-diacetoxy-6-acetoxymethyl-3-acetylamino-tetrahydro-pyran-2-yloxymethyl)-[1,2,3]triazol-1-yl)-ethoxy]-ethoxy)-ethoxy]-ethoxy]-octyl ester **11d****

Yield: 86%

<sup>1</sup>H-NMR (CDCl<sub>3</sub>, 400 MHz): 7.61 (s, 1H, Ar-H), 5.94 (s, 1H, CH<sub>2</sub>), 5.85 (d, *J* = 8.6 Hz, 1H, H1), 5.39 (s, 1H, CH<sub>2</sub>), 5.08 (t, *J* = 9.9 Hz, 1H, H3), 4.94 (t, *J* = 9.6 Hz, 1H, H4), 4.82–4.60 (m, 3H, H2 + Ar–CH<sub>2</sub>–O), 4.41–4.34 (m, 2H, O–CH<sub>2</sub>), 4.25–4.08 (m, 2H, H6), 4.02–3.92 (m, 2H, O–CH<sub>2</sub>), 3.63–3.54 (m, 1H, H5), 3.51–3.45 (m, 10H, O–CH<sub>2</sub>), 3.43–3.39 (m, 2H, O–CH<sub>2</sub>), 3.28 (t, *J* = 6.8 Hz, 2H, O–CH<sub>2</sub>), 1.94 (s, 3H, CH<sub>3</sub>), 1.87 (s, 3H, CH<sub>3</sub>), 1.86 (s, 3H, CH<sub>3</sub>), 1.78 (s, 3H, CH<sub>3</sub>), 1.69 (s, 3H, CH<sub>3</sub>), 1.56–1.37 (m, 5H, CH<sub>2</sub>), 1.22–1.13 (m, 9H, CH<sub>2</sub>).

**2.1.7. General Procedure for Click Reaction of Azidomethacrylates with Propargyl Alcohol**

The click reaction with propargyl alcohol was carried out under conditions as previously published [62]. Briefly, azido methacrylate (1 eq) and propargyl alcohol (1.3 eq) were dissolved in a mixture of dichloromethane/methanol/water (10:10:3). Then, CuSO<sub>4</sub> (0.04 eq), TBTA (0.01 eq), and sodium ascorbate (0.22 eq) were added, and the mixture was heated to reflux overnight. After cooldown and adding water, the solution was extracted 3 times with dichloromethane, the organic layer dried over Na<sub>2</sub>SO<sub>4</sub>, and the solvent evaporated in vacuo. Column chromatography (ethyl acetate/methanol, 4:1) yielded the products as yellow oils.

**2-Methyl-acrylic acid 2-[2-(4-hydroxymethyl-[1,2,3]triazol-1-yl)-ethoxy]-ethyl ester **12a****

Yield: 18%

<sup>1</sup>H-NMR (CDCl<sub>3</sub>, 200 MHz): 7.68 (s, 1H, Ar-H), 6.10 (dd, *J* = 1.5, 1.0 Hz, 1H, CH<sub>2</sub>), 5.60 (p, *J* = 1.6 Hz, 1H, CH<sub>2</sub>), 4.77 (s, 2H, CH<sub>2</sub>), 4.54 (t, *J* = 5.0 Hz, 2H, O–CH<sub>2</sub>), 4.29 (t, *J* = 4.7 Hz, 2H, O–CH<sub>2</sub>), 3.87 (t, *J* = 5.1 Hz, 2H, O–CH<sub>2</sub>), 3.69 (ddd, *J* = 5.4, 4.0, 2.1 Hz, 2H, O–CH<sub>2</sub>), 1.94 (dd, *J* = 1.5, 1.0 Hz, 3H, CH<sub>3</sub>).

<sup>13</sup>C-NMR (CDCl<sub>3</sub>, 50 MHz): 125.88 (C=CH<sub>2</sub>), 115.58, 69.40 (O–CH<sub>2</sub>), 69.20 (O–CH<sub>2</sub>), 69.04 (O–CH<sub>2</sub>), 63.42 (O–CH<sub>2</sub>), 50.30 (N–CH<sub>2</sub>), 18.21 (CH<sub>3</sub>).

**2-Methyl-acrylic acid 2-[2-(4-hydroxymethyl-[1,2,3]triazol-1-yl)-ethoxy]-ethyl ester **12b****

Yield: 39%

<sup>1</sup>H-NMR (CDCl<sub>3</sub>, 200 MHz): 7.76 (s, 1H, Ar-H), 6.11 (dd, *J* = 1.5, 0.9 Hz, 1H, CH<sub>2</sub>), 5.57 (p, *J* = 1.6 Hz, 1H, CH<sub>2</sub>), 4.78 (s, 2H, CH<sub>2</sub>), 4.53 (t, *J* = 5.3 Hz, 2H, CH<sub>2</sub>), 4.29 (dd, *J* = 5.7, 4.2 Hz, 2H, CH<sub>2</sub>), 3.86 (t, *J* = 5.2 Hz, 2H, CH<sub>2</sub>), 3.74 (dd, *J* = 5.5, 4.2 Hz, 2H, CH<sub>2</sub>), 3.67–3.57 (m, 8H, CH<sub>2</sub>), 1.93 (s, 3H, CH<sub>3</sub>).

<sup>13</sup>C-NMR (CDCl<sub>3</sub>, 50 MHz): 125.68 [C(CH<sub>3</sub>)(CH<sub>2</sub>)], 122.87 (C=CH<sub>2</sub>), 70.62 (O–CH<sub>2</sub>), 70.58 (O–CH<sub>2</sub>), 70.51 (O–CH<sub>2</sub>), 70.48 (O–CH<sub>2</sub>), 69.41 (O–CH<sub>2</sub>), 69.12 (O–CH<sub>2</sub>), 63.74 (O–CH<sub>2</sub>), 56.52 (O–CH<sub>2</sub>), 50.23 (N–CH<sub>2</sub>), 18.21 (CH<sub>3</sub>).

**2-Methyl-acrylic acid 2-[2-[2-(2-[2-(4-hydroxymethyl-[1,2,3]triazol-1-yl)-ethoxy]-ethoxy)-ethoxy]-ethoxy]-ethyl ester **12c****

Yield: 96%

<sup>1</sup>H-NMR (CDCl<sub>3</sub>, 600 MHz): 7.86 (s, 1H, Ar-H), 6.12 (dd, *J* = 1.6, 1.0 Hz, 2H, CH<sub>2</sub>), 5.56 (q, *J* = 1.6 Hz, 2H, CH<sub>2</sub>), 4.79 (s, 2H, CH<sub>2</sub>), 4.54 (t, *J* = 4.9 Hz, 2H, CH<sub>2</sub>), 4.30–4.27 (m, 2H, CH<sub>2</sub>), 3.86 (t, *J* = 4.9 Hz, 2H, CH<sub>2</sub>), 3.72 (dd, *J* = 5.5, 4.3 Hz, 2H, CH<sub>2</sub>), 3.65–3.59 (m, 16H, CH<sub>2</sub>), 2.37 (s, 1H, OH), 1.94 (dd, *J* = 1.5, 1.0 Hz, 3H, CH<sub>3</sub>).

<sup>13</sup>C-NMR (CDCl<sub>3</sub>, 200 MHz): 136.12 [C(CH<sub>3</sub>)(CH<sub>2</sub>)], 125.72 (C=CH<sub>2</sub>), 70.60 (O–CH<sub>2</sub>), 70.57 (O–CH<sub>2</sub>), 70.56 (O–CH<sub>2</sub>), 70.54 (O–CH<sub>2</sub>), 70.53 (O–CH<sub>2</sub>), 70.48 (O–CH<sub>2</sub>), 70.46 (O–CH<sub>2</sub>), 70.38 (O–CH<sub>2</sub>), 69.38 (O–CH<sub>2</sub>), 69.10 (O–CH<sub>2</sub>), 64.34 (O–CH<sub>2</sub>), 63.81 (O–CH<sub>2</sub>), 57.20 (O–CH<sub>2</sub>), 56.62 (O–CH<sub>2</sub>), 50.34 (N<sub>3</sub>–CH<sub>2</sub>), 30.57 (CH<sub>2</sub>), 18.28 (CH<sub>3</sub>).

### 2.1.8. General Procedure for Free Radical Polymerization

Combined monomers (in general, dimethacrylamide, benzophenone methacrylate **14** and functional methacrylate **11a–d** or **12a–c** in given ratios (Table 1) were dissolved in water-free THF under Ar atmosphere to a total monomer concentration of 2 M. Azobisisobutyronitrile (AIBN) (0.01 mol%) was added and the reaction mixture heated to reflux for 16 h. Cooldown followed by precipitation of the polymers in 10-fold excess iso-hexane yielded the product as a white precipitate. The precipitate was dissolved in water and lyophilized to obtain the product as a white powder.

**Table 1.** Overview of the synthesized PDMAm-polymers.

Polymer	Calculated Ratio		Found Ratio (via NMR)
	MBP <b>14</b> [%] <sup>(a)</sup>	<b>11</b> or <b>12</b> [%] <sup>(b)</sup>	MBP vs. <b>11/12</b>
GlcNAc-2EG	5%	5% <b>11a</b>	30:1
5%-GlcNAc-4EG	5%	5% <b>11b</b>	2:1
10%-GlcNAc-4EG	5%	10% <b>11b</b>	1:2
25%-GlcNAc-4EG	5%	25% <b>11b</b>	1:5
50%-GlcNAc-4EG <sup>(c)</sup>	5%	50% <b>11b</b>	-
GlcNAc-6EG	5%	5% <b>11c</b>	3:1
GlcNAc-4EG-octyl	5%	5% <b>11d</b>	6:1
HM-2EG	5%	5% <b>12a</b>	1:1
HM-4EG	5%	5% <b>12b</b>	1:1
HM-6EG	5%	5% <b>12c</b>	1:1
PDMAm <sup>(d)</sup>	5%	-	-

<sup>(a)</sup> 4-methacryloyloxy-benzophenone (MBP). <sup>(b)</sup> Functional GlcNAc monomers (**11**), Functional 4-hydroxymethyl monomers (**12**). <sup>(c)</sup> The 50%-GlcNAc-4EG polymer could not be obtained; instead, the reaction resulted in ester hydrolysis of the methacrylic acid ester, yielding the GlcNAc-tetraethylene glycol clickamer only. <sup>(d)</sup> The PDMAm polymer is the dimethacrylamide-co-methacryloyl benzophenone copolymer without additional functionality, serving as control for cell culture and microbiology experiments.

### 2.1.9. General Deprotection Procedure of GlcNAc Polymers

Deprotection was carried out according to a standard Zemplén procedure [63]. GlcNAc polymers were dissolved in dry methanol in a sealed tube under Ar atmosphere. NaOMe (30% solution in methanol; 0.2 eq referring to glycoside content) was added and the mixture stirred at room temperature overnight. Water was added until the precipitated polymers were dissolved. Addition of ion exchange resin (Dowex 50WX8, 200–400 mesh, Carl Roth, Karlsruhe, Germany) followed by filtration and lyophilization yielded the products as yellowish powders. The crude polymer was further purified by 3 times dissolving in methanol and precipitation in 10-fold excess of Et<sub>2</sub>O, followed by dissolution in ddH<sub>2</sub>O and lyophilization. Pure polymers were obtained as white powder.

### 2.2. Preparation of Polymer Coatings

Polymers were diluted to a concentration of 25 or 5 mg/mL in a H<sub>2</sub>O/ethanol 5:1 mixture. The mixture was sterile filtered before use. From the mixture, 20 µL was pipetted into each well of a 48-well plate, 34.6 µL into each well of a 24-well plate, or 5.76 µL into each well of a 96-well plate. The plates were allowed to dry under sterile conditions for at least 4 h and crosslinked with 3 J/cm<sup>2</sup> UV light at 254 nm, followed by 3× washings with 250 µL of phosphate-buffered saline (PBS).

Coverslips were coated by carefully pipetting 10 µL of each polymer solution on a 13-mm PETG coverslip (Tissue Culture Coverslips 13 mm, Sarstedt, Nümbrecht, Germany) to obtain a fully coated surface. The coverslips were let dry in air for at least 4 h, followed by crosslinking with 3 J/cm<sup>2</sup> at 254 nm. Washing 3× with ddH<sub>2</sub>O and 3× with ethanol, followed by drying in an N<sub>2</sub> stream yielded the final coating, which was used directly for IR spectroscopy.

### 2.3. Physicochemical Surface Characterization

IR data was recorded on a Tensor 27 FT-IR Spectrometer (Bruker, Germany). Scanning electron microscope (SEM) images were obtained with an XL-30 SEM (Philips, Amsterdam, Netherlands) at 10 kV. The samples were dried in vacuum and thereafter coated with an approx. 5 nm thick Au/Pd layer (SC7620 sputter coater, Quorum, Laughton, UK). Images were taken at a 40° tilted angle. Atomic force microscope (AFM) images were obtained using a CoreAFM (Nanosurf, Liestal, Switzerland) with a TAP150GD-G tip (BudgetSensors, Sofia, Bulgaria, tip radius <10 nm) in tapping mode.

### 2.4. Biological Evaluation

#### 2.4.1. L-929 Mouse Fibroblast Cell Culture

L-929 mouse fibroblasts were a gift from Dr. Oliver Podlech (CleanControlling GmbH, Emmingen-Liptingen, Germany). Media and reagents were purchased from Sigma-Aldrich (Taufkirchen, Germany). Sterile cell cultureware was purchased from VWR, Germany. Fibroblasts were cultured in low-glucose Dulbecco's Modified Eagle Medium (DMEM), supplemented with 10% (*v/v*) fetal calf serum (FCS), 1% (*v/v*) penicillin-streptomycin (10,000 U/mL) and 1% (*v/v*) L-glutamine. Cells were incubated at 37 °C and 5% CO<sub>2</sub> in a humidified incubator (CB series C150, Binder, Tuttlingen, Germany) and subculturing was performed using trypsin/Ethylenediaminetetraacetic acid (EDTA) before reaching confluency, approximately every third day.

#### 2.4.2. Extract Test Using the MTT Assay

Polymer extracts were prepared according to USP standard [64]. Briefly, after coating a 24-well plate with polymers followed by washing steps, 317 µL of DMEM (20 mL for 120-cm<sup>2</sup> coated surface) was added and the coating incubated for 24 h at 37 °C in a humidified 5% CO<sub>2</sub> atmosphere. A cell suspension of L-929 in DMEM (100,000 cells/mL) was added to an uncoated 96-well plate (treated for cell culture, 100 µL/well) and grown to adherence overnight. Medium in each well was replaced by prepared extract medium (100 µL) or medium containing 6% Dimethyl sulfoxide (DMSO) for the cytotoxicity positive control and incubated for 72 h at 37 °C in a humidified 5% CO<sub>2</sub> atmosphere. After 72 h, medium was replaced by 110 µL of DMEM containing 10% of a 10mM MTT solution in PBS. After incubating for 4 h in the incubator, 100 µL of 10% SDS in 0.01M HCl solution was added and incubated for 4 h. Absorbance was measured at 570 nm using a Tecan Infinite M2000 microplate reader. Cell viability was calculated as the percentage ratio of averaged absorbance of triplicate wells containing extract versus the averaged absorbance of untreated control wells.

#### 2.4.3. Direct Contact Test Using the MTT Assay

Cell suspension (100,000 cells/mL) was added to a polymer-coated 96-well plate (treated for cell culture, 100 µL each) and incubated over 24 and 48 h at 37 °C and 5% CO<sub>2</sub> in a humidified incubator. At the end of incubation, the medium was removed, and 110 µL of medium containing 10% of a 10 mM MTT solution in PBS was added. After incubating the cells for 4 h at 37 °C in a humidified 5% CO<sub>2</sub> atmosphere, 100 µL of 10% SDS in 0.01M HCl was added and incubated for 4 h at 37 °C in 5% CO<sub>2</sub>. The absorbance was measured at 570 nm using a microplate reader. Cell viability was calculated as the percentage ratio of averaged absorbance of each triplicate well containing the same polymer coating versus the averaged absorbance of uncoated control wells.

#### 2.4.4. Bacterial Cell Culture

For antimicrobial tests, bacteria cell lines of *Staphylococcus aureus* (MRSA, DSM 28766) and *Escherichia coli* (K12, DSM 498) were used. Bacterial strains were stored at −80 °C in glycerol stocks. For each experiment, a new vial of bacterial strain was thawed and incubated (Minitron, Infors HT, Bottmingen, Switzerland) overnight at 37 °C and 100 rpm in LB medium before use in the experiments.

#### 2.4.5. Antibacterial Assay by Optical Density

The antibacterial effects of the polymers were evaluated using a direct contact method according to ISO 22196 [65] with a thin film of bacteria solution in LB medium (high-nutrition) or PBS (low-nutrition) between the polymer to be analyzed and a polymer slide to ensure direct contact. A 24-well cell culture tissue plate coated with the polymers to be tested was inoculated with 100  $\mu\text{L}$  of bacterial suspension at a concentration of  $3 \times 10^5$  cells/mL and sealed with a PETG coverslip. Bacterial solutions were prepared in LB medium for the high-nutrition condition and in PBS for the low-nutrition condition. As controls, wells without polymer coating were treated with bacteria suspension and medium without cells. After incubating the plate for 24 h at 37 °C and 90% humidity, bacteria were removed from the plates by addition of 1 mL of soybean casein digest lecithin polysorbate broth (SCDLP), followed by pipetting up and down 4 times to detach all bacteria. From this mixture, 200  $\mu\text{L}$  was transferred to a 96-well plate in a series of dilutions. The 96-well plate was sealed with parafilm and placed in a plate reader preheated to 37 °C. Optical density at 600 nm was measured every 30 min over the next 12 h. The plate was shaken briefly every 10 min to ensure distribution of nutrients. Measured values from each sample were compared to determine the viability relative to that of untreated samples. The evaluation time point was chosen to be in the exponential phase before reaching the inflection point. For evaluation, the last time point was used for which Equation (1) was still fulfilled:

$$\frac{\log(\text{OD}_{600\text{nm},t_{+1}}) - 2 \times \log(\text{OD}_{600\text{nm},t}) + \log(\text{OD}_{600\text{nm},t_{-1}})}{t - t_{-1}} > 0 \quad (1)$$

where  $\text{OD}_{600\text{nm}}$  is the optical density at 600 nm for the different measuring points;  $t$  is the measuring time of the data point to be evaluated;  $t_{+1}$  is the measuring point of the subsequent data point and  $t_{-1}$  is the measuring point of the previous data point.

#### 2.4.6. Antibacterial Assay by Colony-Forming Units

The antibacterial effects of the polymers were evaluated using a direct contact method as a droplet of bacteria solution in PBS on top of the polymer. A bacterial overnight culture in LB medium was centrifuged (10 min,  $4000 \times g$ ) and resuspended in PBS to an  $\text{OD}_{600}$  value of 0.2. Coated and uncoated PETG coverslips were inoculated in a 6-well tissue culture plate with 100  $\mu\text{L}$  of the prepared bacteria suspension. Uncoated PETG coverslips were used as reference. The samples were cultured for 24 h at 37 °C and 90% humidity in a humid chamber. Solutions were removed and transferred to a sterile tube. Each coverslip was transferred to a 15 mL Falcon tube, covered with 900  $\mu\text{L}$  of PBS, and treated in an ultrasonic bath at 50 Hz for 15 min to remove bacteria. Both PBS fractions were combined, vortexed for 1 min, and pipetted in a series of dilutions on LB agar plates in duplicate (100  $\mu\text{L}$  per dilution and plate). Agar plates were cultured at 37 °C in an incubator, followed by counting of colony-forming units (CFU) after 24 h.

#### 2.4.7. Crystal Violet Assay for Biofilm Assessment

Biofilm formation was assessed in 96-well plates by staining with crystal violet dye. Briefly, 200  $\mu\text{L}$  of a bacterial overnight culture, adjusted to a concentration of  $3 \times 10^5$  cells/mL in lysogeny broth (LB) medium, was added to each sample. Empty wells (in the outer row, in particular) were filled with 200  $\mu\text{L}$  of PBS to prevent the samples from drying out. The closed well plate was incubated for 24, 48, or 72 h at 37 °C in an incubator without shaking. Then,  $\text{OD}_{600}$  was measured to ensure comparable cell growth in each well. The medium was gently discarded without removing the biofilm, and the samples were washed carefully 3 times with PBS, followed by fixing with 200  $\mu\text{L}$  of absolute ethanol. The ethanol was aspirated, and the samples were dried for 10 min under sterile conditions. For biofilm staining, 200  $\mu\text{L}$  of 0.5 wt% (*wt/vol*) crystal violet staining solution in PBS was added to each sample, and the plate was incubated for 2 min at room temperature. The staining solution was removed and the samples washed  $6 \times$  with 200  $\mu\text{L}$

of PBS to remove excess dye. The samples were left to dry overnight under a sterile bench, followed by addition of 100  $\mu$ L of ethanol to release the dye. After a 10 min incubation, the mixture in each well was transferred to a new 96-well plate, and absorbance at 595 nm was measured using a plate reader.

#### 2.4.8. Extracellular Polymeric Substance (EPS) Assessment by Phenol-Sulfuric Acid Method

In addition, the biofilm formation was assessed by analyzing the carbohydrates in the formed biofilm. Therefore, the phenol-sulfuric acid method according to Masuko et al. [66] was performed. Briefly, polymer coatings were treated in a 96-well plate as previously described for the crystal violet assay and incubated for 24, 48 and 72 h at 37 °C in an incubator without shaking. OD<sub>600</sub> was measured to ensure comparable cell growth in each well, and the medium was gently discarded. After 3 wash steps with sterile PBS, the samples were fixed with 200  $\mu$ L of absolute ethanol. The ethanol was gently aspirated, and the samples were dried for 10 min under sterile conditions. A volume of 150  $\mu$ L of concentrated sulfuric acid was added to each well, immediately followed by 30  $\mu$ L of 5% phenol in water. The plate was incubated at 90 °C for 5 min and then cooled in an ice bath for an additional 5 min. The absorbance at 490 nm was measured using a plate reader to quantify EPS.

#### 2.4.9. Live/Dead Staining

Besides the Crystal violet staining and EPS assessment, we also performed live/dead staining using the bacteria live/dead staining kit (PromoCell GmbH, Heidelberg, Germany). Polymer coatings were treated in a 96-well plate as previously described for the crystal violet assay and incubated for 24, 48 and 72 h at 37 °C in an incubator without shaking and stained accordingly to the manufacturer's instructions. Briefly, biofilm samples were washed 3 times with sterile 150 mM NaCl solution and stained for 15 min at room temperature in the dark with an appropriate mixture of DMAO (ex/em 490/540) and EthD-III (ex/em 530/630). Live bacteria with an intact cell membrane are stained fluorescent green, whereas dead bacteria with a disrupted cell membrane are stained fluorescent red. Labeled cells were imaged using the fluorescent microscope Observer.Z1 (Carl Zeiss AG, Oberkochen, Germany) and processed using the software ZEN blue edition (Version 3.4, Carl Zeiss AG, Oberkochen, Germany).

#### 2.4.10. Statistical Analysis

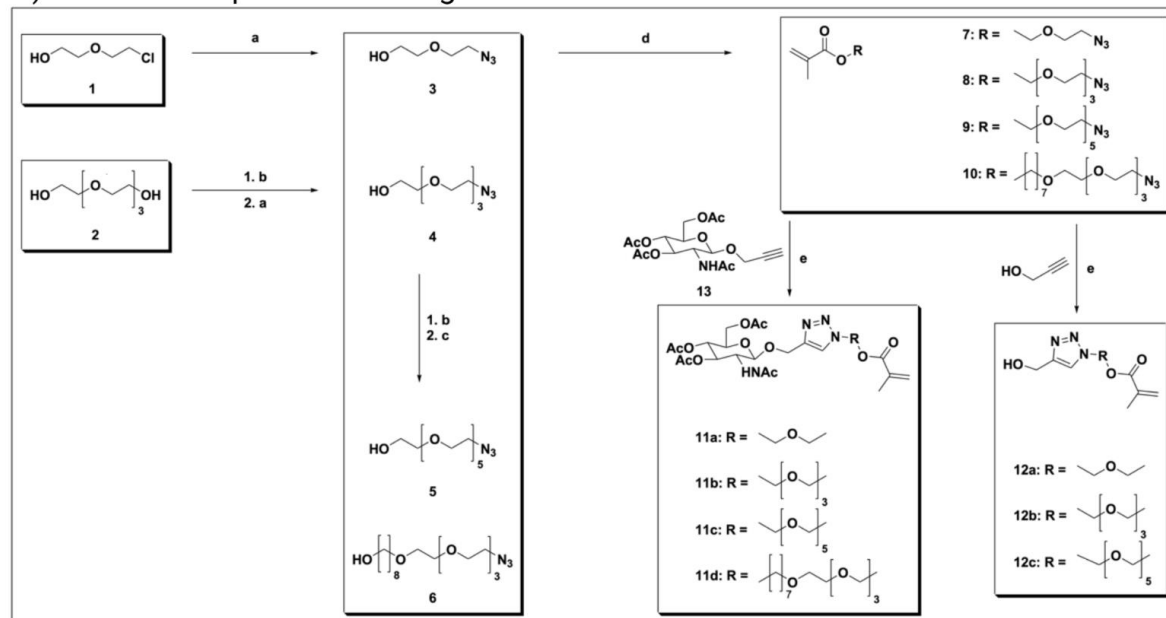
Measurements for biological evaluation (bacterial and cell culture) were replicated with  $n = 3$  and expressed as mean  $\pm$  standard deviation (SD) unless stated otherwise. Statistical significance was analyzed with pairwise Student's *t*-test, and statistically significant values were defined as  $p < 0.05$  (\*).

### 3. Results and Discussion

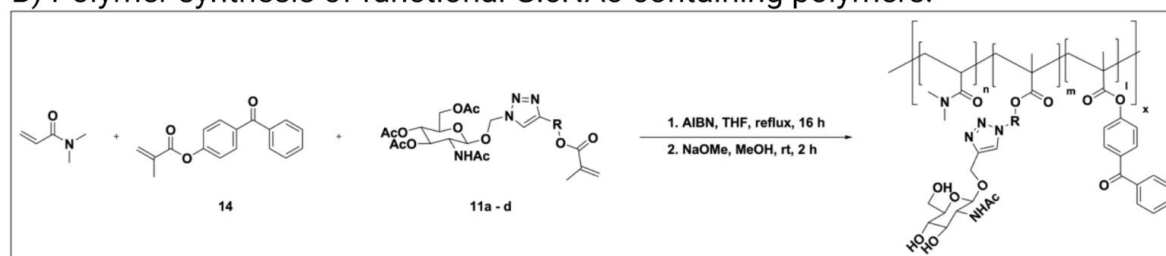
#### 3.1. Monomer Synthesis

Azido linkers **3–6** were synthesized by sequential tosylation steps, followed by substitution with either sodium azide or another linker fragment. Those prolonged linkers were reacted to azido methacrylate **7–10**, followed by click reaction to either functional GlcNAc methacrylate **11a–d** or their corresponding 4-hydroxymethyl methacrylate derivatives **12a–c**. The detailed reaction sequences are shown in Figure 1.

## A) Reaction sequences leading to functional monomers:



## B) Polymer synthesis of functional GlcNAc-containing polymers:



## C) Polymer synthesis of functional 4-hydroxymethyl derivatives:

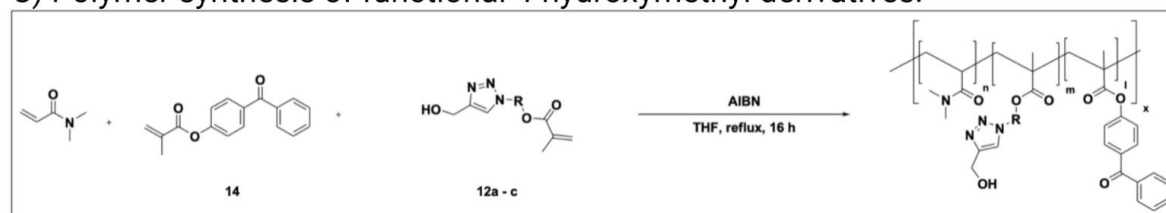


**Figure 1.** Chemical Synthesis. (A) Reaction sequences leading to functional monomers **11a–d** or **12a–c**, respectively. Reaction conditions: (a)  $\text{NaN}_3$ ,  $\text{CH}_3\text{CN}$ , reflux, 16 h; (b)  $\text{TsCl}$ ,  $\text{NEt}_3$ ,  $\text{CH}_2\text{Cl}_2$ , rt, 16 h; (c)  $\text{NaH}$ , THF, reflux, 48 h; (d) methacryloyl chloride,  $\text{NEt}_3$ ,  $\text{CH}_2\text{Cl}_2$ ,  $0^\circ\text{C}$ –rt, 16 h; and (e)  $\text{CuSO}_4$ , TBTA, Na ascorbate,  $\text{H}_2\text{O}/\text{MeOH}/\text{CH}_2\text{Cl}_2$  3:10:10,  $60^\circ\text{C}$ , 1 h. (B) Polymer synthesis of functional *N*-acetylglucosamine (GlcNAc)-containing polymers. Benzophenone methacrylate **14** was copolymerized with glycosidic monomers **11a–d** by free radical polymerization with AIBN, followed by Zemplén deprotection. (C) Polymer synthesis of functional 4-hydroxymethyl derivatives using 4-hydroxymethyl-[1,2,3]-triazolo-1-yl derivatives of functional monomers **12a–c** of the polymers with AIBN.

Azido linker **3** was synthesized by reacting 2-(2-chloroethoxy)-ethanol with sodium azide (a) according to the literature [60]. Azido linkers **4–6** were synthesized via sequen-

tial tosylation (**b**) and substitution steps with either sodium azide (**a**) or another linker for chain prolongment. For the azido hexaethylene glycol linker **5**, diethylene glycol was used for chain prolongment as published Mahou et al. [59], and for the difunctional azido tetraethyleneglycol octyl linker **6**, 1,8-octanediol was used for chain prolongment. Azidomethacrylates **7–10** were synthesized following published protocols, using methacryloyl chloride and triethylamine [61].

The functional glycoside, propargyl GlcNAc **13**, was synthesized as described by Schmidt et al. [62]. *N*-Acetylglucosamine was used as starting material, followed by protection with acetyl groups, conversion of the peracetylated *N*-acetylglucosamine into an oxazoline as glycoside donor, and further glycosidation using propargyl alcohol to *N*-acetylpropargylglucosamine **13**. For click functionalization, the optimized conditions reported by Schmidt et al. [62] were used, yielding the GlcNAc-functionalized monomers **11a–d**. To further elucidate antimicrobial properties of the combined triazole and linker in the polymers, azido oligoethylene glycol methacrylates **7–9** were reacted under the same conditions with propargyl alcohol to their 4-hydroxymethyl-[1,2,3]-triazole-1-yl counterparts **12a–c**. The 4-hydroxymethyl derivatives **12a–c** and the GlcNAc derivatives **11a–d** were used as functional monomers directly for polymerization.

### 3.2. Polymer Synthesis

Functional GlcNAc monomers **11a–d** were successfully polymerized using free radical polymerization with AIBN as radical starter (Figure 1B), followed by several purification steps with precipitation and *O*-acetyl deprotection to the functional glycosidic polymer. Functional 4-hydroxymethyl monomers **12a–c** were polymerized using free radical polymerization with AIBN (Figure 1C) followed by purification and used directly because no protection groups were involved. The 4-methacryloyloxy-benzophenone **14** was synthesized according to the literature [57]. All synthesized polymers with their corresponding abbreviations are listed in Table 1.

Analysis of the polymers and the copolymer ratio between MBP **14** and functional monomers **11** or **12** was performed by <sup>1</sup>H NMR spectroscopy, followed by 2-dimensional measurements for glycosidic structure determination. The triazole proton, showing a relatively isolated singlet at 7.96 ppm, was integrated against the benzophenone aromatic protons and against the *N*-acetyl group of the glycosidic monomers **11a–d**. For the 4-hydroxymethyl derivatives **12a–c** without glycoside, the triazole proton at 7.96 ppm was integrated against the benzophenone protons only. The dimethacrylamide methyl (DMAm) groups showed a broad multiplet at 2.98–2.75 ppm, which overlapped with the ethylene glycol signals of comonomers **11** and **12**; therefore, the integral ratio of those signals did not match the actual copolymer ratio as shown in Figure 2. The multiplet integral was relatively constant over all three copolymers of **11b**, which had decreasing dimethacrylamide content from 90% to 70%, whereas the content of **11b** with a tetraethylene glycol linker increased from 2.5% to 25%. Therefore, the DMAm content was not calculated using the integral ratios. Successful deprotection of GlcNAc-containing polymers was confirmed by disappearance of the *O*-acetyl groups in <sup>1</sup>H NMR after the deprotection step. For the 4-hydroxymethyl-derivative comonomers **12a–c**, adjusted copolymer ratios of 1:1 MBP **14** vs. **12** were obtained. In the GlcNAc copolymer group, consisting of copolymers with comonomers **11a–d**, different copolymer ratios of MBP **14** vs. **11** were obtained. Possible mechanisms are ester hydrolysis during the Zemplén deprotection step of the GlcNAc residue, because the 4-hydroxymethyl-containing polymeric counterparts did not show different copolymer ratios of the benzophenone. Interestingly, the GlcNAc-4EG copolymers showed no reduction in MBP content relative to the GlcNAc residue (Figure 2). Therefore, different reactivities of benzophenone in combination with several GlcNAc-methacrylates and oligoethylene glycol linkers are possible explanations.

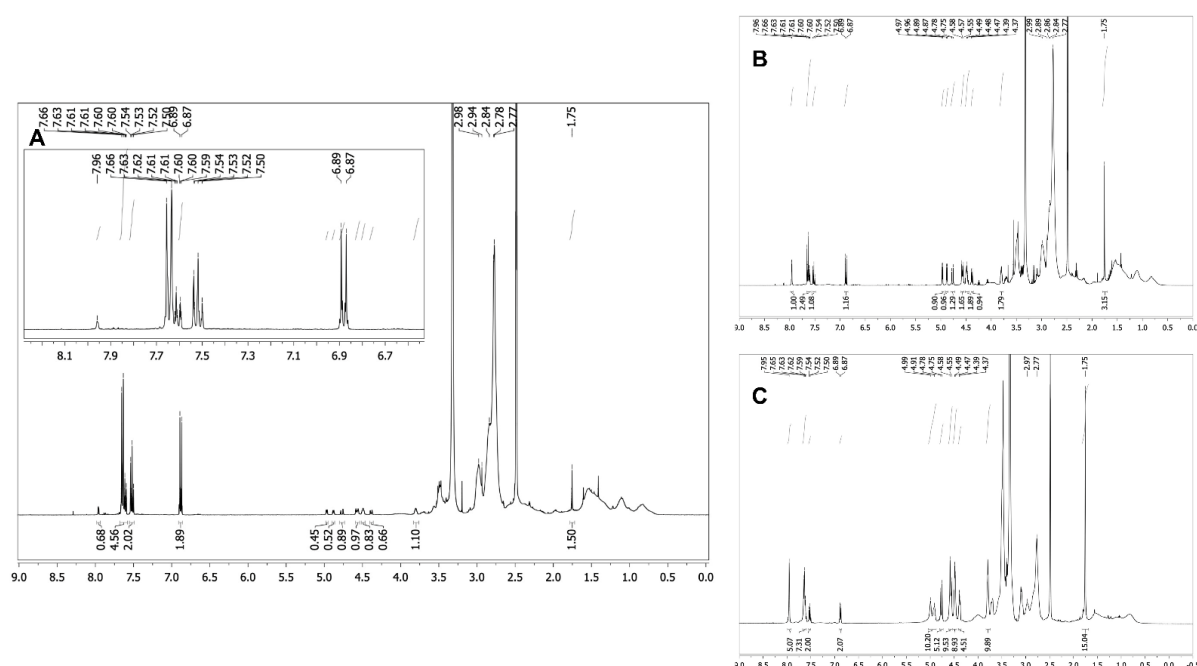


**Figure 2.**  $^1\text{H-NMR}$  spectra (600 MHz) of the 5%—(A), 10%—(B) and 25%—(C) GlcNAc-4EG polymers (Table 1). The GlcNAc and 4-hydroxymethyl triazoles proton gave a distinct singlet at 7.96 ppm, whereas the benzophenones aromatic protons gave signals from 7.66 to 6.67 ppm. Furthermore, the GlcNAc acetyl group singlet showed a signal at 1.75 ppm. The broad multiplet from 2.98 to 2.75 ppm belongs to the dimethacrylamide methyl groups. Copolymer ratio was calculated by the integral ratios of triazole-H vs. NAc vs. aromatic benzophenone-H. For the 4-hydroxymethyl comonomers, only triazole-H was integrated vs. aromatic benzophenone-H. The figure shows the increasing triazole singlet (7.96 ppm) and NAc singlet (1.75 ppm) with increasing comonomer ratio of **11b** vs. the aromatic protons of MBP **14**. The dimethacrylamide multiplet between 2.98 and 2.75 ppm was relatively constant in all three spectra because it overlays the tetraethylene glycol.

Interestingly, the copolymerization of 50% GlcNAc-4EG-methacrylate monomer resulted in ester hydrolysis of the methacrylate ester during polymerization, leading to the propargyl GlcNAc tetraethylene glycol clickamer **15** (data not shown, cf. Supplementary Materials), following the same workup procedure as for the other polymers.

### 3.3. Coating of PETG Coverslips

As the model material, polyethylene terephthalate glycol (PETG) coverslips were coated with the functional polymers. Previous studies with MBP UV crosslinker in different acrylamide scaffolds indicated that  $3\text{ J}/\text{cm}^2$  was the optimum dose of UV irradiation to obtain proper coating stability with minimum unreacted MBP left and minimum coating degradation [57]. Following the crosslinking protocol with UV light ( $3\text{ J}/\text{cm}^2$ , 254 nm) and several washing steps with ddH<sub>2</sub>O and ethanol, stable polymer coatings were obtained using the polymers listed in Table 1. Two concentrations of polymer solutions were applied to the coverslips to obtain coatings of different thicknesses, which were investigated via IR spectroscopy. Recorded spectra of four selected coatings are shown in Figure 3.

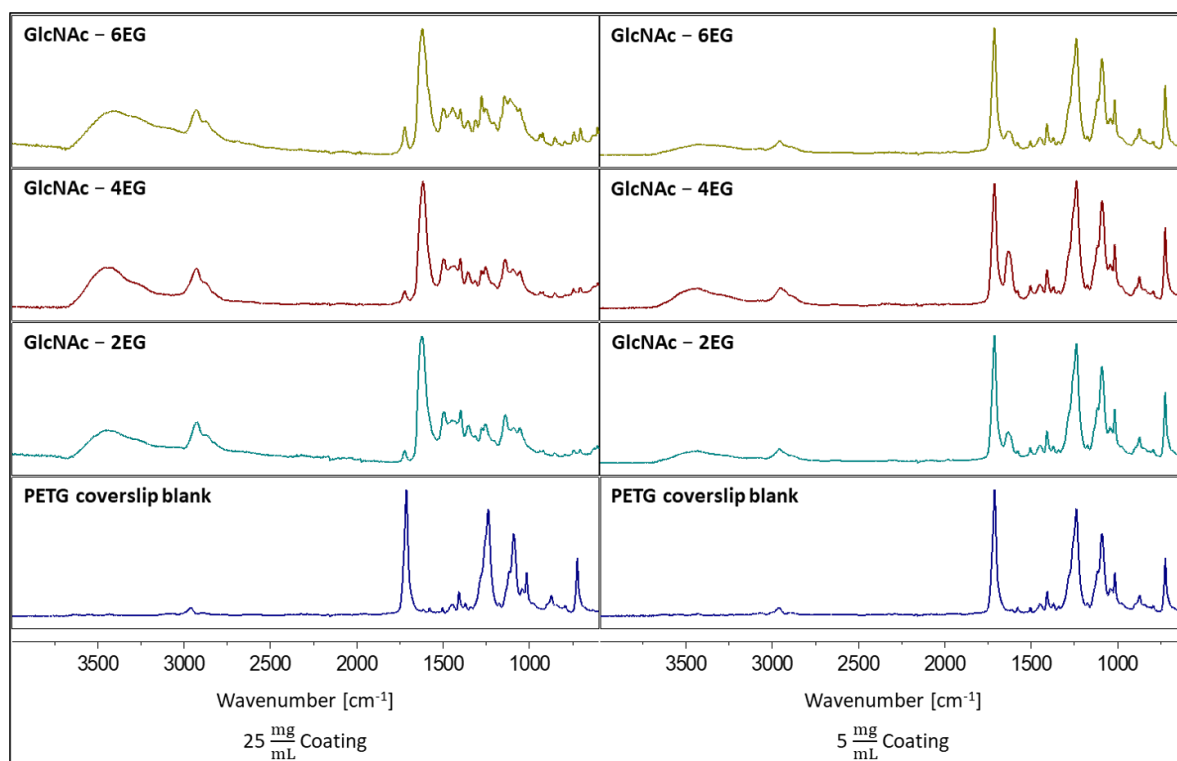


**Figure 3.** Recorded Fourier transform-infrared spectra of selected functional PDMAm-co-P-benzophenone-MA-co-P-GlcNAc-OEG-MA coatings (Table 1) containing 5% GlcNAc copolymer and linkers with 2, 4 and 6 ethylene glycol (EG) units. Coatings obtained with 25 mg mL<sup>-1</sup> coatings could be analyzed properly, whereas with 5 mg mL<sup>-1</sup> coatings, the terephthalate group of the PETG was the dominant signal in the recorded IR spectra.

The dominant peak at 1713 cm<sup>-1</sup> of the terephthalate of PETG from the coverslip blank disappeared in all polymeric coatings obtained by drop casting a 25 mg/mL solution after crosslinking, wherein the peak of the dimethacrylamide dimethyl-carboxamide group at 1621 cm<sup>-1</sup> became visible as well as the copolymer ester groups at 1721 cm<sup>-1</sup>. The presence of the GlcNAc residue was confirmed through the presence of glycosidic OH groups, showing broad peaks at 3450 cm<sup>-1</sup> and at 2925 cm<sup>-1</sup>. The stable coatings were obtained using the polymers as listed in Table 1 with the given MBP copolymer ratios. Therefore, apart from the synthesis, stable coatings using a 25 mg/mL casting solution were obtained.

In coatings obtained by casting a 5 mg/mL polymer solution, the most dominant peak in the IR spectra of the coatings was the PETG terephthalate peak at 1713 cm<sup>-1</sup>, followed by a smaller peak of the dimethacrylamide dimethyl-carboxamide group at 1621 cm<sup>-1</sup>. The copolymer ester groups at 1721 cm<sup>-1</sup> were not visible at all compared with those of the thicker 25 mg/mL coatings, possibly being overlaid by the dominant terephthalate peak. As a result, the polymer coatings for antimicrobial studies and cytotoxicity evaluations were prepared by casting a 25 mg/mL solution to obtain an appropriate coating thickness.

#### 3.4. Surface Morphology

The surface morphology of the bioactive polymer coatings 5%-GlcNAc-6EG-PDMAm and 5%-GlcNAc-4EG-PDMAm was investigated by SEM and AFM as shown in Figure 4. SEM images were recorded at a tilted angle of 40 degrees. For the 5%-GlcNAc-4EG-PDMAm, in the SEM image (Figure 4A), a textured surface showing small pores and a sponge-like structure can be observed. Furthermore, small particles in the size of up to

500 nm are present. The AFM surface topography (Figure 4B) confirms the topography. Similar observations can be made for the GlcNAc-6EG coating (Figure 4C,D), but showing less pore-like structures than the 5%-GlcNAc-PDMAm coating.

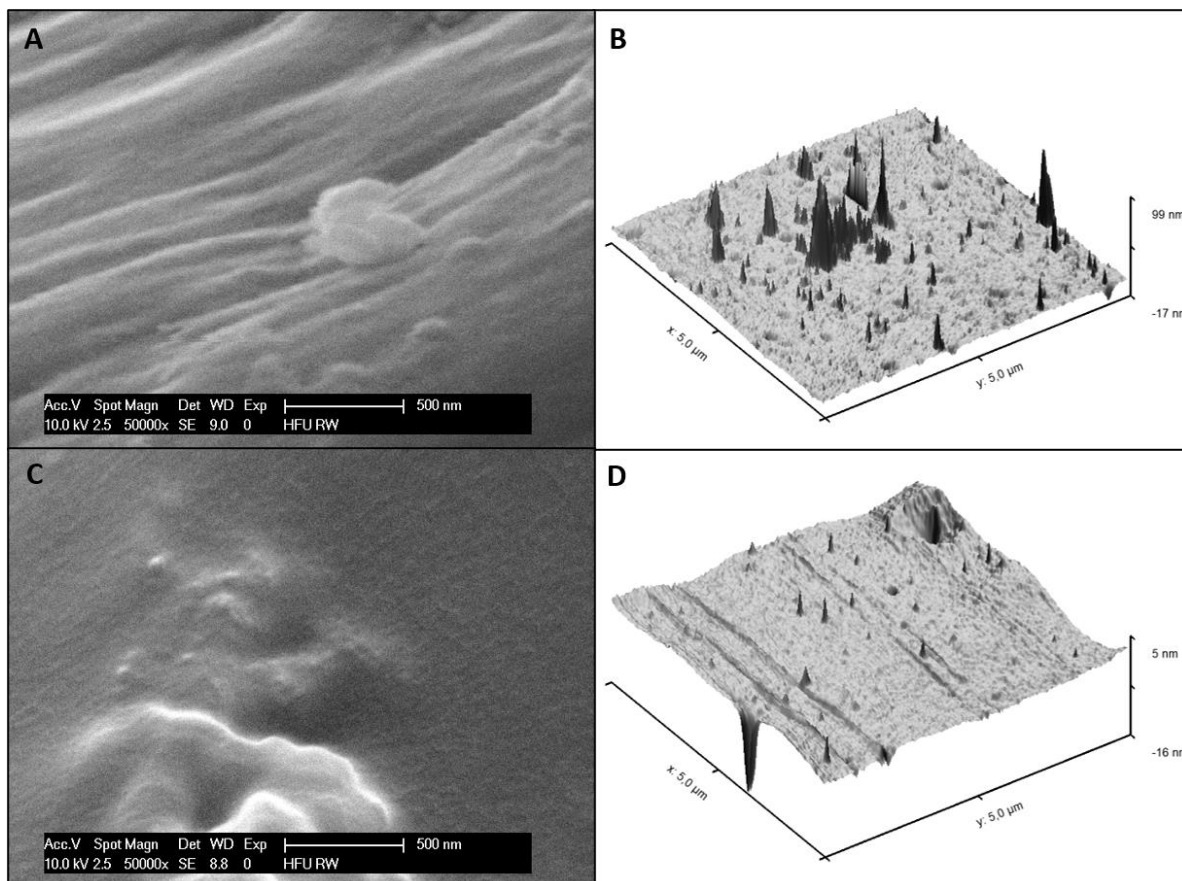


**Figure 4.** SEM (A,C) and AFM (B,D) images of the bioactive PDMAm coatings, 5%-GlcNAc-4EG (A,B) and GlcNAc-6EG (C,D).

### 3.5. Coating Sterilization

Due to the sterile demands for biocompatibility testing as well as for antimicrobial activity testing against specified bacterial strains, the successful sterilization of the coating was established prior to testing. Therefore, polymer solutions were sterile filtered with a 0.2  $\mu\text{m}$  sterile filter and handled under sterile condition in a biosafety cabinet during coating of the corresponding surfaces, followed by crosslinking with 3  $\text{J}/\text{cm}^2$  UV-C light (254 nm). The polymer coated surfaces were then incubated for 24 h at 37  $^\circ\text{C}$  and further 24 h at room temperature in LB media in order to assess the sterility by absence of bacterial growth. No bacterial growth could be observed for the coated chips under these conditions.

UV sterilization is an established method in food packing, water treatment, and surface sterilization in medical settings [67,68]. For example, according to Bak et. al. [69], a 4-log fold reduction in *P. aeruginosa* in catheter disinfection was obtained, using UV-C light with a dosage of 40  $\text{mJ}/\text{cm}^2$ . In addition, clinical studies have shown the efficacy of UV-C light against different fungi, by using a dosage of 41.25  $\text{mJ}/\text{cm}^2$  from a commercially available disinfecting device for medical settings [70,71]. In general, for a 90% inactivation of bacterial pathogens, a UV-C dosage of 8  $\text{mJ}/\text{cm}^2$  is needed [71], whereas, for ssRNA viruses, an irradiation dose of 1.32–3.20  $\text{mJ}/\text{cm}^2$  is needed [72]. Therefore, it can be

concluded that residing pathogens as well as possible viral contaminations are eliminated after the combination of sterile filtration and UV crosslinking of the benzophenone residue in order to form the stable coating.

### 3.6. Antibacterial Activity

The antibacterial properties of the synthesized polymers were evaluated using *Escherichia coli* (*E. coli*) as a Gram-negative model organism and multidrug-resistant *Staphylococcus aureus* (MRSA) as a Gram-positive model organism. These organisms were chosen as model organisms with clinical relevance for infections and biofilm formation [73]. The bacteria were cultured in high-nutrition (LB medium) and low-nutrition (PBS) environments to assess the effect of the polymers in different nutritional conditions.

In the high-nutrition environment, no effect of coatings on bacterial growth of *E. coli* and *S. aureus* could be observed (Figure 5A). In contrast, under low-nutrition conditions (Figure 5B), the 5%-GlcNAc-4EG ( $4061 \pm 2184$  CFU/cm<sup>2</sup>) and 5%-GlcNAc-6EG ( $22,883 \pm 5172$  CFU/cm<sup>2</sup>) modified PDMAM coatings showed a reduction in bacterial viability, compared with the untreated PETG chip ( $63,625 \pm 13,320$  CFU/cm<sup>2</sup>) and the unmodified PDMAM coating ( $60,009 \pm 17,207$  CFU/cm<sup>2</sup>).

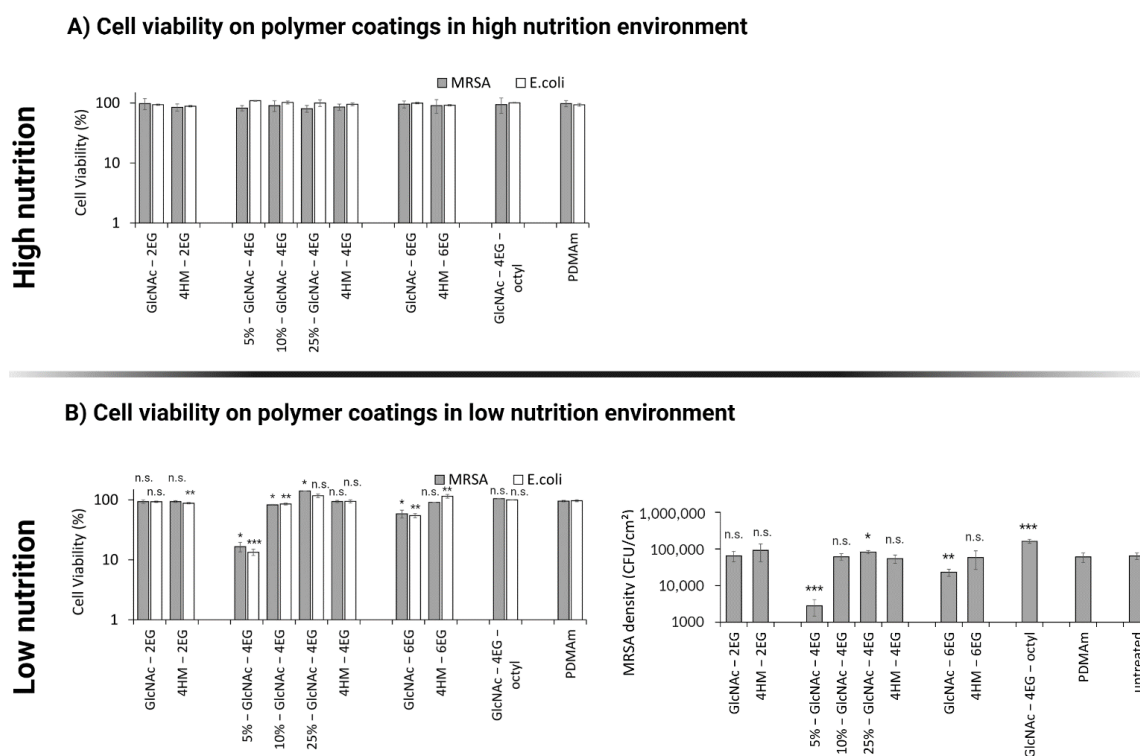


**Figure 5.** Antibacterial evaluation of polymer coatings in high- and low-nutrition environments. PDMAM corresponds to the unmodified acrylate coating. (A) Cell viability of *Escherichia coli* (*E. coli*) and multidrug-resistant *Staphylococcus aureus* (MRSA) on polymer coatings in the high-nutrition environment was assessed according to antibacterial assay (optical density, OD). Values are shown relative to that of the untreated sample. (B) Cell viability on polymer coatings in the low-nutrition environment was assessed for *E. coli* ( $n = 4$ ) and MRSA ( $n = 2$ ) according to antibacterial assay (optical density, OD, left graph) and in addition for MRSA ( $n = 3$ ) according to the more sensitive antibacterial assay (colony-forming units, CFU, right graph). Values are shown as mean  $\pm$  SD. Significant changes were assessed by pairwise Student's *t*-test (n.s., not significant; \*  $p < 0.05$ ; \*\*  $p < 0.01$ ; \*\*\*  $p < 0.001$ ).

Both the GlcNAc-2EG modified polymer and the triazole-bearing 4-hydroxymethyl derivatives (4HM-2EG, 4HM-4EG and 4HM-6EG) did not show a considerable effect compared with unmodified PDMAm, whereas the polymers 5%-GlcNAc-4EG and 5%-GlcNAc-6EG showed a significant reduction in viable MRSA and *E. coli* in direct contact testing under low-nutrition conditions (Figure 5B). Thus, viability was reduced by 1.2 log for the GlcNAc-4EG modified hydrogel and by 0.4 log for the GlcNAc-6EG modified hydrogel. Higher ratios of GlcNAc-4EG copolymer in the hydrogel network did not result in a stronger antibacterial effect but resulted in bacterial viabilities similar to those of 4-hydroxymethyl functionalized coatings.

In addition to evaluating the antibacterial effect on bacterial growth, we assessed biofilm formation on the different hydrogels. The crystal violet assay for biofilm assessment showed a decrease in biofilm formation for several polymers, as shown in Figure 6A,B. In particular, the polymers 5%-GlcNAc-4EG and 5%-GlcNAc-6EG showed a significant decrease in biofilm formation compared with the unfunctionalized PDMAm coating. They showed a decrease in absorption at 595 nm for *S. aureus* of  $0.46 \pm 0.07$  and  $0.52 \pm 0.12$  compared with  $0.89 \pm 0.14$ , respectively. Biofilm formation for *E. coli* decreased even more:  $0.23 \pm 0.07$  and  $0.42 \pm 0.11$  compared with  $1.06 \pm 0.11$ . Higher GlcNAc-4EG copolymer content resulted in less biofilm inhibition (60–80% biofilm content) compared with the unmodified PDMAm hydrogel. The effect was observed over a cultivation time of 72 h (Figure 6B) and was confirmed by EPS analysis with the phenol-sulfuric acid method described by Masuko et al. (Figure 6C) [66]. In addition, we analyzed the quantity and viability of bacteria on the polymer coatings after 24, 48 and 72 h incubation, using live/dead staining (Figure 6D). Even though the live staining with DMAO in combination with the polymer coating resulted in high background noises, so that a low exposure time had to be selected and the intensity of the fluorescent stained bacteria was low, the overall effect of the polymer coatings could be confirmed. The quantity of bacteria was significantly lower for the polymers 5%-GlcNAc-4EG and 5%-GlcNAc-6EG compared to their respective controls 4HM-4EG and 4HM-6EG as can be seen in the brightfield images (Figure 6D). Furthermore, it was observed that the proportion of dead cells, especially on the 5%-GlcNAc-4EG, was higher than on the corresponding controls and particularly on the unmodified PDMAm, where a mix of dead and alive cells was visible. Additional images taken at 24, 48 and 72 h are shown in the supplementary materials (Figures S2–S4).

The inhibition of biofilm formation by GlcNAc was previously observed by Sicard et al. for different *E. coli* strains, but not for *S. aureus* [47]. However, under high-nutrition conditions, there was no longer any effect on bacterial growth observed. Antibacterial effects in the low-nutrition environment were evaluated using the OD-method to identify potential candidates and additionally evaluated for MRSA using the more sensitive CFU-method, which is more conclusive, particularly in the lower measurement range. This is attributed to the measurement procedure itself, since in the OD-method, although cells in the process of dying make up only a small part of the population, they also lead to a signal in the measurement. In contrast, only the most vital cells are taken into account in the CFU-method, as these must be able to form their own colony. The observations in the nutrient-rich environment may indicate that the polymer interferes in the metabolism of specific substrates, as studies have shown that chitosan interferes with RNA and protein synthesis [74–77]. Therefore, these substrates can no longer be used for biofilm formation or as a source of nutrients. This would explain the observed decrease in biofilm formation (high-nutrition) and bacteria viability under nutrient-poor conditions, whereas under nutrient-rich conditions, the bacteria can use other substrates as a source of nutrients, negating the growth-inhibiting effect. Another possible explanation for the lack of effect on growth under high-nutrient levels is that a higher mortality rate might have been present but was not measurable because it was obscured by significantly greater bacterial proliferation. As a result, the effect of the coatings was only observable in the low-nutrition medium, where bacterial growth was negligible and thus the increased mortality rate could be observed [78]. Nevertheless, the antibiofilm effect was observed under the nutrient-rich

conditions, so the effect seems to be only partially dependent on the nutrient condition. The exact mechanism underlying the antibacterial and antibiofilm effect needs further elucidation [76].

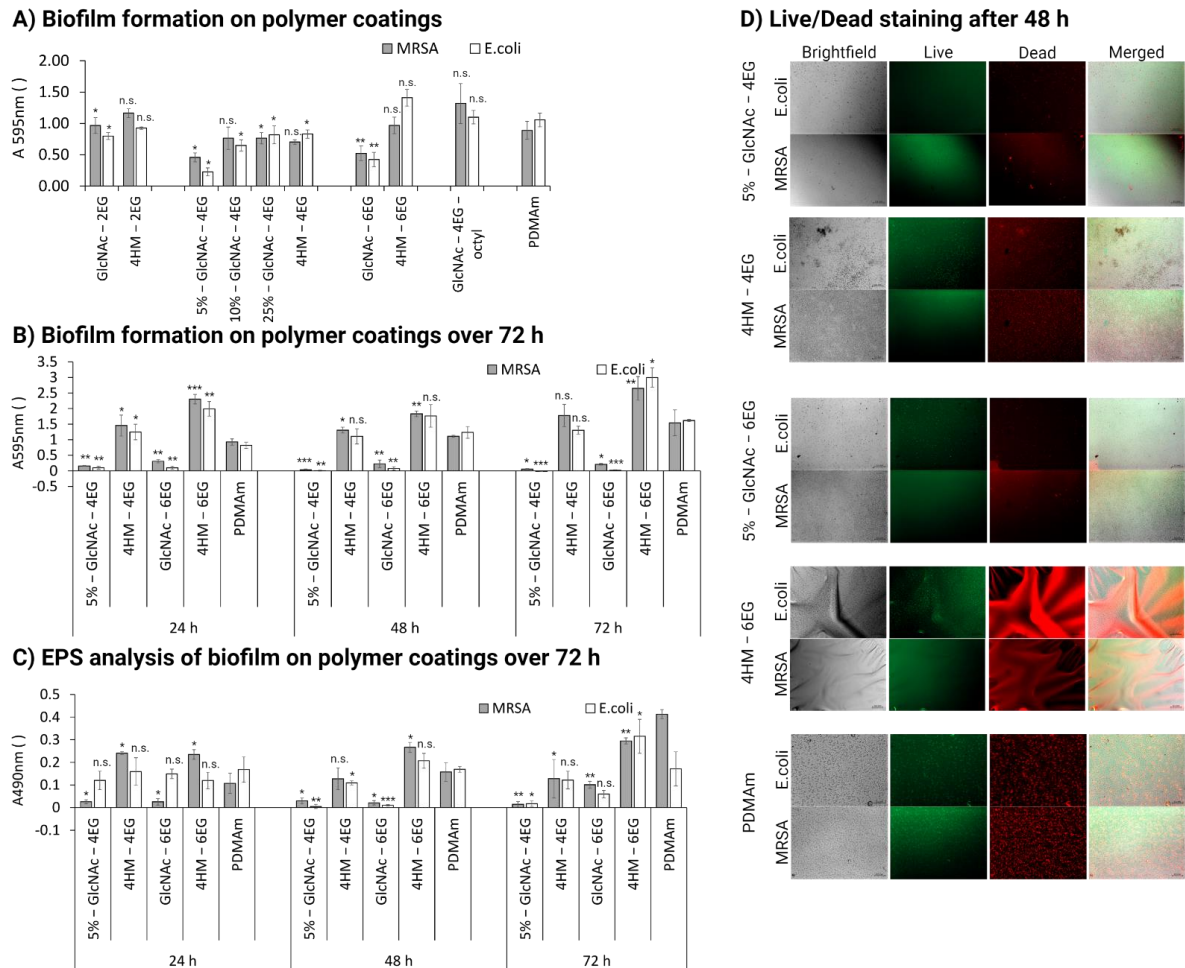


**Figure 6.** Evaluation of biofilm formation of polymer coatings. PDMAm corresponds to the unmodified acrylate coating. (A) Biofilm formation of *E. coli* and MRSA in the high-nutrition environment was assessed by crystal violet staining after 24 h of cultivation for all coatings as a first evaluation. (B) Biofilm formation of *E. coli* and MRSA in the high-nutrition environment was assessed by crystal violet staining after 24, 48 and 72 h of cultivation for the most active polymer coatings and their respective controls. Corresponding brightfield images are available in the supplementary materials (Figure S1) (C) Extracellular polymeric substance (EPS) analysis of formed biofilm by *E. coli* and MRSA in the high-nutrition environment was assessed by phenol-sulfuric acid method after 24, 48 and 72 h of cultivation for the most active polymer coatings and their respective controls. (D) Live/Dead staining of *E. coli* and MRSA in the high-nutrition environment after 24, 48 and 72 h of cultivation for the most active polymer coatings and their respective controls. Magnification is 100 $\times$ ; scale bar measures 0.1 mm. Values are shown as mean  $\pm$  SD. Significant changes were assessed by pairwise Student's *t*-test (n.s., not significant; \*  $p < 0.05$ ; \*\*  $p < 0.01$ ; \*\*\*  $p < 0.001$ ).

Comparison of the different synthesized coatings showed that linker length and the amount of GlcNAc are critical parameters for the antibacterial and antibiofilm functionality of the polymers. We found that the 4EG linker yielded the best results, whereas the 2EG and 6EG linkers had decreased functionality. In addition, GlcNAc content affected the antimicrobial and antibiofilm properties: the highest effect was achieved at 5% GlcNAc and

decreased with higher GlcNAc contents for the 4EG linker. This shows that the 4EG linker itself and therefore the length of the oligoethylene glycol brush affect biofilm formation and antimicrobial properties. The reason for this is most likely the steric arrangement of the functional groups and their distance from the sample surface. Depending on the distance, different interaction possibilities exist between the modified groups and the cell wall or membrane of the bacteria [79].

### 3.7. Cytotoxicity

A cytotoxicity evaluation of the polymeric coatings was carried out according to ISO 10993-5 standards using the extract method and the contact method. Extracts of the coatings were prepared according to ISO 10993-12 and 6% DMSO was chosen as the positive control for cytotoxicity. Cell viability was assessed by the MTT assay.

Cell viability was measured after 72 h of incubation with the prepared extracts (undiluted and diluted 4-fold with medium); results are shown in Figure 7A. No notable cytotoxic effect was observed for any GlcNAc-containing copolymer in the extract test. This included the antimicrobial and antibiofilm polymer, 5% GlcNAc-containing PDMAm hydrogel (5%-GlcNAc-4EG), whose extracts resulted in no loss of fibroblast viability. The 4-hydroxymethyl copolymers containing a tetraethylene glycol (HM-4EG) or a hexaethylene glycol linker (HM-6EG) showed minor decreases in cell viability: a 23% decrease for the 4EG linker and a 12% decrease for the 6EG linker. The extract of the 4-hydroxymethyl derivative with diethylene glycol linker (HM-2EG) showed no cytotoxicity.

For the direct contact test, the cell culture dish was directly coated with the polymers, followed by crosslinking with UV light, 3 washing steps with phosphate buffer, and seeding of cells onto the generated scaffolds. The observed cell viability after 24 and 48 h, determined by MTT assay, is shown in Figure 7B. After 24 h, cell viability was generally lower than that of the untreated cell culture dish, ranging between 60% and 80% for all polymers including the non-modified PDMAm. After 48 h, the most functional polymer against biofilms (5%-GlcNAc-4EG) and most other tested polymers showed only minor reductions in cell viability, within the range of biological systems. Only the GlcNAc-containing polymer with a diethylene glycol linker and the tetraethylene glycol octyl linker showed decreases in cell viability after 48 h (32% and 37%, respectively).

Furthermore, images of the cells grown directly on the polymer coatings were taken, as shown in Figure 8. Morphology of the cells grown directly on the coatings (Figure 8A–E) is altered compared to the uncoated cell culture dish (Figure 8F). It can be observed that the cell morphology is more spheroid like, which implies a lesser adhesion. Due to the experimental conditions, where the coatings were washed after 24 or 48 h incubation prior to addition of fresh media with MTT, an adequate adherence of the cells to the coatings should be given or else the cells would have been washed away in these steps. Thereby, it can be concluded that the L-929 Fibroblasts show adherent behavior to the coatings, albeit lower than on standard cell culture plates. According to ISO 10993:5—evaluation of cytotoxicity of biomaterials, growth inhibition of >30% compared with an untreated control is considered indicative of cytotoxicity [80]. No polymers, except the GlcNAc-2EG and GlcNAc-4EG-octyl polymers showed greater growth inhibition than 30%, and therefore, all polymers except the GlcNAc-2EG and GlcNAc-4EG-octyl polymers can be considered noncytotoxic.

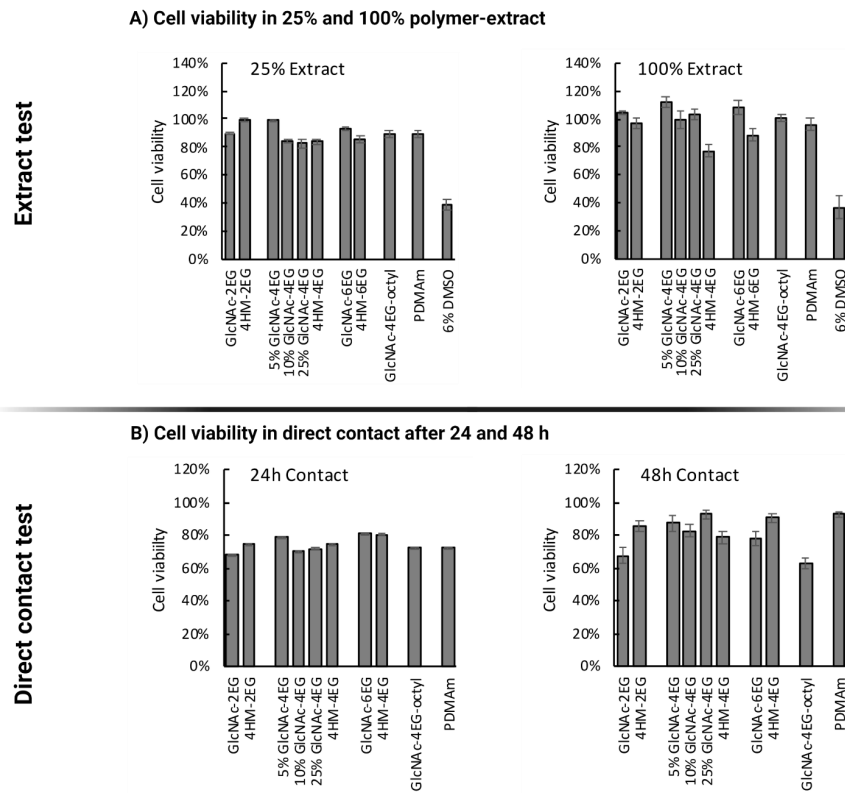


**Figure 7.** Cytotoxicity determination according to ISO 10993-5. (A) Cell viability measured with MTT assay after 72 h of incubation with 100% and 25% extracts; 6% DMSO was used as positive control for cytotoxicity. In both cases, no cytotoxicity was observed for the antimicrobial 5%-GlcNAc-4EG polymer. (B) Cell viability in direct contact test after 24 and 48 h, determined by MTT assay. The main functional polymer, 5%-GlcNAc-4EG, showed no more than a 20% decrease in cell viability by the direct contact test.

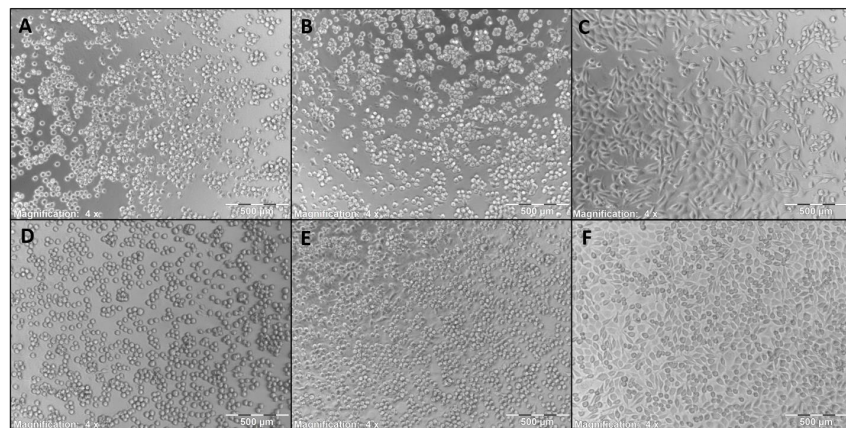


**Figure 8.** L-929 mouse fibroblasts grown on the coatings for 48 h. (A) GlcNAc-2EG-PDMAm, (B) GlcNAc-4EG-PDMAm, (C) 10%-GlcNAc-4EG-PDMAm, (D) GlcNAc-6EG-PDMAm, (E) PDMAm, (F) untreated cell culture dish. Morphology is altered to some extent, but cell viability is still given as shown via MTT test in Figure 7, in which the shown polymers show no more than 20% reduction in cell viability, so no cytotoxicity can be assumed.

#### 4. Conclusions

In summary, we demonstrated the successful synthesis of functionalized PDMAm hydrogel networks, suitable for polymer surface coating via UV-induced C–H insertion reaction. Stable coatings were obtained using benzophenone crosslinker chemistry. A proper sterility of the surface after UV treatment for crosslinking was shown by the absence of bacterial growth in sterile medium. The functionalized coatings showed antimicrobial and antibiofilm properties, leading to a significant reduction of microbial biofilm formation on the coated surface, for both Gram-positive (*S. aureus*) and Gram-negative (*E. coli*) bacteria. We showed up to a 1.2 log decrease in colony-forming units of the clinically relevant pathogen MRSA on surfaces treated with polymer coating. Non-cytotoxicity and biocompatibility toward fibroblast cells, evaluated according to ISO 10993-5 standards, was maintained. Overall, this work describes an interesting approach for decreasing bacterial adhesion to surfaces by selective functionalization with antiadhesive and antimicrobial molecules, preventing bacterial colonization and contamination of wound dressings or surgical implants. The use of such coatings can not only prevent many surgically induced infections or the formation of biofilms in chronic wounds but also help to accelerate wound healing by favoring fibroblasts.

**Supplementary Materials:** The following are available online at <https://www.mdpi.com/article/10.3390/pharmaceutics13101647/s1>. Figure S1: Brightfield images after crystal violet staining of biofilm formation on polymer coatings. Figure S2: Fluorescent images after Live/Dead staining of *E. coli* and MRSA in the high-nutrition environment after 24 h of cultivation. Figure S3: Fluorescent images after Live/Dead staining of *E. coli* and MRSA in the high-nutrition environment after 48 h of cultivation. Figure S4: Fluorescent images after Live/Dead staining of *E. coli* and MRSA in the high-nutrition environment after 72 h of cultivation.

**Author Contributions:** Conceptualization, H.-P.D.; data curation, M.B. and O.R.; funding acquisition, H.-P.D.; investigation, M.B., O.R., T.K. and S.J.; methodology, M.B., O.R. and S.J.; project administration, S.R.; resources, M.S.S., M.E. and H.-P.D.; supervision, S.L., R.C. and H.-P.D.; visualization, M.B. and O.R.; writing—original draft, M.B., O.R. and H.-P.D.; writing—review and editing, M.B., O.R., S.R., M.S.S., S.J., M.E., S.L., R.C. and H.-P.D. All authors have read and agreed to the published version of the manuscript.

**Funding:** This research was funded by Europäischer Fonds für regionale Entwicklung (EFRE) in the program “Interreg VOberrhein” (Ref: 5115/3.17), by the project “CoHMed MS-Tox Test” (FKZ: 13FH5E01IA; BMBF), and the CoHMed-project “FunktioMed” (FKZ: 13FH5I02IA; BMBF).

**Data Availability Statement:** The data presented in this study is available in the supplementary material.

**Acknowledgments:** The authors thank Oliver Podlech, CleanControlling GmbH, for sharing the L-929 cell line and helpful advice regarding cell handling and biocompatibility tests according to ISO 10993-5, and Felix Blendinger for taking the SEM and AFM images. We are grateful to S. the R. for management of all the projects. The authors are grateful for funding of this work provided by the project “TriMaBone—Trinationale Forschungsinitiative: 3D-Druck Materialien für resorbierbare Knochen-implantate” (Europäischer Fonds für regionale Entwicklung—EFRE) in the program “Interreg VOberrhein” (Ref: 5115/3.17), by the project “CoHMed MS-Tox Test” (FKZ: 13FH5E01IA; BMBF) and the CoHMed-project “FunktioMed” (FKZ: 13FH5I02IA; BMBF). The article processing charge was funded by the Baden-Wuerttemberg Ministry of Science, Research, and Culture and the Furtwangen University in the funding program Open Access Publishing.

**Conflicts of Interest:** The authors declare no conflict of interest.

#### References

1. Darouiche, R.O. Device-Associated Infections: A Macroproblem That Starts with Microadherence. *Clin. Infect. Dis.* **2001**, *33*, 1567–1572. [CrossRef]
2. Zhang, A.; Mu, H.; Zhang, W.; Cui, G.; Zhu, J.; Duan, J. Chitosan Coupling Makes Microbial Biofilms Susceptible to Antibiotics. *Sci. Rep.* **2013**, *3*, 1–7. [CrossRef]
3. Olivares, E.; Badel-Berchoux, S.; Provot, C.; Prévost, G.; Bernardi, T.; Jehl, F. Clinical Impact of Antibiotics for the Treatment of *Pseudomonas aeruginosa* Biofilm Infections. *Front. Microbiol.* **2020**, *10*, 2894. [CrossRef]

4. Teerawattanapong, N.; Panich, P.; Kulpokin, D.; Na Ranong, S.; Kongpakwattana, K.; Saksinanon, A.; Goh, B.-H.; Lee, L.-H.; Apisarnthanarak, A.; Chaikyakunapruk, N. A Systematic Review of the Burden of Multidrug-Resistant Healthcare-Associated Infections among Intensive Care Unit Patients in Southeast Asia: The Rise of Multidrug-Resistant *Acinetobacter baumannii*. *Infect. Control Hosp. Epidemiol.* **2018**, *39*, 525–533. [[CrossRef](#)] [[PubMed](#)]
5. Gristina, A.G. Biomaterial-Centered Infection: Microbial Adhesion versus Tissue Integration. *Science* **1987**, *237*, 1588. [[CrossRef](#)]
6. Busscher, H.J.; van der Mei, H.C.; Subbiahdoss, G.; Jutte, P.C.; van den Dungen, J.J.A.M.; Zaat, S.A.J.; Schultz, M.J.; Grainger, D.W. Biomaterial-Associated Infection: Locating the Finish Line in the Race for the Surface. *Sci. Transl. Med.* **2012**, *4*, 153rv10. [[CrossRef](#)] [[PubMed](#)]
7. Poelstra, K.A.; Barezki, N.A.; Rediske, A.M.; Felts, A.G.; Slunt, J.B.; Grainger, D.W. Prophylactic Treatment of Gram-Positive and Gram-Negative Abdominal Implant Infections Using Locally Delivered Polyclonal Antibodies. *J. Biomed. Mater. Res.* **2002**, *60*, 206–215. [[CrossRef](#)] [[PubMed](#)]
8. Fux, C.A.; Costerton, J.W.; Stewart, P.S.; Stoodley, P. Survival Strategies of Infectious Biofilms. *Trends Microbiol.* **2005**, *13*, 34–40. [[CrossRef](#)] [[PubMed](#)]
9. Vuong, C.; Voyich, J.M.; Fischer, E.R.; Braughton, K.R.; Whitney, A.R.; DeLeo, F.R.; Otto, M. Polysaccharide Intercellular Adhesin (PIA) Protects *Staphylococcus epidermidis* against Major Components of the Human Innate Immune System. *Cell. Microbiol.* **2004**, *6*, 269–275. [[CrossRef](#)] [[PubMed](#)]
10. Attinger, C.; Wolcott, R. Clinically Addressing Biofilm in Chronic Wounds. *Adv. Wound Care* **2012**, *1*, 127–132. [[CrossRef](#)]
11. Costerton, J.W.; Stewart, P.S.; Greenberg, E.P. Bacterial Biofilms: A common Cause of Persistent Infections. *Science* **1999**, *284*, 1318. [[CrossRef](#)]
12. Zimmerli, W.; Widmer, A.F.; Blatter, M.; Frei, R.; Ochsner, P.E. Role of Rifampin for Treatment of Orthopedic Implant-Related Staphylococcal Infections: A Randomized Controlled Trial. *J. Am. Med. Assoc.* **1998**, *279*, 1537–1541. [[CrossRef](#)] [[PubMed](#)]
13. Schmidmaier, G.; Lucke, M.; Wildemann, B.; Haas, N.P.; Raschke, M. Prophylaxis and Treatment of Implant-Related Infections by Antibiotic-Coated Implants: A Review. *Injury* **2006**, *37*, 105–112. [[CrossRef](#)]
14. Ghafouri, H.B.; Bagheri-Behzad, B.; Yasinzadeh, M.R.; Modirian, E.; Divsalar, D.; Farahmand, S. Prophylactic Antibiotic Therapy in Contaminated Traumatic Wounds: Two Days versus Five Days Treatment. *BiolImpacts* **2012**, *2*, 33–37. [[CrossRef](#)] [[PubMed](#)]
15. De Kraker, M.E.A.; Stewardson, A.J.; Harbarth, S. Will 10 Million People Die a Year due to Antimicrobial Resistance by 2050? *PLoS Med.* **2016**, *13*, e1002184. [[CrossRef](#)] [[PubMed](#)]
16. Nations, U.; Assembly, G.; York, N.; Humphreys, G.; Fleck, F. United Nations Meeting on Antimicrobial Resistance. *Bull. World Health Organ.* **2016**, *94*, 638–639.
17. Kargupta, R.; Bok, S.; Darr, C.M.; Crist, B.D.; Gangopadhyay, K.; Gangopadhyay, S.; Sengupta, S. Coatings and Surface Modifications Imparting Antimicrobial Activity to Orthopedic Implants. *Wiley Interdiscip. Rev. Nanomed. Nanobiotechnology* **2014**, *6*, 475–495. [[CrossRef](#)]
18. Brooks, B.D.; Brooks, A.E. Therapeutic Strategies to Combat Antibiotic Resistance. *Adv. Drug Deliv. Rev.* **2014**, *78*, 14–27. [[CrossRef](#)]
19. Hebeish, A.; El-Rafie, M.H.; EL-Sheikh, M.A.; Seleem, A.A.; El-Naggar, M.E. Antimicrobial Wound Dressing and Anti-Inflammatory Efficacy of Silver Nanoparticles. *Int. J. Biol. Macromol.* **2014**, *65*, 509–515. [[CrossRef](#)] [[PubMed](#)]
20. Murata, H.; Koepsel, R.R.; Matyjaszewski, K.; Russell, A.J. Permanent, Non-Leaching Antibacterial Surfaces-2: How High Density Cationic Surfaces Kill Bacterial Cells. *Biomaterials* **2007**, *28*, 4870–4879. [[CrossRef](#)]
21. Tiller, J.C.; Liao, C.-J.; Lewis, K.; Klibanov, A.M. Designing Surfaces That Kill Bacteria on Contact. *Proc. Natl. Acad. Sci. USA* **2001**, *98*, 5981–5985. [[CrossRef](#)]
22. Samal, S.K.; Dash, M.; Van Vlierberghe, S.; Kaplan, D.L.; Chiellini, E.; van Blitterswijk, C.; Moroni, L.; Dubruel, P. Cationic Polymers and Their Therapeutic Potential. *Chem. Soc. Rev.* **2012**, *41*, 7147. [[CrossRef](#)]
23. Huang, J.; Murata, H.; Koepsel, R.R.; Russell, A.J.; Matyjaszewski, K. Antibacterial Polypropylene via Surface-Initiated Atom Transfer Radical Polymerization. *Biomacromolecules* **2007**, *8*, 1396–1399. [[CrossRef](#)]
24. Lee, S.B.; Koepsel, R.R.; Morley, S.W.; Matyjaszewski, K.; Sun, Y.; Russell, A.J. Permanent, Nonleaching Antibacterial Surfaces, 1. Synthesis by Atom Transfer Radical Polymerization. *Biomacromolecules* **2004**, *5*, 877–882. [[CrossRef](#)] [[PubMed](#)]
25. Madkour, A.E.; Dabkowski, J.M.; Nüsslein, K.; Tew, G.N. Fast Disinfecting Antimicrobial Surfaces. *Langmuir* **2009**, *25*, 1060–1067. [[CrossRef](#)] [[PubMed](#)]
26. Yang, L.; Weiss, T.M.; Lehrer, R.I.; Huang, H.W. Crystallization of Antimicrobial Pores in Membranes: Magainin and Protegrin. *Biophys. J.* **2000**, *79*, 2002–2009. [[CrossRef](#)]
27. Shai, Y. Mechanism of the Binding, Insertion and Destabilization of Phospholipid Bilayer Membranes by  $\alpha$ -Helical Antimicrobial and Cell Non-Selective Membrane-Lytic Peptides. *Biochim. Biophys. Acta-Biomembr.* **1999**, *1462*, 55–70. [[CrossRef](#)]
28. Matsuzaki, K. Why and How are Peptide-Lipid Interactions Utilized for Self-Defense? Magainins and Tachyplesins as Archetypes. *Biochim. Biophys. Acta-Biomembr.* **1999**, *1462*, 1–10. [[CrossRef](#)]
29. Milović, N.M.; Wang, J.; Lewis, K.; Klibanov, A.M. Immobilized N-Alkylated Polyethylenimine Avidly Kills Bacteria by Rupturing Cell Membranes with No Resistance Developed. *Biotechnol. Bioeng.* **2005**, *90*, 715–722. [[CrossRef](#)]
30. Lin, J.; Tiller, J.C.; Lee, S.B.; Lewis, K.; Klibanov, A.M. Insights into Bactericidal Action of Surface-Attached Poly(Vinyl-N-Hexylpyridinium) Chains. *Biotechnol. Lett.* **2002**, *24*, 801–805. [[CrossRef](#)]

31. Lin, J.; Murthy, S.K.; Olsen, B.D.; Gleason, K.K.; Klibanov, A.M. Making Thin Polymeric Materials, Including Fabrics, Microbicidal and Also Water-Repellent. *Biotechnol. Lett.* **2003**, *25*, 1661–1665. [[CrossRef](#)] [[PubMed](#)]
32. Ikeda, T.; Hirayama, H.; Yamaguchi, H.; Tazuke, S.; Watanabe, M. Polycationic Biocides with Pendant Active Groups: Molecular Weight Dependence of Antibacterial Activity. *Antimicrob. Agents Chemother.* **1986**, *30*, 132–136. [[CrossRef](#)]
33. Ikeda, T.; Yamaguchi, H.; Tazuke, S. New Polymeric Biocides: Synthesis and Antibacterial Activities of Polycations with Pendant Biguanide Groups. *Antimicrob. Agents Chemother.* **1984**, *26*, 139–144. [[CrossRef](#)] [[PubMed](#)]
34. Isquith, A.J.; Abbott, E.A.; Walters, P.A. Surface-Bonded Antimicrobial Activity of an Organosilicon Quaternary Ammonium Chloride. *Appl. Microbiol.* **1972**, *24*, 859–863. [[CrossRef](#)]
35. Luz, G.M.; Boesel, L.; Campo, A.D.; Mano, J.F. Micropatterning of Bioactive Glass Nanoparticles on Chitosan Membranes for Spatial Controlled Biomaterialization. *Langmuir* **2012**, *28*, 6970–6977. [[CrossRef](#)] [[PubMed](#)]
36. Wang, Y.; Shi, R.; Gong, P.; Li, J.; Li, J.; Ao, D.; Wang, P.; Yang, Y.; Man, Y.; Qu, Y. Bioelectric Effect of a Chitosan Bioelectret Membrane on Bone Regeneration in Rabbit Cranial Defects. *J. Bioact. Compat. Polym.* **2012**, *27*, 122–132. [[CrossRef](#)]
37. Kim, I.-Y.; Seo, S.-J.; Moon, H.-S.; Yoo, M.-K.; Park, I.-Y.; Kim, B.-C.; Cho, C.-S. Chitosan and its Derivatives for Tissue Engineering Applications. *Biotechnol. Adv.* **2008**, *26*, 1–21. [[CrossRef](#)]
38. Sivashankari, P.R.; Prabakaran, M. Prospects of Chitosan-Based Scaffolds for Growth Factor Release in Tissue Engineering. *Int. J. Biol. Macromol.* **2016**, *93*, 1382–1389. [[CrossRef](#)]
39. Liu, Z.; Wang, H.; Wang, Y.; Lin, Q.; Yao, A.; Cao, F.; Li, D.; Zhou, J.; Duan, C.; Du, Z.; et al. The Influence of Chitosan Hydrogel on Stem Cell Engraftment, Survival and Homing in the Ischemic Myocardial Microenvironment. *Biomaterials* **2012**, *33*, 3093–3106. [[CrossRef](#)]
40. Shi, W.; Nie, D.; Jin, G.; Chen, W.; Xia, L.; Wu, X.; Su, X.; Xu, X.; Ni, L.; Zhang, X.; et al. BDNF Blended Chitosan Scaffolds for Human Umbilical Cord MSC Transplants in Traumatic Brain Injury Therapy. *Biomaterials* **2012**, *33*, 3119–3126. [[CrossRef](#)]
41. Jayakumar, R.; Prabakaran, M.; Sudheesh Kumar, P.T.; Nair, S.V.; Tamura, H. Biomaterials Based on Chitin and Chitosan in Wound Dressing Applications. *Biotechnol. Adv.* **2011**, *29*, 322–337. [[CrossRef](#)]
42. Jayakumar, R.; Prabakaran, M.; Nair, S.V.; Tokura, S.; Tamura, H.; Selvamurugan, N. Novel Carboxymethyl Derivatives of Chitin and Chitosan Materials and Their Biomedical Applications. *Prog. Mater. Sci.* **2010**, *55*, 675–709. [[CrossRef](#)]
43. Helander, I.M.; Nurmiaho-Lassila, E.L.; Ahvenainen, R.; Rhoades, J.; Roller, S. Chitosan Disrupts the Barrier Properties of the Outer Membrane of Gram-Negative Bacteria. *Int. J. Food Microbiol.* **2001**, *71*, 235–244. [[CrossRef](#)]
44. Je, J.Y.; Kim, S.K. Chitosan Derivatives Killed Bacteria by Disrupting the Outer and Inner Membrane. *J. Agric. Food Chem.* **2006**, *54*, 6629–6633. [[CrossRef](#)] [[PubMed](#)]
45. Divya, K.; Vijayan, S.; George, T.K.; Jisha, M.S. Antimicrobial Properties of Chitosan Nanoparticles: Mode of Action and Factors Affecting Activity. *Fibers Polym.* **2017**, *18*, 221–230. [[CrossRef](#)]
46. Izano, E.A.; Sadovskaya, I.; Vinogradov, E.; Mulks, M.H.; Velliyagounder, K.; Ragunath, C.; Kher, W.B.; Ramasubbu, N.; Jabbouri, S.; Perry, M.B.; et al. Poly-N-Acetylglucosamine Mediates Biofilm Formation and Antibiotic Resistance in *Actinobacillus pleuropneumoniae*. *Microb. Pathog.* **2007**, *43*, 1–9. [[CrossRef](#)] [[PubMed](#)]
47. Sicard, J.F.; Vogeleer, P.; Le Bihan, G.; Rodriguez Olivera, Y.; Beaudry, F.; Jacques, M.; Harel, J. N-Acetyl-Glucosamine Influences the Biofilm Formation of *Escherichia coli*. *Gut Pathog.* **2018**, *10*, 26. [[CrossRef](#)] [[PubMed](#)]
48. Blagodatskikh, I.V.; Kulikov, S.N.; Vyshivannaya, O.V.; Bezrodnykh, E.A.; Yamskov, I.A.; Tikhonov, V.E. Influence of Glucosamine on Oligochitosan Solubility and Antibacterial Activity. *Carbohydr. Res.* **2013**, *381*, 28–32. [[CrossRef](#)]
49. Dheer, D.; Singh, V.; Shankar, R. Medicinal Attributes of 1,2,3-Triazoles: Current Developments. *Bioorg. Chem.* **2017**, *71*, 30–54. [[CrossRef](#)]
50. Kolb, H.C.; Finn, M.G.; Sharpless, K.B. Click Chemistry: Diverse Chemical Function from a Few Good Reactions. *Angew. Chemie Int. Ed.* **2001**, *40*, 2004–2021. [[CrossRef](#)]
51. Kolb, H.C.; Sharpless, K.B. The Growing Impact of Click Chemistry on Drug Discovery. *Drug Discov. Today* **2003**, *8*, 1128–1137. [[CrossRef](#)]
52. Wang, L.; Chen, J.; Shi, L.; Shi, Z.; Ren, L.; Wang, Y. The Promotion of Antimicrobial Activity on Silicon Substrates Using a “click” Immobilized Short Peptide. *Chem. Commun.* **2014**, *50*, 975–977. [[CrossRef](#)] [[PubMed](#)]
53. Głowacka, I.E.; Grzonkowski, P.; Lisiecki, P.; Kalinowski, L.; Piotrowska, D.G. Synthesis and Antimicrobial Activity of Novel 1,2,3-Triazole-Conjugates of Quinazolin-4-Ones. *Arch. Pharm.* **2019**, *352*, 1800302. [[CrossRef](#)] [[PubMed](#)]
54. Petrova, K.T.; Potewar, T.M.; Correia-Da-Silva, P.; Barros, M.T.; Calhelha, R.C.; Ćiric, A.; Soković, M.; Ferreira, I.C.F.R. Antimicrobial and Cytotoxic Activities of 1,2,3-Triazole-Sucrose Derivatives. *Carbohydr. Res.* **2015**, *417*, 66–71. [[CrossRef](#)] [[PubMed](#)]
55. Holla, B.S.; Mahalinga, M.; Karthikeyan, M.S.; Poojary, B.; Akberali, P.M.; Kumari, N.S. Synthesis, Characterization and Antimicrobial Activity of Some Substituted 1,2,3-Triazoles. *Eur. J. Med. Chem.* **2005**, *40*, 1173–1178. [[CrossRef](#)]
56. Abdel-Wahab, F.B.; Mohamed, H.A.; Awad, E.A.G. Synthesis and Biological Activity of Some New 1,2,3-Triazole Hydrazone Derivatives. *Eur. Chem. Bull.* **2015**, *4*, 106–109. [[CrossRef](#)]
57. Pandiyarajan, C.K.; Prucker, O.; Zieger, B.; Rühle, J. Influence of the Molecular Structure of Surface-Attached Poly(N-alkyl Acrylamide) Coatings on the Interaction of Surfaces with Proteins, Cells and Blood Platelets. *Macromol. Biosci.* **2013**, *13*, 873–884. [[CrossRef](#)]
58. Prucker, O.; Brandstetter, T.; Rühle, J. Surface-Attached Hydrogel Coatings via C,H-Insertion Crosslinking for Biomedical and Bioanalytical Applications (Review). *Biointerphases* **2018**, *13*, 010801. [[CrossRef](#)]

59. Mahou, R.; Wandrey, C. Versatile Route to Synthesize Heterobifunctional Poly(Ethylene Glycol) of Variable Functionality for Subsequent Pegylation. *Polymers* **2012**, *4*, 561–589. [[CrossRef](#)]
60. Öztürk, T.; Meyvacı, E.; Arslan, T. Synthesis and Characterization of Poly(Vinyl Chloride-g-ε-Caprolactone) Brush Type Graft Copolymers by Ring-Opening Polymerization and “Click” Chemistry. *J. Macromol. Sci. Part. A* **2020**, *57*, 171–180. [[CrossRef](#)]
61. Sumerlin, B.S.; Tsarevsky, N.V.; Louche, G.; Lee, R.Y.; Matyjaszewski, K. Highly Efficient “Click” Functionalization of Poly(3-azidopropyl methacrylate) Prepared by ATRP. *Macromolecules* **2005**, *38*, 7540–7545. [[CrossRef](#)]
62. Schmidt, M.S.; Leitner, K.; Welter, M.; Wurmthaler, L.A.; Ringwald, M. Carbohydrate-Based Cu(I) Stabilizing Ligands and Their Use in the Synthesis of Carbohydrate–Ferrocene Conjugates. *Carbohydr. Res.* **2014**, *387*, 42–45. [[CrossRef](#)] [[PubMed](#)]
63. Waldvogel, S.R. Zemplén Deacetylation. In *Comprehensive Organic Name Reactions and Reagents*; John Wiley & Sons, Inc.: Hoboken, NJ, USA, 2010; Volume 2010, p. 892.
64. 87: Biological Reactivity Tests, in Vitro. In *The United States Pharmacopeia-The National Formulary*; Pharmacopeial Convention, Inc.: Rockville, MD, USA, 1979; Volume 35, pp. 92–94.
65. Japan Food Research Laboratories. *Measurement of Antibacterial Activity on Plastics and Other Non-Porous Surfaces*; ISO: London, UK, 2011; pp. 1–24.
66. Masuko, T.; Minami, A.; Iwasaki, N.; Majima, T.; Nishimura, S.I.; Lee, Y.C. Carbohydrate Analysis by a Phenol-Sulfuric Acid Method in Microplate Format. *Anal. Biochem.* **2005**, *339*, 69–72. [[CrossRef](#)] [[PubMed](#)]
67. Kowalski, W. *Ultraviolet Germicidal Irradiation Handbook*; Springer: Berlin/Heidelberg, Germany, 2009; ISBN 9783642019982.
68. Cutler, T.D.; Zimmerman, J.J. Ultraviolet Irradiation and the Mechanisms Underlying its Inactivation of Infectious Agents. *Anim. Health Res. Rev.* **2011**, *12*, 15–23. [[CrossRef](#)]
69. Bak, J.; Begovic, T. A Prototype Catheter Designed for Ultraviolet C Disinfection. *J. Hosp. Infect.* **2013**, *84*, 173–177. [[CrossRef](#)]
70. Yang, J.-H.; Wu, U.-I.; Tai, H.-M.; Sheng, W.-H. Effectiveness of an Ultraviolet-C Disinfection System for Reduction of Healthcare-Associated Pathogens. *J. Microbiol. Immunol. Infect.* **2019**, *52*, 487–493. [[CrossRef](#)] [[PubMed](#)]
71. Gora, S.L.; Rauch, K.D.; Ontiveros, C.C.; Stoddart, A.K.; Gagnon, G.A. Inactivation of Biofilm-Bound *Pseudomonas Aeruginosa* Bacteria Using UVC Light Emitting Diodes (UVC LEDs). *Water Res.* **2019**, *151*, 193–202. [[CrossRef](#)]
72. Tseng, C.-C.; Li, C.-S. Inactivation of Viruses on Surfaces by Ultraviolet Germicidal Irradiation. *J. Occup. Environ. Hyg.* **2007**, *4*, 400–405. [[CrossRef](#)]
73. Donlan, R.M. Biofilms and Device-Associated Infections. In *Proceedings of the Emerging Infectious Diseases*; Centers for Disease Control and Prevention (CDC): Atlanta, GA, USA, 2001; Volume 7, pp. 277–281.
74. Liu, X.F.; Guan, Y.L.; Yang, D.Z.; Li, Z.; Yao, K. De Antibacterial Action of Chitosan and Carboxymethylated Chitosan. *J. Appl. Polym. Sci.* **2001**, *79*, 1324–1335. [[CrossRef](#)]
75. LI, M.; CHEN, C.; XIA, X.; GARBA, B.; SHANG, L.; WANG, Y. Proteomic Analysis of the Inhibitory Effect of Chitosan on *Penicillium expansum*. *Food Sci. Technol.* **2020**, *40*, 250–257. [[CrossRef](#)]
76. Khan, F.; Pham, D.T.N.; Oloketuyi, S.F.; Manivasagan, P.; Oh, J.; Kim, Y.-M. Chitosan and Their Derivatives: Antibiofilm Drugs against Pathogenic Bacteria. *Colloids Surf. B Biointerfaces* **2020**, *185*, 110627. [[CrossRef](#)] [[PubMed](#)]
77. Tantala, J.; Thumanu, K.; Rachtanapun, C. An Assessment of Antibacterial Mode of Action of Chitosan on *Listeria innocua* Cells Using Real-Time HATR-FTIR Spectroscopy. *Int. J. Biol. Macromol.* **2019**, *135*, 386–393. [[CrossRef](#)] [[PubMed](#)]
78. Andres, Y.; Giraud, L.; Gerente, C.; Le Cloirec, P. Antibacterial Effects of Chitosan Powder: Mechanisms of Action. *Environ. Technol.* **2007**, *28*, 1357–1363. [[CrossRef](#)] [[PubMed](#)]
79. Liu, H.; Du, Y.; Wang, X.; Sun, L. Chitosan Kills Bacteria through Cell Membrane Damage. *Int. J. Food Microbiol.* **2004**, *95*, 147–155. [[CrossRef](#)] [[PubMed](#)]
80. ISO. *Biological Evaluation of Medical Devices-Part. 5: Tests for In Vitro Cytotoxicity*; ISO: London, UK, 2009.

### **3.2.2 Synthesis of a biocompatible benzophenone-substituted chitosan hydrogel as novel coating for PEEK with extraordinary strong antibacterial and anti-biofilm properties**

#### **Own contribution to the article**

The authors' contribution to this publication was as follows. The conceptualization of the study was carried out by Prof. Deigner and Dr. Borgolte. The synthesis of the chitosan derivatives, UV/vis spectra, NMR characterization, coating formation, FT-IR spectra and biocompatibility studies were performed by Dr. Borgolte. Ms. Quint assisted in analysis of the interleukine gene expression using qPCR. Scanning electron microscope (SEM) and atomic force microscope (AFM) images were prepared and acquired by Dr. Blendinger. Prof. Scotti performed and visualized the X-ray photoelectron spectroscopy (XPS). Microbiological tests, including the antibacterial effect of the coating and monomers, biofilm formation and live/dead staining were performed and visualized by the author of this thesis. Prof. Deigner was responsible for the acquisition of funding and project administration. The supervision of the study was carried out by Prof. Csuk, Prof. Bucher, Prof. Laufer and Prof. Deigner. Writing of the original draft with visualizations was carried out by Dr. Borgolte and the author of this thesis. All authors reviewed, edited and approved the manuscript.

Reprinted with permission from the Authors. Copyright © 2022 The Author(s). Published by Elsevier Ltd. This article is an open access article distributed under a Creative Commons Attribution 4.0 International License (<http://creativecommons.org/licenses/by/4.0/>).

**Borgolte, M.; Riestler, O.; Quint, I.; Blendinger, F.; Bucher, V.; Laufer, S.; Csuk, R.; Scotti, L.; Deigner, H. P. Synthesis of a Biocompatible Benzophenone-Substituted Chitosan Hydrogel as Novel Coating for PEEK with Extraordinary Strong Antibacterial and Anti-Biofilm Properties. *Materials Today Chemistry* 2022, 26, 101176. <https://doi.org/10.1016/j.mtchem.2022.101176>.**



Contents lists available at ScienceDirect

Materials Today Chemistry

journal homepage: [www.journals.elsevier.com/materials-today-chemistry/](http://www.journals.elsevier.com/materials-today-chemistry/)

## Synthesis of a biocompatible benzophenone-substituted chitosan hydrogel as novel coating for PEEK with extraordinary strong antibacterial and anti-biofilm properties



M. Borgolte<sup>a, b</sup>, O. Riester<sup>a, c</sup>, I. Quint<sup>a, c</sup>, F. Blendinger<sup>d, e</sup>, V. Bucher<sup>d</sup>, S. Laufer<sup>c, f</sup>, R. Csuk<sup>b</sup>, L. Scotti<sup>g</sup>, H.-P. Deigner<sup>a, h, i, \*</sup>

<sup>a</sup> Institute of Precision Medicine, Furtwangen University, Jakob-Kienzle Str. 17, 78054 Villingen-Schwenningen, Germany

<sup>b</sup> Martin-Luther University Halle-Wittenberg, Organic Chemistry, Kurt-Mothes-Str. 2, 06120, Halle, Saale, Germany

<sup>c</sup> Institute of Pharmaceutical Sciences, Department of Pharmacy and Biochemistry, Eberhard-Karls-University Tuebingen, Auf der Morgenstelle 8, Tuebingen, 72076, Germany

<sup>d</sup> Institute for Microsystems Technology (iMST), Furtwangen University, Neckartal 142, Rottweil, 78628, Germany

<sup>e</sup> Institute for Applied Physics, Eberhard Karls University Tuebingen, Auf der Morgenstelle 8, Tuebingen, 72076, Germany

<sup>f</sup> Tuebingen Center for Academic Drug Discovery & Development (TüCAD2), Tuebingen, 72076, Germany

<sup>g</sup> Department of Medical, Oral and Biotechnological Sciences, University "G. D'Annunzio" of Chieti-Pescara, Via Dei Vestini, 66100, Chieti, Italy

<sup>h</sup> Faculty of Science, Eberhard Karls University Tuebingen, Auf der Morgenstelle 8, Tuebingen, 72076, Germany

<sup>i</sup> EXIM Department, Fraunhofer Institute IZI (Leipzig), Schillingallee 68, 18057, Rostock, Germany

### ARTICLE INFO

#### Article history:

Received 17 May 2022  
Received in revised form  
10 August 2022  
Accepted 28 August 2022  
Available online xxx

#### Keywords:

Chitosan  
UV-Crosslinker  
Antimicrobial coating  
Anti-biofilm coating  
Biocompatible

### ABSTRACT

Chitosan derivatives substituted with benzophenone groups that can be cross-linked by ultraviolet light were synthesized as coatings for PEEK substrates used in the construction of lumbar cages. The IC<sub>90</sub> values of the benzophenone-modified chitosan polymers in solution before crosslinking were in the same range as those reported for native chitosan. The resulting hydrogel surface after crosslinking exhibited excellent antimicrobial properties and was highly effective (up to 5 log-fold) against clinically relevant strains of methicillin-resistant *S. aureus* and *E. coli*. As a result, the coated surface also significantly reduced biofilm formation. The coatings show good biocompatibility with numerous cell lines as well as low levels of cytotoxicity (ISO 10993–5) and pyrogenicity (ISO 10993–11). The coatings also exhibited strong antioxidant properties toward formed hydroxyl radicals in an in-vitro Fenton reaction. Overall, substitution of chitosan with benzophenone residues is an interesting and important approach to the functionalization of materials used for medical implants that are prone to microbial contamination and mechanical failure. Biocompatible antimicrobial coatings might also be employed in photopatterning methods used in the design of medical devices.

© 2022 The Author(s). Published by Elsevier Ltd. This is an open access article under the CC BY license (<http://creativecommons.org/licenses/by/4.0/>).

### 1. Introduction

Chitosan is the deacetylated derivative of chitin that exhibits antimicrobial properties due to the positive charge of the amino groups of its constituent glucosamines. Due to this cationic properties, chitosan is able to disrupt the outer and inner bacterial cell membrane [1–4], via interactions of its polycationic properties with the negatively charged phosphocholine groups of the bacterial cell wall as suggested by the Shai-Matsuzaki-Huang (SMH) model

of the behavior of cationic antimicrobial peptides in solution, leading to the antimicrobial properties of chitosan as well [5,6]. This is backed by a publication from Li et al., 2010, who investigated *E. coli* after chitosan treatment under an electron microscope, finding partly cell lysis and dissolved cell membranes of *E. coli* [7]. Another publication, analyzing an experimental chitosan coating, showed cell lysis and cytosol leakage of *S. epidermis* on the substrate [8]. As second potential mechanism, chitosan has been proposed to bind DNA inside the bacterial cytosol, inhibiting mRNA synthesis and therefore, inhibiting microbial growth and biofilm formation. This ability also follows the electrostatic interaction model, proposed by the SMH model, but refers to shorter chained chitosan molecules, which are able to penetrate the cell wall. A

\* Corresponding author.

E-mail address: [dei@hs-furtwangen.de](mailto:dei@hs-furtwangen.de) (H.-P. Deigner).

study on *E. coli* using fluorescein-modified chitosan, analyzed with a confocal laser microscope, shows an accumulation of chitosan inside the bacteria [9]. A third proposed mechanism of chitosan is based on its metal chelating ability [10]. Through this chelating ability free  $\text{Ca}^{2+}$  and  $\text{Mg}^{2+}$  cations, present in the bacterial cell wall, are bound, leading to decreased enzyme activity in the cell wall and, therefore, inhibition and disruption of bacterial growth [1,11–14]. In all cases, the bacteria are disturbed in their metabolism upon contact with the coated chitosan surface and, therefore, ultimately killed and unable to biofilm formation.

Due to these unique antimicrobial properties, several publications describe the use of chitosan for its antimicrobial properties in medicine-related applications. For example, thiolated mucoadhesive chitosan fibers prevent the growth of bacteria that cause dental caries while exhibiting no cytotoxicity against relevant cell lines [15]. Similarly, chitosan limits the formation of biofilms of *Actinobacillus pleuromoniae* [16]. Findings reported in another recent publication revealed that the introduction of chitosan *N*-halamine conjugates in hemostatic wound dressings resulted in a one million-fold reduction in the extent of microbial contamination [17]. Other applications for chitosan that have been widely described in the literature include bone tissue engineering [18–20], stem cell encapsulation [21–23], and wound dressings [24,25]. Unmodified chitosan has only limited solubility in both aqueous and organic solvents and exhibits comparatively poor mechanical properties and heat resistance. Thus, the use of chitosan as an antimicrobial coating for medical implants remains limited. However, the aforementioned studies revealed that chitosan may serve as an attractive substrate for specific functionalization designed to improve its properties and use on implant surfaces prone to microbial infection.

Benzophenone is a UV-responsive crosslinker, described in several publications over the last 30 years regarding photopatterning, including the generation of surface-anchored benzophenone hydrogels that promote cell adhesion [26–28] and micropatterning for analytical purposes [28–31] as well as for the design of antimicrobial and anti-adhesive surfaces [26,32–35]. We recently published a description of the synthesis of a benzophenone-acrylamide hydrogel in which *N*-acetyl glucosamine units were connected by various oligoethylene glycol chains. This hydrogel was used successfully to prevent microbial growth and biofilm formation when used as a coating for polyethylene terephthalate glycol (PETG) coverslips [36]. The mechanism of the underlying crosslinking reaction has been extensively reviewed [37–40]. Briefly, by activation through photons, benzophenone forms a highly reactive triplet radical via  $n\text{-}\pi^*$  or  $\pi\text{-}\pi^*$  transition, while the exact orbital transition depends on the wavelength [41]. This transition of a nonbonding  $n$  orbital of the oxygen into the  $\pi^*$ -LUMO of the carbonyl group leads to a biradicaloid state of the benzophenone. The then formed electrophilic ketyl radical can abstract a hydrogen atom from a nearby substrate or polymer chain, leading to two alkyl radicals, undergoing recombination, and therefore, crosslinking [42]. The kinetics of such C–H crosslinking reactions, leading to surface-anchored polymer networks and their surface-bond gelling kinetics, have also been described by R  he et al. 2016, showing unique, non-linear kinetics of the crosslinking reaction inside the coating hydrogel network [43].

Functionalization of glycosidic polymers with benzophenone has been described primarily for the design of UV-protective scaffolds. For example, Heo et al. [44] described the modification of pullulan with benzophenone that exhibited UV-absorption properties while maintaining good biocompatibility, thereby suggesting its use in the formulations of sunscreens [38]. Similarly, Morimoto et al. [38] described the synthesis of UV-absorbing phenolic chitosan derivatives with formaldehyde in a Mannich reaction [37]. Likewise, Hong et al. [45] described the antimicrobial activity of benzophenone-modified

cotton; in this case, benzophenone functioned as an antimicrobial agent after UV irradiation and radical activation [45].

Polyether ether ketone (PEEK) is a high-performance thermoplastic, showing similar mechanical properties like the Ti6Al4V titanium alloy which is commonly used in medical applications [46] and displaying properties similar to human bone [47]. It is not cytotoxic, nor does it degrade or leach ions into the surrounding tissue [48]. Given these properties, it has been used for manufacturing of a variety of medical implants, for example, spinal cages [49–52], endoprotheses for hip replacement [53–55], or implants for cranial reconstructions [56,57] which can also be manufactured in a 3D printing process [58–61]. Given its otherwise bioinert surface, tissue integration and osseointegration of PEEK is still an issue of concern, leading to the need of proper surface functionalization of PEEK implants [62]. Therefore, multiple approaches for surface functionalization have been described, for example, deposition of inorganic substrates via atomic layer deposition (ALD) [63]. Newer works aim at further improving the mechanical properties of PEEK, for example by blending with other polymers and incorporation of carbon fibers [64] or calcium hydroxyapatite together with graphene [65]. A newer approach focuses on polydopamine coating on PEEK, able to complex  $\text{Ca}^{2+}$  ions in order to improve biocompatibility and bone mineralisation on the PEEK surface [66]. Since the PEEK consists of a diphenyl ketone group, similar to those present in benzophenone, this functional group is able to undergo the same radical generation mechanism via the  $n\text{-}\pi^*$  transition induced by UV light as used with benzophenone, [67]. Further, it been employed as radical starter for grafting-on approaches of polymer brushes using free radical polymerization [68,69] and ATRP [70,71], to mention a few examples.

While the antimicrobial properties of benzophenone-modified polysaccharides have been studied extensively, to the best of our best knowledge, there are no publications that describe benzophenone-mediated, covalent surface anchoring of chitosan to polymeric surfaces, especially PEEK, in order to exhibit its antimicrobial action on a real-world material used for medical implants and devices. In this study, we describe the successful synthesis of benzophenone-modified chitosan derivatives with varying degrees of substitution. We herein report the successful surface functionalization of PEEK with these chitosan derivatives including chemical and physical surface characterization. We also examine their antimicrobial activities, their biocompatibility according to ISO 10993–5, and their pyrogenicity as well as potentially anti-inflammatory properties.

## 2. Experimental

### 2.1. Synthesis of chitosan derivatives

Chitosan (molecular weight 100,000–300,000 g/mol, Sigma Aldrich, Germany) was dissolved in 1% (v/v)  $\text{CH}_3\text{COOH}$  in ddH<sub>2</sub>O. A mixture of 4-benzoyl-benzoic acid in tetrahydrofuran (THF, 100 mg/mL) was added, followed by 1-ethyl-3-(3-dimethylaminopropyl)carbodiimide (EDC, 1 eq) was added and the mixture was then stirred at room temperature for 60 h. Derivatized chitosan was precipitated in 5-fold excess of acetone, the precipitate filtered, and re-precipitated two more times. The resulting material was dissolved in 100 mL ddH<sub>2</sub>O and dialyzed 5 times against an excess of 1 mM hydrochloric acid. After lyophilization, the benzophenone-substituted chitosan derivatives were obtained as a white powder.

### 2.2. UV/vis and nuclear magnetic resonance (NMR) measurements

Benzophenone-substituted chitosan derivatives were dissolved to 5 mg/mL in 1 mM HCl. The UV/vis absorbance (220–600 nm) of

various dilutions was measured in a Perkin Elmer Lambda XLS + photometer. Absorption at 263 nm was used to determine the degree of functionalization, which was calculated from a standard curve of 4-benzoyl-benzoic acid dissolved in ethanol, cf. Fig. S1 in Supplementary Material. Degree of substitution is given as the ratio between determined benzophenone concentration in the measured solutions and total polymer amount. NMR measurements were performed in 1 mM deuterium chloride (DCI) in D<sub>2</sub>O in a Varian Unity 500 NMR spectrometer. Chemical shifts are reported in parts per million relative to the solvent signal (D<sub>2</sub>O). Signals were assigned by first-order analysis.

### 2.3. Coating formation

To generate polyether ether ketone (PEEK) sample coatings, a rod of PEEK polymer (2 m length, 25 mm diameter, Schmidt + Bartl GmbH, Villingen-Schwenningen, Germany) was cut into 2 mm chips using a lathe; the cut edges were deburred, and a smooth surface was obtained by grinding with a lathe. The PEEK chips were washed extensively with acetone, ethyl acetate, ethanol and water in an ultrasonic bath. After drying of the chips, a 100 µL sterile-filtered solution of the benzophenone-chitosan derivatives dissolved in 1 mM HCl to a concentration of 10 mg/mL was added to cover the entire surface of the PEEK chip. The PEEK chip immersed in solution was permitted to dry overnight in a sterile cabinet to prevent dust contamination and then subjected to crosslinking with UV-light (254 nm, 3 J/cm<sup>2</sup>) using a UV-crosslinker (Analytikjena UVP Crosslinker 254 nm). After washing 2 times with excess 1 mM HCl and ddH<sub>2</sub>O, the chips were vacuum-dried for 16 h and then used directly in the following experiments.

For cell culture dishes, a sterile-filtered solution of the benzophenone-chitosan derivatives in 1 mM HCl (10 mg/mL for 625 µg/cm<sup>2</sup>, 5 mg/mL for 312 µg/cm<sup>2</sup>, and 1 mg/mL for 62.5 µg/cm<sup>2</sup>) was added at 20 µL per well for 96-well plates or 60 µL per well for 24-well plates. The plate was permitted to dry overnight under a sterile cabinet to prevent contamination and when then subjected to crosslinking with UV light (254 nm, 3 J/cm<sup>2</sup>) as described above. The plates were washed two times with 1 mM HCl and once with ddH<sub>2</sub>O (200 µL per well for 96-well plates or 1 mL per well for 24-well plates). The plates were then dried to generate the final coatings that were evaluated in cell culture and microbiology experiments.

### 2.4. Physicochemical surface characterization

Infrared (IR) spectra of the coated PEEK chips were obtained using a PerkinElmer Spotlight 200 FT-IR microscope that was attached to a PerkinElmer Frontier FT-IR spectrometer unit. A blank PEEK chip was used as background. Difference spectra between coated and uncoated PEEK chips were recorded to eliminate interference from PEEK signals. Microscopic images were collected using the FT-IR microscope in illumination mode and are shown without any further processing. Scanning electron microscope (SEM) images were taken at a 40° tilted angle using an XL-30 SEM (Philips, Amsterdam, Netherlands) operating at 10 kV. Samples were dried in a vacuum chamber, followed by coating with a 5 nm thick Au/Pd layer (SC7620 sputter coater, Quorum, Laughton, UK). X-ray photoelectron spectroscopy (XPS) was carried out using a Physical Instruments Quantera SXM (Physical Instruments, Chanhassen, MN, USA) equipped with a monochromatic Al K<sub>α</sub> (1486.6 eV) X-ray source. X-ray beam had a diameter of 200 µm at 50 W, area of investigation was a square of 1.4 × 1.4 mm. SEM coupled energy dispersive X-ray spectroscopy (SEM-EDS) was carried out using a Phenom XL (Thermo Fisher Scientific, USA) equipped with BDS, SED, and EDS detectors (15 kW of acceleration voltages under high vacuum level). The sample was coated with

carbon prior to analysis and a copper wire was used for electrical conduction between the sample and the manifold. The acquisition data are present in the figures acquired with the instrument. Atomic force microscope (AFM) images were recorded using a CoreAFM (Nanosurf, Liestal, Switzerland) equipped with a TAP150GD-G tip (BudgetSensors, Sofia, Bulgaria, tip radius <10 nm) in tapping mode. Coating roughness on PEEK was measured with an Alphastep 500 surface profiler (KLA Tencor) using a tip with 12.5 µm radius and a force of 61 mg. Profiles with a length of 1000 µm were obtained with a scanning speed of 50 µm/s. Coating thickness was determined by measuring the surface profile with 1000 µm length over a border of the coating to uncoated PEEK and calculated by the difference in surface levels.

### 2.5. Biocompatibility studies

#### 2.5.1. Cell culture

L-929 mouse fibroblasts were obtained from Dr. Oliver Podlech (CleanControlling GmbH, Emmingen-Liptingen, Germany) and cultured in low-glucose Dulbecco's Modified Eagle Medium (DMEM), containing 10% (v/v) fetal calf serum (FCS), 1% penicillin-streptomycin (10,000 U/mL) and 1% (v/v) L-glutamine. Human umbilical vein endothelial cells (HUVECs, neonatal, pooled) were obtained from Sigma Aldrich, Germany, and cultured in endothelial cell growth medium (Sigma Aldrich, Germany). Saos-2 human osteogenic sarcoma cells (Sigma Aldrich, Germany, DSMZ No. ACC 243) were cultured in McCoy's 5a medium supplemented with 10% (v/v) FCS, 2 mM L-glutamine, and 1% penicillin-streptomycin (10,000 U/mL). Mono Mac-6 monocytes (Sigma Aldrich, Germany, DSMZ No. ACC 124) were maintained in RPMI-1640 (Sigma Aldrich, Germany) supplemented with 10% (v/v) FCS, 1 mM sodium pyruvate, 10 µg/mL human insulin (Sigma Aldrich, Germany) and 1% penicillin-streptomycin (10,000 U/mL). All cell lines used in these studies were maintained in a humidified atmosphere supplemented with 5% CO<sub>2</sub> at 37 °C in a tissue culture incubator (CB series C150, Binder, Tuttlingen, Germany).

#### 2.5.2. Cytotoxicity testing: extracts

Cytotoxicity testing of polymer extracts was performed according to United States Pharmacopeia (USP) standards as previously described [36,72]. Polymer extracts were obtained by coating the wells of a 24-well plate with final polymers (Fig. 1) followed by the addition of 317 µL cell culture media identified as suitable for the cell line to be evaluated. After incubation for 24 h at 37 °C in a humidified atmosphere, 100 µL of each polymer extract was added to cells grown to adherence overnight (100,000 cells/mL). Medium supplemented with 6% (v/v) DMSO was used as a positive control. After 72 h, the medium was removed from each well and replaced with 110 µL fresh media supplemented with 10% of a 10 mM 3-(4,5-dimethylthiazol-2-yl)-2,5-diphenyltetrazolium bromide (MTT) solution in phosphate-buffered saline (PBS), followed by 4 h incubation at 37 °C and 5% CO<sub>2</sub> in a humidified atmosphere. in the incubator. The formed formazan crystals were solubilized with 100 µL 10% sodium dodecyl sulfate (SDS; w/v) in 10 mM HCl followed by incubation at 37 °C and 5% CO<sub>2</sub> in an H<sub>2</sub>O-saturated atmosphere. Absorbance measurements (570 nm) obtained using a Tecan Infinite M200 microplate reader provide a measurement of cell viability in response to each extract; this value was calculated from the ratio/percentage of the average absorbance measured in triplicate wells of extract-treated versus non-treated cells. Standard deviations for each of the triplicate samples are shown as error bars.

#### 2.5.3. Cytotoxicity testing: contact

Cytotoxicity testing based on contact with the polymer was performed as described in our previous publication [36]. A 100 µL

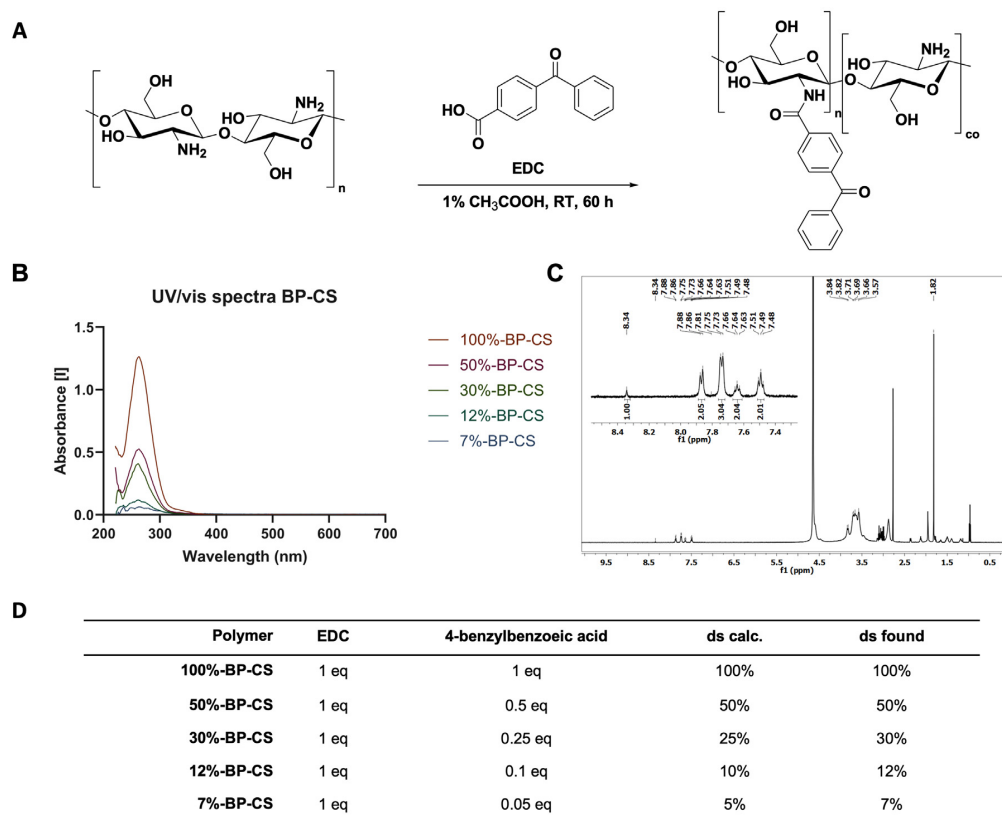


**Fig. 1.** Synthesis (A) and degree of substitution (ds) (D) of the chitosan derivatives. The degree of substitution determined calculated by stoichiometry matches that determined by UV/vis spectroscopy (B). The  $^1\text{H}$  NMR spectrum confirms that the reaction between chitosan and 4-benzoylbenzoic acid is chemoselective and results in substitution at the amino group only (C).

cell suspension containing 100,000 cells/mL was added to a coated 96-well plate which was then incubated for 24 or 72 h. The medium was removed from each well and replaced with 110  $\mu\text{L}$  of fresh medium containing 10% of a 10 mM MTT solution in PBS. The cells were then incubated for 4 h in an incubator. This was followed by the addition of 100  $\mu\text{L}$  of a 10% SDS solution in 10 mM HCl and another incubation for 4 h in an incubator. Absorbance (570 nm) was then measured using a Tecan Infinite M200 pro microplate reader. Cell viability was calculated as mean absorbance measured in wells containing polymer coatings *versus* uncoated control wells. Each measurement was performed in triplicate with error bars indicating standard deviation.

#### 2.5.4. Interleukin (IL)-6 ELISA

Mono Mac-6 cells were used for quantitative evaluation of IL-6 expression. A 200  $\mu\text{L}$  suspension containing 200,000 cells/mL was aliquoted into wells of a polymer-coated 96-well plate, followed by a 16 h incubation either with or without lipopolysaccharide (LPS, 500 ng/mL). Cells in uncoated wells treated with LPS (500 ng/mL) and untreated cells served as positive and negative controls, respectively. After 16 h incubation, the cells were collected by centrifugation (300 g, 5 min at room temperature). Levels of immunoreactive IL-6 were assessed in 100  $\mu\text{L}$  samples of the resulting supernatant by ELISA according to the manufacturer's

instructions (PeproTech Human IL-6 Standard ABTS ELISA Development Kit). Absorbance after reaction quenching was measured at 450 nm using a Tecan Infinite M200 microplate reader. The IL-6 concentration in each biological replicate was calculated using mean values from three triplicate wells. Error bars are used to indicate standard deviation.

#### 2.5.5. Expression of IL-1b, IL-8, and IL-10

One million Mono Mac-6 cells in 2 mL of medium were seeded in wells of a 12-well plate coated with final benzophenone-chitosan polymers and incubated for 16 h. LPS (500 ng/mL) was used as a positive control for cytokine expression. The cells were collected by centrifugation at 350g for 5 min at 4  $^{\circ}\text{C}$ . The cell pellets were washed with 1 mL PBS and collected again by centrifugation. RNA was extracted from the cell pellet using the MACHEREY-NAGEL NucleoSpin $^{\text{®}}$  RNA Plus Kit according to the manufacturer's instructions. From the extracted RNA, 1  $\mu\text{g}$  of each sample was converted into cDNA using the Thermo Scientific RevertAid First Strand cDNA Synthesis Kit according to the manufacturer's instructions. GAPDH was used as the reference gene. Quantitative gene expression analysis was performed in triplicate experiments using the Roche LightCycler $^{\text{®}}$  480 II with Roche SYBR Green I mix according to the manufacturer's instructions. Data shown are the calculated ratios of interleukin RNA to GAPDH. Error bars are used to indicate standard deviation over three triplicates.

Primer sequences include

IL-1b fwd: 5'-GAAGATGCTGGTTC-3'  
IL-1b rev: 5'-TCCCATGTGTCCGAAGAAGATAG-3'  
IL-8 fwd: 5'-GAGCACTCCATAAGGCACAAA-3'  
IL-8 rev: 5'-ATGGTTCCTTCCGGTGT-3'  
IL-10 fwd: 5'-CATAAATTAGAGGTCTCCAAAATCG-3'  
IL-10 rev: 5'-AAGGGGCTGGGTCAGCTAT-3'  
GAPDH fwd: 5'-CTCTGCTCTCTGTTTCGAC-3'  
GAPDH rev: 5'-CAATACGACCAAATCCGTTGAC-3'

## 2.6. Microbiology

### 2.6.1. Bacterial cell culture

Methicillin-resistant *Staphylococcus aureus* (MRSA, DSM 28766) and *Escherichia coli* (K12, DSM 498) were used in the antimicrobial assays. Glycerol stocks of these bacterial strains were stored at  $-80\text{ }^{\circ}\text{C}$ . A new overnight culture was initiated for each experiment. Bacteria were incubated (Minitron, Infors HT, Bottmingen, Switzerland) at  $37\text{ }^{\circ}\text{C}$  with aeration (rotation at 100 rpm) in lysogeny broth (LB) medium. All bacterial suspensions were prepared in LB medium.

### 2.6.2. Antibacterial assay for the evaluation of polymer coatings

A modified version of the direct contact method based on ISO 22196 and Skytta et al. was used to evaluate the antibacterial properties of the polymer coatings [73,74]. Briefly, 200  $\mu\text{L}$  of bacterial suspension at a concentration of  $5 \times 10^3$  cells/mL was added to each well of a coated 96-well plate. A well without polymer treatment was used for reference. The plate was sealed with parafilm to reduce evaporation and incubated for 24 h at  $37\text{ }^{\circ}\text{C}$  in a humidified incubator. The bacterial cell suspension was removed, and the wells were washed twice with 200  $\mu\text{L}$  of sterile PBS. Adherent bacteria that remained in direct contact with the coating were removed with 200  $\mu\text{L}$  of soybean casein digest lecithin polysorbate broth (SCDLP); the suspension was mixed thoroughly and transferred to a new 96-well plate. In addition, serial dilution of a suspension with  $10^4$  cells/well in SCDLP was added to the plate layout for the calculation of a calibration curve to determine the absolute reduction in bacterial count. After all empty wells were filled with sterile PBS, the plate was sealed with parafilm and placed in a Tecan Infinite M200 microplate reader that was preheated to  $37\text{ }^{\circ}\text{C}$ . Optical density at 600 nm was measured every 20 min over the next 16 h. The first derivative of the maximum rate of growth shown in each curve was calculated using GraphPad Prism 8 (San Diego, CA, USA). The live bacteria count was then determined from the calibration curve (Fig. S5) and logarithmic reductions were determined compared to results from the untreated well.

### 2.6.3. Bacteriostatic assay

The bacteriostatic impact of the chitosan polymers before crosslinking was evaluated according to a modified version of the assay described by Skytta et al. [73]. Briefly, 20  $\mu\text{L}$  of polymer solution (concentrations including 10 mg/mL, 5 mg/mL, 1 mg/mL, 500  $\mu\text{g}/\text{mL}$ , 100  $\mu\text{g}/\text{mL}$ , 50  $\mu\text{g}/\text{mL}$ , 10  $\mu\text{g}/\text{mL}$ , 100 ng/mL, and 1 ng/mL) dissolved in 1 mM HCl, or 20  $\mu\text{L}$  of 1 mM HCl as vehicle control were added to 180  $\mu\text{L}$  of a bacterial suspension containing  $5 \times 10^4$  cells/mL in a 96-well plate. In addition, serial dilution of  $10^4$  cells/well in LB media was added to the plate layout as a negative control. After all empty wells were filled with sterile PBS, the plate was sealed with parafilm and placed in a Tecan Infinite M200 microplate reader that was preheated to  $37\text{ }^{\circ}\text{C}$ . Optical density at 600 nm was measured every 20 min over the next 16 h.

The area under the growth curves between the two thresholds was calculated using GraphPad Prism 8; the lower threshold was

defined as the baseline and the upper threshold was defined as the endpoint of the exponential growth phase. The areas under the growth curves for each sample were compared to those observed in suspensions exposed to vehicle control to determine relative bacterial growth. The inhibitory concentration ( $\text{IC}_{90}$ ) value was calculated from these findings.

### 2.6.4. Crystal violet assay for biofilm assessment

Staining with crystal violet was performed to quantify biofilm formation as described previously [36]. Briefly, an overnight bacterial culture was diluted in LB medium to a concentration of  $3 \times 10^5$  cells/mL. These suspensions were added to each well in a 96-well plate after the coating was washed twice with 200  $\mu\text{L}$  sterile PBS. All empty wells were filled with 200  $\mu\text{L}$  sterile PBS to prevent samples from drying out. The plate was then sealed with parafilm and incubated for 24 or 72 h at  $37\text{ }^{\circ}\text{C}$  in a humidified incubator without shaking. The medium was then carefully removed, and the samples were washed three times with 200  $\mu\text{L}$  sterile PBS, with care taken to avoid detaching any biofilm that may have formed. This was followed by fixation with 200  $\mu\text{L}$  of absolute EtOH. EtOH was then aspirated, and the samples were dried for 10 min in a sterile hood. Biofilms were then stained for 2 min in 200  $\mu\text{L}$  of a 0.1% (w/v) crystal violet solution in PBS. The staining solution was removed, and samples were washed six times with 200  $\mu\text{L}$  sterile PBS to remove excess dye. The samples were then dried overnight to avoid dilution errors and the dye was then released from the bacteria by adding 100  $\mu\text{L}$  of absolute EtOH. The crystal violet-containing solution was transferred to a new well after 10 min incubation at room temperature and was quantified by measuring the absorbance at 595 nm in a microplate reader.

### 2.6.5. Live/dead staining

Live/Dead Staining was performed according to the manufacturer's instructions of the live/dead staining kit (PromoCell GmbH, Heidelberg, Germany). Briefly, polymer coatings were crosslinked in a 96-well plate and washed three times with 200  $\mu\text{L}$  sterile PBS to remove residues. The sterile PBS was removed and coatings were inoculated with 200  $\mu\text{L}$  of overnight bacterial culture (*E. coli* or MRSA) diluted to  $3 \times 10^5$  cells/mL with LB medium. Samples were incubated for 24 h at  $37\text{ }^{\circ}\text{C}$  in a humidified incubator without shaking. For staining, medium was carefully removed and samples were washed three times with 200  $\mu\text{L}$  sterile 150 mM NaCl solution and stained with an appropriate mixture of DMAO (ex/em 490/540) and EthD-III.

(ex/em 530/630) for 15 min at room temperature protected from light. Images were taken with the fluorescent microscope Observer Z1 (Carl Zeiss AG, Oberkochen, Germany) and processed with ZEN blue edition (Version 3.4, Carl Zeiss AG, Oberkochen, Germany). The membrane-permeable DNA dye DMAO stains all cells (live and dead), while the membrane-impermeable DNA dye EthD-III stains only dead cells with damaged cell membranes.

## 3. Results and discussion

### 3.1. Synthesis

The reaction of chitosan with 4-benzoyl-benzoic acid in presence of EDC in the ratios shown in Fig. 1D results in the corresponding, substituted benzophenone-chitosan (BP-CS) derivatives (Fig. 1A). The degree of substitution at the chitosan glucosamine moiety was determined by UV/vis spectroscopy using a calibration curve of 4-benzoyl-benzoic acid dissolved in EtOH. The UV/vis spectrum of the benzophenone group shows a strong absorbance peak at 263 nm. The degree of chitosan substitution determined by UV/vis spectroscopy (Fig. 1B) approximately matches the values

that were calculated theoretically. Thus, the degree of chitosan functionalization could be determined stoichiometrically and is shown in Fig. 1D.

To determine whether substitution occurred at one of the hydroxyl groups or was limited to the free amino groups, we performed NMR measurements of the most highly substituted chitosan derivative (100%-BP-CS) in 1 mM DCl in D<sub>2</sub>O (Fig. 1C). The aromatic region of the spectrum includes nine aromatic protons of the benzophenone group in two doublets (at 7.9 ppm and 7.7 ppm) and two triplets (at 7.6 ppm and 7.5 ppm). The spectrum also includes an amide signal at 8.3 ppm that is detected in an integral ratio that matches the benzophenone protons. Collectively, these results indicate that the benzophenone modification of chitosan occurs chemoselectively, as this moiety is linked to the amino but not the free hydroxyl groups. These findings confirm the structure of the benzophenone-chitosan amide derivative shown in Fig. 1A.

### 3.2. Surface functionalization

PEEK is a ductile polymer with mechanical properties that are similar to those of human bone [47]. This compound is not cytotoxic nor does it degrade or leach ions into the surrounding tissue [48]. Given these properties, it has been used to generate a variety of medical implants, for example, spinal cages [49–52] and endo-prostheses for hip replacement [53–55]. Given its otherwise bio-inert surface, multiple approaches for surface functionalization have been described, for example, deposition of inorganic substrates via atomic layer deposition (ALD) [63]. Here, the BP-CS containing solutions were solvent-cast on PEEK chips, used as a model substrate for PEEK implants, followed by UV-crosslinking at 254 nm, washing, and drying *in vacuo*. The surfaces of the solvent-cast coatings were then further investigated by XPS, SEM-EDS and IR spectroscopy.

Recorded XPS spectra of 100%-BP-CS and 30%-BP-CS coatings are shown in Fig. 2A. In general, the presence of oxygen, nitrogen and carbon could be confirmed. Al, Si, S and Cl could be detected in traces <1% (for determined atom ratios cf. Fig. S2). Due to the high presence of nitrogen in the measured coating areas, the successful coating with chitosan could be confirmed. The element ratios of carbon, nitrogen and oxygen in the 100%-BP-CS coating were also determined using SEM-EDS (cf. Fig. S3) and match the values determined via XRD within deviations of 3%, thus showing consistent data over different methods applied.

The C1s signals between 290 and 282 eV show the presence of C–C, C–H, C=C, C–O, C–N and C=O bonds. The ratio in C=O bonds, which is present in non-crosslinked benzophenone, matches the ratio 3:1 between 100%-BP-CS and 30%-BP-CS, and, therefore, is in accordance with the measurements of the degree of substitution, where 100% and 30% benzophenone content could be determined in the coatings. The relatively high difference in C–O bonds between 100%-BP-CS and 30%-BP-CS also shows successful crosslinking, since the content of C–O and C–N resulting from chitosan itself is constant, while the benzophenones carbonyl is converted into a biradicaloid triplet state, followed by hydrogen abstraction from a neighboring C–H bond and formation of a hydroxy ketyl radical, which undergoes recombination into a C–C bond while a hydroxy group is left as residue [37]. Therefore, the content of hydroxyl groups, as shown in 100%-BP-CS C1s and 30%-BP-CS C1s graphs (Fig. 2A), also differs to a certain factor, which indicates successful crosslinking of the benzophenone photophore through the C–H insertion reaction. Further, it is an additional confirmation of the degrees of substitution as determined on the chitosan polymers.

Microscopic images (200x magnification) of the coatings are shown in Fig. S4. The coarse structure of the PEEK substrate (final panel) caused by milling while cutting PEEK into slices on a lathe

includes circular, groove-like structures of approximately 40 μm thickness. Coatings 100%-BP-CS, 50%-BP-CS, 12%-BP-CS, and 7%-BP-CS applied to the PEEK substrate cover these structures; by contrast, the groove-like structures remain in evidence in PEEK substrates coated with 30%-BP-CS polymer.

IR spectra of those microscopically analyzed areas are shown in Fig. 2B. The IR spectrum of the coating is generally characterized by dominant C–H bands at 2929 cm<sup>-1</sup> and 2881 cm<sup>-1</sup> as well as the O–H band detected at 3284 cm<sup>-1</sup> which are the result of glycosidic carbon backbone C–H stretching vibrations and the free glycosidic hydroxyl groups, respectively. These measurements are consistent with literature reports of bands associated with the parent chitosan molecule [75]. Of these, the most dominant bands are those associated with the glycosidic hydroxyl groups at 3284 cm<sup>-1</sup>; these are also detected in compound 30%-BP-CS, which was not visible microscopically as noted above. Collectively, these results lead us to conclude that all five coatings were formed appropriately upon UV-crosslinking of the benzophenone group with the PEEK substrate.

### 3.3. Surface topology

The surface topology of the coatings formed on the PEEK substrate was examined further using AFM and SEM measurements for the formed nanoscale surface topology. SEM images of the surfaces with each of the five coatings are shown in Fig. 3A. Coatings 100%-BP-CS, 50%-BP-CS, and 12%-BP-CS appear as coarse, sponge-like structures with pore diameters of ~2 μm (100%-BP-CS and 50%-BP-CS) and ~4–5 μm (12%-BP-CS). Coatings 30%-BP-CS and 7%-BP-CS appear relatively flat with lamellar-like structures. The uncoated PEEK substrate is also relatively flat; the 40 μm grooves cannot be detected at this resolution. The surface topology of the PEEK substrate measured by AFM reveals grooves of ~40 μm within the borders of resolution (Fig. 3B). The sponge-like structures associated with coatings 100%-BP-CS, 12%-BP-CS, and (to some extent) 50%-BP-CS can also be detected by this method. By contrast, coatings 30%-BP-CS and 7%-BP-CS appear as flat surfaces with underlying grooves that can be attributed to the PEEK substrate.

The surface thickness has been determined using a surface profiler, measuring over a formed edge of the polymer coating. Measured values are shown in Table 1. Overall, a surface thickness ranging between 1 and 4 μm was obtained for the coatings using the solvent casting method. The standard derivatives determined by triplicate measurements of the thickness approximately match the determined values for surface roughness, where R<sub>a</sub> is the arithmetic average of the profile height deviations and R<sub>q</sub> the quadratic average of profile height deviations.

Differences in the topology, resulting in either sponge-like structures or relatively flat surfaces, could be caused by differences in the degree of substitution, resulting in different solubilities in the used solvent (1 mM HCl). Chitosan itself is insoluble in water or 1 mM HCl, therefore, the reaction with 4-benzoylbenzoic acid was carried out in 1% CH<sub>3</sub>COOH. The solubility in 1 mM HCl is, therefore, caused by the conversion of the amine into the amide functionality (cf. Fig. 1), which still leads to different solubilities through different amide-amine ratios. Solubility differences in solvent casting have been shown to influence the formation of topology using the solvent casting method and leading to inconsistencies [76]. Furthermore, the same crosslinking conditions of 3 J/cm<sup>2</sup> UV-light of 254 nm were applied to all coatings with different benzophenone content; we, therefore, expected differences in coating topology as shown in the SEM and AFM images. Nevertheless, the surface thickness is relatively constant in the range of 1–4 μm over all coatings as well as the determined surface roughness is.

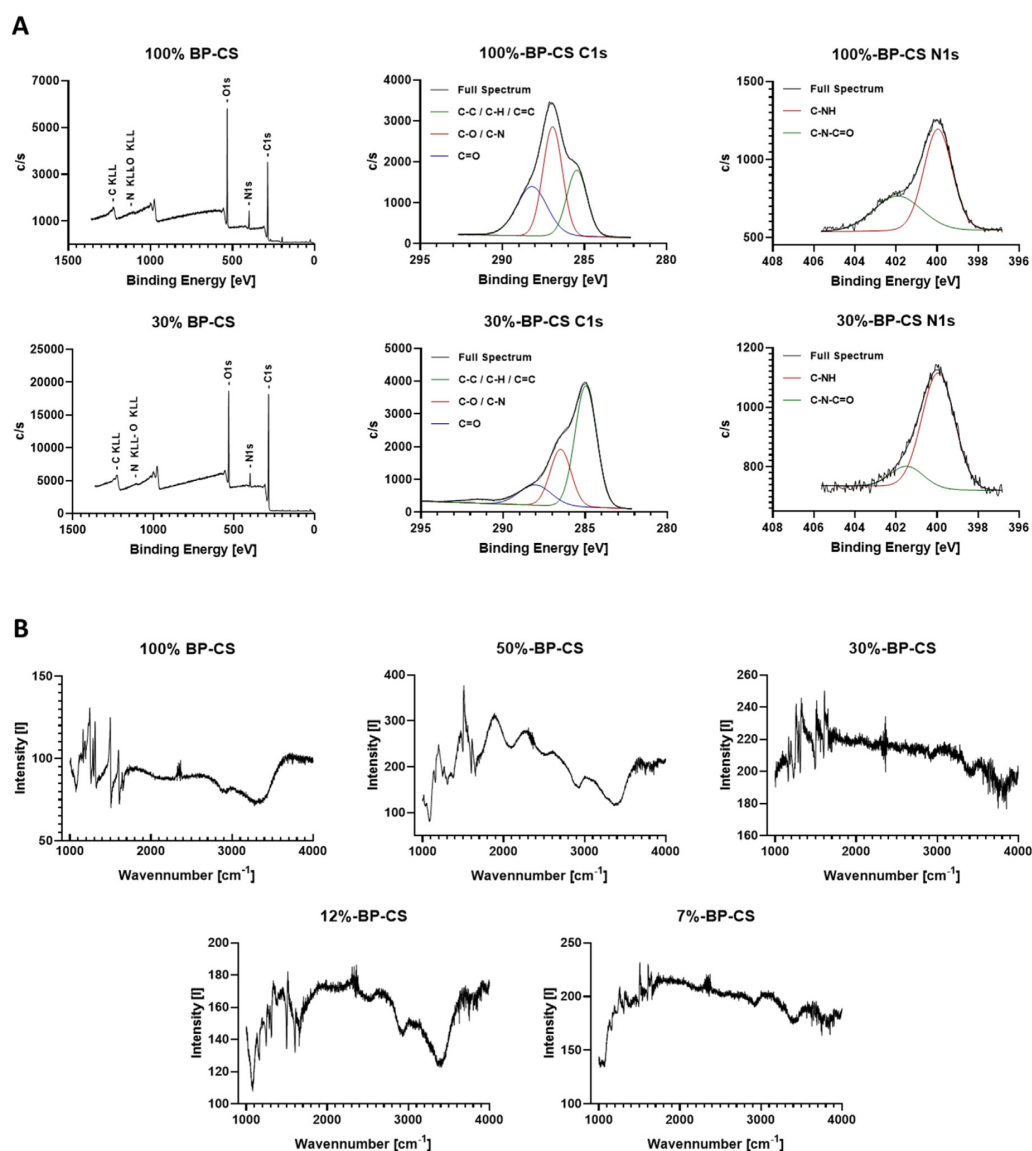


**Fig. 2.** XPS spectra of 100%-BP-CS and 30%-BP-CS coating on PEEK after crosslinking with UV light at 254 nm. The presence of nitrogen confirms the presence of chitosan on the coating, furthermore, the presence of C=O bonds in spectra C1s for both coatings confirm the presence of benzophenone through non-reacted residues (A). IR spectra of the material (B). The most dominant peaks in IR spectra are the glycosidic O–H bounds at 3284 cm<sup>-1</sup>, followed by the glycosidic C–H stretching vibrations at both 2929 cm<sup>-1</sup> and 2881 cm<sup>-1</sup>. These spectra match those obtained for chitosan in this region [75] and indicate successful crosslinking of this material on the surface of the PEEK chip.

### 3.4. Cytotoxicity

Cytotoxicity of the synthesized coatings was determined in experiments targeting the L-929 mouse embryonal fibroblast cell line, human umbilical vein endothelial cells (HUVECs), Saos-2 osteosarcoma cell line, and Mono Mac-6 monocytes. Both extract and direct contact methods were used according to ISO 10993–5 [72,77,78]. Growth inhibition of L-929 cells in response to all extract dilutions was comparatively low (Fig. 4A). By contrast, these same dilutions (except for 30%-BP-CS) promote somewhat more substantial growth inhibition of the HUVEC cell line (Fig. 4B). Overall, little to no growth inhibition was observed in response to the 30% substituted chitosan derivative (30%-BP-CS). More substantial

growth inhibition of both L-929 cells and HUVECs was observed in response to functionalized chitosan derivatives with both higher as well lower benzophenone content.

Direct contact cytotoxicity tests were performed that targeted HUVECs as well as the L929, Saos-2, and Mono Mac-6 cell lines (Fig. 4C–F). The results of these cytotoxicity tests were similar to one another. Similar to the extract tests, the 30% benzophenone-substituted chitosan derivative was minimally cytotoxic in direct contact assays targeting both HUVECs and L929 cells. Among our other results, inhibition of Saos-2 cell growth was enhanced after 72 h of contact with all chitosan derivatives evaluated; inhibition in response to compound 30%-BP-CS increased from <0% at 24 h to 40% at this time point (Fig. 4E). By contrast, the proliferation of

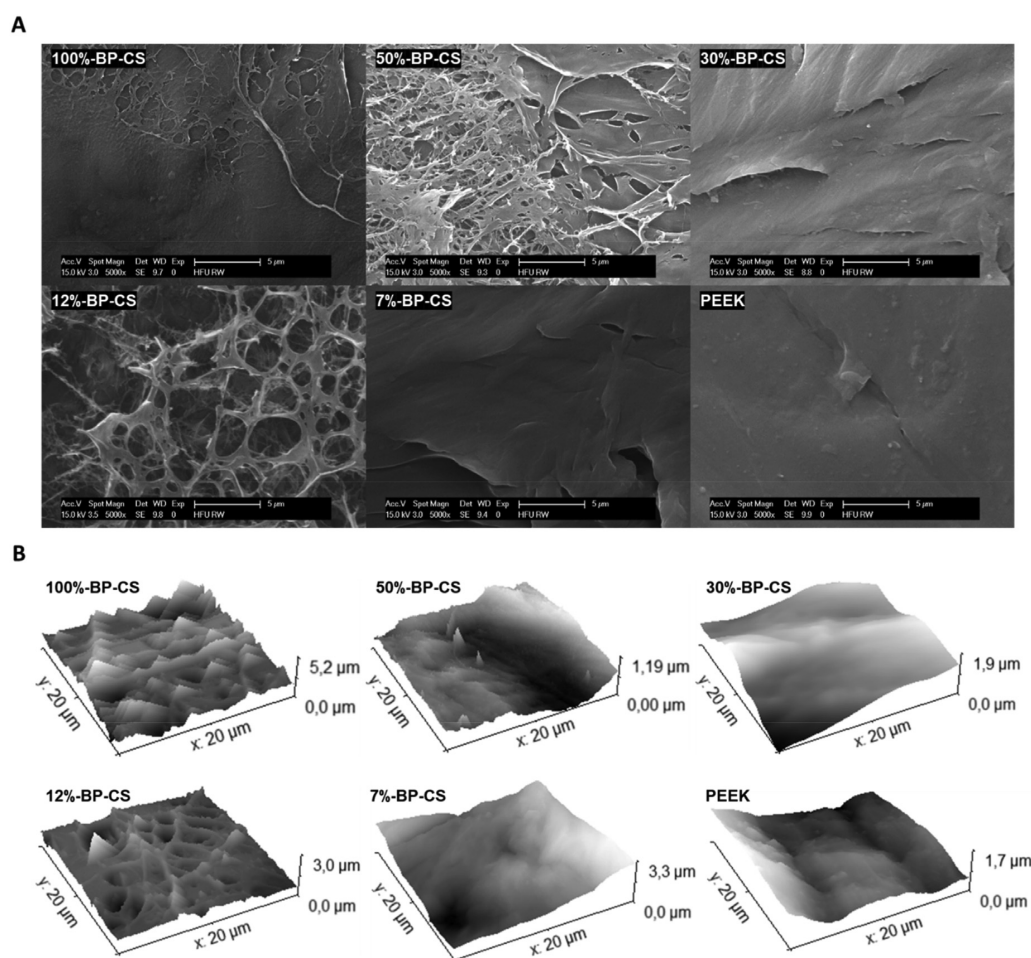


Fig. 3. SEM images (A) and AFM measurements (B) of the coatings, applied to the PEEK substrate (final panel).

Table 1

Surface thickness and surface roughness of the BP-CS coatings determined using a surface profiler.

Sample	Surface thickness [μm]	Surface roughness $R_a$ [nm]	Surface roughness $R_q$ [nm]
100%-BP-CS	2.15 ± 0.13	456.1	509.2
50%-BP-CS	1.46 ± 0.41	615.5	739.5
30%-BP-CS	1.51 ± 0.48	287.2	334.4
12%-BP-CS	3.75 ± 0.60	271.6	339.7
7%-BP-CS	2.12 ± 0.98	323.3	398.6

Mono Mac-6 cells remained constant, with slightly less inhibition observed in response to coatings 12%-BP-CS and 7%-BP-CS (Fig. 4F).

Benzophenone derivatives of N-acetyl glucosamine and short-chain chito oligosaccharides have been characterized as matrix metalloproteinase (MMP) inhibitors with potent activity against cancer cells [79] with potential utility as adjuvant anti-cancer therapy [80]. The activity of these compounds against sarcoma-type cells may explain some of the growth inhibition and decreased cell viability observed in cytotoxicity assays performed in this study. The doubling time of the Saos-2 sarcoma cell line is 40 h [81]. Thus, the growth inhibition of this cell type is observed most

prominently at the 72 h time point, most notably in experiments performed with coating 30%-BP-CS. Downregulation of MMP2 and MMP-9 has also been linked to diminished angiogenesis and reduced migration of human endothelial cells [82]; these findings may explain the decreased viability observed in HUVEC cultures at 24 and 72 h. Results from previous studies suggest that chitosan may form polyelectrolyte complexes in culture medium that sequester growth factors provided by FCS and that this will ultimately result in decreased fibroblast proliferation. In literature, this effect was not observed in cell cultures that were not supplemented with FCS [83]. In the current study, exposure to the 30% substituted chitosan derivative 30%-BP-CS results in the retention of ~70% of the original proliferative activity relative to untreated cells at both 24 and 72 h in all cell lines evaluated. Thus, derivative 30%-BP-CS has been identified as non-cytotoxic. Interestingly, the 30%-BP-CS chitosan derivative is also most effective at inhibiting the growth and viability of both *E. Coli* and *S. aureus* bacterial strains.

### 3.5. Anti-inflammatory potential

The pyrogenicity of the coating surface and/or the presence of potential pyrogenic residues or contaminants was elucidated by a

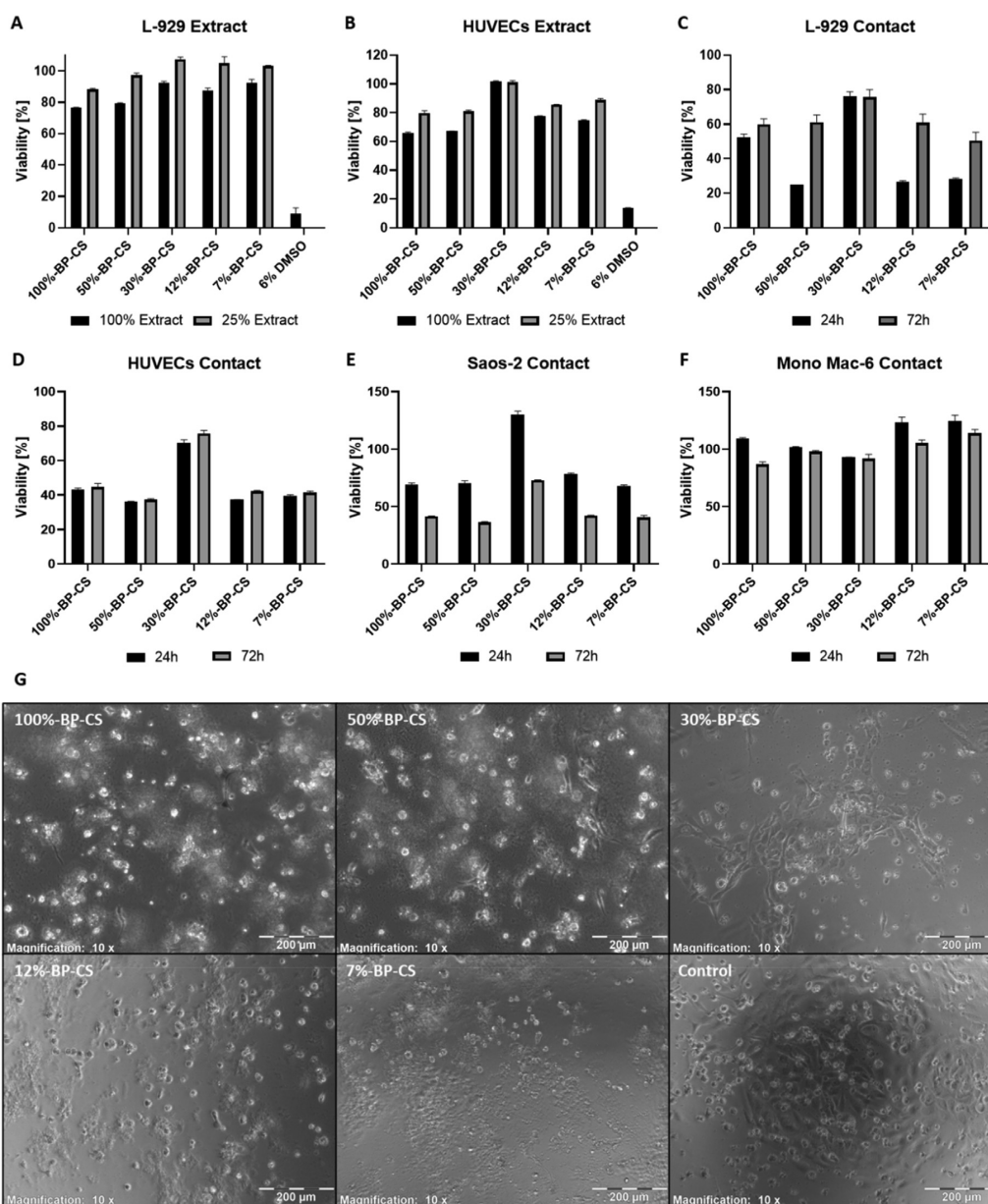


**Fig. 4.** Cytotoxicity at 24 and 72 h associated with exposure to extracts of BP-CS coatings in L-929 cells and HUVECs with 6% DMSO as positive control (A, B). Cytotoxicity at 24 and 72 h associated with direct contact of L-929, HUVECs, Saos-2, and Mono Mac-6 with BP-CS coatings (C–F). Error bars are given as standard deviation of triplicates each. In (G) L-929 mouse fibroblasts growing on the coated surface at 72 h before the addition of the MTT reagent. Cytotoxicity is observed in response to contact with polymers 100%-BP-CS, 50%-BP-CS, 12%-BP-CS, and 7%-BP-CS. By contrast, relatively little cytotoxicity is observed in response to contact with polymer 30%-BP-CS. This result was confirmed by the cell viability test evaluated quantitatively in (C); the images shown are at 10x magnification.

monocyte activation test using the Mono Mac-6 cell line and an enzyme-linked immunosorbent assay (ELISA) for quantitative detection of IL-6 secretion [84,85]. An approximately two-fold increase in IL-6 was detected in the medium of cultures grown in wells with 625  $\mu\text{g}/\text{cm}^2$  of 100%-BP-CS, 50%-BP-CS, 12%-BP-CS and 7%-BP-CS coatings compared to negative controls (Fig. 5A, left). By contrast, no increase in IL-6 levels was detected in wells coated with 30%-BP-CS derivative. No significant increases in IL-6 release

were observed over control levels in cultures grown in wells coated with lower concentrations of these chitosan derivatives. Thus, all coatings can be considered non-pyrogenic when used at concentrations at or below 312.5  $\mu\text{g}/\text{cm}^2$ ; 30%-BP-CS derivative is non-pyrogenic at concentrations as high as 625  $\mu\text{g}/\text{cm}^2$ . We also evaluated the expression of genes encoding the cytokines IL-1b, IL-8, and IL-10 in monocytes that were cultivated for 16 h in coated wells. We detected no significant increase in IL-1b expression in

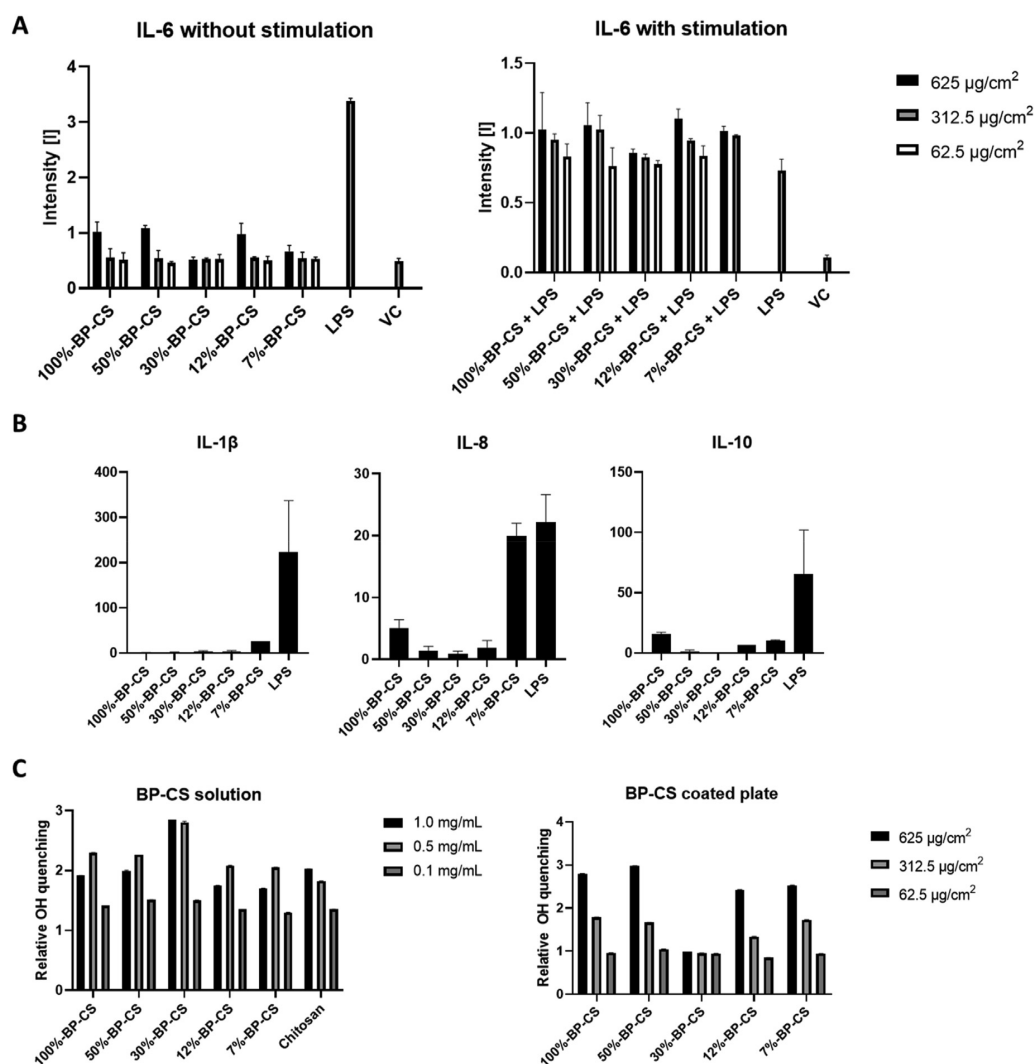


**Fig. 5.** Secreted IL-6 from Mono Mac-6 monocytes (A) detected in the medium by ELISA at 16 h both with (left) and without (right) stimulation with 500 ng/mL LPS together with LPS and vehicle control (VC) alone. IL-6 levels are twice as high in LPS-stimulated monocytes exposed to 625  $\mu\text{g}/\text{cm}^2$  coatings compared to vehicle control (VC). By contrast, IL-6 levels remain at baseline in cell cultures exposed to lower coating concentrations. IL-6 levels remained at baseline in all cultures exposed to coating 30%-BP-CS. Expression of IL-1 $\beta$ , IL-8, and IL-10 genes (B) determined by qPCR after 16 h cultivation on a benzophenone-substituted chitosan-coated microtiter plate (625  $\mu\text{g}/\text{cm}^2$ ). Expression of all three cytokine genes remained at or near baseline in cultures exposed to polymer 30%-BP-CS. (C) Radical ( $\text{OH}\cdot$ ) quenching mediated by benzophenone-substituted chitosan polymers in solution compared to unmodified chitosan (left) and as coatings on microtiter plates.

Mono Mac 6 cells cultured with derivatives 100%-, 50%-, 30%- and 12%-BP-CS, compared to the LPS-positive control [63]. A similar pattern was observed for IL-8; this might be related to findings indicating that IL-8 expression is induced by exogenous IL-1 $\beta$  in monocytes [86]. The lowest level of IL-8 expression was detected in cells cultured with 30%-BP-CS derivative; expression levels increase from 50%-BP-CS to 100%-BP-CS and from 12%-BP-CS, reaching a maximum in the presence of 7%-BP-CS, approaching the levels observed in response to the LPS positive control. Expression of the anti-inflammatory cytokine, IL-10 increases in a similar pattern, which may represent its capacity to modulate the responses of the proinflammatory cytokines IL-1 $\beta$ , IL-6, and IL-8. Interestingly, the expression of IL-10 is more prominent in response to 100%-BP-CS derivative than 7%-BP-CS; the 100%-BP-CS derivative also elicits comparatively lower levels of both IL-6 and IL-8. Overall, we can

conclude that the 30%-BP-CS coating is non-inflammatory, while the 100%-BP-CS coating exhibits anti-inflammatory properties as described above.

LPS induces oxidative stress via the production of reactive oxygen species (ROS) in both monocytes and macrophages. LPS-mediated monocyte activation also leads to the synthesis and release of proinflammatory cytokines, including IL-1 $\beta$ , followed by IL-6 and IL-8, which are cytokines that stimulate local inflammation [87–89]. Chitosan has characterized antioxidative properties and is capable of quenching hydroxyl- and superoxide radicals in solution [90]. Chitosan also exhibits anti-inflammatory properties including its capacity to limit the expression of cyclooxygenase (COX)-2 [91–93]. We tested the radical scavenging potential of each coating and examined their capacity to suppress monocyte-mediated IL-6 release in response to 500 ng/mL LPS. ROS is generated in biological

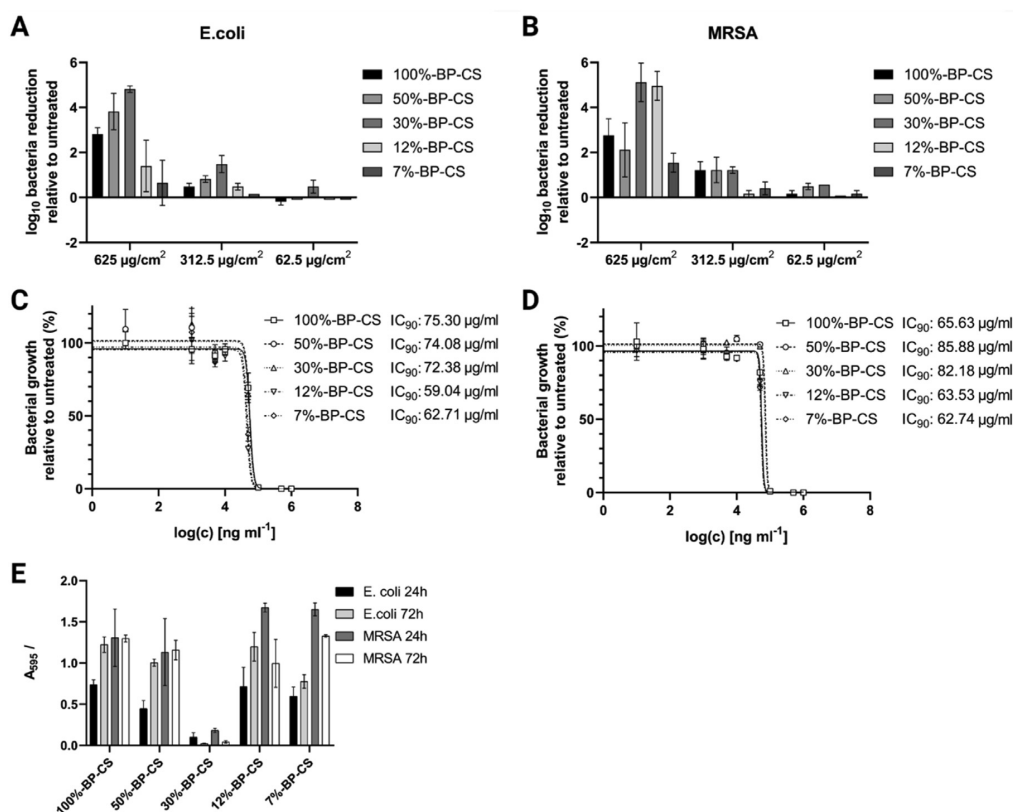


**Fig. 6.** Antimicrobial activity of benzophenone-substituted chitosan coatings and solubilized chitosan derivatives. Shown are reductions in the number of viable *E. coli* (A) and MRSA (B) that are adherent to coatings relative to the untreated surface of a tissue culture plate. The impact of solubilized chitosan derivatives at various concentrations on the growth of *E. coli* (C) and MRSA (D) and the calculated  $IC_{90}$  values. (E) Biofilms of *E. coli* and MRSA at 24 and 72 h were evaluated by crystal violet staining. All values represent means  $\pm$  standard deviations;  $n = 3$ .

systems mainly via the Fenton reaction [94]. Thus, we performed this reaction in an *ex vivo* as described by Li et al. [90] that utilized photometric measurements of Safranin O degradation mediated by hydroxyl radicals [90]. We found that compound 30%-BP-CS was most effective at radical quenching; exposure to polymers of this compound in solution resulted in a 3-fold increase in OH-quenching compared to the negative control (Fig. 5C). Interestingly, the effectiveness of coating 30%-BP-CS exceeds that of chitosan alone by a factor of 1.5, also compared to the negative control. However, these anti-oxidant activities were not detected when compound 30%-BP-CS was evaluated as a coating. Furthermore, and despite their capacity for radical quenching, none of the coatings had an impact on monocytes-mediated IL-6 secretion compared to the responses of unstimulated monocytes alone (see Fig. 5A, right).

In conclusion, we found that exposure to coating 30%-BP-CS resulted in no increase in proinflammatory cytokine release; this coating also had a negligible effect on modulating the responses of LPS-stimulated monocytes. Monocyte viability remained at or near 100% after 24 or 72 h in a contact with this coating. Based on these results, we identify coating 30%-BP-CS as both inert and biocompatible in experiments performed in relevant *ex vivo* settings.

### 3.6. Antimicrobial properties

The antibacterial properties of soluble chitosan are well-characterized. Among these findings, Li et al. [95] reported that

chitosan at  $\sim 0.1\%$  (w/v) resulted in  $>80\%$  inhibition of several bacterial strains. In this study, we tested our compounds within a general range of concentrations to determine the 90% inhibitory concentration ( $IC_{90}$ ) based on the results of growth curves of *E. coli* and MRSA (Fig. S3). Our findings revealed that all five BP-CS derivatives retained their antibacterial properties when evaluated in solution (Fig. 6C and D). The  $IC_{90}$ s determined for benzophenone chitosan derivatives targeting *E. coli* were 75, 74, 72, 59, and 63  $\mu\text{g}/\text{mL}$ , respectively;  $IC_{90}$ s determined for chitosan derivatives targeting MRSA were 66, 86, 82, 64, and 63  $\mu\text{g}/\text{mL}$ , respectively. These calculated  $IC_{90}$  values are comparable to the minimum inhibitory concentrations previously reported for non-functionalized chitosan against *E. coli* (50  $\mu\text{g}/\text{mL}$ ) and MRSA (100  $\mu\text{g}/\text{mL}$ ) [96]. Interestingly, although benzophenone is considered toxic to bacteria [97], higher  $IC_{90}$  values were observed for compounds with higher benzophenone content. The reduced impact associated with more extensive substitution may be explained by reductions in the number of free amino groups contributing to the overall cationic charge of the polymer. Of note, according to the SMH model, cationic charge is the critical feature underlying chitosan-mediated antimicrobial activity [5,6]. Thus, our results suggest that the impact of the loss of cationic charge may exceed the potential for increased toxicity associated with an increase in the benzophenone content. This net effect may result in an overall reduction of its antibacterial properties.

We then examined the antibacterial properties of coatings prepared from the dissolved chitosan derivatives after UV-

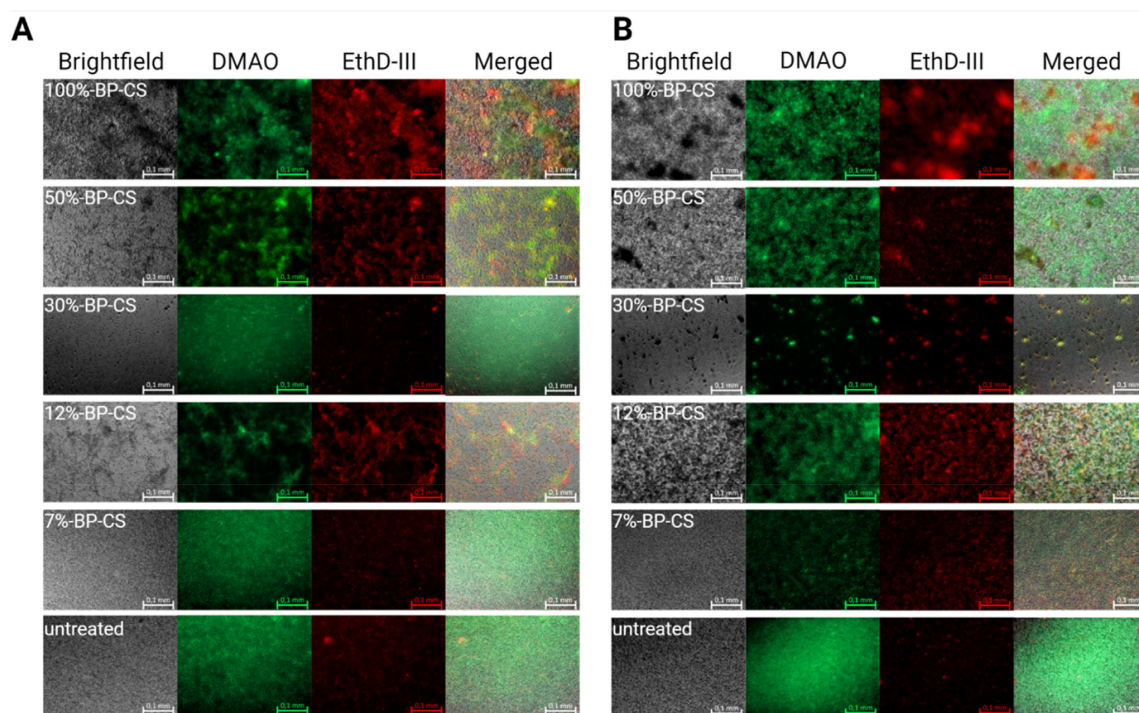


**Fig. 7.** Representative microscopic images of Live/Dead stained *E. coli* (A) and MRSA (B) after 24 h incubation on the corresponding polymer-coated or untreated surface of a 96-well cell culture plate. Magnification is 200x; scale bar measures 0.1 mm.

crosslinking. Polymer coatings were prepared at mass-to-surface ratios of 625, 312.5, and 62.5  $\mu\text{g}/\text{cm}^2$ . Our results revealed a net reduction in antibacterial efficacy of all coatings that paralleled the decreases in mass-to-surface ratios (Figs. S2, 6A, and 6B).

Maximum antibacterial activity was observed for coating of 30%-BP-CS applied at 625  $\mu\text{g}/\text{cm}^2$ . Direct contact with this coating (30% benzophenone) resulted in an approximately 5-log reduction of viable *E. coli* or MRSA. Compounds with higher (100%-BP-CS and 50%-BP-CS) and lower (12%-BP-CS and 7%-BP-CS) benzophenone contents were not as effective at limiting bacterial viability (Fig. 6A and B). These results indicate that the antibacterial activity of the cross-linked compound in the form of a coating may be more effective than the individual components in solution. In the case of benzophenone derivatives, crosslinking is critical to ensure a uniform and functional coating.

We also examined biofilm formation on the polymer coatings at 24 and 72 h by crystal violet (CV) staining (Fig. 6E) and Live/Dead staining (Fig. 7). These observations confirmed the results of previous experiments as they revealed that coating 30%-BP-CS was more effective than the other four benzophenone-substituted coatings evaluated. Coating 30%-BP-CS was the only derivative that promoted a reduction in the level of CV stained *E. coli* biofilm between the 24 and 72 h time points, to a point at which it was nearly undetectable. Similar results were obtained in experiments targeting MRSA. However, it is also worth noting that no increases in biofilm formation were observed by CV staining between 24 and 72 h for MRSA in experiments performed with the four additional coatings; experiments performed with coatings 12%-BP-CS and 7%-BP-CS revealed reductions in the amounts of CV stained MRSA biofilms during this time interval. Live/dead staining confirmed that, after 24 h, there was considerably less biofilm on coating 3c

and almost all cells still present were stained as dead. In contrast, the other coatings had developed biofilms, albeit with a higher percentage of dead cells compared to the untreated control. Collectively, the results suggest that these compounds are more effective against biofilms generated by Gram-positive bacteria such as MRSA compared to Gram-negative bacteria, such as *E. coli*.

#### 4. Conclusion

In this study, our findings document the successful functionalization of the free amino groups of chitosan with benzophenone moieties. The degree of functionalization obtained approximately matched the stoichiometrically-calculated ratios. Chemoselective functionalization of the free amino groups via amide formation was confirmed by NMR spectroscopy. Coatings prepared from 30% functionalized derivative, named 30%-BP-CS, were the most effective of the group against the bacterial pathogens MRSA and *E. coli*, which were used as clinically relevant microbial strains in antimicrobial testing. The 30%-BP-CS derivative also exhibited the least cytotoxicity when evaluated in cultures of L-929 fibroblasts, HUVECs, Saos-2 osteoblasts, and Mono Mac-6 monocytes using ISO 10993-5 testing methodology for cytotoxicity assessment. No inflammation was observed in response to the 30%-BP-CS coating in the pyrogen test performed as per ISO 10993-11. Thus, the 30%-BP-CS coating can be considered biologically inert. Interestingly, this 30% functionalized chitosan shows the optimum properties with respect to antimicrobial action and biocompatibility under the UV-crosslinking conditions applied. Different levels of benzophenone substitution (both higher and lower) lead to reduced biocompatibility, a greater potential for inflammation, and diminished antimicrobial activity. This may relate at least in part to differences in

M. Borgolte, O. Riemer, I. Quint et al.

Materials Today Chemistry 26 (2022) 101176

crosslinking efficiency under the applied conditions (3 J/cm<sup>2</sup>, 254 nm), leading to different amounts of uncrosslinked benzophenone residues, which have been shown in the XPS spectra (Fig. 2A). The appropriate combination of these factors may lead to the thinnest possible coating and a smoother surface by minimizing pore formation and the concentration of benzophenone residues that remain uncrosslinked. Previous studies have suggested that the smoothness of the surface is a critical determinant of the biocompatibility and inflammatory potential of biomedical implants [98]. The XPS and IR spectra (Fig. 2) and AFM and SEM measurements (Fig. 3) support this conclusion; these studies revealed that the 30%-BP-CS coating exhibited a relatively smooth surface with no visible pores or sponge-like structures that may promote cell adhesion and inflammation. However, the surface roughness of the 30%-BP-CS coating is slightly higher than the roughness of the 12%-BP-CS coating. This property might also explain the limited capacity for OH-radical quenching (Fig. 4); coatings prepared from 30%-BP-CS derivative display comparatively less active surface area for radical quenching. This can explain the relatively bioinert properties of this coating despite the fact that IC<sub>50</sub> of the polymers were within range of those exhibited by the other compounds when they were all examined in solution. However, when applied as a coating, their capacity for growth inhibition differed significantly (Fig. 5). While the exactly optimized parameters for crosslinking conditions and surface properties of the coatings still need more adjustment, overall, our study presents an interesting chemical approach that can be used to generate chitosan-derived coatings for implant materials that are biocompatible, non-inflammatory, and antimicrobial with potential for use in photopatterning applications.

#### Credit author statement

Max Borgolte: Conceptualization, Methodology, Investigation, Writing – Original Draft, Writing – Review & Editing, Visualization. Oliver Riemer: Methodology, Investigation, Writing – Original Draft, Writing – Review & Editing, Visualization. **Isabel Quint**: Investigation, Writing – Review & Editing. Felix Blending: Investigation, Visualization, Writing – Review & Editing. **Volker Bucher**: Resources, Writing – Review & Editing. Stefan Laufer: Resources, Writing – Review & Editing. René Csuk: Resources, Writing – Review & Editing. Luca Scotti: Investigation, Visualization, Resources. Hans-Peter Deigner: Conceptualization, Writing – Review & Editing, Project administration, Funding acquisition, Resources.

#### Funding

Funding was granted by CoHMed FunctioMed (FKz: 13FH5102IA), CoHMed MS-ToxTest (FKz 13FH5E01IA) and CoHMed PersonaMed (FKz: 13FH5106IA), all BMBF, as well as TriMaBone–Trinationale Forschungsinitiative: 3D-Druck Materialien für resorbierbare Knochen-implantate” (Europäischer Fonds für regionale Entwicklung–EFRE) in the program “Interreg VOberrhein” (Ref: 5115/3.17).

#### Declaration of competing interest

The authors declare that they have no known competing financial interests or personal relationships that could have appeared to influence the work reported in this paper.

#### Data availability

No data was used for the research described in the article.

#### Acknowledgments

We thank Dr. Oliver Podlech, CleanControlling GmbH, for providing us with the L-929 cell line used for biocompatibility testing as well as technical support regarding cell handling and ISO 10993-5 biocompatibility testing. We also thank Dr. Dagmar Martin and Duva Giuliano from the Natural and Medical Sciences Institute (NMI) at the University of Tübingen, Germany, for performing the XPS measurements and gratefully acknowledge their support regarding analysis and discussion of the obtained data. Continuous stimulation by N.C.R. is gratefully acknowledged.

#### Appendix A. Supplementary data

Supplementary data to this article can be found online at <https://doi.org/10.1016/j.mtchem.2022.101176>.

#### References

- [1] I.M. Helander, E.L. Nurmiaho-Lassila, R. Ahvenainen, J. Rhoades, S. Roller, Chitosan disrupts the barrier properties of the outer membrane of Gram-negative bacteria, *Int. J. Food Microbiol.* 71 (2001) 235–244, [https://doi.org/10.1016/S0168-1605\(01\)00609-2](https://doi.org/10.1016/S0168-1605(01)00609-2).
- [2] J.Y. Je, S.K. Kim, Chitosan derivatives killed bacteria by disrupting the outer and inner membrane, *J. Agric. Food Chem.* 54 (2006) 6629–6633, <https://doi.org/10.1021/jf061310p>.
- [3] K. Divya, S. Vijayan, T.K. George, M.S. Jisha, Antimicrobial properties of chitosan nanoparticles: mode of action and factors affecting activity, *Fibers Polym.* 18 (2017) 221–230, <https://doi.org/10.1007/s12221-017-6690-1>.
- [4] R.C. Chien, M.T. Yen, J.L. Mau, Antimicrobial and antitumor activities of chitosan from shiitake stipes, compared to commercial chitosan from crab shells, *Carbohydr. Polym.* 138 (2016) 259–264, <https://doi.org/10.1016/j.carbpol.2015.11.061>.
- [5] Y. Shai, Mechanism of the binding, insertion and destabilization of phospholipid bilayer membranes by  $\alpha$ -helical antimicrobial and cell non-selective membrane-lytic peptides, *Biochim. Biophys. Acta Biomembr.* 1462 (1999) 55–70, [https://doi.org/10.1016/S0005-2736\(99\)00200-X](https://doi.org/10.1016/S0005-2736(99)00200-X).
- [6] K. Matsuzaki, Why and how are peptide–lipid interactions utilized for self-defense? Magainin and tachyplesins as archetypes, *Biochim. Biophys. Acta, Biomembr.* 1462 (1999) 1–10, [https://doi.org/10.1016/S0005-2736\(99\)00197-2](https://doi.org/10.1016/S0005-2736(99)00197-2).
- [7] X. Li, X. Feng, S. Yang, G. Fu, T. Wang, Z. Su, Chitosan kills *Escherichia coli* through damage to be of cell membrane mechanism, *Carbohydr. Polym.* 79 (2010) 493–499, <https://doi.org/10.1016/j.carbpol.2009.07.011>.
- [8] R.P. Carlson, R. Taffs, W.M. Davison, P.S. Stewart, Anti-biofilm properties of chitosan-coated surfaces, *J. Biomater. Sci. Polym. Ed.* 19 (2008) 1035–1046, <https://doi.org/10.1163/156856208784909372>.
- [9] X. Fei Liu, Y. Lin Guan, D. Zhi Yang, K. de Yao, Antibacterial Action of Chitosan and Carboxymethylated Chitosan, 2000, <https://doi.org/10.1002/1097-4628>.
- [10] A.J. Varma, S.V. Deshpande, J.F. Kennedy, Metal complexation by chitosan and its derivatives: a review, *Carbohydr. Polym.* 55 (2004) 77–93, <https://doi.org/10.1016/j.carbpol.2003.08.005>.
- [11] P. Sahariah, M. Måsson, Antimicrobial chitosan and chitosan derivatives: a review of the structure–activity relationship, *Biomacromolecules* 18 (2017) 3846–3868, <https://doi.org/10.1021/ACS.BIOMAC.7B01058>.
- [12] Y.C. Chung, H.L. Wang, Y.M. Chen, S.L. Li, Effect of abiotic factors on the antibacterial activity of chitosan against waterborne pathogens, *Bioresour. Technol.* 88 (2003) 179–184, [https://doi.org/10.1016/S0960-8524\(03\)00002-6](https://doi.org/10.1016/S0960-8524(03)00002-6).
- [13] H. Liu, Y. Du, J. Yang, H. Zhu, Structural characterization and antimicrobial activity of chitosan/betaine derivative complex, *Carbohydr. Polym.* 55 (2004) 291–297, <https://doi.org/10.1016/j.carbpol.2003.10.001>.
- [14] H. Liu, Y. Du, X. Wang, L. Sun, Chitosan kills bacteria through cell membrane damage, *Int. J. Food Microbiol.* 95 (2004) 147–155, <https://doi.org/10.1016/j.ijfoodmicro.2004.01.022>.
- [15] W. Samprasit, R. Kaomongkolgit, M. Sukma, T. Rojanarata, T. Ngawhirunpat, P. Opanasopit, Mucoadhesive electrospun chitosan-based nanofibre mats for dental caries prevention, *Carbohydr. Polym.* 117 (2015) 933–940, <https://doi.org/10.1016/j.carbpol.2014.10.026>.
- [16] E.A. Izano, I. Sadovskaya, E. Vinogradov, M.H. Mulks, K. Velliyagounder, C. Raganath, W.B. Kher, N. Ramasubbu, S. Jabbari, M.B. Perry, J.B. Kaplan, Poly-N-acetylglucosamine mediates biofilm formation and antibiotic resistance in *Actinobacillus pleuropneumoniae*, *Microb. Pathog.* 43 (2007) 1–9, <https://doi.org/10.1016/j.micpath.2007.02.004>.
- [17] Y. Zheng, N. Pan, Y. Liu, X. Ren, Novel porous chitosan/N-halamine structure with efficient antibacterial and hemostatic properties, *Carbohydr. Polym.* 253 (2021), 117205, <https://doi.org/10.1016/j.carbpol.2020.117205>.

- [18] G.M. Luz, L. Boesel, A. Del Campo, J.F. Mano, Micropatterning of bioactive glass nanoparticles on chitosan membranes for spatial controlled biomineralization, *Langmuir* 28 (2012) 6970–6977, <https://doi.org/10.1021/la300667g>.
- [19] Y. Wang, R. Shi, P. Gong, J. Li, J. Li, D. Ao, P. Wang, Y. Yang, Y. Man, Y. Qu, Bioelectric effect of a chitosan bioelectret membrane on bone regeneration in rabbit cranial defects, *J. Bioact. Compat. Polym.* 27 (2012) 122–132, <https://doi.org/10.1177/0883911512436773>.
- [20] L.-Y. Kim, S.-J. Seo, H.-S. Moon, M.-K. Yoo, L.-Y. Park, B.-C. Kim, C.-S. Cho, Chitosan and its derivatives for tissue engineering applications, *Biotechnol. Adv.* 26 (2008) 1–21, <https://doi.org/10.1016/j.biotechadv.2007.07.009>.
- [21] P.R. Sivashankari, M. Prabaharan, Prospects of chitosan-based scaffolds for growth factor release in tissue engineering, *Int. J. Biol. Macromol.* 93 (2016) 1382–1389, <https://doi.org/10.1016/j.ijbiomac.2016.02.043>.
- [22] Z. Liu, H. Wang, Y. Wang, Q. Lin, A. Yao, F. Cao, D. Li, J. Zhou, C. Duan, Z. Du, Y. Wang, C. Wang, The influence of chitosan hydrogel on stem cell engraftment, survival and homing in the ischemic myocardial microenvironment, *Biomaterials* 33 (2012) 3093–3106, <https://doi.org/10.1016/j.biomaterials.2011.12.044>.
- [23] W. Shi, D. Nie, G. Jin, W. Chen, L. Xia, X. Wu, X. Su, X. Xu, L. Ni, X. Zhang, X. Zhang, J. Chen, BDNF blended chitosan scaffolds for human umbilical cord MSC transplants in traumatic brain injury therapy, *Biomaterials* 33 (2012) 3119–3126, <https://doi.org/10.1016/j.biomaterials.2012.01.009>.
- [24] R. Jayakumar, M. Prabaharan, P.T. Sudheesh Kumar, S.V. Nair, H. Tamura, Biomaterials based on chitin and chitosan in wound dressing applications, *Biotechnol. Adv.* 29 (2011) 322–337, <https://doi.org/10.1016/j.biotechadv.2011.01.005>.
- [25] R. Jayakumar, M. Prabaharan, S.V. Nair, S. Tokura, H. Tamura, N. Selvamurugan, Novel carboxymethyl derivatives of chitin and chitosan materials and their biomedical applications, *Prog. Mater. Sci.* 55 (2010) 675–709, <https://doi.org/10.1016/j.pmatsci.2010.03.001>.
- [26] B. Pidhatika, N. Zhao, M. Zinggeler, J. Rühle, Surface-attached dual-functional hydrogel for controlled cell adhesion based on poly(N,N-dimethylacrylamide), *J. Polym. Res.* 26 (2019) 1–12, <https://doi.org/10.1007/s10965-019-1728-2>.
- [27] P. Samyn, M. Biesalski, O. Prucker, J. Rühle, Confining acrylate-benzophenone copolymers into adhesive micropads by photochemical crosslinking, *J. Photochem. Photobiol. Chem.* 377 (2019) 80–91, <https://doi.org/10.1016/j.jphotochem.2019.03.040>.
- [28] F.D. Scherag, R. Niestroj-Pahl, S. Krusekopf, K. Lücke, T. Brandstetter, J. Rühle, Highly selective capture surfaces on medical wires for fishing tumor cells in whole blood, *Anal. Chem.* 89 (2017) 1846–1854, <https://doi.org/10.1021/acs.analchem.6b04219>.
- [29] F.D. Scherag, A. Mader, M. Zinggeler, N. Birsner, R.E. Kneusel, T. Brandstetter, J. Rühle, Blocking-free and substrate-independent serological microarray immunoassays, *Biomacromolecules* 19 (2018) 4641–4649, <https://doi.org/10.1021/acs.biomac.8b01334>.
- [30] L. Yuan, B. Qu, J. Chen, H. Lv, X. Yang, Engineering modifiers bearing benzophenone with enhanced reactivity to construct surface microstructures, *Polym. Chem.* 10 (2019) 4859–4865, <https://doi.org/10.1039/c9py00764d>.
- [31] Y. Iwasaki, S. Bunuasunthon, V.P. Hoven, Protein patterning with antifouling polymer gel platforms generated using visible light irradiation, *Chem. Commun.* 56 (2020) 5472–5475, <https://doi.org/10.1039/d0cc02092c>.
- [32] O. Prucker, C.A. Naumann, J. Rühle, W. Knoll, C.W. Frank, Photochemical attachment of polymer films to solid surfaces via monolayers of benzophenone derivatives, *J. Am. Chem. Soc.* 121 (1999) 8766–8770, <https://doi.org/10.1021/ja990962+>.
- [33] Q. Liu, J.L. Locklin, Photocross-linking kinetics study of benzophenone containing zwitterionic copolymers, *ACS Omega* 5 (2020) 9204–9211, <https://doi.org/10.1021/acsomega.9b04493>.
- [34] K. Ishihara, K. Suzuki, Y. Inoue, K. Fukazawa, Effects of molecular architecture of photoreactive phospholipid polymer on adsorption and reaction on substrate surface under aqueous condition, *J. Biomater. Sci. Polym. Ed.* 32 (2020) 419–437, <https://doi.org/10.1080/09205063.2020.1839340>.
- [35] J. Koc, E. Schönemann, R. Wanka, N. Aldred, A.S. Clare, H. Gardner, G.W. Swain, K. Hunsucker, A. Laschewsky, A. Rosenhahn, Effects of crosslink density in zwitterionic hydrogel coatings on their antifouling performance and susceptibility to silt uptake, *Biofouling* 36 (2020) 646–659, <https://doi.org/10.1080/08927014.2020.1796983>.
- [36] M. Borgolte, O. Riestler, T. Kacerova, S. Rentschler, M.S. Schmidt, S. Jacksch, M. Egert, S. Laufer, R. Csuk, H.P. Deigner, Methacryloyl-glcnaC derivatives copolymerized with dimethylacrylamide as a novel antibacterial and biocompatible coating, *Pharmaceutics* 13 (2021) 1647, <https://doi.org/10.3390/pharmaceutics13101647>.
- [37] G. Dormán, H. Nakamura, A. Pulsipher, G.D. Prestwich, The life of pi star: exploring the exciting and forbidden worlds of the benzophenone photophore, *Chem. Rev.* 116 (2016) 15284–15398, <https://doi.org/10.1021/acs.chemrev.6b00342>.
- [38] G. Dormán, G.D. Prestwich, Benzophenone photophores in biochemistry, *Biochemistry* 33 (1994) 5661–5673, <https://doi.org/10.1021/bi00185a001>.
- [39] O. Prucker, T. Brandstetter, J. Rühle, Surface-attached hydrogel coatings via C,H-insertion crosslinking for biomedical and bioanalytical applications (Review), *Biointerphases* 13 (2018), 010801, <https://doi.org/10.1116/1.4999786>.
- [40] M.M. Hassan, O.O. Olaye, Recent advances in chemical biology using benzophenones and diazirines as radical precursors, *Molecules* 25 (2020) 2285, <https://doi.org/10.3390/molecules25102285>.
- [41] H. Orelma, M. Vuoriluoto, L.S. Johansson, J.M. Campbell, I. Filpponen, M. Biesalski, O.J. Rojas, Preparation of photoreactive nanocellulosic materials: via benzophenone grafting, *RSC Adv.* 6 (2016) 85100–85106, <https://doi.org/10.1039/c6ra15015b>.
- [42] G. Dormán, G.D. Prestwich, Benzophenone photophores in biochemistry, *Biochemistry* 33 (1994) 5661–5673, [https://doi.org/10.1021/Bi00185A001/ASSET/Bi00185A001.FP.PNG\\_V03](https://doi.org/10.1021/Bi00185A001/ASSET/Bi00185A001.FP.PNG_V03).
- [43] M. Körner, O. Prucker, J. Rühle, Kinetics of the generation of surface-attached polymer networks through C, H-insertion reactions, *Macromolecules* 49 (2016) 2438–2447, <https://doi.org/10.1021/acs.macromol.5b02734>.
- [44] M. Morimoto, T. Nakajima, M. Ishikura, Y. Shigemasa, S. Ifuku, H. Saimoto, Synthesis of organosoluble chitosan derivatives with polyphenolic side chains, *Carbohydr. Polym.* 90 (2012) 1259–1264, <https://doi.org/10.1016/j.carbpol.2012.06.067>.
- [45] K.H. Hong, G. Sun, Antimicrobial and chemical detoxifying functions of cotton fabrics containing different benzophenone derivatives, *Carbohydr. Polym.* 71 (2008) 598–605, <https://doi.org/10.1016/j.carbpol.2007.07.004>.
- [46] D. Garcia-Gonzalez, A. Rusinek, T. Jankowiak, A. Arias, Mechanical impact behavior of polyether–ether–ketone (PEEK), *Compos. Struct.* 124 (2015) 88–99, <https://doi.org/10.1016/j.compstruct.2014.12.061>.
- [47] S.M. Kurtz, J.N. Devine, PEEK biomaterials in trauma, orthopedic, and spinal implants, *Biomaterials* 28 (2007) 4845–4869, <https://doi.org/10.1016/j.biomaterials.2007.07.013>.
- [48] A. Godara, D. Raabe, S. Green, The influence of sterilization processes on the micromechanical properties of carbon fiber-reinforced PEEK composites for bone implant applications, *Acta Biomater.* 3 (2007) 209–220, <https://doi.org/10.1016/j.actbio.2006.11.005>.
- [49] Lumbar interbody fusion using the brantigan I/F cage for pos... : Spine, (n.d.), [https://journals.lww.com/spinejournal/Fulltext/2000/06010/Lumbar\\_Interbody\\_Fusion\\_Using\\_the\\_Brantigan\\_I\\_F.17.aspx](https://journals.lww.com/spinejournal/Fulltext/2000/06010/Lumbar_Interbody_Fusion_Using_the_Brantigan_I_F.17.aspx) (accessed 15, December 2021).
- [50] D.-Y. Cho, W.-R. Liao, W.-Y. Lee, J.-T. Liu, C.-L. Chiu, P.-C. Sheu, Preliminary experience using a polyetheretherketone (PEEK) cage in the treatment of cervical disc disease, *Neurosurgery* 51 (2002) 1343–1350, <https://doi.org/10.1227/01.NEU.0000309109.71345.19>.
- [51] J.W. Brantigan, A. Neidre, J.S. Toohey, The lumbar I/F cage for posterior lumbar interbody fusion with the variable screw placement system: 10-year results of a food and drug administration clinical trial, *Spine J.* 4 (2004) 681–688, <https://doi.org/10.1016/j.spinee.2004.05.253>.
- [52] J.M. Toth, M. Wang, B.T. Estes, J.L. Scifert, H.B. Seim, A.S. Turner, Polyetheretherketone as a biomaterial for spinal applications, *Biomaterials* 27 (2006) 324–334, <https://doi.org/10.1016/j.biomaterials.2005.07.011>.
- [53] A. Wang, R. Lin, C. Stark, J.H. Dumbleton, Suitability and limitations of carbon fiber reinforced PEEK composites as bearing surfaces for total joint replacements, *Wear* 225–229 (1999) 724–727, [https://doi.org/10.1016/S0043-1648\(99\)00026-5](https://doi.org/10.1016/S0043-1648(99)00026-5).
- [54] A Low Stiffness Composite Biologically Fixed Prosthesis : Clinical Orthopaedics and Related Research®, (n.d.), [https://journals.lww.com/clinorthop/Fulltext/2001/12000/A\\_Low\\_Stiffness\\_Composite\\_Biologically\\_Fixed.15.aspx](https://journals.lww.com/clinorthop/Fulltext/2001/12000/A_Low_Stiffness_Composite_Biologically_Fixed.15.aspx) (accessed 15 December, 2021).
- [55] S. Akhavan, M.M. Matthiesen, L. Schulte, T. Penoyer, M.J. Kraay, C.M. Rinnac, V.M. Goldberg, Clinical and histologic results related to a low-modulus composite total hip replacement stem, *Journal of Bone and Joint Surgery - Series A* 88 (2006) 1308–1314, <https://doi.org/10.2106/JBJS.E.00316>.
- [56] F. el Halabi, J.F. Rodriguez, L. Rebollo, E. Hurtós, M. Doblare, Mechanical characterization and numerical simulation of polyether–ether–ketone (PEEK) cranial implants, *J. Mech. Behav. Biomed. Mater.* 4 (2011) 1819–1832, <https://doi.org/10.1016/j.jmbmm.2011.05.039>.
- [57] S. Lovald, S.M. Kurtz, Applications of Polyetheretherketone in Trauma, Arthroscopy, and Cranial Defect Repair, *PEEK Biomaterials Handbook*, 2012, pp. 243–260, <https://doi.org/10.1016/B978-1-4377-4463-7.10015-6>.
- [58] T.J. Hoskins, K.D. Dearn, S.N. Kukureka, Mechanical performance of PEEK produced by additive manufacturing, *Polym. Test.* 70 (2018) 511–519, <https://doi.org/10.1016/j.polymertesting.2018.08.008>.
- [59] M. Rinaldi, T. Ghidini, F. Cecchini, A. Brandao, F. Nanni, Additive layer manufacturing of poly (ether ether ketone) via FDM, *Compos. B Eng.* 145 (2018) 162–172, <https://doi.org/10.1016/j.compositesb.2018.03.029>.
- [60] B. Hu, X. Duan, Z. Xing, Z. Xu, C. Du, H. Zhou, R. Chen, B. Shan, Improved design of fused deposition modeling equipment for 3D printing of high-performance PEEK parts, *Mech. Mater.* 137 (2019), 103139, <https://doi.org/10.1016/j.mechmat.2019.103139>.
- [61] S. Berretta, K. Evans, O. Ghita, Additive manufacture of PEEK cranial implants: manufacturing considerations versus accuracy and mechanical performance, *Mater. Des.* 139 (2018) 141–152, <https://doi.org/10.1016/j.matdes.2017.10.078>.
- [62] S. Najeeb, Z.K. Bds, S.Z. Bds, M.S.Z. Bds, Bioactivity and osseointegration of PEEK are inferior to those of titanium: a systematic review, *J. Oral Implantol.* 42 (2016) 512–516, <https://doi.org/10.1563/aid-joi-D-16-00072>.
- [63] F. Blendinger, D. Seitz, A. Ottenschlager, M. Fleischer, V. Bucher, Atomic layer deposition of bioactive TiO<sub>2</sub> thin films on polyetheretherketone for orthopedic implants, *ACS Appl. Mater. Interfaces* 13 (2021) 3536–3546, <https://doi.org/10.1021/ACSAMI.0C17990>.
- [64] A. Diouf-Lewis, R.D. Farahani, F. Iervolino, J. Pierre, Y. Abderrafai, M. Lévesque, N. Picirelli, D. Theriault, Design and characterization of carbon fiber-reinforced PEEK/PEI blends for Fused Filament Fabrication additive

- manufacturing, *Mater. Today Commun.* 31 (2022), 103445, <https://doi.org/10.1016/j.mtcomm.2022.103445>.
- [65] B.I. Oladapo, S.A. Zahedi, Improving bioactivity and strength of PEEK composite polymer for bone application, *Mater. Chem. Phys.* 266 (2021), 124485, <https://doi.org/10.1016/j.materchemphys.2021.124485>.
- [66] K. Hu, Z. Yang, Y. Zhao, Y. Wang, J. Luo, B. Tuo, H. Zhang, Bioinspired surface functionalization of poly(ether ether ketone) for enhancing osteogenesis and bacterial resistance, *Langmuir* 38 (2022) 5924–5933, [https://doi.org/10.1021/ACS.LANGMUIR.2C00600/SUPPL\\_FILE/LA2C00600\\_SI\\_002.MP4](https://doi.org/10.1021/ACS.LANGMUIR.2C00600/SUPPL_FILE/LA2C00600_SI_002.MP4).
- [67] M. Kyomoto, K. Ishihara, Self-initiated surface graft polymerization of 2-methacryloyloxyethyl phosphorylcholine on poly(ether ether ketone) by photoirradiation, *ACS Appl. Mater. Interfaces* 1 (2009) 537–542, [https://doi.org/10.1021/AM800260T/ASSET/IMAGES/MEDIUM/AM-2008-00260T\\_0005.GIF](https://doi.org/10.1021/AM800260T/ASSET/IMAGES/MEDIUM/AM-2008-00260T_0005.GIF).
- [68] M. Kyomoto, T. Moro, S. Yamane, M. Hashimoto, Y. Takatori, K. Ishihara, Poly(ether-ether-ketone) orthopedic bearing surface modified by self-initiated surface grafting of poly(2-methacryloyloxyethyl phosphorylcholine), *Biomaterials* 34 (2013) 7829–7839, <https://doi.org/10.1016/j.biomaterials.2013.07.023>.
- [69] M. Kyomoto, T. Moro, Y. Takatori, H. Kawaguchi, K. Nakamura, K. Ishihara, Self-initiated surface grafting with poly(2-methacryloyloxyethyl phosphorylcholine) on poly(ether-ether-ketone), *Biomaterials* 31 (2010) 1017–1024, <https://doi.org/10.1016/j.biomaterials.2009.10.055>.
- [70] C.J. Frisrup, K. Jankova, S. Hvilsted, Hydrophilization of poly(ether ether ketone) films by surface-initiated atom transfer radical polymerization, *Polym. Chem.* 1 (2010) 1696–1701, <https://doi.org/10.1039/C0PY00142B>.
- [71] B. Yameen, M. Álvarez, O. Azzaroni, U. Jonas, W. Knoll, Tailoring of poly(ether ether ketone) surface properties via surface-initiated atom transfer radical polymerization, *Langmuir* 25 (2009) 6214–6220, [https://doi.org/10.1021/LA900010Z/ASSET/IMAGES/MEDIUM/LA-2009-00010Z\\_0004.GIF](https://doi.org/10.1021/LA900010Z/ASSET/IMAGES/MEDIUM/LA-2009-00010Z_0004.GIF).
- [72] 87: Biological reactivity tests , in vitro, in: *The United States Pharmacopeia. The National Formulary, United States Pharmacopeial Convention, Inc., Rockville, Md, 1979*, pp. 92–94.
- [73] E. Skyttä, T. Mattila-Sandholm, A quantitative method for assessing bactericins and other food antimicrobials by automated turbidimetry, *J. Microbiol. Methods* 14 (1991) 77–88, [https://doi.org/10.1016/0167-7012\(91\)90036-P](https://doi.org/10.1016/0167-7012(91)90036-P).
- [74] Japan Food Research Laboratories, ISO, 2011, pp. 1–24. ISO 22196: Measurement of antibacterial activity on plastics and other non-porous surfaces.
- [75] M.F. Queiroz, K.R.T. Melo, D.A. Sabry, G.L. Sasaki, H.A.O. Rocha, Does the use of chitosan contribute to oxalate kidney stone formation? *Mar. Drugs* 13 (2015) 141–158, <https://doi.org/10.3390/MD13010141>, 13 (2014) 141–158.
- [76] Z.G. Tang, R.A. Black, J.M. Curran, J.A. Hunt, N.P. Rhodes, D.F. Williams, Surface properties and biocompatibility of solvent-cast poly( $\epsilon$ -caprolactone) films, *Biomaterials* 25 (2004) 4741–4748, <https://doi.org/10.1016/j.biomaterials.2003.12.003>.
- [77] ISO 10993-5:2009 Biological Evaluation of Medical Devices — Part 5: Tests for in Vitro Cytotoxicity, n.d.
- [78] 88: Biological reactivity tests , in vivo, in: *The United States Pharmacopeia. The National Formulary, United States Pharmacopeial Convention, Inc., Rockville, Md, 1979*, pp. 94–98.
- [79] A.D. Baxter, R. Bhogal, J. Bird, J.F. Keily, D.T. Manallack, J.G. Montana, D.A. Owen, W.R. Pitt, R.J. Watson, R.E. Wills, Arylsulphonyl hydroxamic acids: potent and selective matrix metalloproteinase inhibitors, *Bioorg. Med. Chem. Lett* 11 (2001) 1465–1468, [https://doi.org/10.1016/S0960-894X\(01\)00259-1](https://doi.org/10.1016/S0960-894X(01)00259-1).
- [80] E.I. Heath, L.B. Grochow, Clinical potential of matrix metalloproteinase inhibitors in cancer therapy, *Drugs* 59 (2000) 1043–1055, <https://doi.org/10.2165/00003495-200059050-00002>.
- [81] S.B. Rodan, Y. Imai, M.A. Thiede, G. Wesolowski, D. Thompson, Z. Bar-Shavit, S. Shull, K. Mann, G.A. Rodan, Characterization of a human osteosarcoma cell line (Saos-2) with osteoblastic properties, *Cancer Res.* 47 (1987) 4961–4966.
- [82] C. Sun, S. bin Feng, Z.W. Cao, J.J. Bei, Q. Chen, X.J. Xu, Z. Zhou, Z.P. Yu, H.Y. Hu, Up-regulated expression of matrix metalloproteinases in endothelial cells mediates platelet microvesicle-induced angiogenesis, *Cell. Physiol. Biochem.* 41 (2017) 2319–2332, <https://doi.org/10.1159/000475651>.
- [83] T. Mori, M. Okumura, M. Matsuura, K. Ueno, S. Tokura, Y. Okamoto, S. Minami, T. Fujinaga, Effects of chitin and its derivatives on the proliferation and cytokine production of fibroblasts in vitro, *Biomaterials* 18 (1997) 947–951, [https://doi.org/10.1016/S0142-9612\(97\)00017-3](https://doi.org/10.1016/S0142-9612(97)00017-3).
- [84] J. Brown, Using the monocyte activation test as a stand-alone release test for medical devices, *ALTEX* (2021) 151–156, <https://doi.org/10.14573/altex.2012021>.
- [85] Y. Nakagawa, H. Maeda, T. Murai, Evaluation of the in vitro pyrogen test system based on proinflammatory cytokine release from human monocytes: comparison with a human whole blood culture test system and with the rabbit pyrogen test, *Clin. Diagn. Lab. Immunol.* 9 (2002) 588–597, <https://doi.org/10.1128/CDLI.9.3.588-597.2002>.
- [86] Y.v. Chaly, R.S. Selvan, K.v. Fegeding, T.S. Kolesnikova, N.N. Voitenok, Expression of IL-8 gene in human monocytes and lymphocytes: differential regulation by tnf and IL-1, *Cytokine* 12 (2000) 636–643, <https://doi.org/10.1006/CYTO.1999.0664>.
- [87] H.-Y. Hsu, M.-H. Wen, Lipopolysaccharide-mediated reactive oxygen species and signal transduction in the regulation of interleukin-1 gene expression, *J. Biol. Chem.* 277 (2002) 22131–22139, <https://doi.org/10.1074/jbc.M111883200>.
- [88] H. Yuan, C.N. Perry, C. Huang, E. Iwai-Kanai, R.S. Carreira, C.C. Glembotski, R.A. Gottlieb, LPS-induced autophagy is mediated by oxidative signaling in cardiomyocytes and is associated with cryoprotection, *Am. J. Physiol. Heart Circ. Physiol.* (2009) 296, <https://doi.org/10.1152/AJPHEART.01051.2008/ASSET/IMAGES/LARGE/ZH40030987000009.JPG>.
- [89] J.C. Gray, G. Chandra, W.C. Clay, S.W. Stinnett, S.A. Haneline, J.J. Lorenz, I.R. Patel, G. Bruce Wisely, P.J. Furdon, J.D. Taylor, T.A. Kost, A CRE/ATF-like site in the upstream regulatory sequence of the human interleukin 1 beta gene is necessary for induction in U937 and THP-1 monocytic cell lines, *Mol. Cell Biol.* 13 (1993) 6678–6689, <https://doi.org/10.1128/MCB.13.11.6678-6689.1993>.
- [90] K. Li, R. Xing, S. Liu, R. Li, Y. Qin, X. Meng, P. Li, Separation of chito-oligomers with several degrees of polymerization and study of their antioxidant activity, *Carbohydr. Polym.* 88 (2012) 896–903, <https://doi.org/10.1016/j.carbpol.2012.01.033>.
- [91] H. Anggani, E. Hasriati, E. Winiati Bachtari, Evaluation of IL-1 $\alpha$  and IL-1 $\beta$ , COX-2, and iNOS mRNA expression in orthodontic patients given chitosan mouthwash during treatment with miniscrew, *J. Int. Soc. Prev. Community Dent.* 11 (2021) 561–565, [https://doi.org/10.4103/JISPCD.JISPCD\\_163\\_21](https://doi.org/10.4103/JISPCD.JISPCD_163_21).
- [92] T.-C. Chou, E. Fu, E.-C. Shen, Chitosan inhibits prostaglandin E2 formation and cyclooxygenase-2 induction in lipopolysaccharide-treated RAW 264.7 macrophages, *Biochem. Biophys. Res. Commun.* 308 (2003) 403–407, [https://doi.org/10.1016/S0006-291X\(03\)01407-4](https://doi.org/10.1016/S0006-291X(03)01407-4).
- [93] G.-W. Oh, S.-C. Ko, J.-Y. Je, Y.-M. Kim, J. Oh, W.-K. Jung, Fabrication, characterization and determination of biological activities of poly( $\epsilon$ -caprolactone)/chitosan-cafeic acid composite fibrous mat for wound dressing application, *Int. J. Biol. Macromol.* 93 (2016) 1549–1558, <https://doi.org/10.1016/j.ijbiomac.2016.06.065>.
- [94] M. Valko, K. Jomova, C.J. Rhodes, K. Kuča, K. Musilek, Redox- and Non-redox-metal-induced Formation of Free Radicals and Their Role in Human Disease, 2016, <https://doi.org/10.1007/s00204-015-1579-5>.
- [95] Z. Li, F. Yang, R. Yang, Synthesis and characterization of chitosan derivatives with dual-antibacterial functional groups, *Int. J. Biol. Macromol.* 75 (2015) 378–387, <https://doi.org/10.1016/j.ijbiomac.2015.01.056>.
- [96] L. Hu, X. Meng, R. Xing, S. Liu, X. Chen, Y. Qin, H. Yu, P. Li, Design, synthesis and antimicrobial activity of 6-N-substituted chitosan derivatives, *Bioorg. Med. Chem. Lett* 26 (2016) 4548–4551, <https://doi.org/10.1016/j.bmcl.2015.08.047>.
- [97] H. Liu, P. Sun, H. Liu, S. Yang, L. Wang, Z. Wang, Acute toxicity of benzophenone-type UV filters for Photobacterium phosphoreum and Daphnia magna: QSAR analysis, interspecies relationship and integrated assessment, *Chemosphere* 135 (2015) 182–188, <https://doi.org/10.1016/j.chemosphere.2015.04.036>.
- [98] A.K. Refai, M. Textor, D.M. Brunette, J.D. Waterfield, Effect of titanium surface topography on macrophage activation and secretion of proinflammatory cytokines and chemokines, *J. Biomed. Mater. Res.* 70A (2004) 194–205, <https://doi.org/10.1002/jbm.a.30075>.

### 3.3 Glycomimetic Adjuvants: Carbasugar-precursors

#### 3.3.1 Synergy of R-(–)carvone and cyclohexenone-based carbasugar precursors with antibiotics to enhance antibiotic potency and inhibit biofilm formation

##### Own contribution to the article

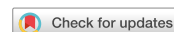
The authors' contribution to this publication was as follows. The conceptualization of the study was carried out by Prof. Deigner, Prof. Schmidt and the author of this thesis. Synthesis of carbasugar-precursors was performed by Ms. Burkhardtmaier and Ms. Gurung. NMR characterization was performed by Prof. Schmidt. Cell culture with biocompatibility studies, including cytotoxicity and cellular reactive oxygen species assays, as well as microbiological tests, including antibacterial assays and biofilm formation were performed and visualized by the author of this thesis. Prof. Deigner and Prof. Schmidt were responsible for funding acquisition and resources. The study was supervised by Prof. Schmidt, Prof. Laufer and Prof. Deigner. Writing of the original draft with visualizations was carried out by Prof. Deigner, Prof. Schmidt and the author of this thesis. All authors reviewed, edited and approved the manuscript.

Reprinted with permission from the Authors. Scientific Reports published by BioMed Central Ltd (Part of Springer Nature). Copyright © 2022, The Author(s). This article is an open access article distributed under a Creative Commons Attribution 4.0 International License

(<http://creativecommons.org/licenses/by/4.0/>).

**Riester, O.; Burkhardtmaier, P.; Gurung, Y.; Laufer, S.; Deigner, H. P.; Schmidt, M. S. Synergy of R-(–)Carvone and Cyclohexenone-Based Carbasugar Precursors with Antibiotics to Enhance Antibiotic Potency and Inhibit Biofilm Formation. *Scientific Reports* 2022, 12 (1), 1–13.**

<https://doi.org/10.1038/s41598-022-22807-8>.



OPEN **Synergy of R-(–)carvone and cyclohexenone-based carbasugar precursors with antibiotics to enhance antibiotic potency and inhibit biofilm formation**

Oliver Riester<sup>1,2</sup>, Pia Burkhardtmaier<sup>1</sup>, Yuna Gurung<sup>1</sup>, Stefan Laufer<sup>2,3</sup>, Hans-Peter Deigner<sup>1,4,5,6</sup> & Magnus S. Schmidt<sup>1,6</sup>✉

The widespread use of antibiotics in recent decades has been a major factor in the emergence of antibiotic resistances. Antibiotic-resistant pathogens pose increasing challenges to healthcare systems in both developing and developed countries. To counteract this, the development of new antibiotics or adjuvants to combat existing resistance to antibiotics is crucial. Glycomimetics, for example carbasugars, offer high potential as adjuvants, as they can inhibit metabolic pathways or biofilm formation due to their similarity to natural substrates. Here, we demonstrate the synthesis of carbasugar precursors (CSPs) and their application as biofilm inhibitors for *E. coli* and MRSA, as well as their synergistic effect in combination with antibiotics to circumvent biofilm-induced antibiotic resistances. This results in a biofilm reduction of up to 70% for the CSP rac-7 and a reduction in bacterial viability of MRSA by approximately 45% when combined with the otherwise ineffective antibiotic mixture of penicillin and streptomycin.

#### Abbreviations

AR	Antibiotic resistance
CSPs	Carbasugar precursors
p-TsOH	p-Toluenesulfonic acid
hMSC	Human mesenchymal stem cells
HUVEC	Human umbilical vein endothelial cells
VC	Vehicle control
CV	Crystal violet
MTT	3-(4,5-Dimethylthiazol-2-yl)-2,5-diphenyltetrazolium bromide
PenStrep	Penicillin and streptomycin
QS	Quorum sensing
agr	Accessory gene regulator
AHL	N-Acyl L-homoserine lactone
FAO	Fatty acid oxidation
DCFDA	2',7'-Dichlorofluorescein diacetate

<sup>1</sup>Institute of Precision Medicine, Furtwangen University, Jakob-Kienzle-Strasse 17, 78054 Villingen-Schwenningen, Germany. <sup>2</sup>Institute of Pharmaceutical Sciences, Department of Pharmacy and Biochemistry, Eberhard-Karls-University Tuebingen, Auf Der Morgenstelle 8, 72076 Tuebingen, Germany. <sup>3</sup>Tuebingen Center for Academic Drug Discovery and Development (TUCAD2), 72076 Tuebingen, Germany. <sup>4</sup>Faculty of Science, Eberhard-Karls-University Tuebingen, Auf Der Morgenstelle 8, 72076 Tuebingen, Germany. <sup>5</sup>EXIM Department, Fraunhofer Institute IZI (Leipzig), Schillingallee 68, 18057 Rostock, Germany. <sup>6</sup>These authors jointly supervised this work: Peter Deigner and Magnus S. Schmidt. ✉email: smag@hs-furtwangen.de

NAC *N*-Acetylcysteine  
 BHA Butylated hydroxyanisole

The increase in antibiotic resistance (AR) and the associated health problems represent one of the major medical challenges for the next decades. In 2019, approximately 4.95 million (64 per 100,000) deaths worldwide could be associated with AR, of which 1.27 million (16.4 per 100,000) deaths were directly attributable to infections with antibiotic resistant pathogens<sup>1</sup>. Even in the case of non-fatal infections with antibiotic resistant pathogens, particularly in the case of chronic courses of disease, patients must cope with considerable loss in quality of life. To counteract this, several approaches must be pursued simultaneously. For example, it is necessary to minimize the development of new AR by a more targeted use of current antibiotics with the help of more accurate diagnostic tools, while at the same time developing new antibiotics or adjuvants that can successfully treat existing resistant pathogens<sup>2,3</sup>. There are several known mechanisms by which ARs act, including alteration or protection of the target, direct inactivation of antibiotics, or reduction in intracellular drug concentration<sup>4</sup>. Furthermore, biofilm formation is known as a widespread defense mechanism that causes resistance or increased tolerance of bacteria to antibiotics or host response<sup>5,6</sup> and is significantly involved in implant infections, cystic fibrosis or chronic wounds<sup>7,8</sup>. One compound class with promising potential as antimicrobial and anti-biofilm agents that can be used to combat ARs, particularly ARs caused by biofilm formation, are carbasugars<sup>9,10</sup>.

Nowadays, carbasugars are discussed in medicinal and pharmaceutical chemistry as promising glycomimetics with potentially broad antibacterial characteristics and advanced properties, especially in terms of metabolic stability and bioorthogonality<sup>11–14</sup>. As early as the 1960s, MacCasland et al. described the synthesis of various carbasugars, such as pseudo-talopyranose or pseudo-galactopyranose, which they referred to as pseudosugars, which term today also includes iminosugars and thiosugars<sup>15,16</sup>. Many more approaches followed, which have been summarized in various review articles to date, focusing on either more applied or synthetic applications and research<sup>11,13,17,18</sup>. Many of the reported synthetic approaches have in common, that they start from simple monosaccharidic structures such as glucosamine and use several sequential derivatization techniques resulting in a multistep synthesis with low to moderate overall yields<sup>19–22</sup>. In addition, these pathways often contain transition metal-catalyzed synthetic steps involving, for example, mercury salts, which can be problematic in scale-up and ultimately in the pharmaceutical application itself<sup>9</sup>. Therefore a more straightforward approach based on other starting materials such as cyclic monoterpenoids, which can be categorized as precursors for substituted cyclohexane derivatives is of great interest. Other strategies based on non-carbohydrate sources as starting materials such as cyclohexadienol<sup>23</sup>, norbornene<sup>24</sup>, iodobenzene<sup>25</sup> or benzoquinone<sup>26</sup> try to overcome these disadvantages and have already been researched.

Herein, we present the first synthesis of simple carbasugar precursors (CSPs) based on R(-)-carvone and cyclohexenone as starting materials. They are called CSPs as they are no exact mimics of natural monosaccharides, but are similar to them and can be further modified to match the definition of carbasugars. These CSPs were evaluated for their potential in biomedical applications. This includes their cytotoxicity to human cells, their effect on bacterial growth and biofilm formation, and their synergistic effect in combination with antibiotics against biofilm formation and antibiotic-resistant bacteria.

## Results

**Synthetic approach to carbasugar precursors.** Many approaches towards carbasugar derivatives based on non-carbohydrate sources start, as mentioned in the introduction, from cyclohexene, cyclohexadiene or benzene derivatives, mainly because these allows the introduction of hydroxy groups by using various addition reactions, ideally stereo- and regioselectively. During our research for an appropriate starting material we decided to use R(-)-carvone (**1**) because of the already present stereochemistry of the propenyl residue and the cyclic carbonyl group, which should allow the introduction of a substituted amino group later on via reductive amination. For related reasons we also chose cyclohexenone (**5**) as another starting material allowing the introduction of cyclic 1,2-diol functionalities. Based on the patent from Surburg et al.<sup>27</sup> which describes the synthesis of compound **2** we initially tried to perform the ketal formation using KHSO<sub>4</sub> or p-toluenesulfonic acid (p-TsOH). Figure 1 shows an overview of the used reaction conditions.

Additionally, to the use of the acids mentioned in the patent we also tried NaHSO<sub>4</sub> as an alternative catalyst (conditions (e) in Fig. 1). Unfortunately, we were not able to reproduce the published results in lab scale (low gram quantities). Instead of compound **2** we were only able to isolate the literature known aromatic compound **4** as a sole main product in yields > 50% (spectral data agree with published data<sup>28,29</sup>). After additional literature research we decided to use polyanilinium sulfate as an alternative acidic catalyst based on the work of Palaniappan et al.<sup>30</sup>. The polyanilinium sulfate was synthesized according to the published data and after some optimization steps we succeeded in synthesizing compound **2** in isolated yields between 42–48%. For the stereoselective intramolecular bishydroboration we adapted the work of Brown and Pfaffenberger<sup>31</sup> which used thexylborane for the cyclic hydroboration of dienes, especially of D-(+)-limonene, which has the same diene structure as compound **2**. After the optimization of the reaction, we could obtain compound **3** in yields around 40%. The trans configuration of the cyclic OH- and methyl-group could be confirmed by identifying the corresponding protons (see Fig. 2; red and blue colorized protons) via COSY (SI, Fig. S8) and by determination of the <sup>3</sup>J<sub>H,H</sub> coupling constant between these two protons, which, with a value of 10.5 Hz, correlates to the expected value estimated by the Karplus equation.

Furthermore, we were able to confirm the stereochemistry of the exocyclic alcoholic residue by NOESY (SI, Fig. S9) cross coupling between the green protons and the red in Fig. 2.

Unfortunately, we were not able to identify the stereochemistry of the exocyclic tertiary carbon. The fact, that the <sup>13</sup>C spectrum (SI, Fig. S7) partially shows two very narrow signals for various carbons of compound

www.nature.com/scientificreports/

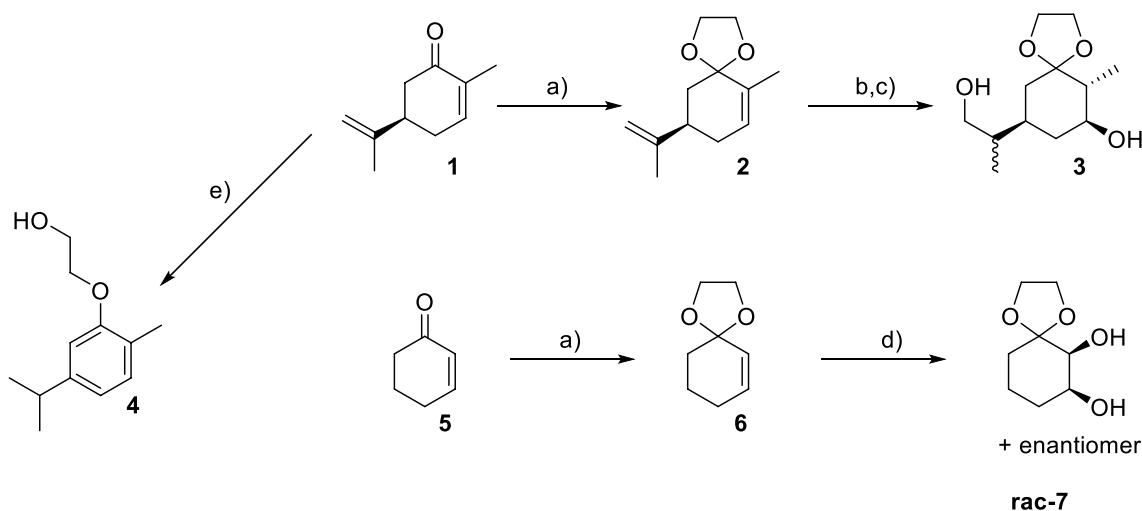


**Figure 1.** Synthetic approach to carbasugar precursors. (a) polyaniliniumsulfate, ethylene glycol, toluene, reflux (Dean–Stark apparatus); (b)  $\text{BH}_3 \cdot \text{THF}$ , 2,3-Dimethyl-2-butene; (c)  $\text{H}_2\text{O}_2/\text{NaOH}$ ; (d)  $\text{KMnO}_4$ ,  $\text{MgSO}_4$ ,  $\text{H}_2\text{O}$ ; (e)  $\text{pTsOH}$  or  $\text{KHSO}_4$  or  $\text{NaHSO}_4$ , ethylene glycol, toluene reflux (Dean–Stark apparatus).

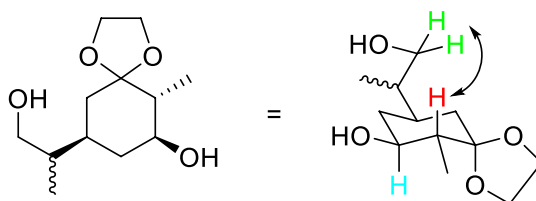


**Figure 2.** Chair conformation of compound 3 with indicated coupling in 2D NMR.

3, indicates though, that we isolated a mixture of two diastereomers which presumably differ at the exocyclic tertiary carbon and cannot be identified or isolated by chromatographic techniques.

Comparing the method of Brown and Pfaffenberger with the use of simple borane  $\text{BH}_3$ , it is interesting to mention that in case of using  $\text{BH}_3$ , we only could obtain the exocyclic monohydroxy-compound selectively. The cyclic double bond has not been attacked by the borane.

For the synthesis of precursor **rac-7**, we started from compound 5 using polyanilinium sulfate as acidic catalyst resulting in compound 6 in 52% yield. Afterwards we used standard reaction conditions (conditions (d) in Fig. 1) for the diol formation leading to compound **rac-7** as racemic mixture in 30% yield. Compounds 3 and **rac-7** have then been used for the following biological evaluation.

**Biocompatibility.** The potential for biomedical application depends fundamentally on the biocompatibility of the substance or material in question, otherwise the side effects of a treatment will exceed the benefits. To address this issue, we tested the synthesized CSPs for their biocompatibility with human cells. For this purpose, concentration-dependent metabolic activity and cellular reactive oxygen species (ROS) were determined for human osteogenic sarcoma SaOS-2 cells (SaOS-2), human bone marrow derived mesenchymal stem cells (hMSC), and human umbilical vein endothelial cells (HUVEC) (Fig. 3). No cytotoxic effects were observed for all three cell types at concentrations up to 100  $\mu\text{M}$  (Fig. 3A–C), and a concentration of 1 mM proved toxic only for SaOS-2 cells, resulting in a reduction of metabolic activity for **rac-7** by up to 55  $\pm$  9% ( $p < 0.001$ ) and for 3 by up to 66  $\pm$  2% ( $p < 0.001$ ) compared to the control sample. However, the highest tested concentration of 10 mM resulted in strong cytotoxic effects in all cell types, resulting in metabolic activity of -3  $\pm$  4% ( $p < 0.001$ ), 63  $\pm$  3% ( $p = 0.002$ ), and 9  $\pm$  2% ( $p < 0.001$ ) for hMSC, HUVEC, and SaOs-2 cells for **rac-7** and 72  $\pm$  7% ( $p = 0.46$ ), 52  $\pm$  3% ( $p < 0.001$ ), and 26  $\pm$  4% ( $p < 0.001$ ) for 3, respectively. This trend was confirmed by the measurements of cellular ROS level normalized to the metabolic activity (Fig. 3D–F), as seen by an increased cellular ROS level per metabolic activity with increasing concentrations of CSPs for hMSCs and SaOS-2 cells. HUVECs, on the other hand, seem to be less affected by the CSPs than the other two cell types, indicated by no significant increase of cellular ROS, except for 10 mM 3. In addition, no significant change of cellular ROS level was observed for HUVECs between 24 and 48 h (Two-way ANOVA with Tukey post-hoc test, 24 against 48 h:  $p = 0.805$  (**rac-7**);  $p = 0.9998$

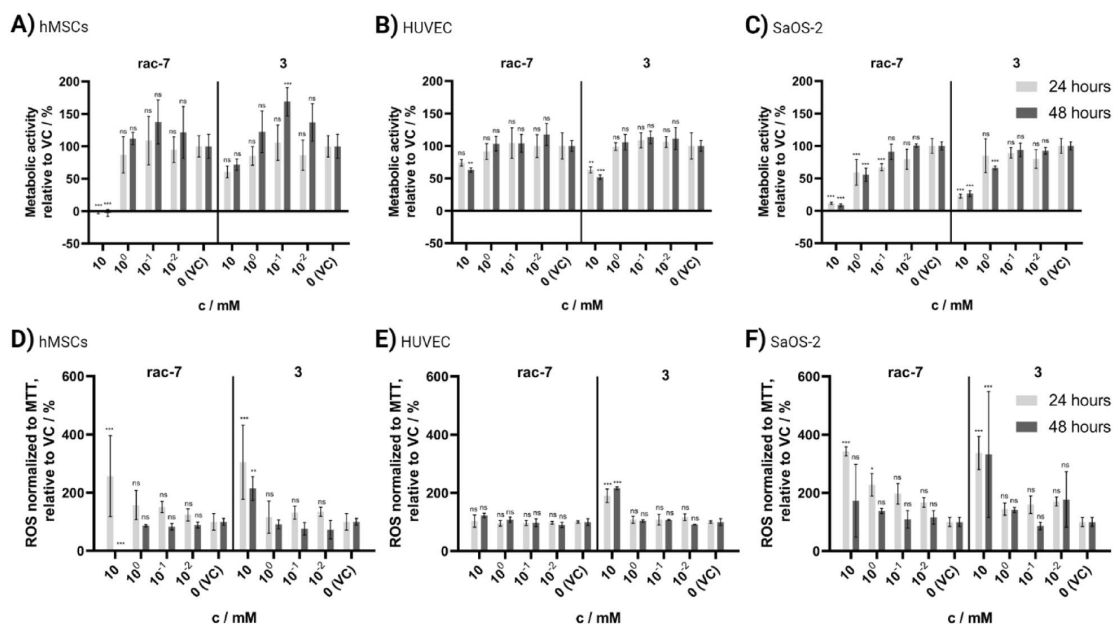


**Figure 3.** Biocompatibility of the compounds **rac-7** and **3**. Human mesenchymal stem cells (hMSC), human umbilical vein endothelial cells (HUVEC) and SaOS-2 human osteogenic sarcoma cells treated for 24 and 48 h. (A–C) Evaluation of metabolic activity at different concentrations of CSPs with MTT-assay in comparison to vehicle control (VC). (D–F) Cellular reactive oxygen species (ROS) normalized to MTT-assay and compared to VC. VC was treated with PBS instead of CSPs stock solution. Values are shown as mean  $\pm$  SD ( $n=3$ ). Statistical significance was analyzed with Two-way ANOVA and Dunnett post-hoc test against respective VC (ns not significant; \* $p < 0.05$ ; \*\* $p < 0.01$ ; \*\*\* $p < 0.001$ ). For additional concentrations, as well as microscopic images, see Supplemental Fig. S1.

(3)), whereas a significant change over time was observed for hMSCs (Two-way ANOVA with Tukey post-hoc test, 24 against 48 h:  $p < 0.001$  (**rac-7**);  $p < 0.001$  (**3**)) and the compound **rac-7** for the SaOS-2 cells (Two-way ANOVA with Tukey post-hoc test, 24 against 48 h:  $p = 0.0021$  (**rac-7**);  $p = 0.2312$  (**3**)).

**Microbial growth.** For biomedical applications, in addition to biocompatibility, the functional properties, particularly the antimicrobial properties, of the substance are important. Therefore, we investigated whether CSPs affect the growth of the gram-negative bacteria *Escherichia coli* (*E. coli*) and the gram-positive bacteria multi-resistant *Staphylococcus aureus* (MRSA) and whether they are used as a carbon source for growth. The growth of both bacterial strains in LB medium supplemented with the indicated concentrations of CSPs (Fig. 4A,B) differed only minimally or to a non-significant extent from the vehicle control without supplementation. Thus, no significant increase in generation time of *E. coli* was observed even for the highest tested concentration of 10 mM for both the compound **rac-7** with  $36.1 \pm 0.7$  min ( $p = 0.35$ ) and **3** with  $35.1 \pm 0.3$  min ( $p = 0.95$ ) compared to the vehicle control with  $34.4 \pm 0.4$  min. For MRSA, a non-significant effect for **rac-7** with  $49.9 \pm 0.9$  min ( $p = 0.15$ ) and a significant effect for **3** with  $50.3 \pm 0.4$  min ( $p = 0.05$ ) on the generation time compared to the vehicle control with  $48.1 \pm 0.6$  min was observed. Furthermore, it was observed that 10 mM **rac-7** leads to a considerable prolongation of the initial lag phase in MRSA growth (SI, Fig. S2A), which was not observed for *E. coli*, respectively compound **3** (SI, Fig. S2B–D). While there appears to be a concentration-dependent effect on bacterial growth, this effect is negligible and occurs only at concentrations that are not desirable for biocompatibility reasons (above 100  $\mu$ M).

In addition, it was investigated whether the compounds **rac-7** and **3** are used as a carbon source for bacterial growth, which would indicate their metabolization. Our initial assumption that the CSPs could not be used as a carbon source was confirmed, as can be seen in Fig. 4C,D. No growth was observed in PBS or PBS with CSPs, but growth was observed when the same concentration of glucose was added.

**Biofilm.** After investigating the effects on bacterial growth, we focused our attention on another important aspect of antimicrobial properties for biomedical applications: biofilm inhibition. Therefore, the biofilm formed in the presence of compounds **rac-7** and **3** was determined and compared with the vehicle control (VC) to which the same volume of PBS was added. In all combinations of the two compounds and bacterial strains, a significant decrease in biofilm after 24–72 h of incubation (Fig. 5) compared to the respective control was observed. There were only minor differences between the two compounds tested, most of which were within the range of the standard deviation. In addition, it is noteworthy that the compounds showed higher-relative-biofilm inhibition

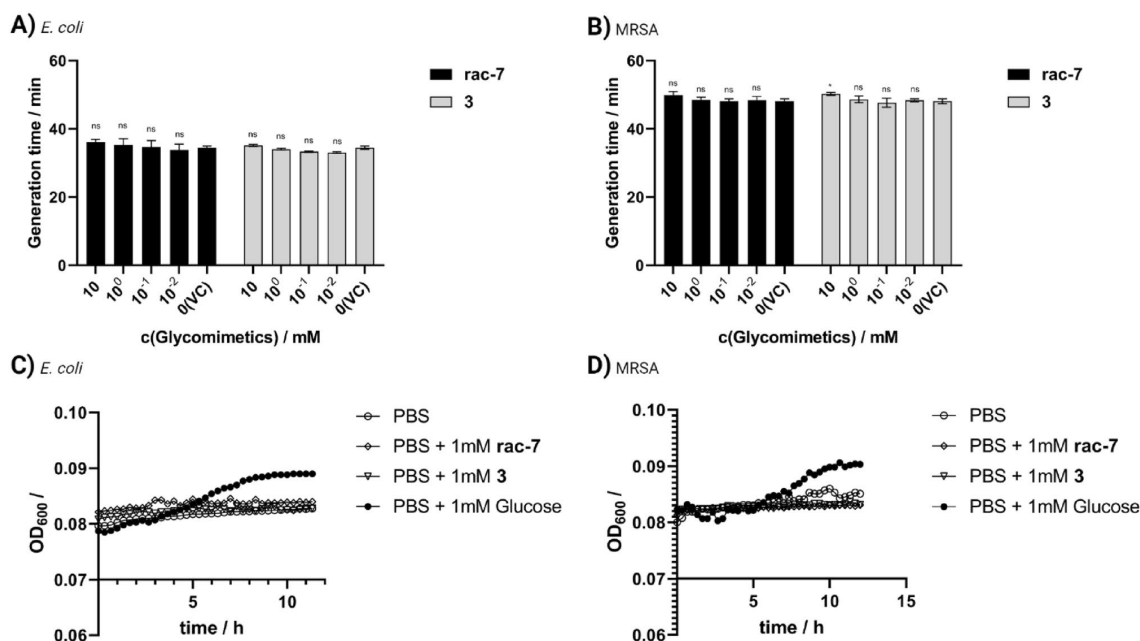


**Figure 4.** Effects of the compounds **rac-7** and **3** on the bacterial growth of *Escherichia coli* (*E. coli*) and multi-resistant *Staphylococcus aureus* (MRSA). Concentration-dependent influence of CSPs on the generation time of *E. coli* (A) and MRSA (B) in LB medium. Growth of *E. coli* (C) or MRSA (D) in PBS supplemented with CSPs or glucose. VC was treated with PBS instead of CSPs stock solution. Values are shown as mean  $\pm$  SD (A,B:  $n=3$ ) or mean (C,D:  $n=3$ ). Statistical significance was analyzed with Two-way ANOVA and Dunnett post-hoc test against respective vehicle control (VC) (ns not significant; \* $p < 0.05$ ; \*\* $p < 0.01$ ; \*\*\* $p < 0.001$ ).

for the weak biofilm former *E. coli* (Fig. 5A,B) than for the good biofilm former MRSA (Fig. 5C,D), even though in absolute terms the biofilm formed by MRSA was more inhibited (SI, Fig. S3). Overall, 100  $\mu$ M proved to be the concentration with the best compromise between good biocompatibility (Fig. 3) and biofilm inhibition for both compounds. Concentrations of 100  $\mu$ M resulted in a reduction of biofilm formed by  $64 \pm 1\%$  (**rac-7**,  $p=0.001$ ) and  $70 \pm 5\%$  (**3**,  $p < 0.001$ ) for *E. coli* as well as  $39 \pm 1\%$  (**rac-7**,  $p=0.02$ ) and  $42 \pm 2\%$  (**3**,  $p=0.008$ ) for MRSA after 72 h of treatment with 100  $\mu$ M CSPs.

**Synergistic effect: carbasugar precursors and antibiotics.** The formation of biofilms is a widespread defense mechanism of bacteria, not only as a protection against harsh environmental conditions, but also to reduce the effectiveness of antibiotics and increase bacterial tolerance. Therefore, it is important to prevent the formation of biofilm, e.g. in wounds or on surgical implants, to ensure promising treatment success for infections caused by multidrug-resistant microorganisms and to minimize the development of further resistance. We investigated a combinatorial approach of the synthesized CSPs in combination with the antibiotic mixture of penicillin and streptomycin (PenStrep) for synergistic effects. It was observed that *E. coli* was sensitive to PenStrep antibiotic mixture (Fig. 6A,E,K), while MRSA showed resistance (Fig. 6B,H,N) and even formed more biofilm at low antibiotic concentrations than without (Fig. 6F). Addition of PenStrep without CSPs to a growing biofilm or non-biofilm cultivation of *E. coli* prevented biofilm formation and resulted in nearly no viable cells remaining with no metabolic activity of the population. In contrast, the addition of PenStrep did not completely eliminate an already developed biofilm of *E. coli*, but significantly reduced it (Fig. 6I: Two-way ANOVA with Tukey post-hoc test; VC, 100 U/mL PenStrep against VC, 0 U/mL PenStrep:  $p < 0.001$ ) and the number of viable cells (Fig. 6K: Two-way ANOVA with Bonferroni post-hoc test; VC, 100 U/mL PenStrep against VC, 0 U/mL PenStrep:  $p=0.03$ ), even though metabolic activity of the population could still be detected (Fig. 6J: Two-way ANOVA with Tukey post-hoc test; VC, 100 U/mL PenStrep against VC, 0 U/mL PenStrep:  $p=0.01$ ). The combined use of PenStrep with the compounds **rac-7** and **3** resulted for *E. coli* in a non-significant further reduction of the biofilm formed, metabolic activity and viable cells. As mentioned, the addition of PenStrep at low concentrations had a counterproductive effect on biofilm formation of MRSA, both in the developed biofilm and in the growing biofilm. The addition of CSPs was able to counteract this effect, such that when **rac-7** was added in combination with 100  $\mu$ M PenStrep, biofilm formation was comparable to **rac-7** without PenStrep, but significantly less than 100  $\mu$ M PenStrep without **rac-7** (Fig. 6F,L). However, the addition of CSPs, particularly **rac-7**, in combination with PenStrep (**rac-7** + PenStrep,  $216 \pm 33 \times 10^6$  CFU/cm<sup>2</sup>) resulted in a significant reduction of viable bacterial cells (Fig. 6H) compared to separate addition (**rac-7**,  $316 \pm 16 \times 10^6$  CFU/cm<sup>2</sup>; PenStrep,  $395 \pm 31 \times 10^6$  CFU/cm<sup>2</sup>; VC,  $379 \pm 21 \times 10^6$  CFU/cm<sup>2</sup>) when the compounds were present during the process

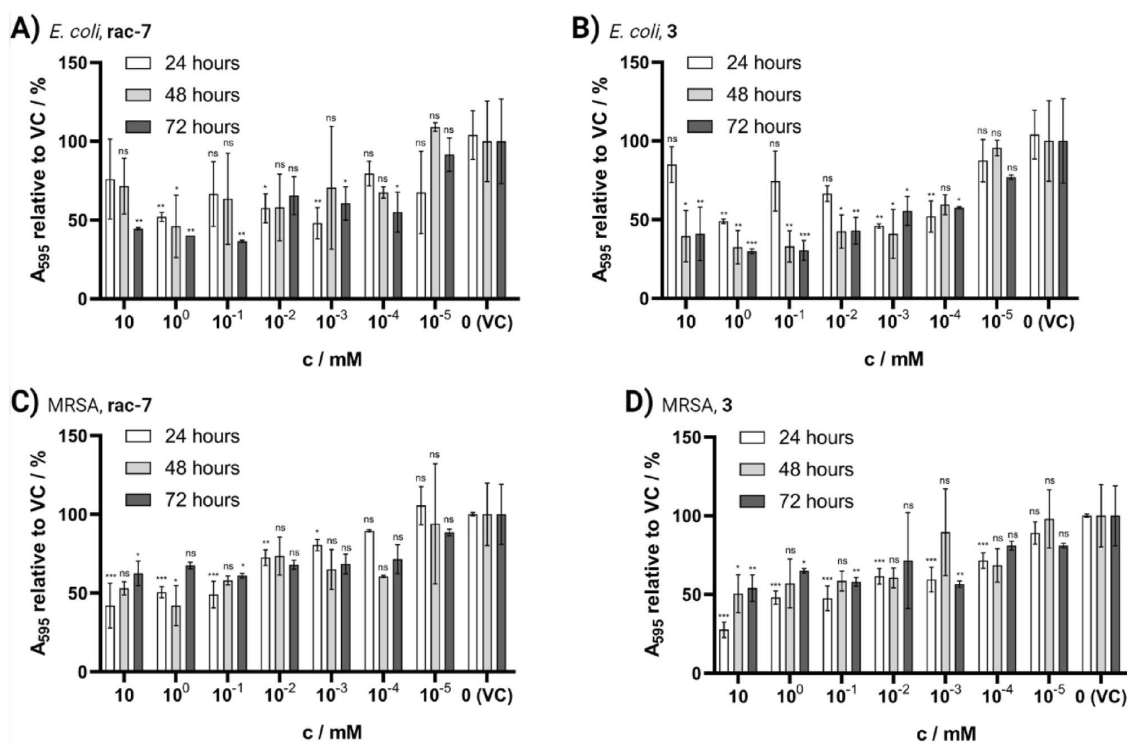


**Figure 5.** Evaluation of biofilm formation in the presence of CSPs with crystal violet (CV) assay. Biofilm formation of *Escherichia coli* (*E. coli*; **A,B**) and multi-resistant *Staphylococcus aureus* (MRSA; **C,D**) after 24, 48 and 72 h of incubation in the presence of 10 mM to 10 nM CSPs. Values are shown in relation to vehicle control (VC; PBS instead of compound stock solution) as mean  $\pm$  SD ( $n=2$ ). Statistical significance was analyzed with Two-way ANOVA and Dunnett post-hoc test against respective VC (*ns* not significant; \* $p < 0.05$ ; \*\* $p < 0.01$ ; \*\*\* $p < 0.001$ ).

of biofilm formation. A similar effect was observed for compound **3** on the viable bacterial cells (**3** + PenStrep,  $229 \pm 41 \times 10^6$  CFU/cm<sup>2</sup>; **3**,  $362 \pm 41 \times 10^6$  CFU/cm<sup>2</sup>; PenStrep,  $395 \pm 31 \times 10^6$  CFU/cm<sup>2</sup>; VC,  $379 \pm 21 \times 10^6$  CFU/cm<sup>2</sup>). The addition of 100  $\mu$ M **rac-7** in addition to 100 U/mL PenStrep reduced the biofilm formed by 64% ( $p=0.003$ ), the metabolic activity by 28% ( $p=0.009$ ) and the viable cells by 45% ( $p=0.006$ ) compared to the respective VC. Interestingly, **rac-7** also showed an effect on already developed biofilm of MRSA when administered in combination with 100 U/mL PenStrep (Fig. 6L), reducing biofilm by 52% ( $p < 0.001$ ), cell viability by 46% ( $p=0.1$ ) but only non-significantly decreasing metabolic activity of the population with an absorption at 570 nm of  $0.86 \pm 0.02$  ( $p=0.59$ ) compared to an absorption at 570 nm of  $1.07 \pm 0.02$  for the corresponding VC.

### Discussion

The synthetic approaches for the mentioned CSPs, starting from simple and cheap compounds, turned out to be less trivial than expected. Especially the formation of the aromatic compound **4** seems to be problematic for the important first protection step of the keto-group of R-(−)carvone when using standard conditions like catalytic amount of pTsOH and a Dean–Stark apparatus. The use of polyanilinium sulfate helped to overcome these challenge, resulting in passable yields, which makes this catalyst very interesting for further studies using other simple natural products with predefined stereochemistry such as camphor or other terpenes containing keto-groups. Furthermore, intramolecular bishydroboration leading stereoselectively to compound **3**, has shown to be a very good tool on the way to stereoselective carbasugar synthesis.

For the biological evaluation, we demonstrate the synergistic effect of the compounds **3** and **rac-7** in combination with antibiotics against the bacteria *E. coli* and MRSA. When treated solely with the PenStrep antibiotic mixture, *E. coli* were susceptible and MRSA resistant to it (Fig. 6). When administered in combination against MRSA, the effects of PenStrep and the compound **rac-7** complemented each other and reduced both biofilm formation and viable bacteria beyond the level of single administration. For *E. coli*, no statement can be made about synergistic effects, since the addition of antibiotics alone had a strong effect, so that further effects could be barely detected. Thus, the proportion of biofilm present was reduced on the one hand, and the proportion of viable bacteria was reduced on the other hand, for both the already developed and the still growing biofilm, but not for the non-biofilm condition. Furthermore, it is worth mentioning that the reduction of viable cells was significant only for growing biofilm and not for developed biofilm, suggesting that the formation of new biofilm

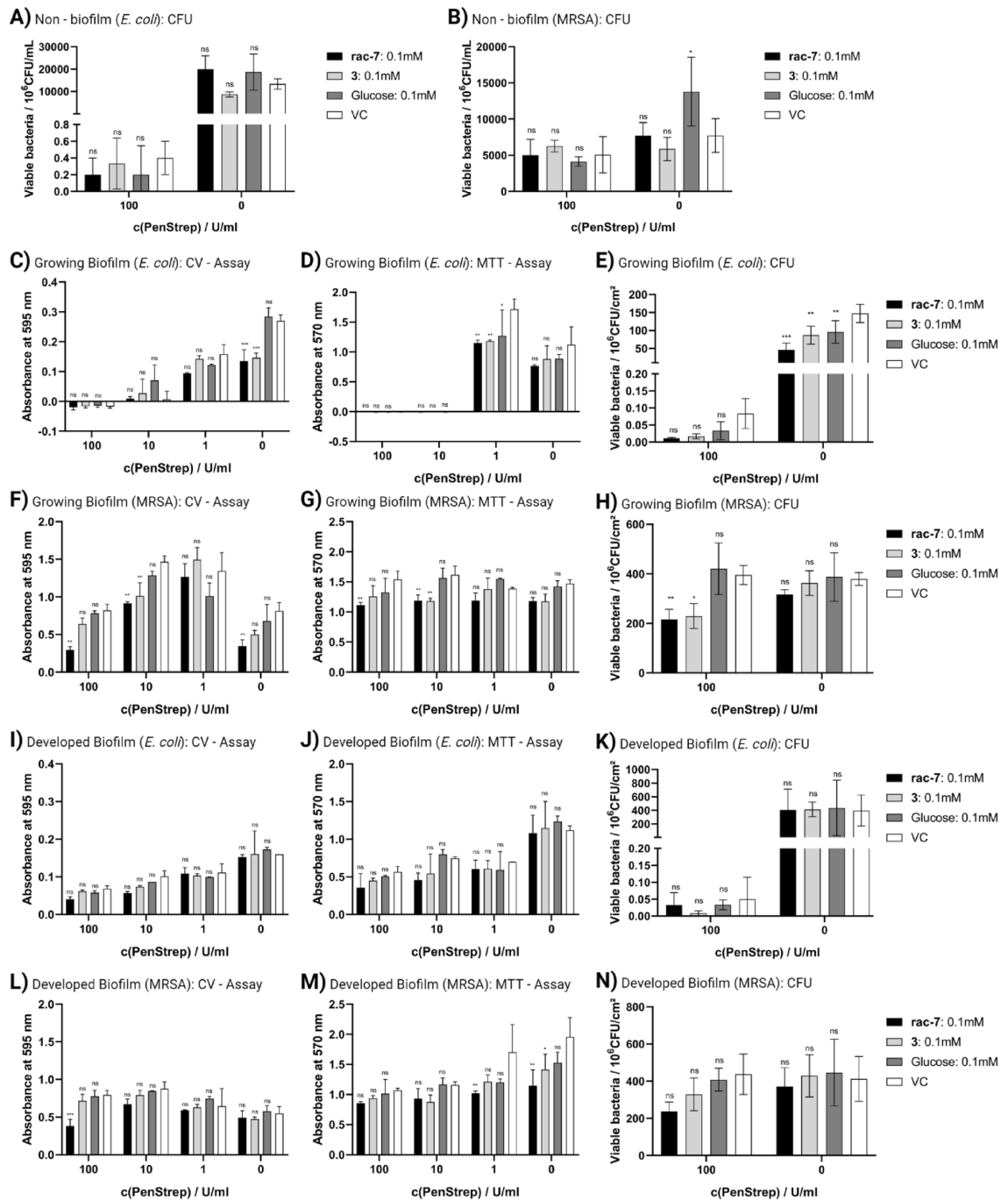


**Figure 6.** Synergistic effects of CSPs and antibiotics. Biofilm formation, metabolic activity and viable cells of *Escherichia coli* (*E. coli*; **A, C–E, I–K**) and multi-resistant *Staphylococcus aureus* (MRSA; **B, F–H, L–N**) under the influence of the compounds **rac-7** and **3** in combination with the antibiotics mixture of penicillin and streptomycin (PenStrep). Biofilm formation was evaluated via crystal violet (CV) assay (**C, F, I, L**), metabolic activity via MTT assay (**D, G, J, M**) and viable cells via CFU counting (**A, B, E, H, K, N**) after 48 h of treatment. Treatment was performed on non-biofilm cells (liquid culture in LB medium), growing biofilm and on developed biofilm. VC was treated with PBS instead of CSPs stock solution. Values are shown as mean  $\pm$  SD (CV, MTT:  $n=2$ ; CFU:  $n=3$ ). Statistical significance was analyzed with Two-way ANOVA and Dunnett post-hoc test against respective VC (*ns* not significant; \* $p < 0.05$ ; \*\* $p < 0.01$ ; \*\*\* $p < 0.001$ ).

is inhibited, but existing biofilm is not actively disrupted. This demonstrates the potential of adjuvants to antibiotics for applications where antibiotic resistance is expected as a result of biofilm formation, for example in open wounds, especially chronic wounds or after surgical implantation<sup>32</sup>. Various classes of substances with anti-biofilm properties have already been identified and tested for their suitability to inhibit biofilm, such as carbohydrate derivatives (e.g. derivatives of  $\alpha$ -D-mannoside<sup>40</sup>, fucose or xylose<sup>33</sup>), D-amino acids<sup>34</sup>, polysaccharides (e.g. group II capsular polysaccharides<sup>35</sup>, chitosan derivatives<sup>36</sup>) or antimicrobial peptides<sup>37</sup>. These substances have different modes of actions and intervene at different stages of biofilm maturation, e.g., initial cell adhesion, secretion of extracellular polymeric substances, or biofilm degradation, as reviewed by Srinivasan et al.<sup>38</sup> or Verderosa et al.<sup>39</sup>.

The mode of action of CSPs was not investigated in this study, but we hypothesize that they mitigate biofilm formation either through enzyme inhibition/protein binding, quorum sensing (QS) or a combination of both. Inhibition of biofilm formation by CSPs could occur through structural similarity to a natural substrate and act as a competitive inhibitor to cause enzymatic inhibition, as shown for example by Ren et al.<sup>40</sup> for carbasugars and glycoside hydrolases, or cause reduced protein-target interaction, as shown by Sommer et al.<sup>10</sup> for derivatives of methyl  $\alpha$ -D-mannoside and the bacterial carbohydrate-binding protein LecB. A reduced protein-target interaction by competition for carbohydrate binding sites of lectins affects the bacterial adhesion of *E. coli* to surfaces, which in turn leads to inhibition of biofilm formation<sup>41</sup>. It is also possible that the CSPs activate QS systems: in gram positive MRSA, the accessory gene regulator (*agr*) system, as observed by Ueda et al. upon addition of 5.6 mM glucose and for gram negative *E. coli* the *N*-acyl L-homoserine lactone (AHL) mediated QS system<sup>42,43</sup>. Activation of the respective QS system leads to biofilm detachment and swarming motility, whereas repression of the *agr* system is necessary for biofilm formation<sup>44,45</sup>. Upon biofilm disruption, the bacteria leave the protective biofilm and enter the planktonic state, making them susceptible to antibiotics and human macrophages from which they were previously protected in the biofilm<sup>6,46</sup>. Moreover, unlike carbohydrates, the tested compounds have the advantage of not being used for bacterial growth (Fig. 4C,D), thus, on the one hand, they do not contribute to aggravation of the infection condition by bacterial growth and, on the other hand, they are present in a long-term effective concentration. Furthermore, the additional biofilm formed by MRSA as a defense response to PenStrep was significantly reduced when PenStrep was administered in combination with CSPs (Fig. 6FL). Thus, the addition of CSPs not only allows circumvention of existing antibiotic resistance, but also ensures the efficacy of subsequent antibiotic treatments, as a more developed biofilm reduces the chances of success and even promotes the emergence of new antibiotic resistances<sup>47</sup>.

For the three human cell types tested, no toxicity was observed for concentrations up to 100  $\mu$ M, nevertheless concentrations of 10 mM were toxic, especially for **rac-7**. Indeed, we observed that the CSPs had less toxic effects on HUVECs than on the hMSCs and SaOS-2 cells, which may readily be explained by an inhibition of glycolysis and differential dependence of cell types on it for ATP production. The energy metabolism of all three cell types is preferentially based on glycolysis and subsequent mitochondrial respiration, even in SaOS-2 cells, which does not show the Warburg effect typical for cancer cell lines<sup>48–50</sup>. The inhibition of glycolysis as a consequence of the high concentration of CSPs subsequently leads to a loss of ATP, both directly via the inhibition of glycolysis and indirectly by lowered generation of acetyl-CoA for the tricarboxylic acid cycle and NADH for oxidative phosphorylation. As an alternative energy source, cells are left with fatty acid oxidation (FAO) or glutaminolysis. In contrast to HUVECs, SaOS-2 cells and hMSCs have no significant FAO, which may be the reason that HUVECs showed higher tolerance to the tested CSPs (Fig. 3), since they can not only rely on glutaminolysis but also on FAO for ATP generation<sup>51,52</sup>.

The study presented here initially focused on the effect and applicability of the synthesized substances. The exact mechanisms leading to the toxic effects on human cells are interesting to rule out potential side effects, however, these only occur at very high concentrations of 10 mM, so they can be easily avoided in real conditions. In contrast, the exact mechanism for biofilm inhibition is of particular interest as it occurs at lower concentrations in the micromolar range, and by identifying the mode of action, novel glycomimetics can be functionalized in a targeted manner to achieve a better effect at even lower concentrations. Nevertheless, the presented study demonstrated the synergistic potential of CSPs or carbasugars in general to prevent biofilm-associated infections, supporting antibiotic treatments, and the possibility of reducing the impact of antibiotic resistance and the emergence of new resistances.

## Materials and methods

**Materials.** Absorbance measurements were performed with a TECAN infinite M200 PRO (TECAN, Switzerland) plate reader. Microscopic images were taken with the microscope Olympus CXK41 (Olympus, Japan) mounted with the camera Olympus XM10 (Olympus, Japan) and the associated software cellSens Standard (Version 1.9 Build 11514, Olympus, Japan). 100 mM stock solutions of the compounds **rac-7** and **3** were prepared in phosphate buffered saline (PBS), sterile filtered with 0.2  $\mu$ m nylon sterile filters (Carl Roth GmbH + Co. KG, Karlsruhe, Germany) and stored at 8 °C. T-75 cell culture flasks were purchased from VWR International GmbH (Bruchsal, Germany) and 96-well tissue culture plates were purchased from TPP Techno Plastic Products AG (Trasadingen, Switzerland). SaOS-2 human osteogenic sarcoma cells (SaOS-2, ACC 243) and human bone marrow derived mesenchymal stem cells (hMSC) were purchased from Sigma Aldrich (Taufkirchen, Germany) and human umbilical vein endothelial cells (HUVEC) were purchased from Fisher Scientific GmbH (Schwerte, Germany). 100  $\times$  penicillin–streptomycin mixture (PenStrep) containing 10,000 U/mL penicillin and 10,000 U/mL streptomycin was purchased from Lonza Group Ltd (Basel, Switzerland). Chemicals and reagents for the chemical synthesis were purchased from Acros, Sigma-Aldrich, Carl Roth or ABCR and were used without further purification. Chemicals and culture media for the biological evaluation were purchased from Sigma Aldrich (Taufkirchen, Germany) unless stated otherwise.

**Synthesis of carbasugar precursors.** TLC was carried out on Silica Gel 60 F254 (Merck, layer thickness 0.2 mm) or on M&N RP-18 W/UV254 with detection by UV light (254 nm) and/or by charring with 15% sulfuric acid in ethanol. Flash column chromatography (FC) was performed on M&N Silica Gel 60 (0.063–0.200 mm) or on Macherey-Nagel (M&N) Silica Gel 100 C18 in case of RP-FC. <sup>1</sup>H NMR and <sup>13</sup>C NMR spectra were recorded either on a Bruker Avance 400 or on a Magritek Carbon 60. Chemical shifts are reported in ppm relative to solvent signals (CDCl<sub>3</sub>: δH=7.26 ppm, δC=77.0 ppm; DMSO-d<sub>6</sub>: δH=2.49 ppm, δC=39.7 ppm; CD<sub>3</sub>OD: δH=4.78 ppm, δC=49.3 ppm). Signals were assigned by first-order analysis and assignments were supported, where feasible, by two-dimensional <sup>1</sup>H, <sup>1</sup>H and <sup>1</sup>H, <sup>13</sup>C correlation spectroscopy. Coupling constants are reported in Hz. Electrospray ionization mass spectra (ESI) were performed on Sciex API QTRAP Mass Spectrometer (AB Sciex LLC, Framingham, MA, USA). The mass spectrometer was operated in the positive ion mode with an electrospray voltage of 5000 V at 200 °C, curtain gas at 25 psi, collision gas at 6 psi, nebulizing gas at 25 psi and auxiliary gas at 25 psi. All quadrupoles were working at unit resolution. RP-UPLC was performed on an Acquity system from Waters with a BEH C18 1.7 μm column (2.1 × 50 mm) from Waters and a gradient of water (eluent A) and methanol (eluent B) as an eluent. All compounds synthesized are >95% pure by UPLC analysis.

**Carvone-ketal (2).** 10 g (66.6 mmol) R(-)-carvone, 11.1 g (179 mmol) ethylene glycol and 250 mg of polyanilinium sulfate were added to 100 mL of toluene in a 250 mL double-necked round bottom flask equipped with a Dean–Stark trap and a condenser. The mixture was heated to reflux for 8 h during the daytime and to 80 °C over night for a period of 4 days. Each day 2 more mL of ethylene glycol were added, and the reaction was monitored by TLC. After filtration over celite and purification by flash-chromatography (ethyl acetate/isohehexane 9:1) compound **2** was isolated in 48% yield as a colourless oil. TLC: R<sub>f</sub>=0.35 (ethyl acetate/isohehexane 9:1); RP-UPLC: t<sub>r</sub>=4.04 min (10–90% B in 7 min, 95.5% purity); <sup>1</sup>H-NMR: (200.1 MHz, CDCl<sub>3</sub>) δ=5.68 (m, 1 H, cycl. HC=C), 4.70 (m, 2 H, H<sub>2</sub>C=C), 4.10–3.87 (m, 4 H, OCH<sub>2</sub>CH<sub>2</sub>O), 2.43 (dddd, J=13.6 Hz, 12.0 Hz, 4.8 Hz, 2.9 Hz, 1 H, CH<sub>2</sub>CHCH<sub>2</sub>), 2.16 (dt, J=17.5 Hz, 5.3 Hz, 1.4 Hz, 1 H, 1 × CH<sub>2</sub>), 1.97–1.65 (m, 3 H, 3 × CH<sub>2</sub>), 1.71 (m, 3 H, CH<sub>3</sub>), 1.66 (m, 3 H, CH<sub>3</sub>); <sup>13</sup>C-NMR (50.3 MHz, CDCl<sub>3</sub>) δ=148.6 (C-8), 134.1 (C-5), 128.3 (C-4), 109.0 (C-9), 108.2 (C-6), 65.7 (C-12), 64.74 (C-13), 39.9 (C-2), 38.8 (C-1), 30.9 (C-3), 20.5 (C-10), 15.9 (C-7); (ESI-MS): m/z 195.3 [M + H]<sup>+</sup>.

**Carvone-ketal diol (3).** 10.4 mL (10.4 mmol) of a 1 M borane-THF complex solution and 1.3 mL (11 mmol) of 2,3-Dimethyl-2-butene were dissolved in 25 mL dry THF in a 250 mL Schlenk flask under nitrogen and stirred for 10 min. Then 2 g of compound **2** (8.7 mmol) was added and the mixture was stirred for additional 2 h at room temperature till no more starting material was detected by RP-TLC. Finally 1.1 g of NaOH dissolved in 1.8 mL of deionized water were added dropwise followed by the addition of 30% H<sub>2</sub>O<sub>2</sub>. After 2 h the mixture was diluted with 20 mL of deionized water and extracted several times with small amounts of ethyl acetate. The combined organic layers were washed with brine, dried (MgSO<sub>4</sub>) and the solvent was evaporated. After purification by RP-flash-chromatography (ethanol/water 1:9) compound **3** was isolated in 42% yield as a colourless oil. RP-TLC: R<sub>f</sub>=0.3 (ethanol/water=1:9); RP-UPLC: t<sub>r</sub>=0.33 min (5–50% B in 7 min, 97.4% purity); <sup>1</sup>H-NMR: (200.1 MHz, DMSO-d<sub>6</sub>) δ=4.48 (d, J=5.8 Hz, 1 H, cycl. OH), 4.34 (dt, J=8.6 Hz, 5.1 Hz, CH<sub>2</sub>OH), 3.30–3.05 (m, 3 H, CH<sub>2</sub>OH, cycl. CHOH), 1.80–1.67 (m, 1 H, CHCH<sub>2</sub>OH), 1.65–1.31 (m, 3 H, 3 × CH<sub>2</sub>), 1.41 (dd, J=10.5 Hz, 6.5 Hz, 1H, cycl. CH(CH<sub>3</sub>)), 1.15–0.91 (m, 2H, CH and 1 × CH<sub>2</sub>), 0.85 (d, J=6.5 Hz, 3 H, cycl. CH<sub>3</sub>), 0.77 (dd, J=6.5 Hz, 4.8 Hz, 3 H, CH<sub>3</sub>); <sup>13</sup>C-NMR (50.3 MHz, CDCl<sub>3</sub>) δ=110.7 (C-6), 72.1 (C-4), 65.3 (C-9), 64.6 (C-14), 64.5 (C-15), 47.8 (C-5), 37.3 (C-8), 33.0 (C-1), 32.6 (C-3), 14.1 (C-2), 13.5 (C-10), 10.1 (C-7); (ESI-MS): m/z 231.5 [M + H]<sup>+</sup>.

**Cyclohexenone-ketal (6).** 13.46 g (140 mmol) 2-cyclohexenone (**5**), 26.4 g (425 mmol) ethylene glycol and 130 mg of polyanilinium sulfate were added to 200 mL of toluene in a 500 mL double-necked round bottom flask equipped with a Dean–Stark trap and a condenser. The mixture was heated to reflux for 8 h during the daytime and to 80 °C over night for a period of 2 days. The reaction was monitored by TLC. After filtration over celite and purification by flash-chromatography (ethyl acetate/isohehexane 1:5) compound **6** was isolated in 52% yield as a colourless oil. TLC: R<sub>f</sub>=0.46 (ethyl acetate/isohehexane 1:5); RP-UPLC: t<sub>r</sub>=4.24 min (10–90% B in 7 min, 96.4% purity); <sup>1</sup>H-NMR: (200.1 MHz, CDCl<sub>3</sub>) δ=5.62 (m, 2 H, HC=CH), 3.98 (m, 4H, OCH<sub>2</sub>CH<sub>2</sub>O), 2.26 (m, 4 H, 2 × CH<sub>2</sub>), 1.75 (m, 2 H, 2 × CH<sub>2</sub>); <sup>13</sup>C-NMR (50.3 MHz, CDCl<sub>3</sub>) δ=126.5 (C-5), 124.3 (C-4), 107.9 (C-6), 64.3 (C-8 and C-9), 35.7 (C-1), 31.0 (C-3), 24.5 (C-2); (ES-MS): m/z 141.1 [M + H]<sup>+</sup>.

**Cyclohexandiol-ketal (7).** 5 g (35.7 mmol) of compound **6** were dissolved in 70 mL ethanol and cooled to 0 °C while a solution of 6.2 g KMnO<sub>4</sub> and 3.1 g of MgSO<sub>4</sub> in 70 mL deionized water was prepared and which was afterwards added dropwise to the reaction mixture during 30 min. After two more hours the mixture was filtered over celite and concentrated in vacuum to a volume of 80 mL. The concentrated aqueous mixture was saturated with NaCl and extracted a dozen times with CH<sub>2</sub>Cl<sub>2</sub>. Each extract was analyzed by TLC and extracts containing starting material or byproducts were dismissed. The combined product fractions were dried (MgSO<sub>4</sub>) and the solvent was evaporated. The residue was recrystallized from isohehexane to yield compound **7** in 26% yield. TLC: R<sub>f</sub>=0.14 (ethyl acetate/isohehexane 1:1); RP-UPLC: t<sub>r</sub>=0.33 min (5–50% B in 7 min, 95.4% purity); <sup>1</sup>H-NMR: (200.1 MHz, CDCl<sub>3</sub>) δ=4.08–3.86 (m, 5 H, CHOH and OCH<sub>2</sub>CH<sub>2</sub>O), 3.67 (ddd, J=12.6 Hz, 5.3 Hz, 3.0 Hz, 1 H, CHOH), 2.51 (br. s, 2 H, 2 × OH) 1.99 (ddd, J=13.7 Hz, 6.0 Hz, 2.2 Hz, 1 H, 1 × CH<sub>2</sub>CHOH) 1.86–1.43 (m, 5 H, CH<sub>2</sub>). (ESI-MS): m/z 197.2 [M + H]<sup>+</sup>.

**Cell culture.** Biocompatibility assays were performed with three human cell types: SaOS-2 cells, hMSC and HUVEC. All three cell types were purchased from Sigma Aldrich (Taufkirchen, Germany). SaOS-2 cells were cultured in McCoy's 5A medium supplemented with 10% fetal calf serum; hMSCs were cultured in stem cell expansion medium SCM015; HUVECs were cultured in endothelial cell growth medium. All cell culture media were supplemented with 100 U/mL PenStrep. Cells were cultured in T-75 cell culture flasks at 37 °C and 5% CO<sub>2</sub> and subcultured at 80% confluency with 0.25% Trysin-EDTA solution. hMSCs and HUVECs were expanded for no more than 3 passages before use.

**Metabolic activity—MTT assay.** Biocompatibility of CSPs was evaluated with SaOS-2 cells, hMSCs and HUVECs using 3-(4,5-dimethylthiazol-2-yl)-2,5-diphenyltetrazolium bromide (MTT) assay. Briefly, trypsinated cells were seeded into 96-well tissue culture plates at a density of 10,000 cells/well and incubated at 37 °C and 5% CO<sub>2</sub> for 4 h in 180 µL of appropriate culture medium. Meanwhile, a serial dilution of the compounds **rac-7** and **3** stock solutions was prepared in sterile PBS and 20 µL of each was added to the respective well, resulting in effective concentrations of 10–10<sup>-5</sup> mM. As a vehicle control, 20 µL sterile PBS without CSPs was used. Cells were cultured for another 24 or 48 h in the incubator. After 24 or 48 h, medium was replaced by 1 mg/mL MTT in culture medium and incubated for 2 h. Then, MTT solution was removed and wells were washed three times with 200 µL sterile PBS. By adding 100 µL DMSO per well and incubation at 37 °C for 1 h, the formed formazan crystals were dissolved and subsequently quantified at 570 nm in a plate reader. Metabolic activity was calculated as the ratio of absorbance between samples and the vehicle control.

**Cellular reactive oxygen species—DCFDA assay.** Cellular reactive oxygen species (ROS) were analyzed by 2',7'-dichlorofluorescein diacetate (DCFDA) assay for SaOS-2 cells, hMSCs and HUVECs. Cells were prepared as described for the MTT-assay, resulting in cells treated for 24 or 48 h with 10–10<sup>-5</sup> mM CSPs. As additional controls, the ROS quenchers *N*-acetylcysteine (NAC) or butylated hydroxyanisole (BHA) were added to indicated controls to a final concentration of 250 µM or 5 µM, respectively. After 24 or 48 h of treatment, 2 µL 2 mM DCFDA in culture medium was added to each well and incubated at 37 °C for 30 min. Culture medium was removed and cells were washed three times with 200 µL sterile PBS. Oxidized dye was quantified with a plate reader at Ex/Em wavelengths of 485 nm/535 nm.

**Microbial evaluation.** Gram negative *Escherichia coli* (DSM 498) and gram-positive multi-resistant *Staphylococcus aureus* (MRSA, DSM 28766) were purchased from Leibniz Institute DSMZ-German Collection of Microorganisms and Cell Cultures GmbH (Braunschweig, Germany) and stored at –80 °C in glycerol stocks. A new vial was thawed for each experiment and incubated overnight at 37 °C and 100 rpm in Lennox LB medium.

**Bacterial growth.** Bacterial growth in PBS or LB medium was recorded in 96-well plates. Therefore, 180 µL of sterile PBS or LB medium containing the appropriate concentration of CSPs or glucose was added to each well and inoculated with 50,000 bacteria/well to reach a total volume of 200 µL. The lid of the 96-well plate was closed and sealed with parafilm. OD<sub>600</sub> was measured every 30 min in a plate reader for a total of 16 h at 37 °C without shaking. The logarithmic growth curves were used to calculate bacterial generation time. For this purpose, a linear regression of the exponential growth phase was performed with GraphPad Prism 8 (GraphPad Software, San Diego, USA) and the slope *k* was determined. Then, generation time (*t*) was calculated according to Eq. (1).

$$t = \frac{\ln 2}{k} \quad (1)$$

**Sample preparation and treatment.** Non-biofilm bacteria growing in liquid broth were prepared by adding 2 mL of LB medium to a sterile 15 mL conical plastic tube, and the appropriate volume of PenStrep and compound stock solution or sterile PBS, as vehicle control, were added. Samples were inoculated with 20 µL of an bacterial overnight culture diluted to OD<sub>600</sub>=0.1, resulting in approximately 10<sup>5</sup> CFU/mL, and incubated in a humidified incubator at 37 °C and shaking (130 rpm) for 48 h before analysis by spot plating as described below.

Developed biofilm was prepared in 96-well plates by incubating 200 µL of an bacterial overnight culture diluted to OD<sub>600</sub>=0.2 with LB medium at 37 °C in a humidified incubator for 72 h without shaking. For treatment, the supernatant was carefully removed and 200 µL of LB medium containing CSPs, glucose and PenStrep antibiotic mixture was added at the indicated concentrations and combinations.

Treatment for the experiments during biofilm formation was performed in the same way, except that 20 µL of a bacterial solution containing 2.5 × 10<sup>6</sup> cells/mL was added instead of prepared biofilm. The lid of the 96-well plate was closed, sealed with parafilm and incubated in a humidified incubator at 37 °C without shaking for 24, 48 or 72 h, as indicated. Samples were analyzed for biofilm formation using crystal violet assay, MTT assay for metabolic activity or spot plating for cell viability, as described below.

**Crystal violet-assay.** To assess the biofilm formed, the supernatant was carefully removed, and the biofilm was fixed with 200 µL of 100% ethanol for 2 min. Ethanol was removed, and samples were dried for 10 min with the lid open under the sterile work bench. Afterwards, 200 µL 0.05 (wt/vol)% crystal violet dye dissolved in sterile PBS were added and incubated at room temperature. Dye was removed after 2 min, the stained biofilm was gently washed 5 times with 200 µL sterile PBS and microscopic images were taken. For quantification, the remaining PBS was removed, and samples were dried over night with the lid open under the sterile work bench.

Then, 100  $\mu$ L 100% ethanol was added and incubated for 10 min at room temperature. The released dye was quantified by measuring the absorbance at 595 nm in a plate reader.

**MTT-assay.** To assess metabolic activity of bacteria in the remaining or newly formed biofilm, the supernatant was carefully removed and replaced by 1 mg/mL MTT in LB medium and incubated for 30 min at 37 °C. MTT solution was removed, and samples were washed three times with 200  $\mu$ L PBS, without removing the biofilm. Then, 100  $\mu$ L DMSO was added and incubated at 37 °C for 30 min. The amount of metabolic active bacteria was quantified by measuring the absorbance at 570 nm in a plate reader and compared to the respective vehicle controls.

**Spot plating—CFU.** To assess the cell viability of bacteria, the supernatant of treated biofilm samples was removed and the biofilm was washed with 200  $\mu$ L sterile PBS. Then, 200  $\mu$ L soybean casein digest lecithin polysorbate broth (SCDLP) was added, incubated at 37 °C for 15 min, and pipetted up and down at least ten times to remove biofilm<sup>53</sup>. A serial dilution of suspended biofilm was prepared in SCDLP, and 5  $\mu$ L of each dilution were spot plated to a 60 mm petri dish filled with LB agar as described by Wang et al.<sup>54</sup> and incubated overnight in a humidified incubator at 37 °C. Colony forming units (CFU) were counted and CFU/cm<sup>2</sup> were calculated in relation to the area of biofilm tested. For treated non-biofilm samples, the dilution series was prepared directly from the sample in LB medium and analyzed as described.

**Statistical analysis.** Measurements for biological assessment were repeated with three biological replicates (n = 3) and expressed as mean  $\pm$  standard deviation (SD), unless stated otherwise. Calculations of statistical significance were performed with GraphPad Prism 8 (GraphPad Software, San Diego, USA). A two-way ANOVA and Dunnett post-hoc test were used unless otherwise indicated.

#### Data availability

All data generated or analysed during this study are included in this published article (and its Supplementary Information files).

Received: 14 July 2022; Accepted: 19 October 2022

Published online: 26 October 2022

#### References

1. Murray, C. J. et al. Global burden of bacterial antimicrobial resistance in 2019: A systematic analysis. *Lancet* **399**, 629–655 (2022).
2. Talebi Bezin Abadi, A., Rizvanov, A. A., Haertlé, T. & Blatt, N. L. World Health Organization Report: Current crisis of antibiotic resistance. *Bionanoscience* **9**, 778–788 (2019).
3. Douafer, H., Andrieu, V., Phanstiel, O. & Brunel, J. M. Antibiotic adjuvants: Make antibiotics great again!. *J. Med. Chem.* **62**, 8665–8681 (2019).
4. Blair, J. M. A., Webber, M. A., Baylay, A. J., Ogbolu, D. O. & Piddock, L. J. V. Molecular mechanisms of antibiotic resistance. *Nat. Rev. Microbiol.* **13**, 42–51 (2015).
5. Boisvert, A.-A., Cheng, M. P., Sheppard, D. C. & Nguyen, D. Microbial biofilms in pulmonary and critical care diseases. *Ann. Am. Thorac. Soc.* **13**, 1615–1623 (2016).
6. Craft, K. M., Nguyen, J. M., Berg, L. J. & Townsend, S. D. Methicillin-resistant: *Staphylococcus aureus* (MRSA): Antibiotic-resistance and the biofilm phenotype. *MedChemComm* **10**, 1231–1241 (2019).
7. Leaper, D., Assadian, O. & Edmiston, C. E. Approach to chronic wound infections. *Br. J. Dermatol.* **173**, 351–358 (2015).
8. Olsen, I. Biofilm-specific antibiotic tolerance and resistance. *Eur. J. Clin. Microbiol. Infect. Dis.* **34**, 877–886 (2015).
9. Lünse, C. E., Schmidt, M. S., Wittmann, V. & Mayer, G. Carba-sugars activate the glmS-riboswitch of *Staphylococcus aureus*. *ACS Chem. Biol.* **6**, 675–678 (2011).
10. Sommer, R. et al. Glycomimetic, orally bioavailable LecB inhibitors block biofilm formation of *Pseudomonas aeruginosa*. *J. Am. Chem. Soc.* **140**, 2537–2545 (2018).
11. Zorin, A., Klenk, L., Mack, T., Deigner, H.-P. & Schmidt, M. S. Current synthetic approaches to the synthesis of carbasugars from non-carbohydrate sources. *Top. Curr. Chem.* **380**, 12 (2022).
12. Awolade, P. et al. Therapeutic significance of  $\beta$ -glucuronidase activity and its inhibitors: A review. *Eur. J. Med. Chem.* **187**, 111921 (2020).
13. Lahiri, R., Ansari, A. A. & Vankar, Y. D. Recent developments in design and synthesis of bicyclic azasugars, carbasugars and related molecules as glycosidase inhibitors. *Chem. Soc. Rev.* **42**, 5102 (2013).
14. Osborn, H. M. I., Evans, P. G., Gemmill, N. & Osborne, S. D. Carbohydrate-based therapeutics. *J. Pharm. Pharmacol.* **56**, 691–702 (2010).
15. McCasland, G. E., Furuta, S. & Durham, L. J. Alicyclic carbohydrates XXXIII. Epimerization of pseudo- $\alpha$ -DL- Talopyranose to pseudo- $\alpha$ -DL-galactopyranose. Proton magnetic resonance studies. *J. Org. Chem.* **33**, 2841–2844 (1968).
16. McCasland, G. E., Furuta, S. & Durham, L. J. Alicyclic carbohydrates. XXIX. 1,2 The synthesis of a pseudo-hexose (2,3,4,5-tetrahydroxycyclohexanemethanol). *J. Org. Chem.* **31**, 1516–1521 (1966).
17. Arjona, O., Gómez, A. M., López, J. C. & Plumet, J. Synthesis and conformational and biological aspects of carbasugars. *Chem. Rev.* **107**, 1919–2036 (2007).
18. Roscales, S. & Plumet, J. Biosynthesis and biological activity of carbasugars. *Int. J. Carbohydr. Chem.* **2016**, 1–42 (2016).
19. Babu, D. C., Rao, C. B., Venkatesham, K., Selvam, J. J. P. & Venkateswarlu, Y. Toward synthesis of carbasugars (+)-gabosine C, (+)-COTC, (+)-pericosine B, and (+)-pericosine C. *Carbohydr. Res.* **388**, 130–137 (2014).
20. Banachowicz, P. & Buda, S. Gram-scale carbasugar synthesis via intramolecular seleno-Michael/aldol reaction. *RSC Adv.* **9**, 12928–12935 (2019).
21. Sun, Y. & Nitz, M. Syntheses of carbocyclic analogues of  $\alpha$ -D-glucosamine,  $\alpha$ -D-mannose,  $\alpha$ -D-mannuronic acid,  $\beta$ -1-idosamine, and  $\beta$ -1-gulose. *J. Org. Chem.* **77**, 7401–7410 (2012).
22. Li, Q., Yuan, F., Zhou, C., Plashkevych, O. & Chattopadhyaya, J. Free-radical ring closure to conformationally locked  $\alpha$ -l-Carba-LNAs and synthesis of their oligos: Nuclease stability, target RNA specificity, and elicitation of RNase H. *J. Org. Chem.* **75**, 6122–6140 (2010).

23. Boyd, D. R. *et al.* Chemoenzymatic synthesis of carbasugars (+)-pericosines A–C from diverse aromatic cis-dihydrodiol precursors. *Org. Lett.* **12**, 2206–2209 (2010).
24. Mehta, G., Mohal, N. & Lakshminath, S. A norbornyl route to cyclohexitols: Structural diversity in fragmentation through functional group switching. Synthesis of  $\alpha$ - and  $\beta$ -galactose,  $\alpha$ -talose and  $\alpha$ -fucopyranose carbasugars. *Tetrahedron Lett.* **41**, 3505–3508 (2000).
25. Boyd, D. R. *et al.* Chemoenzymatic synthesis of carbasugars from iodobenzene. *Org. Biomol. Chem.* **3**, 1953 (2005).
26. Leermann, T., Block, O., Podeschwa, M. A. L., Pfüller, U. & Altenbach, H.-J. De novo synthesis and lectin binding studies of unsaturated carba-pyranoses. *Org. Biomol. Chem.* **8**, 3965 (2010).
27. Surburg, H. & Loges, A. M. Carvonacetale als Aromastoffe 1–7 (2002).
28. Birch, A. J. & Mukherji, S. M. 532. Reduction by dissolving metals. Part VI. Some applications in synthesis. *J. Chem. Soc.* **532**, 2531. <https://doi.org/10.1039/jr9490002531> (1949).
29. Nomura, M. *et al.* Synthesis of physiologically active substances from several cyclic monoterpenyl ketones. *J. Jpn. Oil Chem. Soc.* **45**, 865–870 (1996).
30. Palaniappan, S., Narender, P., Saravanan, C. & Rao, V. J. Polyaniline-supported sulfuric acid salt as a powerful catalyst for the protection and deprotection of carbonyl compounds. *Synlett* 1793–1796. <https://doi.org/10.1055/s-2003-41412> (2003).
31. Brown, H. C. & Pfaffenberger, C. D. Hexylborane as a convenient reagent for the cyclic hydroboration of dienes. Stereospecific syntheses via cyclic hydroboration. *J. Am. Chem. Soc.* **89**, 5475–5477 (1967).
32. Schulze, A., Mitterer, F., Pombo, J. P. & Schild, S. Biofilms by bacterial human pathogens: Clinical relevance—Development, composition and regulation—Therapeutical strategies. *Microb. Cell* **8**, 28–56 (2021).
33. Ishchuk, O. P., Sterner, O., Ellervik, U. & Manner, S. Simple carbohydrate derivatives diminish the formation of biofilm of the pathogenic yeast *Candida albicans*. *Antibiotics* **9**, 10 (2019).
34. Kolodkin-Gal, I. *et al.* Amino acids trigger biofilm disassembly. *Science* **328**, 627–629 (2010).
35. Valle, J. *et al.* Broad-spectrum biofilm inhibition by a secreted bacterial polysaccharide. *Proc. Natl. Acad. Sci. U.S.A.* **103**, 12558–12563 (2006).
36. Liu, Y., Jiang, Y., Zhu, J., Huang, J. & Zhang, H. Inhibition of bacterial adhesion and biofilm formation of sulfonated chitosan against *Pseudomonas aeruginosa*. *Carbohydr. Polym.* **206**, 412–419 (2019).
37. Segev-Zarko, L., Saar-Dover, R., Brumfeld, V., Mangoni, M. L. & Shai, Y. Mechanisms of biofilm inhibition and degradation by antimicrobial peptides. *Biochem. J.* **468**, 259–270 (2015).
38. Srinivasan, R. *et al.* Bacterial biofilm inhibition: A focused review on recent therapeutic strategies for combating the biofilm mediated infections. *Front. Microbiol.* **12**, 1–19 (2021).
39. Verderosa, A. D., Totsika, M. & Fairfull-Smith, K. E. Bacterial biofilm eradication agents: A current review. *Front. Chem.* **7**, 1–17 (2019).
40. Ren, W. *et al.* Revealing the mechanism for covalent inhibition of glycoside hydrolases by carbasugars at an atomic level. *Nat. Commun.* **9**, 3243 (2018).
41. Boden, S., Reise, F., Kania, J., Lindhorst, T. K. & Hartmann, L. Sequence-defined introduction of hydrophobic motifs and effects in lectin binding of precision glycomacromolecules. *Macromol. Biosci.* **19**, 1–11 (2019).
42. Ueda, T., Kaito, C., Omae, Y. & Sekimizu, K. Sugar-responsive gene expression and the agr system are required for colony spreading in *Staphylococcus aureus*. *Microb. Pathogens* **51**, 178–185 (2011).
43. Ha, J.-H. *et al.* Evidence of link between quorum sensing and sugar metabolism in *Escherichia coli* revealed via cocrystal structures of LsrK and HPr. *Sci. Adv.* **4**, eaar7063 (2018).
44. Tan, L., Li, S. R., Jiang, B., Hu, X. M. & Li, S. Therapeutic targeting of the *Staphylococcus aureus* accessory gene regulator (agr) system. *Front. Microbiol.* **9**, 55 (2018).
45. Gatta, R., Wiese, A., Iwanicki, A. & Obuchowski, M. Influence of glucose on swarming and quorum sensing of *Dickeya solani*. *PLoS One* **17**, e0263124 (2022).
46. Hernández-Jiménez, E. *et al.* Biofilm vs. planktonic bacterial mode of growth: Which do human macrophages prefer? *Biochem. Biophys. Res. Commun.* **441**, 947–952 (2013).
47. Uruén, C., Chopo-Escuin, G., Tommassen, J., Mainar-Jaime, R. C. & Arenas, J. Biofilms as promoters of bacterial antibiotic resistance and tolerance. *Antibiotics* **10**, 3 (2020).
48. Fillmore, N. *et al.* Effect of fatty acids on human bone marrow mesenchymal stem cell energy metabolism and survival. *PLoS One* **10**, e0120257 (2015).
49. Giang, A.-H. *et al.* Mitochondrial dysfunction and permeability transition in osteosarcoma cells showing the Warburg effect. *J. Biol. Chem.* **288**, 33303–33311 (2013).
50. Yetkin-Arik, B. *et al.* The role of glycolysis and mitochondrial respiration in the formation and functioning of endothelial tip cells during angiogenesis. *Sci. Rep.* **9**, 12608 (2019).
51. Dalla Valle, A. *et al.* Induction of stearoyl-CoA 9-desaturase 1 protects human mesenchymal stromal cells against palmitic acid-induced lipotoxicity and inflammation. *Front. Endocrinol. (Lausanne)* **10**, 726 (2019).
52. Dagher, Z., Ruderman, N., Tornheim, K. & Ido, Y. Acute regulation of fatty acid oxidation and AMP-activated protein kinase in human umbilical vein endothelial cells. *Circ. Res.* **88**, 1276–1282 (2001).
53. Japan Food Research Laboratories. ISO 22196: Measurement of antibacterial activity on plastics and other non-porous surfaces. ISO 1–24 (2011).
54. Wang, J., Woo, M. & Yan, C. Spot plating assay for the determination of survival and plating efficiency of *Escherichia coli* in sub-MIC levels of antibiotics. *JEMI Methods* **1**, 26–29 (2017).

### Acknowledgements

We like to thank the ReAching program of the faculty MLS, Furtwangen University, for support. This research was funded by the intramural “Tandem” program financed by the Institute of Applied Research (IAF) of the HFU.

### Author contributions

Conceptualizations: O.R., H.-P.D., M.S.S. Methodology: O.R., M.S.S. Formal analysis: O.R., M.S.S. Investigation: O.R., P.B., Y.G. Chemical Synthesis: P.B., Y.G. Resources: H.-P.D., M.S.S. Writing—Original Draft: O.R., H.-P.D., M.S.S. Writing—Review and Editing: O.R., P.B., Y.G., S.L., H.-P.D., M.S.S. Visualization: O.R., M.S.S. Supervision: S.L., H.-P.D., M.S.S.

### Funding

Open Access funding enabled and organized by Projekt DEAL.

### Competing interests

The authors declare no competing interests.

www.nature.com/scientificreports/

#### Additional information

**Supplementary Information** The online version contains supplementary material available at <https://doi.org/10.1038/s41598-022-22807-8>.

**Correspondence** and requests for materials should be addressed to M.S.S.

**Reprints and permissions information** is available at [www.nature.com/reprints](http://www.nature.com/reprints).

**Publisher's note** Springer Nature remains neutral with regard to jurisdictional claims in published maps and institutional affiliations.



**Open Access** This article is licensed under a Creative Commons Attribution 4.0 International License, which permits use, sharing, adaptation, distribution and reproduction in any medium or format, as long as you give appropriate credit to the original author(s) and the source, provide a link to the Creative Commons licence, and indicate if changes were made. The images or other third party material in this article are included in the article's Creative Commons licence, unless indicated otherwise in a credit line to the material. If material is not included in the article's Creative Commons licence and your intended use is not permitted by statutory regulation or exceeds the permitted use, you will need to obtain permission directly from the copyright holder. To view a copy of this licence, visit <http://creativecommons.org/licenses/by/4.0/>.

© The Author(s) 2022

## 4 Summary and Outlook

In this thesis, three approaches to overcome the antibiotic crisis were investigated, with a primary focus on AST. The other two approaches, antibacterial coatings based on chitosan derivatives and glycomimetic adjuvants, also have their *raison d'être*, but AST has shown the greatest potential as it has a more fundamental impact and is essential for targeted antibiotic therapy. The designed concept and basic experimental setting may be a game changer within this field.

In Chapter 3.3, a proof-of-concept study demonstrated that glycomimetic adjuvants in the form of carbasugar precursors (CSP) are useful in the treatment of biofilm-associated infections. The tested CSP showed a reduction of up to 70% in biofilm formation, as assessed by crystal violet-stained extracellular polymeric substance (EPS). Even at concentrations as low as 100 nM, a reduction in EPS of around 50% was observed for *E. coli*. The best concentrations, regarding anti-biofilm activity and cytotoxicity for human cell lines were around 100  $\mu$ M, as the CSP showed significant anti-biofilm activity against *E. coli* and multidrug-resistant *Staphylococcus aureus* (MRSA) at this concentration; however, it still did not exhibit significant cytotoxic effects against the tested human cell lines, which was observed at  $\geq 1$  mM. Interestingly, the tested CSP only reduced the amount of EPS, but had no effect on the growth or viability of the bacteria. A combinatorial approach of CSP with a mixture of penicillin and streptomycin (PenStrep) showed complementary effects in treating the tested MRSA strain, both in growing and already developed biofilms. It resulted in a reduction of bacterial viability for growing MRSA biofilms, which was not the case for each compound individually. In addition, the combination of the tested rac-7 CSP with PenStrep prevented the increase in EPS production that occurred when PenStrep was administered alone. It can be summarized that the CSP rac-7 inhibits the formation of new biofilm and can thus contribute to the resensitization of bacteria to antibiotics that are rendered ineffective by biofilms. However, in order to improve efficacy by developing new, more effective and more selective molecules, the exact mechanism must be understood in the future. Nevertheless, the study showed the potential of glycomimetics as adjuvants, which could be used as wound dressings in the treatment of chronic wounds, for example.

For the second approach, two antibacterial coatings were designed and synthesized using chitosan as a model. The first coating (Chapter 3.2.1) used a poly-dimethacrylamide methyl (PDMAm) network, which was substituted with benzophenone for UV-

induced anchoring and a residue consisting of N acetyl-glucosamine, a triazole and a linker, mimicking a chitosan surface. Several linker lengths and copolymer ratios were evaluated for their biocompatibility and antibacterial effect using polyethylene terephthalate glycol (PETG) coverslips as a base substrate. Of the tested combinations, the 5%-GlcNAc-4EG coating has shown the most effective antimicrobial activity in combination with good biocompatibility in direct contact and extract for L-929 Fibroblasts according to ISO 10993-5 standards. Although the antibacterial effect (viability was reduced 1.2-fold) was only observed under low-nutrient conditions, the significant reduction in biofilm was also observed under nutrient-rich conditions.

However, the observed effects were not sufficient to meet high clinical expectations. Therefore, the second coating design (Chapter 3.2.2) focused on the functionalization of chitosan and not on the imitation of chitosan. Substitution of the amino groups of chitosan with benzophenone made it possible to apply a covalent coating to polyether ether ketone (PEEK) surfaces by UV crosslinking. Several chitosan derivatives with different degrees of substitution were synthesized and evaluated; as chitosan derivatives in solution and as cross-linked coatings. All tested benzophenone-chitosan derivatives retained their antimicrobial properties in solution to a degree comparable to the IC90 values of unmodified chitosan as reported in the literature. However, when the derivatives were applied as a coating, their effects were different, with the 30% substituted chitosan displaying the most favorable properties. The 30% substituted chitosan coating demonstrated a reduction in viable bacteria by up to 5-fold and inhibition of biofilm to the extent that EPS was almost undetectable by crystal violet staining. This was combined with good biocompatibility for several cell lines evaluated according to ISO 10993-5 and a uniform coating on a PEEK surface.

The third and central part of this thesis (Chapter 3.1) was the development of a rapid AST system, that enables the transition from current empirical antibiotic therapy to evidence-based, targeted antibiotic therapy as the clinical standard. For this purpose, it was crucial to reduce the overall turnaround time from sampling to AST result from the current 24 hours or more to around 8 hours, enabling the physician to start targeted antibiotic therapy within one working shift. This required two major achievements: Firstly, a device had to be produced that allowed the test to be performed under controllable and advantageous conditions, e.g., in terms of evaporation and handling. Secondly, the test had to be able to be injected directly with the patient sample without time-consuming sample preparation, as preculture and transportation are excessively time-consuming.

The first achievement was realized with a fused deposition modeling 3D printer, whose

suitability in terms of adaptability for different geometries, accuracy and also the non-toxicity of the printing material was demonstrated. In chapter 3.1.1 it was shown that microfluidic structures with dimensions of approximately 100  $\mu\text{m}$  can be produced and that the design can be easily adapted to create distribution networks, concentration gradients or measurement chambers suitable for biomedical applications. This was demonstrated for a cytotoxicity screening system and an osteoblast differentiation assay. The flexibility in device design was essential for the development of a 3D-printed device that enabled the electrochemical AST described in chapter 3.1.2. The electrochemical test setup benefited from the 3D-printed device in several ways: low evaporation, easy handling and sample injection, integration of the electrode into the measuring chamber, non-toxicity of the material and sterilizability via UV light.

For realizing the second mentioned achievement, the direct testing of the patients sample without extensive sample treatment like preculture, the 3D printed device was combined with electrochemical measurement methods for bacterial growth. The electrochemical measurement of bacterial growth had a decisive advantage over other methods, particularly fluorescence. It offered comparable sensitivity at lower cost and lower power consumption, the possibility of sequential online measurement of different electrochemical methods with the same experimental setup and compatibility with microfabrication technology [132]. By combining all the benefits described above with computer-assisted analysis using a Python script, the AST presented is able to provide a result 5 to 10 hours after sampling. This was demonstrated for serum samples spiked with clinically relevant pathogens (*Escherichia coli*, *Staphylococcus aureus*, *Klebsiella pneumoniae* and *Pseudomonas aeruginosa*) in realistic concentrations (1000 CFU/ml in spiked serum) corresponding to a bloodstream infection. Validation of the AST against the gold standard by agar diffusion test showed a sensitivity of 94.44% and a specificity of 95.83%. This was accomplished by considering each replicate individually and 100% for both when considering the majority of results from each triplicate.

Future improvements of the method, particularly in terms of feasibility in a clinical setting, must address the automation of the workflow such that the system provides the physician with a report containing information on the minimum inhibitory concentration and resistances of the sample to the antibiotics tested. From this perspective, it would also be necessary to validate the method in a multi-chamber device with pre-loaded antibiotics in the future, which would resemble a disposable cassette allowing samples to be loaded immediately into the device and automatically distributed to the measuring chambers.

Overall, it can be concluded that the approaches demonstrated in this thesis may con-

tribute significantly to overcome the antibiotic crisis. In particular the AST system presented could impact the challenge of multidrug-resistant pathogens at a fundamental level by providing the information needed for evidence-based, targeted antibiotic therapy. This would both improve treatment outcomes for patients together with the rate of emerging resistance correlating with the total amount of antibiotics used, in particular broad-spectrum antibiotics. However, even if antibiotics are used responsibly and appropriately, new resistances will still emerge in the long-term rendering existing antibiotics useless. The development of new antibiotics and strategies, such as the antibacterial coatings or glycomimetic adjuvants presented, is therefore essential alongside conventional antibiotics in order to continue to offer the healthcare system effective treatment options for infectious diseases in the future.

# Bibliography

- [1] World Health Organization: Urgent Health Challenges for the next Decade. 2023; <https://www.who.int/news-room/photo-story/photo-story-detail/urgent-health-challenges-for-the-next-decade>.
- [2] Murray, C. J. L. et al. Global Burden of Bacterial Antimicrobial Resistance in 2019: A Systematic Analysis. *The Lancet* **2022**, *399*, 629–655.
- [3] Humphreys, G.; Fleck, F. United Nations Meeting on Antimicrobial Resistance. *Bulletin of the World Health Organization* **2016**, *94*, 638–639.
- [4] Mestrovic, T. et al. The Burden of Bacterial Antimicrobial Resistance in the WHO European Region in 2019: A Cross-Country Systematic Analysis. *The Lancet Public Health* **2022**, *7*, e897–e913.
- [5] OECD *High-Level One Health Ministerial Meeting On Antimicrobial Resistance, French Presidency of the EU Council Paris, France*; 2022.
- [6] Europäische Gesundheitsunion EU Geht Verstärkt Gegen Antimikrobielle Resistenzen Vor. 2023; [https://ec.europa.eu/commission/presscorner/detail/de/IP\\_23\\_3187](https://ec.europa.eu/commission/presscorner/detail/de/IP_23_3187).
- [7] Article 49 - LOI N° 2014-1170 Du 13 Octobre 2014 d'avenir Pour l'agriculture, l'alimentation et La Forêt (1) - Légifrance. [https://www.legifrance.gouv.fr/loda/article\\_lc/LEGIARTI000029575187](https://www.legifrance.gouv.fr/loda/article_lc/LEGIARTI000029575187).
- [8] Ministère des Solidarités et de la Santé “ONE HEALTH” FRENCH NATIONAL ACTION PLAN ON ANTIMICROBIAL RESISTANCE: AN OVERVIEW; 2022.
- [9] World Health Organization: More Countries Committing to Tackling Antimicrobial Resistance. 2021; <https://www.who.int/news/item/11-11-2021-more-countries-committing-to-tackling-antimicrobial-resistance>.
- [10] Charani, E. et al. An Analysis of Existing National Action Plans for Antimicrobial Resistance—Gaps and Opportunities in Strategies Optimising Antibiotic Use in Human Populations. *The Lancet Global Health* **2023**, *11*, e466–e474.
- [11] Browne, A. J. et al. Global Antibiotic Consumption and Usage in Humans, 2000–18: A Spatial Modelling Study. *The Lancet Planetary Health* **2021**, *5*, e893–e904.
- [12] Mulchandani, R.; Wang, Y.; Gilbert, M.; Van Boeckel, T. P. Global Trends in Antimicrobial Use in Food-Producing Animals: 2020 to 2030. *PLOS Global Public Health* **2023**, *3*, e0001305.

- [13] Goossens, H. Antibiotic Consumption and Link to Resistance. *Clinical Microbiology and Infection* **2009**, *15*, 12–15.
- [14] Chokshi, A.; Sifri, Z.; Cennimo, D.; Horng, H. Global Contributors to Antibiotic Resistance. *Journal of Global Infectious Diseases* **2019**, *11*, 36.
- [15] Beyer, P.; Paulin, S. The Antibacterial Research and Development Pipeline Needs Urgent Solutions. *ACS Infectious Diseases* **2020**, *6*, 1289–1291.
- [16] Walesch, S.; Birkelbach, J.; Jézéquel, G.; Haeckl, F. P. J.; Hegemann, J. D.; Hesterkamp, T.; Hirsch, A. K. H.; Hammann, P.; Müller, R. Fighting Antibiotic Resistance—Strategies and (Pre)Clinical Developments to Find New Antibacterials. *EMBO reports* **2023**, *24*, 1–33.
- [17] *Centers for Disease Control and Prevention: Antibiotic Resistance Threats in the United States, 2019*; 2019.
- [18] Poku, E.; Cooper, K.; Cantrell, A.; Harnan, S.; Sin, M. A.; Zanuzdana, A.; Hoffmann, A. Systematic Review of Time Lag between Antibiotic Use and Rise of Resistant Pathogens among Hospitalized Adults in Europe. *JAC-Antimicrobial Resistance* **2022**, *5*, dlad001.
- [19] Tabak, Y. P.; Vankeepuram, L.; Ye, G.; Jeffers, K.; Gupta, V.; Murray, P. R. Blood Culture Turnaround Time in U.S. Acute Care Hospitals and Implications for Laboratory Process Optimization. *Journal of Clinical Microbiology* **2018**, *56*, e00500–18.
- [20] MacBrayne, C. E.; Williams, M. C.; Prinzi, A.; Pearce, K.; Lamb, D.; Parker, S. K. Time to Blood Culture Positivity by Pathogen and Primary Service. *Hospital Pediatrics* **2021**, *11*, 953–961.
- [21] Vasala, A.; Hytönen, V. P.; Laitinen, O. H. Modern Tools for Rapid Diagnostics of Antimicrobial Resistance. *Frontiers in Cellular and Infection Microbiology* **2020**, *10*.
- [22] van Belkum, A.; Bachmann, T. T.; Lüdke, G.; Lisby, J. G.; Kahlmeter, G.; Mohess, A.; Becker, K.; Hays, J. P.; Woodford, N.; Mitsakakis, K.; Moran-Gilad, J.; Vila, J.; Peter, H.; Rex, J. H.; Dunne, W. M. Developmental Roadmap for Antimicrobial Susceptibility Testing Systems. *Nature Reviews Microbiology* **2019**, *17*, 51–62.
- [23] Buehler, S. S.; Madison, B.; Snyder, S. R.; Derzon, J. H.; Cornish, N. E.; Saubolle, M. A.; Weissfeld, A. S.; Weinstein, M. P.; Liebow, E. B.; Wolk, D. M. Effectiveness of Practices To Increase Timeliness of Providing Targeted Therapy for Inpatients with Bloodstream Infections: A Laboratory Medicine Best Practices

- Systematic Review and Meta-analysis. *Clinical Microbiology Reviews* **2016**, *29*, 59–103.
- [24] Sankar, J.; Garg, M.; Ghimire, J. J.; Sankar, M. J.; Lodha, R.; Kabra, S. K. Delayed Administration of Antibiotics Beyond the First Hour of Recognition Is Associated with Increased Mortality Rates in Children with Sepsis/Severe Sepsis and Septic Shock. *The Journal of Pediatrics* **2021**, *233*, 183–190.e3.
- [25] Walsh, T. L.; Bremmer, D. N.; Moffa, M. A.; Trienski, T. L.; Buchanan, C.; Stefano, K.; Hand, C.; Taylor, T.; Kasarda, K.; Shively, N. R.; Bhanot, N.; Cheronis, N.; DiSilvio, B. E.; Cho, C. Y.; Carr, D. R. Impact of an Antimicrobial Stewardship Program-bundled Initiative Utilizing Accelerate Pheno™ System in the Management of Patients with Aerobic Gram-negative Bacilli Bacteremia. *Infection* **2021**, *49*, 511–519.
- [26] Puttaswamy, S.; Gupta, S. K.; Regunath, H.; Smith, L. P.; Sengupta, S. A Comprehensive Review of the Present and Future Antibiotic Susceptibility Testing (AST) Systems. *Archives of Clinical Microbiology* **2018**, *09*, 1–9.
- [27] Kumar, A.; Roberts, D.; Wood, K. E.; Light, B.; Parrillo, J. E.; Sharma, S.; Suppes, R.; Feinstein, D.; Zanotti, S.; Taiberg, L.; Gurka, D.; Kumar, A.; Cheang, M. Duration of Hypotension before Initiation of Effective Antimicrobial Therapy Is the Critical Determinant of Survival in Human Septic Shock\*. *Critical Care Medicine* **2006**, *34*, 1589–1596.
- [28] Van Belkum, A.; Burnham, C.-A. D.; Rossen, J. W. A.; Mallard, F.; Rochas, O.; Dunne, W. M. Innovative and Rapid Antimicrobial Susceptibility Testing Systems. *Nature Reviews Microbiology* **2020**, *18*, 299–311.
- [29] Ellington, M. J. et al. The Role of Whole Genome Sequencing in Antimicrobial Susceptibility Testing of Bacteria: Report from the EUCAST Subcommittee. *Clinical Microbiology and Infection* **2017**, *23*, 2–22.
- [30] Esteban, J. et al. Multicenter Evaluation of the BIOFIRE Joint Infection Panel for the Detection of Bacteria, Yeast, and AMR Genes in Synovial Fluid Samples. *Journal of Clinical Microbiology* **2023**, *61*, e00357–23.
- [31] Berinson, B.; Both, A.; Berneking, L.; Christner, M.; Lütgehetmann, M.; Aepfelbacher, M.; Rohde, H. Usefulness of BioFire FilmArray BCID2 for Blood Culture Processing in Clinical Practice. *Journal of Clinical Microbiology* **2021**, *59*, e00543–21.
- [32] Salimnia, H. et al. Evaluation of the FilmArray Blood Culture Identification Panel: Results of a Multicenter Controlled Trial. *Journal of Clinical Microbiology* **2016**,

- 54, 687–698.
- [33] Jamal, W.; Al Roomi, E.; AbdulAziz, L. R.; Rotimi, V. O. Evaluation of Curetis Unyvero, a Multiplex PCR-Based Testing System, for Rapid Detection of Bacteria and Antibiotic Resistance and Impact of the Assay on Management of Severe Nosocomial Pneumonia. *Journal of Clinical Microbiology* **2014**, *52*, 2487–2492.
- [34] Gadsby, N. J.; McHugh, M. P.; Forbes, C.; MacKenzie, L.; Hamilton, S. K. D.; Griffith, D. M.; Templeton, K. E. Comparison of Unyvero P55 Pneumonia Cartridge, in-House PCR and Culture for the Identification of Respiratory Pathogens and Antibiotic Resistance in Bronchoalveolar Lavage Fluids in the Critical Care Setting. *European Journal of Clinical Microbiology & Infectious Diseases* **2019**, *38*, 1171–1178.
- [35] Thakku, S. G.; Ackerman, C. M.; Myhrvold, C.; Bhattacharyya, R. P.; Livny, J.; Ma, P.; Gomez, G. I.; Sabeti, P. C.; Blainey, P. C.; Hung, D. T. Multiplexed Detection of Bacterial Nucleic Acids Using Cas13 in Droplet Microarrays. *PNAS Nexus* **2022**, *1*, pgac021.
- [36] Perreten, V.; Vorlet-Fawer, L.; Slickers, P.; Ehricht, R.; Kuhnert, P.; Frey, J. Microarray-Based Detection of 90 Antibiotic Resistance Genes of Gram-Positive Bacteria. *Journal of Clinical Microbiology* **2005**, *43*, 2291–2302.
- [37] Zhang, L.; Huang, W.; Zhang, S.; Li, Q.; Wang, Y.; Chen, T.; Jiang, H.; Kong, D.; Lv, Q.; Zheng, Y.; Ren, Y.; Liu, P.; Jiang, Y.; Chen, Y. Rapid Detection of Bacterial Pathogens and Antimicrobial Resistance Genes in Clinical Urine Samples With Urinary Tract Infection by Metagenomic Nanopore Sequencing. *Frontiers in Microbiology* **2022**, *13*, 858777.
- [38] Sakai, J.; Tarumoto, N.; Kodana, M.; Ashikawa, S.; Imai, K.; Kawamura, T.; Ikebuchi, K.; Murakami, T.; Mitsutake, K.; Maeda, T.; Maesaki, S. An Identification Protocol for ESBL-producing Gram-negative Bacteria Bloodstream Infections Using a MinION Nanopore Sequencer. *Journal of Medical Microbiology* **2019**, *68*, 1219–1226.
- [39] Conzemius, R.; Bergman, Y.; Májek, P.; Beisken, S.; Lewis, S.; Jacobs, E. B.; Tamma, P. D.; Simner, P. J. Automated Antimicrobial Susceptibility Testing and Antimicrobial Resistance Genotyping Using Illumina and Oxford Nanopore Technologies Sequencing Data among Enterobacteriaceae. *Frontiers in Microbiology* **2022**, *13*, 973605.
- [40] Gaston, D. C.; Miller, H. B.; Fissel, J. A.; Jacobs, E.; Gough, E.; Wu, J.; Klein, E. Y.; Carroll, K. C.; Simner, P. J. Evaluation of Metagenomic and Targeted Next-Generation Sequencing Workflows for Detection of Respiratory Pathogens

- from Bronchoalveolar Lavage Fluid Specimens. *Journal of Clinical Microbiology* **2022**, *60*, e00526–22.
- [41] Janes, V. A.; Matamoros, S.; Munk, P.; Clausen, P. T. L. C.; Koekkoek, S. M.; Koster, L. A. M.; Jakobs, M. E.; De Wever, B.; Visser, C. E.; Aarestrup, F. M.; Lund, O.; De Jong, M. D.; Bossuyt, P. M. M.; Mende, D. R.; Schultsz, C. Metagenomic DNA Sequencing for Semi-Quantitative Pathogen Detection from Urine: A Prospective, Laboratory-Based, Proof-of-Concept Study. *The Lancet Microbe* **2022**, *3*, e588–e597.
- [42] Peterson, S.; Demczuk, W.; Martin, I.; Adam, H.; Bharat, A.; Mulvey, M. Identification of Bacterial and Fungal Pathogens Directly from Clinical Blood Cultures Using Whole Genome Sequencing. *Genomics* **2023**, *115*, 110580.
- [43] Jacobs, M. R.; Colson, J. D.; Rhoads, D. D. Recent Advances in Rapid Antimicrobial Susceptibility Testing Systems. *Expert Review of Molecular Diagnostics* **2021**, *21*, 563–578.
- [44] Rebelo, A. R.; Bortolaia, V.; Leekitcharoenphon, P.; Hansen, D. S.; Nielsen, H. L.; Ellermann-Eriksen, S.; Kemp, M.; Røder, B. L.; Frimodt-Møller, N.; Søndergaard, T. S.; Coia, J. E.; Østergaard, C.; Westh, H.; Aarestrup, F. M. One Day in Denmark: Comparison of Phenotypic and Genotypic Antimicrobial Susceptibility Testing in Bacterial Isolates From Clinical Settings. *Frontiers in Microbiology* **2022**, *13*, 1–12.
- [45] Trotter, A. J.; Aydin, A.; Strinden, M. J.; O’Grady, J. Recent and Emerging Technologies for the Rapid Diagnosis of Infection and Antimicrobial Resistance. *Current Opinion in Microbiology* **2019**, *51*, 39–45.
- [46] Suzuki, S.; Horinouchi, T.; Furusawa, C. Prediction of Antibiotic Resistance by Gene Expression Profiles. *Nature Communications* **2014**, *5*, 5792.
- [47] Baltekin, Ö.; Boucharin, A.; Tano, E.; Andersson, D. I.; Elf, J. Antibiotic Susceptibility Testing in Less than 30 Min Using Direct Single-Cell Imaging. *Proceedings of the National Academy of Sciences of the United States of America* **2017**, *114*, 9170–9175.
- [48] Kandavalli, V.; Karempudi, P.; Larsson, J.; Elf, J. Rapid Antibiotic Susceptibility Testing and Species Identification for Mixed Samples. *Nature Communications* **2022**, *13*, 6215.
- [49] Li, X.; Liu, X.; Yu, Z.; Luo, Y.; Hu, Q.; Xu, Z.; Dai, J.; Wu, N.; Shen, F. Combinatorial Screening SlipChip for Rapid Phenotypic Antimicrobial Susceptibility Testing. *Lab on a Chip* **2022**, *22*, 3952–3960.

- [50] Schoepp, N. G.; Schlappi, T. S.; Curtis, M. S.; Butkovich, S. S.; Miller, S.; Humphries, R. M.; Ismagilov, R. F. Rapid Pathogen-Specific Phenotypic Antibiotic Susceptibility Testing Using Digital LAMP Quantification in Clinical Samples. *Science Translational Medicine* **2017**, *9*, 1–13.
- [51] Jiang, X.; Borkum, T.; Shprits, S.; Boen, J.; Arshavsky-Graham, S.; Rofman, B.; Strauss, M.; Colodner, R.; Sulam, J.; Halachmi, S.; Leonard, H.; Segal, E. Accurate Prediction of Antimicrobial Susceptibility for Point-of-Care Testing of Urine in Less than 90 Minutes via iPRISM Cassettes. *Advanced Science* **2023**, *10*, 2303285.
- [52] Nemr, C. R.; Smith, S. J.; Liu, W.; Mephram, A. H.; Mohamadi, R. M.; Labib, M.; Kelley, S. O. Nanoparticle-Mediated Capture and Electrochemical Detection of Methicillin-Resistant *Staphylococcus Aureus*. *Analytical Chemistry* **2019**, *91*, 2847–2853.
- [53] Crane, B.; Hughes, J. P.; Rowley Neale, S. J.; Rashid, M.; Linton, P. E.; Banks, C. E.; Shaw, K. J. Rapid Antibiotic Susceptibility Testing Using Resazurin Bulk Modified Screen-Printed Electrochemical Sensing Platforms. *Analyst* **2021**, *146*, 5574–5583.
- [54] Besant, J. D.; Sargent, E. H.; Kelley, S. O. Rapid Electrochemical Phenotypic Profiling of Antibiotic-Resistant Bacteria. *Lab on a Chip* **2015**, *15*, 2799–2807.
- [55] Nagar, B.; Silva, W. O.; Girault, H. H. Voltammetry in Two-Electrode Mode for Rapid Electrochemical Screening Using a Fully Printed and Flexible Multiplexer Sensor. *ChemElectroChem* **2021**, *8*, 3700–3706.
- [56] Nagar, B.; Jović, M.; Bassetto, V. C.; Zhu, Y.; Pick, H.; Gómez-Romero, P.; Merkoçi, A.; Girault, H. H.; Lesch, A. Highly Loaded Mildly Edge-Oxidized Graphene Nanosheet Dispersions for Large-Scale Inkjet Printing of Electrochemical Sensors. *ChemElectroChem* **2020**, *7*, 460–468.
- [57] Spencer, D. C.; Paton, T. F.; Mulroney, K. T.; Inglis, T. J.; Sutton, J. M.; Morgan, H. A Fast Impedance-Based Antimicrobial Susceptibility Test. *Nature Communications* **2020**, *11*.
- [58] Hannah, S.; Dobra, A.; Lasserre, P.; Blair, E. O.; Alcorn, D.; Hoskisson, P. A.; Corrigan, D. K. Development of a Rapid, Antimicrobial Susceptibility Test for *E. Coli* Based on Low-Cost, Screen-Printed Electrodes. *Biosensors* **2020**, *10*.
- [59] Cira, N. J.; Ho, J. Y.; Dueck, M. E.; Weibel, D. B. A Self-Loading Microfluidic Device for Determining the Minimum Inhibitory Concentration of Antibiotics. *Lab on a Chip* **2012**, *12*, 1052–1059.

- [60] Azizi, M.; Zaferani, M.; Dogan, B.; Zhang, S.; Simpson, K. W.; Abbaspourrad, A. Nanoliter-Sized Microchamber/Microarray Microfluidic Platform for Antibiotic Susceptibility Testing. *Analytical Chemistry* **2018**, *90*, 14137–14144.
- [61] Lei, W.; Demir, K.; Overhage, J.; Grunze, M.; Schwartz, T.; Levkin, P. A. Droplet-Microarray: Miniaturized Platform for High-Throughput Screening of Antimicrobial Compounds. *Advanced Biosystems* **2020**, *4*, 1–9.
- [62] Ihssen, J.; Jovanovic, N.; Sirec, T.; Spitz, U. Real-Time Monitoring of Extracellular ATP in Bacterial Cultures Using Thermostable Luciferase. *PLoS ONE* **2021**, *16*, 1–23.
- [63] Sinn, I.; Kinnunen, P.; Albertson, T.; McNaughton, B. H.; Newton, D. W.; Burns, M. A.; Kopelman, R. Asynchronous Magnetic Bead Rotation (AMBR) Biosensor in Microfluidic Droplets for Rapid Bacterial Growth and Susceptibility Measurements. *Lab on a Chip* **2011**, *11*, 2604–2611.
- [64] Mulrone, K. T.; Hall, J. M.; Huang, X.; Turnbull, E.; Bzdyl, N. M.; Chakera, A.; Naseer, U.; Corea, E. M.; Ellington, M. J.; Hopkins, K. L.; Wester, A. L.; Ekelund, O.; Woodford, N.; Inglis, T. J. J. Rapid Susceptibility Profiling of Carbapenem-Resistant *Klebsiella Pneumoniae*. *Scientific Reports* **2017**, *7*, 1903.
- [65] Vocat, A.; Sturm, A.; Józwiak, G.; Cathomen, G.; Świątkowski, M.; Buga, R.; Wielgoszewski, G.; Cichocka, D.; Greub, G.; Opota, O. Nanomotion Technology in Combination with Machine Learning: A New Approach for a Rapid Antibiotic Susceptibility Test for *Mycobacterium Tuberculosis*. *Microbes and Infection* **2023**, *25*, 105151.
- [66] Andersen, L. Ø.; Olesen, H. V.; Spannow, A. H.; Rubak, S. L. M. Validation of Nasal Tracheal Aspiration in Children with Lung Disease. *BMC Pulmonary Medicine* **2022**, *22*, 1–12.
- [67] Hare, K. M.; Grimwood, K.; Leach, A. J.; Smith-Vaughan, H.; Torzillo, P. J.; Morris, P. S.; Chang, A. B. Respiratory Bacterial Pathogens in the Nasopharynx and Lower Airways of Australian Indigenous Children with Bronchiectasis. *Journal of Pediatrics* **2010**, *157*, 1001–1005.
- [68] Yagupsky, P.; Nolte, F. S. Quantitative Aspects of Septicemia. *Clinical Microbiology Reviews* **1990**, *3*, 269–279.
- [69] Boardman, A. K.; Campbell, J.; Wirz, H.; Sharon, A.; Sauer-Budge, A. F. Rapid Microbial Sample Preparation from Blood Using a Novel Concentration Device. *PLoS ONE* **2015**, *10*, 1–13.

- [70] Smith, W. P.; Wucher, B. R.; Nadell, C. D.; Foster, K. R. Bacterial Defences: Mechanisms, Evolution and Antimicrobial Resistance. *Nature Reviews Microbiology* **2023**, *21*, 519–534.
- [71] Darby, E. M.; Trampari, E.; Siasat, P.; Gaya, M. S.; Alav, I.; Webber, M. A.; Blair, J. M. Molecular Mechanisms of Antibiotic Resistance Revisited. *Nature Reviews Microbiology* **2023**, *21*, 280–295.
- [72] Blair, J. M. A.; Webber, M. A.; Baylay, A. J.; Ogbolu, D. O.; Piddock, L. J. V. Molecular Mechanisms of Antibiotic Resistance. *Nature Reviews Microbiology* **2015**, *13*, 42–51.
- [73] Wilson, D. N.; Haurlyliuk, V.; Atkinson, G. C.; O'Neill, A. J. Target Protection as a Key Antibiotic Resistance Mechanism. *Nature Reviews Microbiology* **2020**, *18*, 637–648.
- [74] Maviza, T. P.; Zarechenskaia, A. S.; Burmistrova, N. R.; Tchoub, A. S.; Dontsova, O. A.; Sergiev, P. V.; Osterman, I. A. RtcB2-PrfH Operon Protects E. Coli ATCC25922 Strain from Colicin E3 Toxin. *International Journal of Molecular Sciences* **2022**, *23*, 6453.
- [75] Hersch, S. J.; Watanabe, N.; Stietz, M. S.; Manera, K.; Kamal, F.; Burkinshaw, B.; Lam, L.; Pun, A.; Li, M.; Savchenko, A.; Dong, T. G. Envelope Stress Responses Defend against Type Six Secretion System Attacks Independently of Immunity Proteins. *Nature Microbiology* **2020**, *5*, 706–714.
- [76] Munita, J. M.; Arias, C. A. Mechanisms of Antibiotic Resistance. *Microbiology Spectrum* **2016**, *4*, 4.2.15.
- [77] Du, D.; Wang-Kan, X.; Neuberger, A.; Van Veen, H. W.; Pos, K. M.; Piddock, L. J. V.; Luisi, B. F. Multidrug Efflux Pumps: Structure, Function and Regulation. *Nature Reviews Microbiology* **2018**, *16*, 523–539.
- [78] Cascioferro, S.; Carbone, D.; Parrino, B.; Pecoraro, C.; Giovannetti, E.; Cirrincione, G.; Diana, P. Therapeutic Strategies To Counteract Antibiotic Resistance in MRSA Biofilm-Associated Infections. *ChemMedChem* **2021**, *16*, 65–80.
- [79] Singh, S.; Datta, S.; Narayanan, K. B.; Rajnish, K. N. Bacterial Exopolysaccharides in Biofilms: Role in Antimicrobial Resistance and Treatments. *Journal of Genetic Engineering and Biotechnology* **2021**, *19*, 140.
- [80] Sijbom, M.; Büchner, F. L.; Saadah, N. H.; Numans, M. E.; De Boer, M. G. J. Trends in Antibiotic Selection Pressure Generated in Primary Care and Their Association with Sentinel Antimicrobial Resistance Patterns in Europe. *Journal of Antimicrobial Chemotherapy* **2023**, *78*, 1245–1252.

- [81] Tello, A.; Austin, B.; Telfer, T. C. Selective Pressure of Antibiotic Pollution on Bacteria of Importance to Public Health. *Environmental Health Perspectives* **2012**, *120*, 1100–1106.
- [82] Davies, J.; Davies, D. Origins and Evolution of Antibiotic Resistance. *Microbiology and Molecular Biology Reviews : MMBR* **2010**, *74*, 417–433.
- [83] Roope, L. S. J.; Smith, R. D.; Pouwels, K. B.; Buchanan, J.; Abel, L.; Eibich, P.; Butler, C. C.; Tan, P. S.; Walker, A. S.; Robotham, J. V.; Wordsworth, S. The Challenge of Antimicrobial Resistance: What Economics Can Contribute. *Science* **2019**, *364*, eaau4679.
- [84] Biba, E. How We Can Stop Antibiotic Resistance. 2024; <https://www.bbc.com/future/article/20170607-how-we-can-stop-antibiotic-resistance>.
- [85] Ghosh, C.; Sarkar, P.; Issa, R.; Haldar, J. Alternatives to Conventional Antibiotics in the Era of Antimicrobial Resistance. *Trends in Microbiology* **2019**, *27*, 323–338.
- [86] Theuretzbacher, U.; Piddock, L. J. Non-Traditional Antibacterial Therapeutic Options and Challenges. *Cell Host & Microbe* **2019**, *26*, 61–72.
- [87] Lakemeyer, M.; Zhao, W.; Mandl, F. A.; Hammann, P.; Sieber, S. A. Thinking Outside the Box—Novel Antibacterials To Tackle the Resistance Crisis. *Angewandte Chemie International Edition* **2018**, *57*, 14440–14475.
- [88] Calvert, M. B.; Jumde, V. R.; Titz, A. Pathoblockers or Antivirulence Drugs as a New Option for the Treatment of Bacterial Infections. *Beilstein Journal of Organic Chemistry* **2018**, *14*, 2607–2617.
- [89] Blaskovich, M. A. T. Antibiotic Alternatives Special Issue. *ACS Infectious Diseases* **2021**, *7*, 2025–2026.
- [90] Lei, J.; Sun, L.; Huang, S.; Zhu, C.; Li, P.; He, J.; Mackey, V.; Coy, D. H.; He, Q. The Antimicrobial Peptides and Their Potential Clinical Applications. *Antimicrobial peptides*
- [91] Frei, A.; Verderosa, A. D.; Elliott, A. G.; Zuegg, J.; Blaskovich, M. A. T. Metals to Combat Antimicrobial Resistance. *Nature Reviews Chemistry* **2023**, *7*, 202–224.
- [92] Andy Brunning A Brief Overview of Classes of Antibiotics. 2014; <https://www.compoundchem.com/2014/09/08/antibiotics/>.
- [93] Centers for Disease Control and Prevention: Antibiotic Resistance & Patient Safety Portal. 2024; <https://arpsp.cdc.gov/resources/OAU-Antibiotic-Class-Definitions.pdf>.
- [94] *World Health Organization: 2021 Antibacterial Agents in Clinical and Preclinical*

*Development: An Overview and Analysis*; 2022.

- [95] Romanò, C. L.; Tsuchiya, H.; Morelli, I.; Battaglia, A. G.; Drago, L. Antibacterial Coating of Implants: Are We Missing Something? *Bone & Joint Research* **2019**, *8*, 199–206.
- [96] Alt, V. Antimicrobial Coated Implants in Trauma and Orthopaedics—A Clinical Review and Risk-Benefit Analysis. *Injury* **2017**, *48*, 599–607.
- [97] Zimmerli, W.; Sendi, P. Pathogenesis of Implant-Associated Infection: The Role of the Host. *Seminars in Immunopathology* **2011**, *33*, 295–306.
- [98] Romanò, C. L.; Scarponi, S.; Gallazzi, E.; Romanò, D.; Drago, L. Antibacterial Coating of Implants in Orthopaedics and Trauma: A Classification Proposal in an Evolving Panorama. *Journal of Orthopaedic Surgery and Research* **2015**, *10*, 157.
- [99] Chen, X.; Zhou, J.; Qian, Y.; Zhao, L. Antibacterial Coatings on Orthopedic Implants. *Materials Today Bio* **2023**, *19*, 100586.
- [100] Shahid, A.; Aslam, B.; Muzammil, S.; Aslam, N.; Shahid, M.; Almatroudi, A.; Allemailem, K. S.; Saqalein, M.; Nisar, M. A.; Rasool, M. H.; Khurshid, M. The Prospects of Antimicrobial Coated Medical Implants. *Journal of Applied Biomaterials & Functional Materials* **2021**, *19*, 228080002110403.
- [101] Bohara, S.; Suthakorn, J. Surface Coating of Orthopedic Implant to Enhance the Osseointegration and Reduction of Bacterial Colonization: A Review. *Biomaterials Research* **2022**, *26*, 26.
- [102] Liu, Z.; Liu, X.; Ramakrishna, S. Surface Engineering of Biomaterials in Orthopedic and Dental Implants: Strategies to Improve Osteointegration, Bacteriostatic and Bactericidal Activities. *Biotechnology Journal* **2021**, *16*, 2000116.
- [103] Cambridge Dictionary - "resensitize". 2023; <https://dictionary.cambridge.org/de/worterbuch/englisch/resensitize>.
- [104] Chen, C.; Cai, J.; Shi, J.; Wang, Z.; Liu, Y. Resensitizing Multidrug-Resistant Gram-negative Bacteria to Carbapenems and Colistin Using Disulfiram. *Communications Biology* **2023**, *6*, 810.
- [105] Baym, M.; Stone, L. K.; Kishony, R. Multidrug Evolutionary Strategies to Reverse Antibiotic Resistance. *Science* **2016**, *351*.
- [106] Parrino, B.; Diana, P.; Cirrincione, G.; Cascioferro, S. Bacterial Biofilm Inhibition in the Development of Effective Anti-Virulence Strategy. *The Open Medicinal Chemistry Journal* **2018**, *12*, 84–87.
- [107] Kumar, V.; Yasmeen, N.; Pandey, A.; Ahmad Chaudhary, A.; Alawam, A. S.;

- Ahmad Rudayni, H.; Islam, A.; Lakhawat, S. S.; Sharma, P. K.; Shahid, M. Antibiotic Adjuvants: Synergistic Tool to Combat Multi-Drug Resistant Pathogens. *Frontiers in Cellular and Infection Microbiology* **2023**, *13*, 1293633.
- [108] Yahav, D.; Giske, C. G.; Grāmatniece, A.; Abodakpi, H.; Tam, V. H.; Leibovici, L. New  $\beta$ -Lactam– $\beta$ -Lactamase Inhibitor Combinations. *Clinical Microbiology Reviews* **2020**, *34*, e00115–20.
- [109] Tehrani, K. H. M. E.; Martin, N. I.  $\beta$ -Lactam/ $\beta$ -Lactamase Inhibitor Combinations: An Update. *MedChemComm* **2018**, *9*, 1439–1456.
- [110] Drawz, S. M.; Bonomo, R. A. Three Decades of  $\beta$ -Lactamase Inhibitors. *Clinical Microbiology Reviews* **2010**, *23*, 160–201.
- [111] Bush, K.; Bradford, P. A.  $\beta$ -Lactams and  $\beta$ -Lactamase Inhibitors: An Overview. *Cold Spring Harbor Perspectives in Medicine* **2016**, *6*, a025247.
- [112] Narendrakumar, L.; Chakraborty, M.; Kumari, S.; Paul, D.; Das, B.  $\beta$ -Lactam Potentiators to Re-Sensitize Resistant Pathogens: Discovery, Development, Clinical Use and the Way Forward. *Frontiers in Microbiology* **2023**, *13*, 1092556.
- [113] Tehrani, K. H. M. E.; Brūchle, N. C.; Wade, N.; Mashayekhi, V.; Pesce, D.; Van Haren, M. J.; Martin, N. I. Small Molecule Carboxylates Inhibit Metallo- $\beta$ -lactamases and Resensitize Carbapenem-Resistant Bacteria to Meropenem. *ACS Infectious Diseases* **2020**, *6*, 1366–1371.
- [114] Sun, H.; Zhang, Q.; Wang, R.; Wang, H.; Wong, Y.-T.; Wang, M.; Hao, Q.; Yan, A.; Kao, R. Y.-T.; Ho, P.-L.; Li, H. Resensitizing Carbapenem- and Colistin-Resistant Bacteria to Antibiotics Using Aurano-fin. *Nature Communications* **2020**, *11*, 5263.
- [115] Mu, S.; Zhu, Y.; Wang, Y.; Qu, S.; Huang, Y.; Zheng, L.; Duan, S.; Yu, B.; Qin, M.; Xu, F.-J. Cationic Polysaccharide Conjugates as Antibiotic Adjuvants Resensitize Multidrug-Resistant Bacteria and Prevent Resistance. *Advanced Materials* **2022**, *34*, 2204065.
- [116] Edgar, R.; Friedman, N.; Molshanski-Mor, S.; Qimron, U. Reversing Bacterial Resistance to Antibiotics by Phage-Mediated Delivery of Dominant Sensitive Genes. *Applied and Environmental Microbiology* **2012**, *78*, 744–751.
- [117] Parrino, B.; Carbone, D.; Cirrincione, G.; Diana, P.; Cascioferro, S. Inhibitors of Antibiotic Resistance Mechanisms: Clinical Applications and Future Perspectives. *Future Medicinal Chemistry* **2020**, *12*, 357–359.
- [118] Del Pozo, J. L.; Patel, R. The Challenge of Treating Biofilm-associated Bacterial Infections. *Clinical Pharmacology & Therapeutics* **2007**, *82*, 204–209.

- [119] Chung, P. Y.; Toh, Y. S. Anti-Biofilm Agents: Recent Breakthrough against Multi-Drug Resistant *Staphylococcus Aureus*. *Pathogens and Disease* **2014**, *70*, 231–239.
- [120] Itoh, Y.; Wang, X.; Hinnebusch, B. J.; Preston, J. F.; Romeo, T. Depolymerization of  $\beta$ -1,6- N -Acetyl- d -Glucosamine Disrupts the Integrity of Diverse Bacterial Biofilms. *Journal of Bacteriology* **2005**, *187*, 382–387.
- [121] Deng, W.; Lei, Y.; Tang, X.; Li, D.; Liang, J.; Luo, J.; Liu, L.; Zhang, W.; Ye, L.; Kong, J.; Wang, K.; Chen, Z. DNase Inhibits Early Biofilm Formation in Pseudomonas Aeruginosa- or Staphylococcus Aureus-Induced Empyema Models. *Frontiers in Cellular and Infection Microbiology* **2022**, *12*, 917038.
- [122] Mann, E. E.; Rice, K. C.; Boles, B. R.; Endres, J. L.; Ranjit, D.; Chandramohan, L.; Tsang, L. H.; Smeltzer, M. S.; Horswill, A. R.; Bayles, K. W. Modulation of eDNA Release and Degradation Affects Staphylococcus Aureus Biofilm Maturation. *PLoS ONE* **2009**, *4*, e5822.
- [123] Whiteley, M.; Diggle, S. P.; Greenberg, E. P. Progress in and Promise of Bacterial Quorum Sensing Research. *Nature* **2017**, *551*, 313–320.
- [124] Li, Y.-H.; Tian, X. Quorum Sensing and Bacterial Social Interactions in Biofilms. *Sensors* **2012**, *12*, 2519–2538.
- [125] Yi, L.; Dong, X.; Grenier, D.; Wang, K.; Wang, Y. Research Progress of Bacterial Quorum Sensing Receptors: Classification, Structure, Function and Characteristics. *Science of The Total Environment* **2021**, *763*, 143031.
- [126] Proctor, C. R.; McCarron, P. A.; Ternan, N. G. Furanone Quorum-Sensing Inhibitors with Potential as Novel Therapeutics against Pseudomonas Aeruginosa. *Journal of Medical Microbiology* **2020**, *69*, 195–206.
- [127] Ren, D.; Sims, J. J.; Wood, T. K. Inhibition of Biofilm Formation and Swarming of *Escherichia Coli* by ( 5Z )-4-bromo-5-(Bromomethylene)-3-butyl-2( 5H )-furanone. *Environmental Microbiology* **2001**, *3*, 731–736.
- [128] Milton, M. E.; Minrovic, B. M.; Harris, D. L.; Kang, B.; Jung, D.; Lewis, C. P.; Thompson, R. J.; Melander, R. J.; Zeng, D.; Melander, C.; Cavanagh, J. Re-Sensitizing Multidrug Resistant Bacteria to Antibiotics by Targeting Bacterial Response Regulators: Characterization and Comparison of Interactions between 2-Aminoimidazoles and the Response Regulators BfmR from Acinetobacter Baumannii and QseB from Francisella Spp. *Frontiers in Molecular Biosciences* **2018**, *5*, 15.
- [129] Ishida, T.; Ikeda, T.; Takiguchi, N.; Kuroda, A.; Ohtake, H.; Kato, J. Inhibition of

Quorum Sensing in *Pseudomonas Aeruginosa* by *N* -Acyl Cyclopentylamides. *Applied and Environmental Microbiology* **2007**, *73*, 3183–3188.

- [130] Kim, A.; Abdelhay, N.; Levin, L.; Walters, J. D.; Gibson, M. P. Antibiotic Prophylaxis for Implant Placement: A Systematic Review of Effects on Reduction of Implant Failure. *British Dental Journal* **2020**, *228*, 943–951.
- [131] Leusmann, S.; Ménová, P.; Shanin, E.; Titz, A.; Rademacher, C. Glycomimetics for the Inhibition and Modulation of Lectins. *Chemical Society Reviews* **2023**, *52*, 3663–3740.
- [132] Goral, V. N.; Zaytseva, N. V.; Baeumner, A. J. Electrochemical Microfluidic Biosensor for the Detection of Nucleic Acid Sequences. *Lab on a Chip* **2006**, *6*, 414–421.

# List of Figures

1.1	Vicious cycle of antimicrobial resistance (AMR) leading to the use of more antibiotics (ABs) and decrease of still effective critical ABs. Examples of policy initiatives, positive and negative effects and the interaction of the publications listed in the results on the cycle are presented. Figure created with biorender.com. . . . .	2
1.2	Workflow from sample collection until targeted antibiotic (AB) therapy. A generalized overview of several phenotypic [47–65] and genotypic [30–42] approaches for antimicrobial susceptibility testing (AST) methods is illustrated. Figure created with biorender.com. . . . .	6
1.3	Generalized overview of most prominent traditional [92, 93] and non-traditional [94] antimicrobials, antimicrobial resistances and resensitization approaches. Figure created with biorender.com. . . . .	9

# **A Appendix**

## **A.1 Supporting Material for Chapter 3.1**

### **A.1.1 Supporting Material: Direct 3D Printed Biocompatible Microfluidics: Assessment of Human Mesenchymal Stem Cell Differentiation and Cytotoxic Drug Screening in a Dynamic Culture System**

## Direct 3D printed biocompatible microfluidics: assessment of human mesenchymal stem cell differentiation and cytotoxic drug screening in a dynamic culture system

Oliver Riester <sup>1,2</sup>, Stefan Laufer <sup>2,3</sup> and Hans-Peter Deigner <sup>\*,1,4,5</sup>

<sup>1</sup> Institute of Precision Medicine, Furtwangen University, Jakob-Kienzle-Strasse 17, Villingen-Schwenningen, 78054, Germany

<sup>2</sup> Institute of Pharmaceutical Sciences, Department of Pharmacy and Biochemistry, Eberhard-Karls-University Tuebingen, Auf der Morgenstelle 8, Tuebingen, 72076, Germany

<sup>3</sup> Tuebingen Center for Academic Drug Discovery & Development (TüCAD2), 72076 Tuebingen, Germany

<sup>4</sup> Faculty of Science, Eberhard-Karls-University Tuebingen, Auf der Morgenstelle 8, Tuebingen, 72076, Germany

<sup>5</sup> EXIM Department, Fraunhofer Institute IZI (Leipzig), Schillingallee 68, Rostock, 18057, Germany

### Influence of printing parameters

The influence of the parameters, printing temperature ( $\vartheta$ ), printing speed ( $v$ ), layer height ( $h$ ) and fan speed ( $fan$ ) on the achieved printing resolution was analyzed. The following diagrams show the results for each tested polymer and parameter. The original parameters are based on the manufacturer's specifications for the respective polymer.

#### Analyzed parameter: printing temperature ( $\vartheta$ )

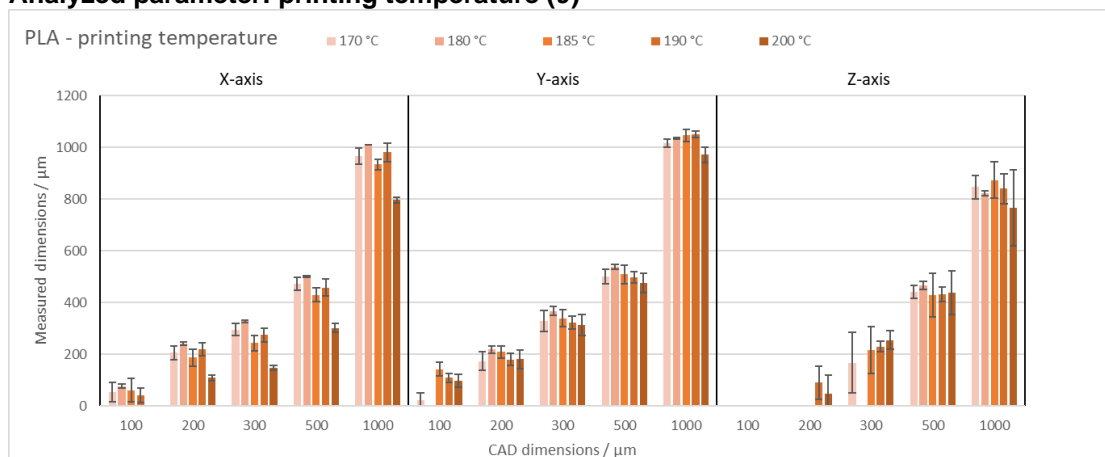


**Fig. S1 | Obtained dimensions of the 3D printed poly (lactic acid) (PLA) test device for various printing temperatures.** Remaining parameters were kept constant at  $v = 30$  mm/s,  $h = 50$   $\mu$ m and  $fan = 100\%$ . Results are shown for the X-, Y- and Z-axis separately. Values shown as mean  $\pm$  standard deviation of 3 devices.

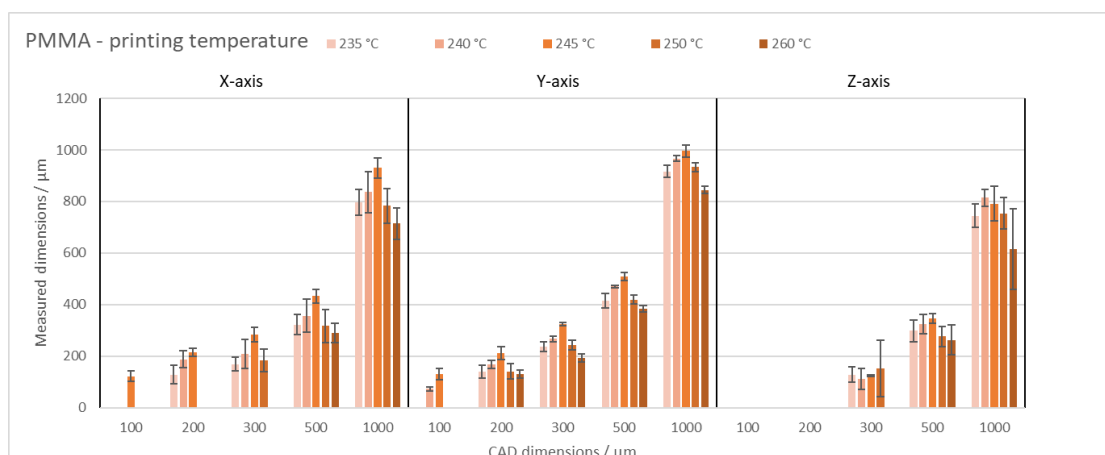


**Fig. S2 | Obtained dimensions of the 3D printed poly (methyl methacrylate) (PMMA) test device for various printing temperatures.** Remaining parameters were kept constant at  $v = 50$  mm/s,  $h = 100$   $\mu$ m and  $fan = 50\%$ . Results are shown for the X-, Y- and Z-axis separately. Values shown as mean  $\pm$  standard deviation of 3 devices.

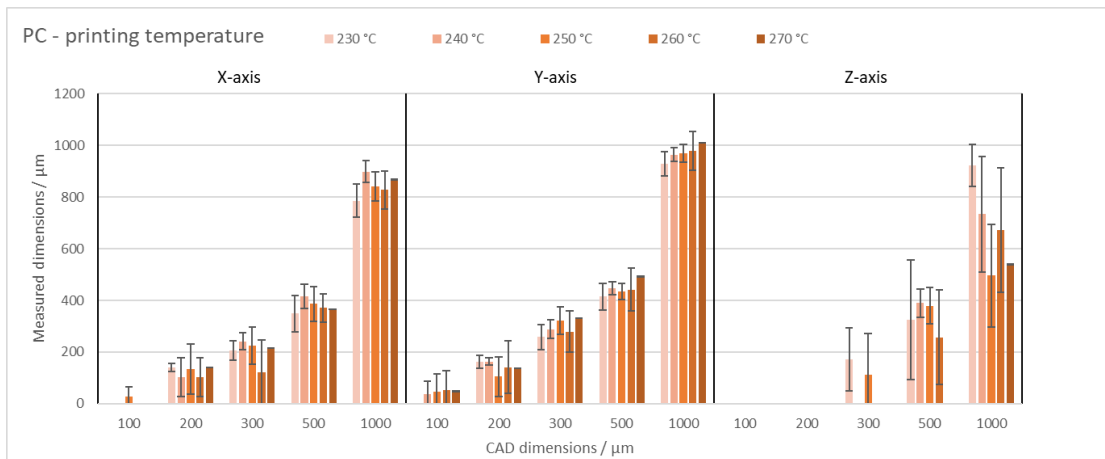


**Fig. S3** | Obtained dimensions of the 3D printed polycarbonate (PC) test device for various printing temperatures. Remaining parameters were kept constant at  $v = 50 \text{ mm/s}$ ,  $h = 100 \mu\text{m}$  and  $\text{fan} = 0\%$ . Results are shown for the X-, Y- and Z-axis separately. Values shown as mean  $\pm$  standard deviation of 3 devices.

**Analyzed parameter: printing speed (v)**

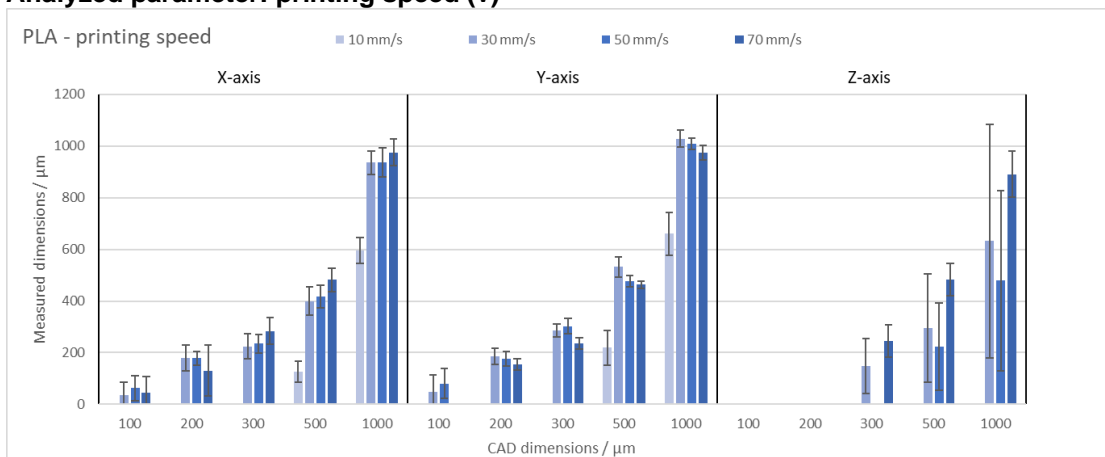


**Fig. S4** | Obtained dimensions of the 3D printed poly (lactic acid) (PLA) test device for various printing speeds. Remaining parameters were kept constant at  $\vartheta = 190 \text{ }^\circ\text{C}$ ,  $h = 50 \mu\text{m}$  and  $\text{fan} = 100\%$ . Results are shown for the X-, Y- and Z-axis separately. Values shown as mean  $\pm$  standard deviation of 3 devices.

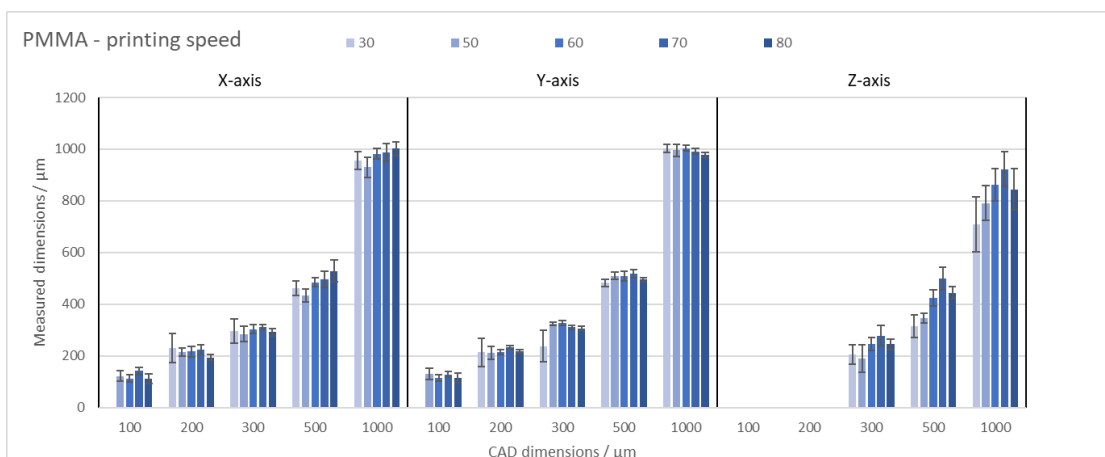


**Fig. S5** | Obtained dimensions of the 3D printed poly (methyl methacrylate) (PMMA) test device for various printing speeds. Remaining parameters were kept constant at  $\vartheta = 245 \text{ }^\circ\text{C}$ ,  $h = 100 \mu\text{m}$  and  $\text{fan} = 50\%$ . Results are shown for the X-, Y- and Z-axis separately. Values shown as mean  $\pm$  standard deviation of 3 devices.

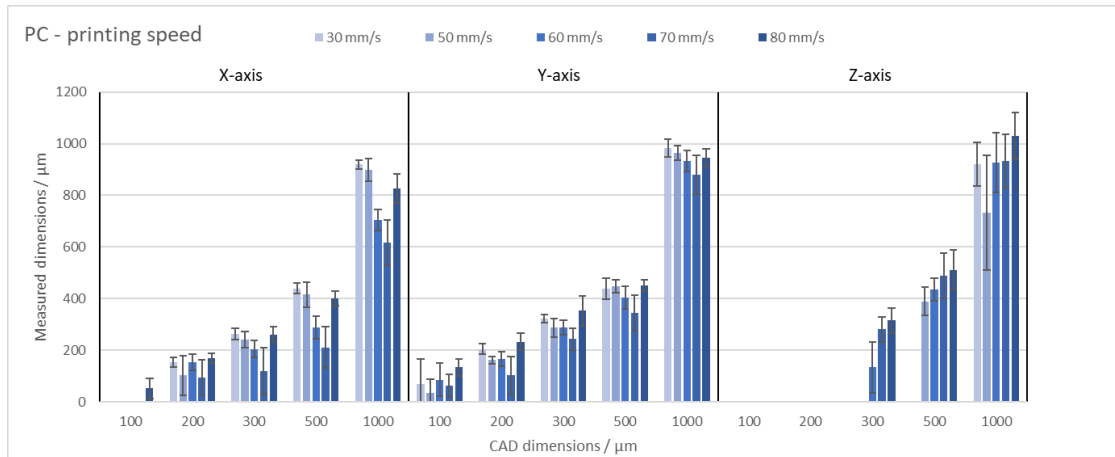


**Fig. S6|** Obtained dimensions of the 3D printed polycarbonate (PC) test device for various printing speeds. Remaining parameters were kept constant at  $\vartheta = 240\text{ }^\circ\text{C}$ ,  $h = 100\text{ }\mu\text{m}$  and fan = 0%. Results are shown for the X-, Y- and Z-axis separately. Values shown as mean  $\pm$  standard deviation of 3 devices.

**Analyzed parameter: layer height (h)**

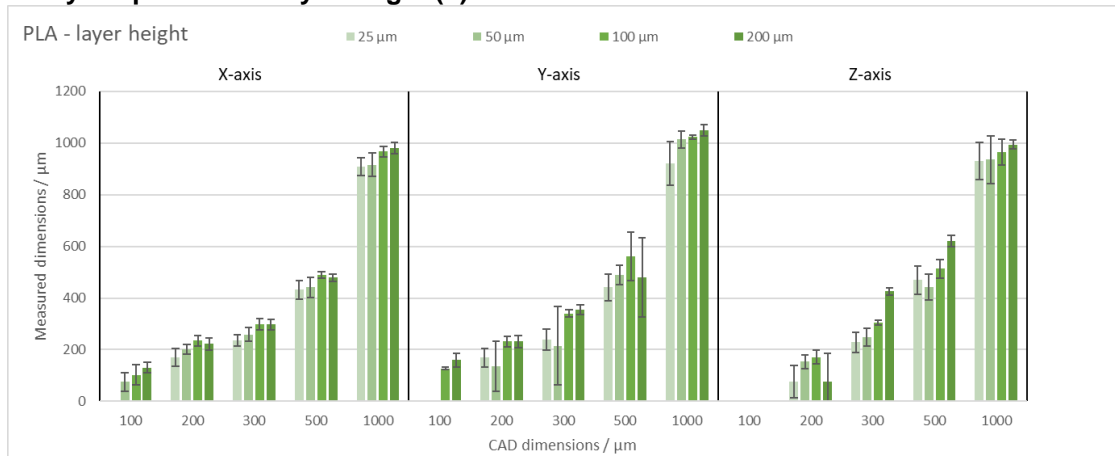


**Fig. S7|** Obtained dimensions of the 3D printed poly (lactic acid) (PLA) test device for various layer heights. Remaining parameters were kept constant at  $\vartheta = 190\text{ }^\circ\text{C}$ ,  $v = 70\text{ mm/s}$  and fan = 100%. Results are shown for the X-, Y- and Z-axis separately. Values shown as mean  $\pm$  standard deviation of 3 devices.

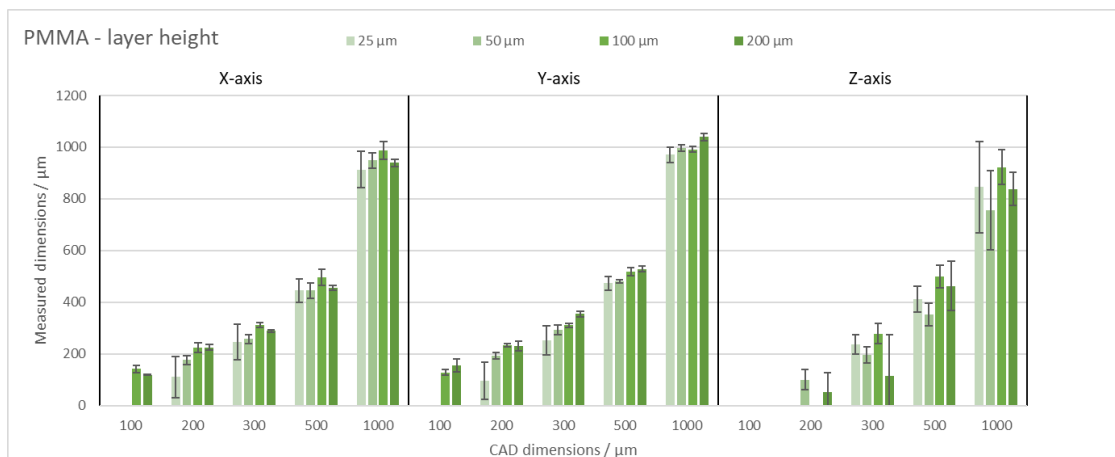


**Fig. S8|** Obtained dimensions of the 3D printed poly (methyl methacrylate) (PMMA) test device for various layer heights. Remaining parameters were kept constant at  $\vartheta = 245\text{ }^\circ\text{C}$ ,  $v = 70\text{ mm/s}$  and fan = 50%. Results are shown for the X-, Y- and Z-axis separately. Values shown as mean  $\pm$  standard deviation of 3 devices.

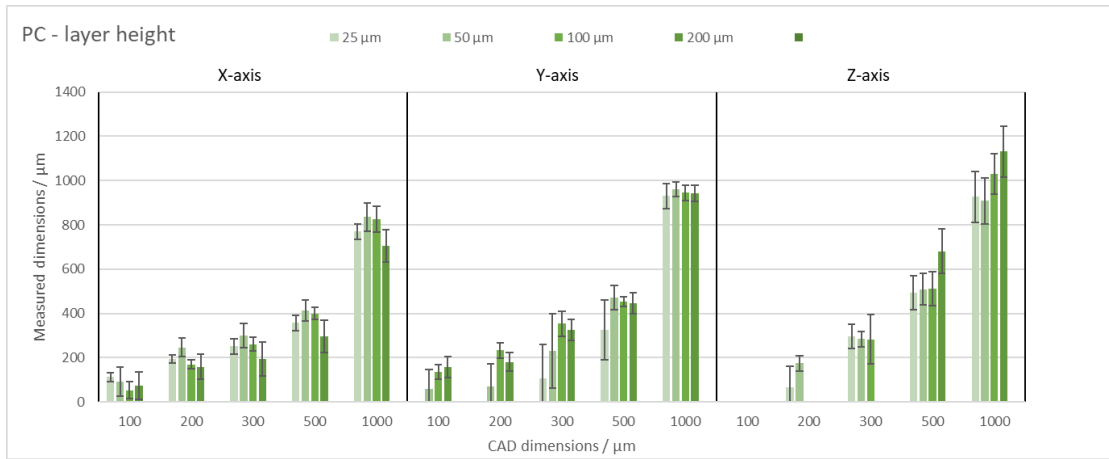


**Fig. S9** | Obtained dimensions of the 3D printed polycarbonate (PC) test device for various layer heights. Remaining parameters were kept constant at  $\vartheta = 240\text{ }^\circ\text{C}$ ,  $v = 80\text{ mm/s}$  and fan = 0%. Results are shown for the X-, Y- and Z-axis separately. Values shown as mean  $\pm$  standard deviation of 3 devices.

**Analyzed parameter: fan speed (fan)**

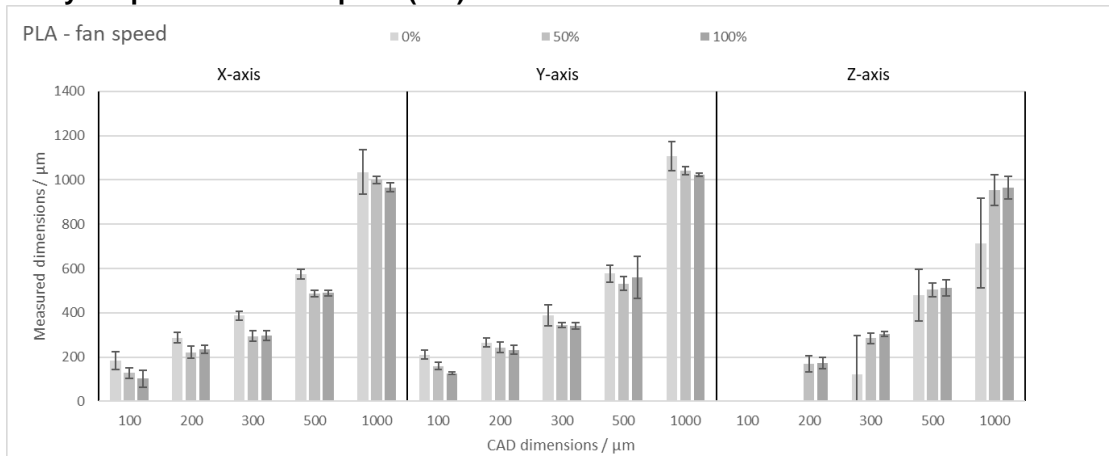


**Fig. S10** | Obtained dimensions of the 3D printed poly (lactic acid) (PLA) test device for various fan speeds. Remaining parameters were kept constant at  $\vartheta = 190\text{ }^\circ\text{C}$ ,  $v = 70\text{ mm/s}$  and  $h = 100\text{ }\mu\text{m}$ . Results are shown for the X-, Y- and Z-axis separately. Values shown as mean  $\pm$  standard deviation of 3 devices.

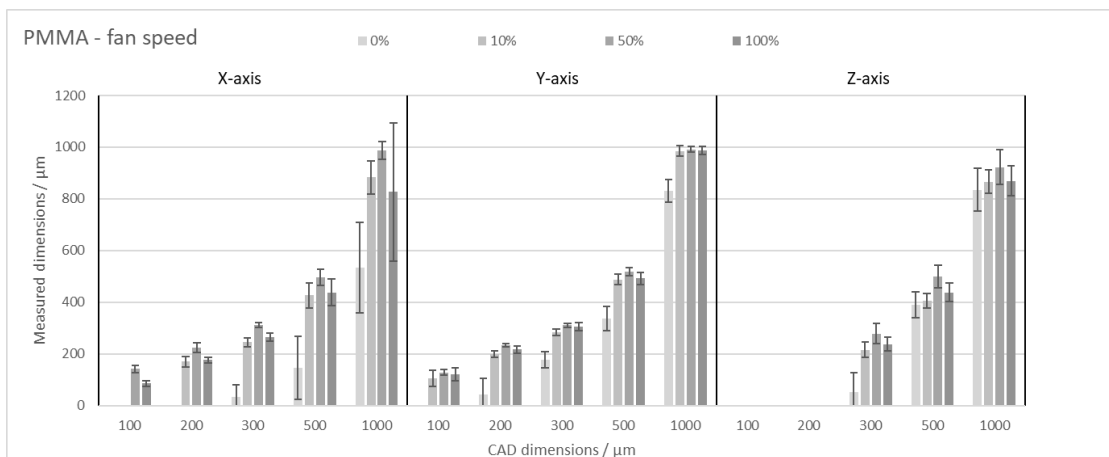


**Fig. S11** | Obtained dimensions of the 3D printed poly (methyl methacrylate) (PMMA) test device for various fan speeds. Remaining parameters were kept constant at  $\vartheta = 245\text{ }^\circ\text{C}$ ,  $v = 70\text{ mm/s}$  and  $h = 100\text{ }\mu\text{m}$ . Results are shown for the X-, Y- and Z-axis separately. Values shown as mean  $\pm$  standard deviation of 3 devices.

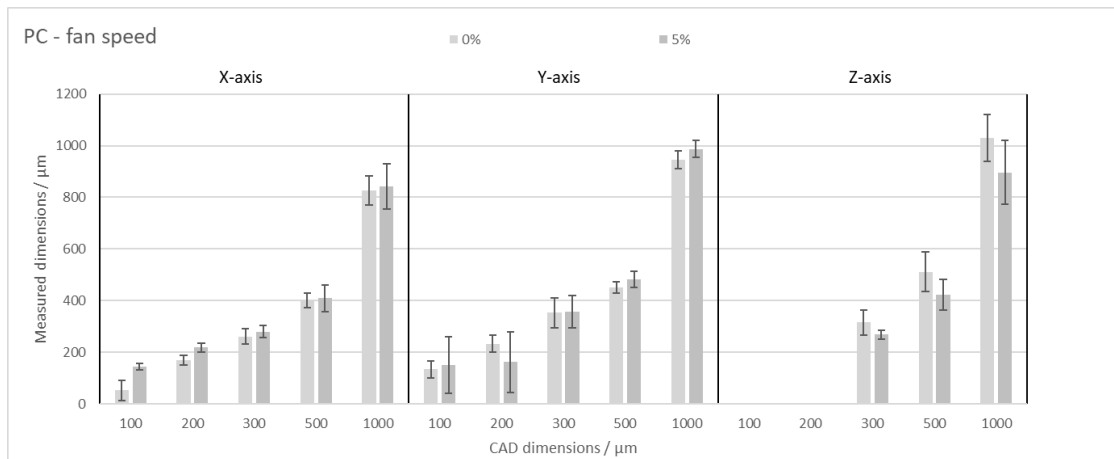


**Fig. S12| Obtained dimensions of the 3D printed polycarbonate (PC) test device for various fan speeds.** Remaining parameters were kept constant at  $\vartheta = 240\text{ }^{\circ}\text{C}$ ,  $v = 80\text{ mm/s}$  and  $h = 100\text{ }\mu\text{m}$ . Results are shown for the X-, Y- and Z-axis separately. Values shown as mean  $\pm$  standard deviation of 3 devices.

**Microscopic images of the 3D-printed test devices**

**PLA test device**

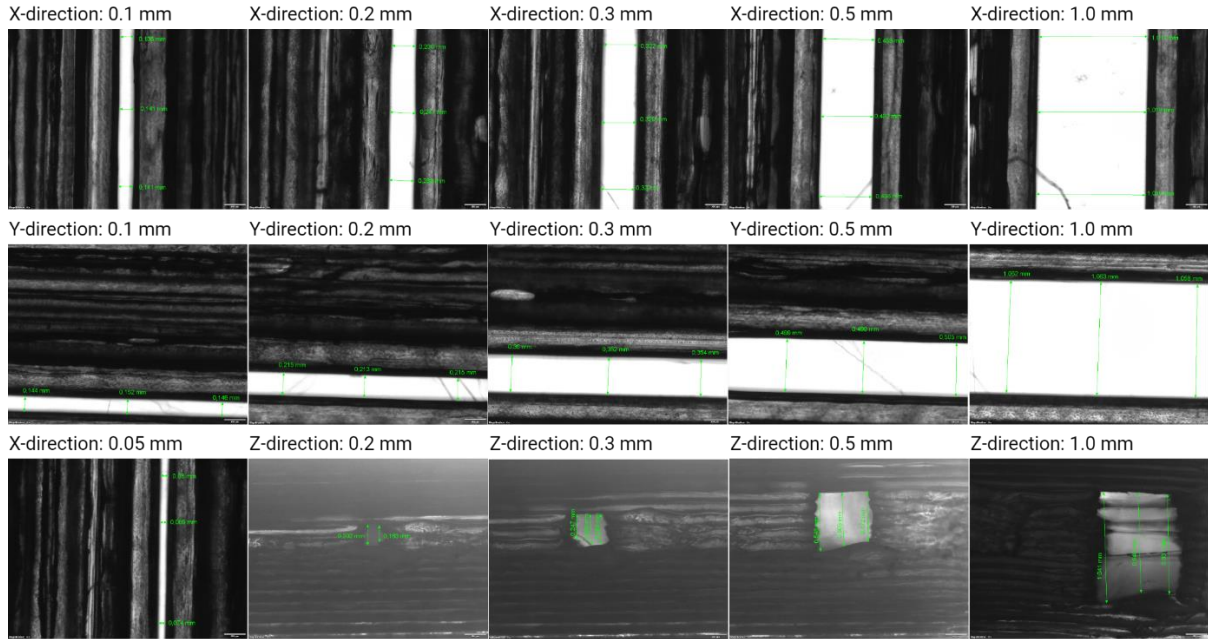


**Fig. S13 | Representative microscopic images of FDM printed micro channels in a poly (lactic acid) (PLA) test device.** Analysis performed with “imageJ” (Version 1.52a, National Institutes of Health, USA). Scale bar measures 200  $\mu$ m.

**PMMA test device**

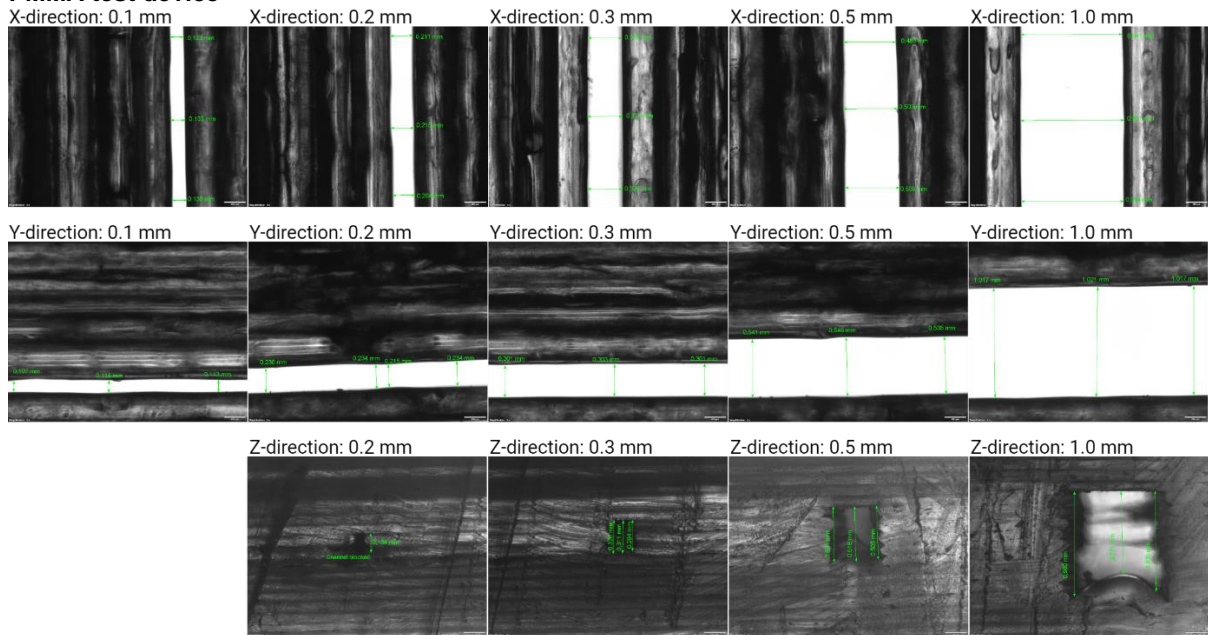


**Fig. S14 | Representative microscopic images of FDM printed micro channels in a poly (methyl methacrylate) (PMMA) test device.** Analysis performed with “imageJ” (Version 1.52a, National Institutes of Health, USA). Scale bar measures 200  $\mu$ m.

**PC test device**

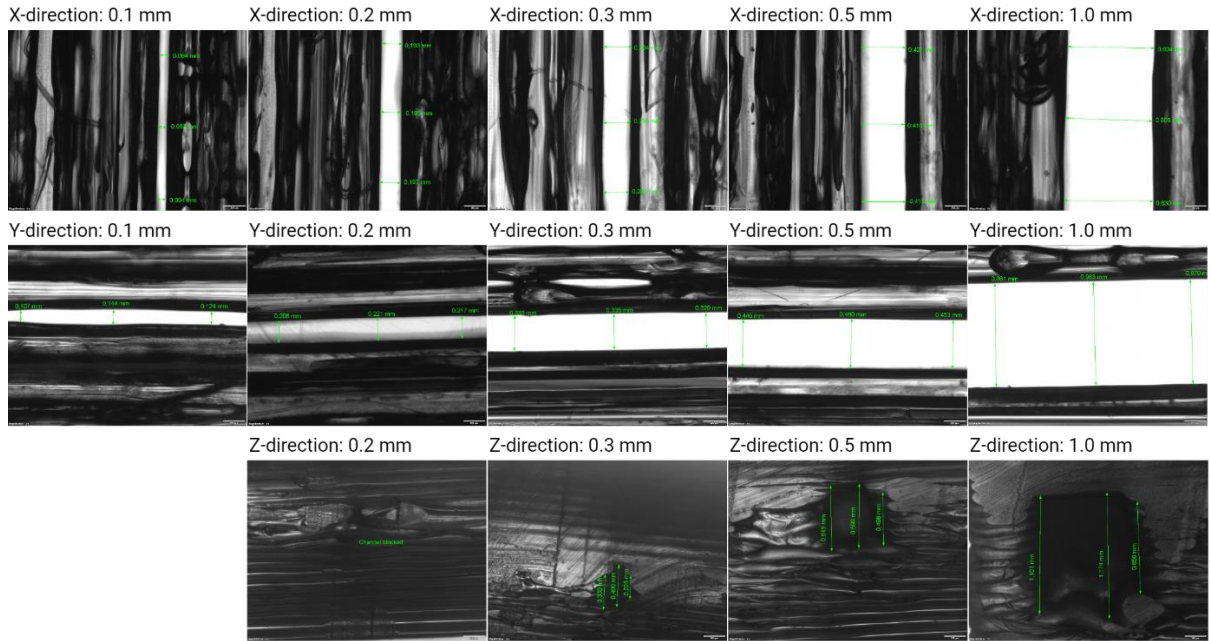


Fig. S15|Representative microscopic images of FDM printed micro channels in a PC test device. Analysis performed with “imageJ” (Version 1.52a, National Institutes of Health, USA). Scale bar measures 200 µm.

**Relative deviation between experimental dimensions and CAD dimensions**

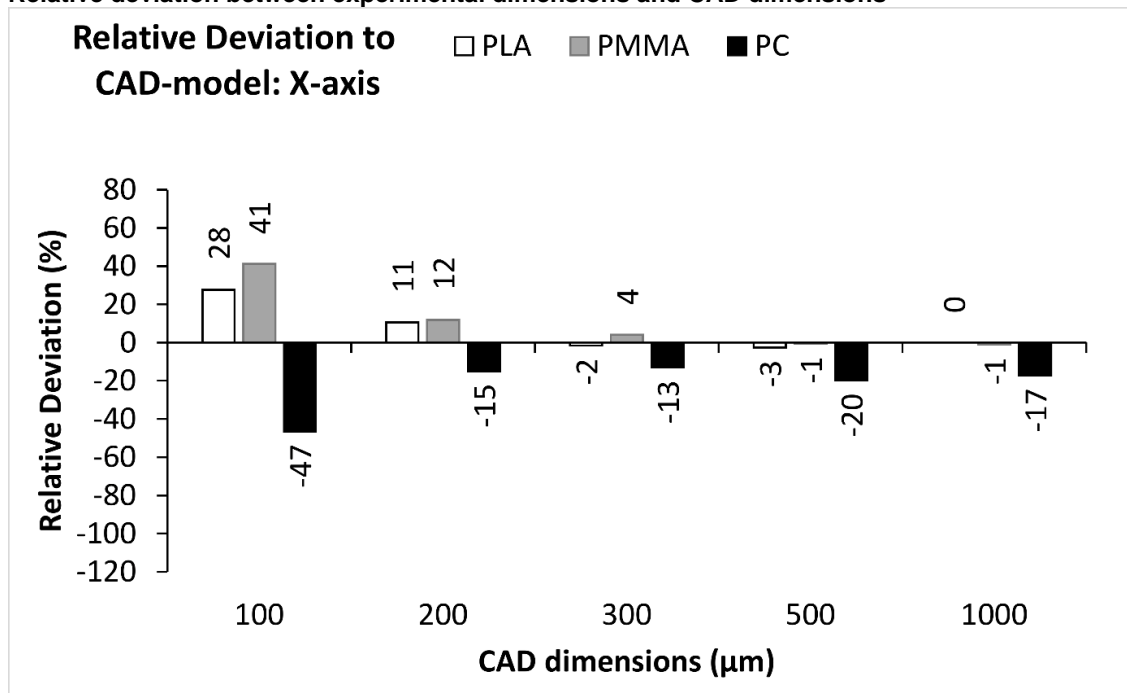


Fig.S16|Relative deviation between experimental dimensions and CAD dimensions in X-direction.

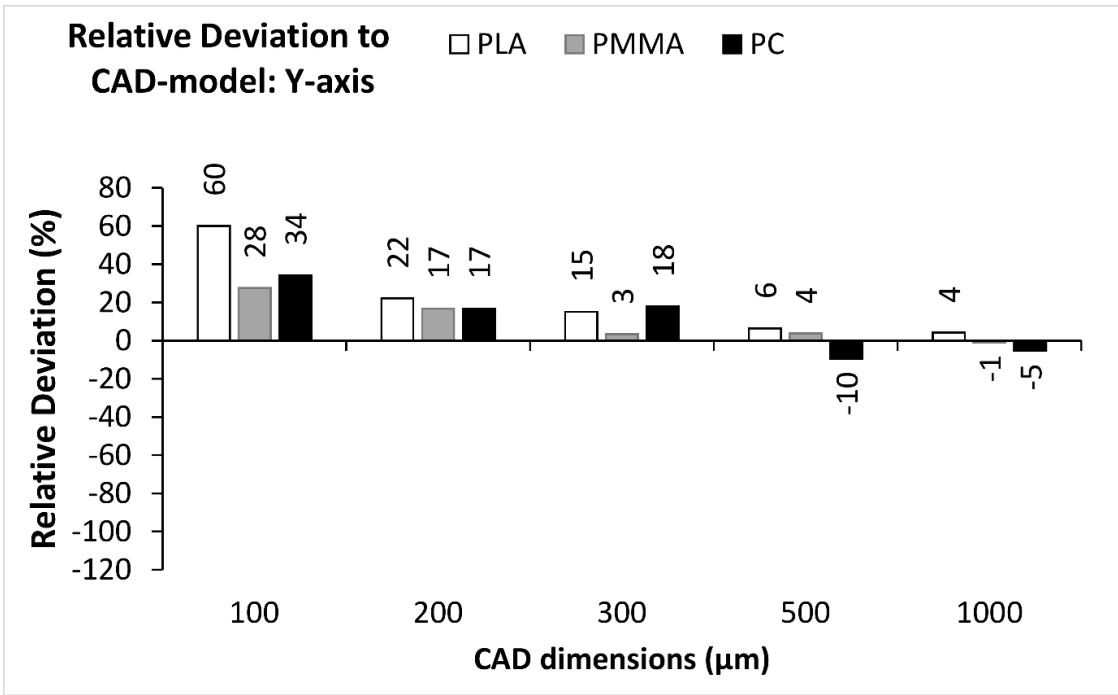


Fig.S17|Relative deviation between experimental dimensions and CAD dimensions in X-direction.

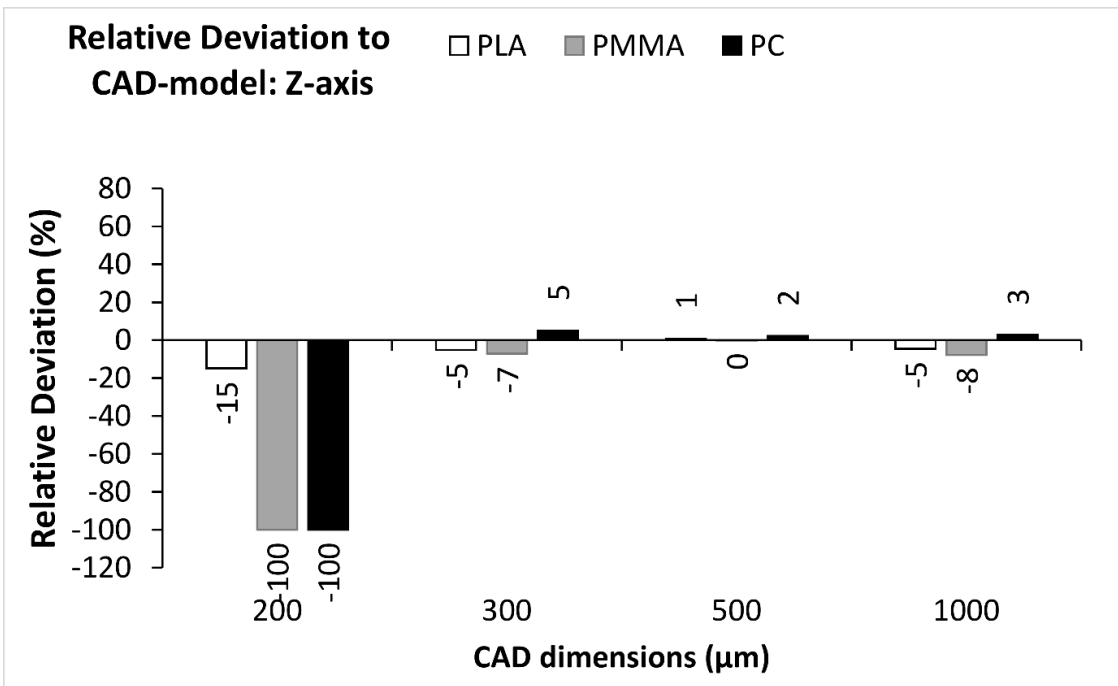
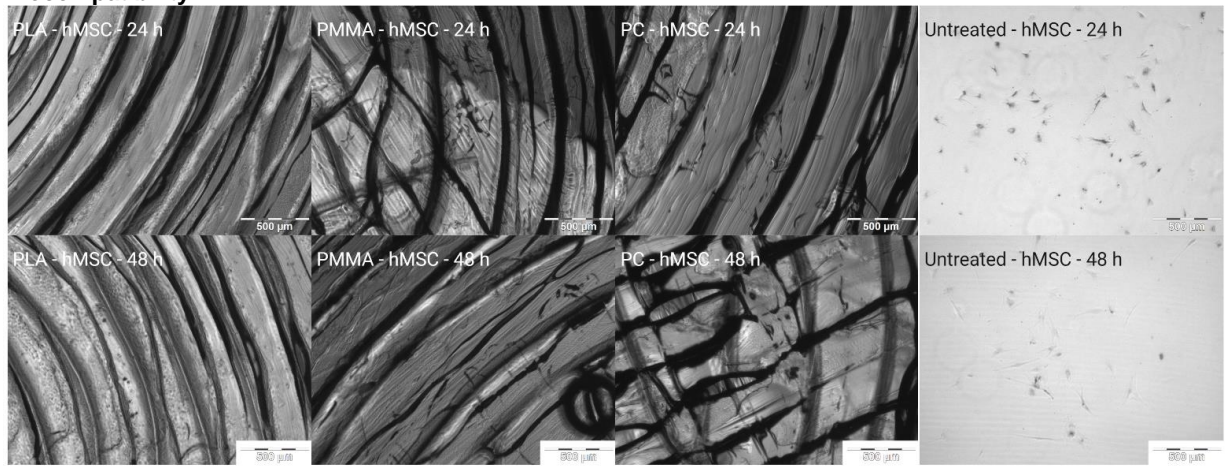


Fig.S18|Relative deviation between experimental dimensions and CAD dimensions in X-direction.

**Biocompatibility**

**Fig. S19|**Representative microscopic images of FDM printed polymer discs cultivated with human mesenchymal stem cells (hMSC) for 24 and 48 hours. Viability of hMSC cultivated on PLA, PMMA and PC discs was analyzed with MTT assay and compared to untreated hMSCs cultivated in a standard tissue culture 24-well plate. Images were taken after staining with MTT. Scale bar measures 500 µm.

## A.1.2 Supporting Material: Rapid Phenotypic Antibiotics Susceptibility Analysis by a 3D Printed Prototype



Supporting Information

for *Adv. Sci.*, DOI 10.1002/adv.202308806

Rapid Phenotypic Antibiotics Susceptibility Analysis by a 3D Printed Prototype

*Oliver Riester, Lars Kaiser, Stefan Laufer and Hans-Peter Deigner\**

## Supporting Information

### **Rapid Phenotypic Antibiotics Susceptibility Analysis by a 3D Printed Prototype**

*Oliver Riester, Lars Kaiser, Stefan Laufer, Hans-Peter Deigner \**

\* Corresponding author. Email: deigner@gmx.de

#### **Abstract**

One of the most important public health concerns is the increase in antibiotic-resistant pathogens and corresponding treatment of associated infections. Addressing this challenge requires more efficient use of antibiotics, achievable by the use of evidence-based, effective antibiotics identified by antibiotic susceptibility testing (AST). However, the current standard method of phenotypic AST used for this purpose requires 48 hours or more from sample collection to result. Until results are available, broad-spectrum antibiotics are used to avoid delaying treatment. The turnaround time must therefore be shortened in order for the results to be available before the second administration of antibiotics. The phenotypic electrochemical AST method presented here identifies effective antibiotics within 5 - 10 hours after sampling. Spiked serum samples, including polymicrobial samples, with clinically relevant pathogens and respective concentrations commonly found in bloodstream infections (*E. coli*, *S. aureus*, *K. pneumoniae* and *P. aeruginosa*) are used. Direct loading of the test with diluted serum eliminates the need for a pre-culture, as required by existing methods. Furthermore, by combining several electrochemical measurement procedures with computational analysis, allowing the method to be used both online and offline, the AST achieves a sensitivity of 94.44% and a specificity of 95.83% considering each replicate individually.

Keywords: antibiotic susceptibility testing, phenotypic, antibiotic resistances, 3D printer, screen printed electrodes, no preculture

## Experimental Section

### Differential Pulse Voltammetry (DPV) for Concentration Determination of Resazurin

Measurement of resazurin by the DPV method was investigated with two SPEs for linearity and signal strength. Electrodes were electrochemically cleaned before use by 5 cycles of cyclic voltammetry in PBS. Solutions with 0; 0.01; 0.05; 0.1; 0.5 and 1 mM Resazurin solved in PBS, 25/75% FCS/LB medium or 100% FCS were tested. Measurements were performed with the PalmSens4 potentiostat and the Software PSTrace after equilibrium was reached. The following parameters were used for DPV measurement: IS-C electrode ( $E_{\text{begin}} = -0.8 \text{ V}$ ;  $E_{\text{end}} = 0.0 \text{ V}$ ;  $E_{\text{pulse}} = 0.05 \text{ V}$ ;  $t_{\text{pulse}} = 0.01 \text{ s}$ ; Scan rate = 0,05 V/s) and BVT-AC1 electrode ( $E_{\text{begin}} = -1.4 \text{ V}$ ;  $E_{\text{end}} = 0 \text{ V}$ ;  $E_{\text{pulse}} = 0.5 \text{ V}$ ;  $t_{\text{pulse}} = 0.01 \text{ s}$ ; Scan rate = 0,05 V/s). DPV curves were exported from PSTrace after moving average baseline correction and plotted using GraphPad Prism 8 (GraphPad Software, USA).

### Pre-wetting of Electrodes

Devices were pre-treated to evaluate the influence of wetting effects on the initial time to reach an equilibrium state. Therefore, sterile devices (aerobic design, one chamber) were loaded with 100  $\mu\text{l}$  millipore water, PBS, LB-medium, 75% LB 25% FCS, 100% FCS or none (untreated) and incubated at 37°C in a humidified incubator for 2 h. Afterwards, the added liquid was removed and the devices were loaded with 200  $\mu\text{l}$  sample consisting of 50  $\mu\text{l}$  FCS and 150  $\mu\text{l}$  LB medium with 0.2 mM Resazurin. For this test samples were used without bacteria and antibiotics as these have shown no effect on the initial phase of the measurement so far.

### Polymicrobial Samples

The suitability of the electrochemical prototype for evaluating efficacy of tested antibiotics for polymicrobial samples was tested for combinations of three strains spiked (each strain to 333 CFU/ml) in human plasma from healthy donors purchased from Sigma-Aldrich (Sigma-Aldrich Chemie GmbH, Taufkirchen, Germany). Strain combinations were selected from the 7 strains to obtain 4 combinations ranging from 3 sensitive (S) to 3 resistant (R) strains (SSS, RSS, RRS, RRR) per antibiotic to be tested. Each polymicrobial sample was mixed in a labeled 1.5 ml reaction tube by adding 180  $\mu\text{l}$  LB-medium, 5  $\mu\text{l}$  of 10 mM Resazurin stock, 2.5  $\mu\text{l}$  of the respective 10 mg/ml antibiotic stock and 62.5  $\mu\text{l}$  spiked human plasma (each strain 333 CFU/ml; combined around 1000 CFU/ml). Then, 200  $\mu\text{l}$  of samples were transferred to electrochemical devices (aerobic design, one chamber), connected to the potentiostat PalmSens4 and incubated in a humidified incubator at 37°C. DPV and EIS measurements were performed every 10 minutes for 20 h and growth was detected using the combined method approach.

### Minimum Inhibitory Concentration Assay

Minimum inhibitory concentration (MIC) was tested according to an adapted version of Kowalska-Krochmal et al.<sup>[1]</sup> and ISO 20776-1.<sup>[2]</sup> The assay was performed as broth microdilution in a 96-wellplate (TPP Techno Plastic Products AG, Trasadingen, Switzerland) design and on the electrochemical devices to evaluate comparability for MIC measurements with the prototype using human serum samples from healthy donors purchased from Sigma-Aldrich (Sigma-Aldrich Chemie GmbH, Taufkirchen, Germany) spiked with corresponding bacteria of an overnight culture to match a clinical blood sample. The sensitive strains *S. aureus* (DSM 799) and *K. pneumoniae* (DSM 30104) were chosen as example strains based on their relevance for bloodstream infections (BSI) and their sensitive character to the test antibiotics kanamycin and oxytetracycline.

For comparability reasons, both MIC assays (broth microdilution and prototype) were performed in an overall volume of 200  $\mu\text{l}$  25% human serum 75% LB-medium. For the broth microdilution method a 96-wellplate was loaded with 50  $\mu\text{l}$  of a 10-fold dilution series (400  $\mu\text{g/ml}$  – 0.4  $\mu\text{g/ml}$  corresponding to 100  $\mu\text{g/ml}$  – 0.1  $\mu\text{g/ml}$  in endvolume of 200  $\mu\text{l}$ ) of kanamycin or oxytetracycline in LB-medium. Then, 50  $\mu\text{l}$  human plasma spiked with  $2 \times 10^6$  CFU/ml (final concentration in 200  $\mu\text{l}$  according to Kowalska-Krochmal et al.:<sup>[1]</sup>  $5 \times 10^5$  CFU/ml) and 100  $\mu\text{l}$  LB-medium were added, resulting in 200  $\mu\text{l}$  per well. The lid of the wellplate was closed, sealed with parafilm and incubated for 24 h at 37°C in an incubator. After 24 h photos were taken and growth was visually analyzed.

The MIC assay in the electrochemical prototype was performed similarly with some modifications: 250  $\mu\text{l}$  were prepared in 1.5 ml reaction tubes, of which 200  $\mu\text{l}$  were added to the device. 62.5  $\mu\text{l}$  of a 10-fold dilution series (400  $\mu\text{g/ml}$  – 0.4  $\mu\text{g/ml}$  corresponding to 100  $\mu\text{g/ml}$  – 0.1  $\mu\text{g/ml}$  in endvolume of 250  $\mu\text{l}$ ) of kanamycin or oxytetracycline in LB-medium were added to labeled 1.5 ml reaction tubes. Then, 62.5  $\mu\text{l}$  human plasma spiked with 1000 CFU/ml and 125  $\mu\text{l}$  LB-medium containing 0.4 mM Resazurin (corresponds to 0.2 mM Resazurin in 250  $\mu\text{l}$ ) was added, resulting in 250  $\mu\text{l}$  per tube. The sample was mixed and 200  $\mu\text{l}$  were loaded into an electrochemical device (aerobic design, one chamber), connected to the potentiostat PalmSens4 and incubated in a humidified incubator at 37°C without shaking. DPV and EIS measurements were performed every 10 minutes for 20 h and growth was detected using the combined method approach.

## Results and Discussion

### DPV - Signal Changes

The measurement of resazurin metabolism by DPV was indicated by a change in current flow at the peak characteristic of resazurin. An increase in bacterial growth was usually accompanied by a decrease in current intensity (e.g. Figure S2 to S8). In the case of *K. pneumoniae*, however, in addition to the decrease, a time-shifted increase was also observed, which also occurred in the case of *P. aeruginosa*, but without the characteristic decrease. As this behavior was specific for these pathogens, it was tested whether it also occurs without the addition of resazurin, which occurred to be the case, as shown in Figure S11, although to a lesser extent. As the signal is not entirely related to resazurin, it is assumed, that it originates from a metabolic product. Nevertheless, a detailed evaluation of the underlying mechanisms has not yet been carried out. For the measurement of growth, however, the use of this effect is also suitable, since it only occurs when growth is present.

### Antibiotic Susceptibility Test by Bacterial Metabolism of Resazurin – Linearity by Differential Pulsed Voltammetry (DPV)

Several concentrations of resazurin in PBS or 25/75% FCS/LB were analyzed by DPV. The results obtained are shown in Figure S9 for IS-C and BVT screen printed electrodes (SPEs). Measurements in PBS showed nonlinear behavior for IS-C but not for BVT SPEs, as shown in Figure S10, which is likely caused by diffusion limitations at the electrode surface, since the carbon-based (IS-C) SPEs have a larger surface area than the tested gold electrodes (BVT) due to the porous structures of the electrode material.<sup>[3,4]</sup> However, when tested in 25/75% FCS/LB, the IS-C electrodes also showed a linear behavior, probably due to the biomolecules present in the FCS and LB media, which blocked part of the electrochemically available surfaces and reduced the reaction rate, making diffusion limitation less crucial. A decrease in the reaction rate of resazurin in PBS to 25/75% FCS/LB is also evident when comparing the maximum current values for the same resazurin concentration, e.g.,  $52.13 \pm 4.80 \mu\text{A}$  in PBS versus  $21.37 \pm 6.31 \mu\text{A}$  in 25/75% FCS/LB for 0.5 mM resazurin at the IS-C electrode. This trend continued in 100% FCS (Figure S10) to  $4.093 \mu\text{A}$  for 0.5 mM resazurin. As shown in Figure S10, DPV measurements were possible in 100% FCS, but 25/75% FCS/LB was chosen in the antibiotic susceptibility testing (AST) experiments since the parallel EIS measurements in 100% FCS led to non-reproducible results and interference.

### Effect of Pre-wetting Electrodes on Time to Initial Equilibrium

The effect of pre-treatment of the electrodes by wetting prior to the experiment was assessed by the time until a stable current ( $I_{\text{initial increase}}$ ), according to Dalheim et al.,<sup>[5]</sup> and the time from which a steady rise in the measured impedance from the minimum ( $Z_{\text{low}}$ ) was observed. The initial increase in  $I$ , which was observed in all measurements with and without bacteria and was accompanied by an initial decrease in  $Z$ , was shortened by the pre-treatment of the electrode. However, different effects were observed depending on the medium used. As shown in Figure S12, using millipore water for pre-treatment showed no effect ( $I_{\text{initial increase}}$ : 3h10min;  $Z_{\text{low}}$ : 0h20min – 1h40min) compared to the untreated device ( $I_{\text{initial increase}}$ : 3h30min;  $Z_{\text{low}}$ : 0h20min – 1h40min), whereas PBS led to a reduction in the time to reach a stable current by more than one hour, but did not reduce time until impedance increased ( $I_{\text{initial increase}}$ : 2h20min;  $Z_{\text{low}}$ : 0h30min – 1h50min). The use of LB medium to pre-wet the electrodes showed a similar trend as PBS but to a greater extent, as the equilibrium of  $I$  was observed after 30 min, but was unstable as it dropped rapidly thereafter. In addition, no change was observed for  $Z_{\text{low}}$  (0h10min - 1h50min) compared to the untreated device. Pre-treatment with 75% LB 25% FCS showed better results, although  $I_{\text{initial increase}}$  was reached later, the current was more stable afterwards and  $Z$  increased

from its low value after only 1 hour and 10 minutes ( $I_{\text{initial increase}}$ : 2h00min;  $Z_{\text{low}}$ : 0h10min - 1h10min), shortening the initial equilibrium phase to about 2 hours. The same was observed for the pre-treatment with 100% FCS ( $I_{\text{initial increase}}$ : 2h00min;  $Z_{\text{low}}$ : 0h20min - 1h10min), whereas pre-treatment with FCS also showed a permanent drop in the measured current to around 4  $\mu\text{A}$ , while values between 6 and 5  $\mu\text{A}$  were observed for the untreated device.

### Polymicrobial Samples

The method was further tested for samples containing multiple strains in order to demonstrate its suitability for assessing antibiotic susceptibility for polymicrobial infections directly from the patient sample without prior isolation of the strains. The pathogen combinations for the tests with 3 resistant pathogens differ, as only 2 of the tested strains were resistant to oxytetracycline (see Figure 3). Therefore, instead of *S. aureus* (DSM 28766), which was only resistant to kanamycin, *P. aeruginosa* (DSM 25123) was added as a third strain for treatment with oxytetracycline, as it showed tolerance to oxytetracycline, although not complete resistance. The method presented, determines whether growth is present or not, i.e. it can determine whether one or more strains present in the sample are resistant to the treatment (growth is detected) or whether all strains present are susceptible (no growth is detected). For clinical decision-making an antibiotic effective against all bacteria present in the sample is then selected.

The results presented in Figure S13 show good agreement between the expected growth when one or more of the three pathogens are resistant and the growth observed with the combined method. The exception concerned treatments with kanamycin when 1 or 2 resistant pathogens were present. Contrary to expectations, no growth was observed in the test with these combinations. Two hypotheses were tested: firstly, as kanamycin has already been shown to slow the growth of *K. pneumoniae* (DSM103706) (see Figure S5), it was hypothesised that sufficient growth would only be present after 20 hours and, therefore, was not detected. However, no growth was visually observed in the device even after 48 hours of incubation. The second hypothesis was that the resistance mechanism is dependent on the bacterial concentration, e.g. in the case of enzymatic inactivation of the aminoglycoside kanamycin.<sup>[6]</sup> Since the initial concentration of bacteria in the test was only around 333 CFU/ml per strain (1000 CFU/ml in total), compared to 1000 CFU/ml in the experiments where resistance (growth) was detected (see Figure S5), the experiment was repeated for these combinations with 1000 CFU/ml per strain (3000 CFU/ml in total). Growth was observed at the higher initial concentrations of bacteria (see Figure S14), indicating that the resistance mechanism of the pathogens depends on the amount of bacteria present.

### Minimum Inhibitory Concentration (MIC)

A combination of two sensitive strains were randomly selected from the strains used in the study and the MIC for these was evaluated using both standard broth microdilution and 3D printed prototype with electrochemical detection by the combined method. The results are shown in Figure S15 and demonstrate agreement between the broth microdilution test adapted from ISO 20776-1<sup>[2]</sup> and the combined method in the 3D printed prototype.

**Table S1.** Overview of AST results by measurement methods for treatment without antibiotic (None), with Kanamycin (K) or with Oxytetracycline (O). Sensitivity, specificity, PPV and NPV were calculated for each replicate in comparison to the result of the agar diffusion assay.

Bacterial Strain	Treatment	Resistance		Current @ - 0.3 V (DPV)		Potential of current maximum (DPV)		Impedance @ 100 kHz (EIS)		Combination of Current, Potential and Impedance (Score)	
		BacDive Library	Agar diffusion	growth detected (No.of repl.)	Detection time / h	growth detected (No.of repl.)	Detection time / h	growth detected (No.of repl.)	Detection time / h	growth detected (No.of repl.)	Detection time / h
<i>E. coli</i> (DSM 498)	None	N/A	N/A	3/3	4.89 ± 0.21	3/3	5.56 ± 0.44	3/3	6.5 ± 0.14	3/3	5.06 ± 0.08
	K	-	-	1/3	5.83	0/3	N/A	1/3	13.5	0/3	N/A
	O	-	-	2/3	6.75 ± 1.42	0/3	N/A	0/3	N/A	0/3	N/A
<i>S. aureus</i> (DSM 28766)	None	N/A	N/A	3/3	7.67 ± 1.53	3/3	10.05 ± 0.57	3/3	8.11 ± 0.48	3/3	7.72 ± 0.75
	K	+	+	3/3	6.56 ± 0.44	3/3	10.39 ± 0.67	3/3	8.28 ± 0.34	3/3	7.06 ± 0.83
	O	-	-	0/3	N/A	0/3	N/A	1/3	18.67	0/3	N/A
<i>S. aureus</i> (DSM 799)	None	N/A	N/A	3/3	7.06 ± 0.96	3/3	8.17 ± 0.36	3/3	6.45 ± 0.91	3/3	5.33 ± 0.72
	K	-	-	0/3	N/A	0/3	N/A	0/3	N/A	0/3	N/A
	O	-	-	1/3	13.17	0/3	N/A	2/3	16.84 ± 1.34	0/3	N/A
<i>K. pneumonia</i> (DSM 103706)	None	N/A	N/A	3/3	5 ± 0.36	3/3	5.28 ± 0.21	3/3	5.44 ± 0.08	3/3	4.94 ± 0.28
	K	+	+	3/3	8 ± 0.94	3/3	9.5 ± 0.98	3/3	10.11 ± 1.1	3/3	9.28 ± 0.88
	O	+	+	3/3	7.11 ± 0.16	3/3	5.17 ± 0.41	3/3	5.5 ± 0	3/3	5.11 ± 0.16
<i>K. pneumonia</i> (DSM 30104)	None	N/A	N/A	3/3	5.67 ± 0.62	3/3	6.67 ± 0.62	3/3	6.83 ± 0.27	3/3	6.11 ± 0.16
	K	-	-	2/3	5.17 ± 0.5	0/3	N/A	3/3	13.39 ± 6.05	1/3	4.33
	O	-	-	0/3	N/A	0/3	N/A	2/3	15.67 ± 1.67	0/3	N/A
<i>P. aeruginosa</i> (DSM 102273)	None	N/A	N/A	2/3	9.25 ± 0.58	0/3	N/A	1/3	11.67	3/3	7.72 ± 0.52
	K	-	-	2/3	8.17 ± 0.5	0/3	N/A	2/3	9.42 ± 0.59	2/3	7.58 ± 1.25
	O	-	+	1/3	9	1/3	7.83	1/3	18.5	3/3	8.61 ± 0.87
<i>P. aeruginosa</i> (DSM 25123)	None	N/A	N/A	3/3	6.56 ± 0.28	1/3	18.5	3/3	7.84 ± 0.24	3/3	7.22 ± 0.28
	K	-	-	0/3	N/A	0/3	N/A	0/3	N/A	0/3	N/A
	O	-	+	3/3	8.55 ± 0.21	1/3	8.17	3/3	11.17 ± 1.47	3/3	10.22 ± 1.59
Sensitivity   Specificity				83.33 %   75 %		61.11 %   100 %		83.33%   62.5 %		94.44 %   95.83 %	
PPV   NPV				71.43 %   85.71 %		100 %   77.42 %		62.5 %   83.33 %		94.44 %   95.83 %	



**Figure S1.** Pictures of possible 3D printed device designs. Devices with implemented SPEs (A: IS-C; B, C: BVT) filled with 25/75% FCS/LB containing 1 mM Resazurin. A) Aerobic design with air space for oxygen exchange and Luer-Lock cap for sterile sealing. B) Anaerobic design without air space for oxygen exchange and Luer lock closure for sterile sealing. C) Multi-chamber variant of the anaerobic design with Luer-Lock closures (inlet and outlet) for sterile sealing. Devices were printed from PMMA (very low oxygen permeability).

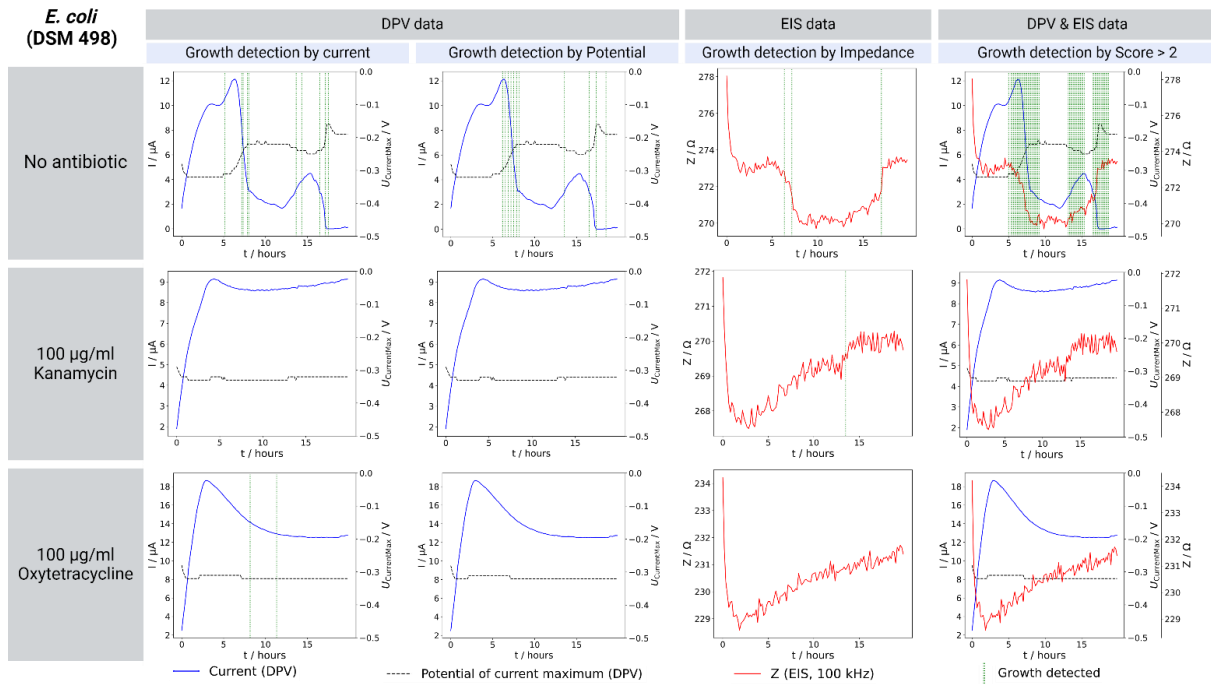


**Figure S2.** Electrochemical measurement and bioinformatics analysis for antibiotic susceptibility of *Escherichia coli* (DSM 498). Bacterial growth of *E. coli* with 100 µg/ml kanamycin, 100 µg/ml oxytetracycline, or without antibiotic was measured by differential pulsed voltammetry (DPV) and electrochemical impedance spectroscopy (EIS) in aerobic test device with an IS-C screen printed electrode. The plots show one of three representative replicates with evidence of growth by different parameters (current ( $I$ ), potential ( $U$ ), impedance ( $Z$ ) and combined method (score)).

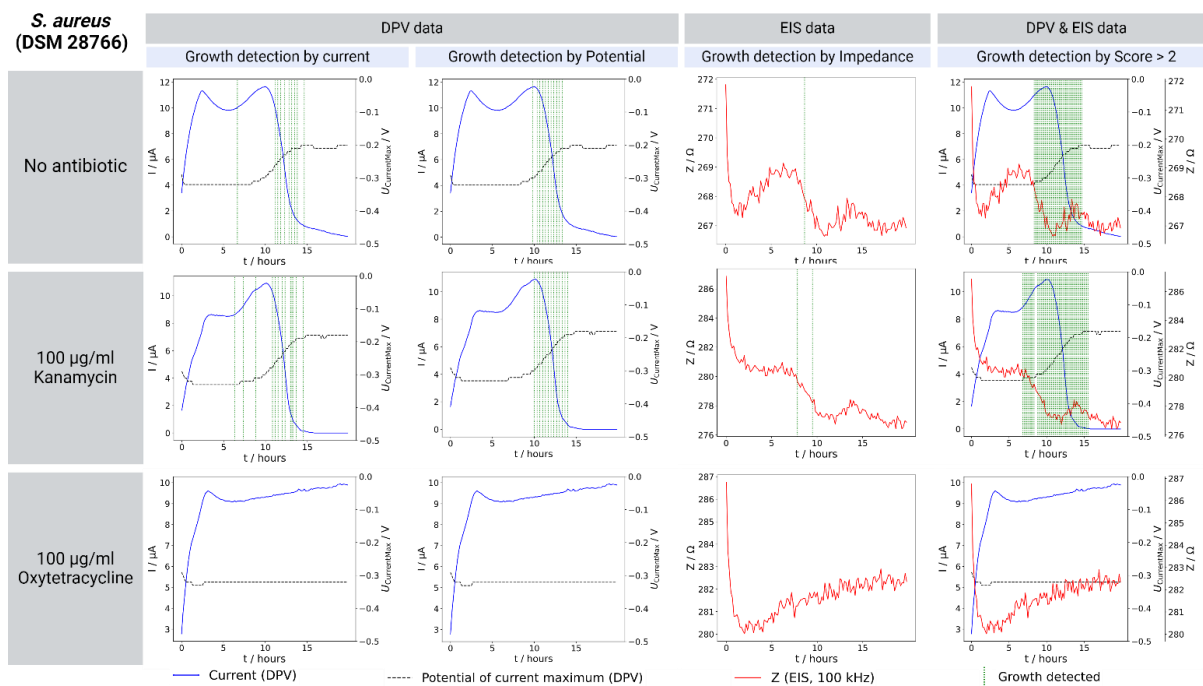


**Figure S3.** Electrochemical measurement and bioinformatics analysis for antibiotic susceptibility of *Staphylococcus aureus* (DSM 28766).

Bacterial growth of *S. aureus* with 100 μg/ml kanamycin, 100 μg/ml oxytetracycline, or without antibiotic was measured by differential pulsed voltammetry (DPV) and electrochemical impedance spectroscopy (EIS) in aerobic test device with an IS-C screen printed electrode. The plots show one of three representative replicates with evidence of growth by different parameters (current ( $I$ ), potential ( $U$ ), impedance ( $Z$ ) and combined method (score)).

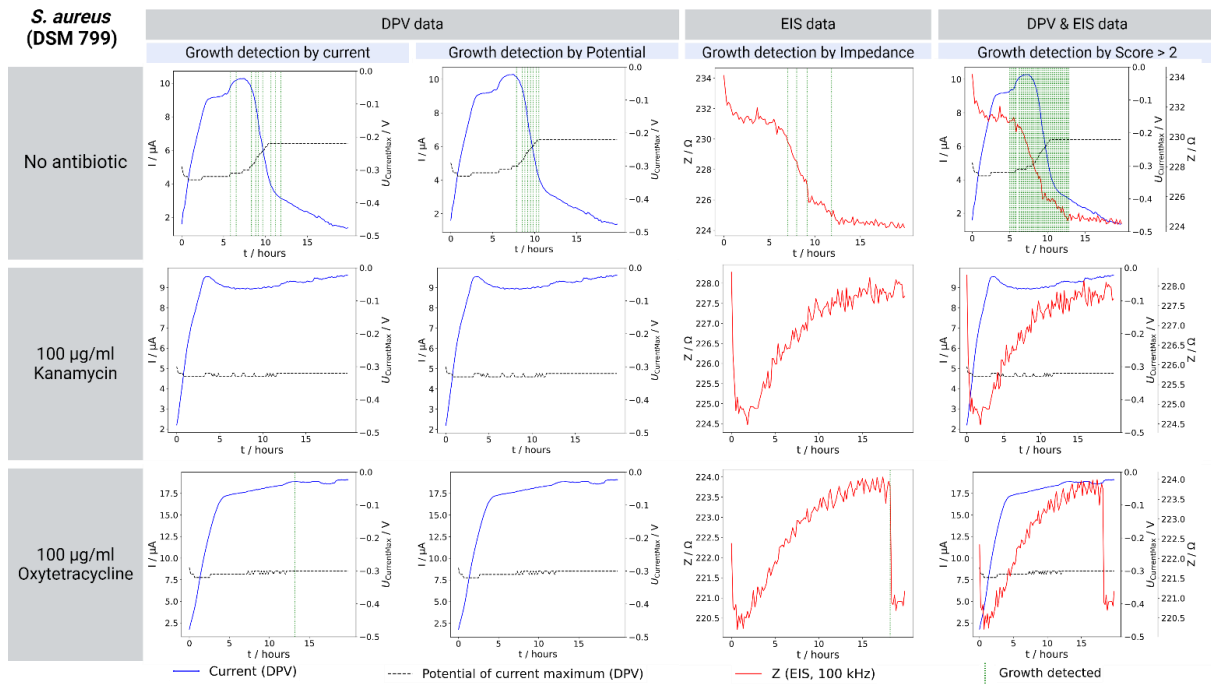


**Figure S4.** Electrochemical measurement and bioinformatics analysis for antibiotic susceptibility of *Staphylococcus aureus* (DSM 799). Bacterial growth of *S. aureus* with 100 µg/ml kanamycin, 100 µg/ml oxytetracycline, or without antibiotic was measured by differential pulsed voltammetry (DPV) and electrochemical impedance spectroscopy (EIS) in aerobic test device with an IS-C screen printed electrode. The plots show one of three representative replicates with evidence of growth by different parameters (current ( $I$ ), potential ( $U$ ), impedance ( $Z$ ) and combined method (score)).

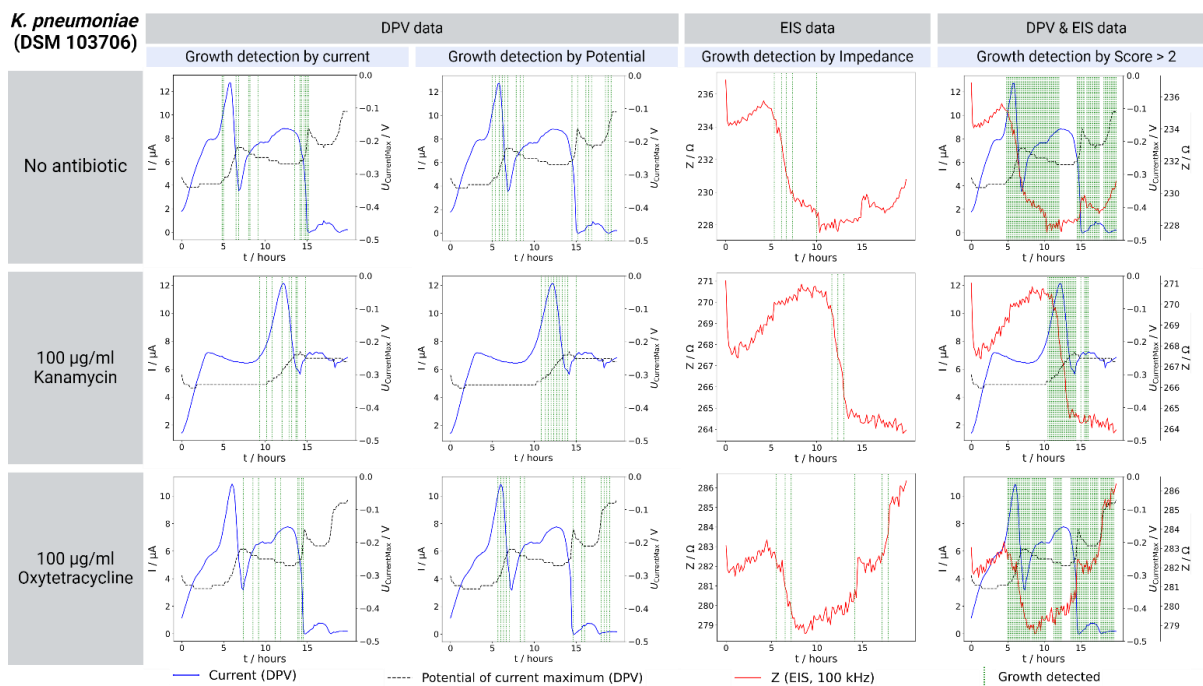


**Figure S5.** Electrochemical measurement and bioinformatics analysis for antibiotic susceptibility of *Klebsiella pneumoniae* (DSM 103706).

Bacterial growth of *K. pneumoniae* with 100 μg/ml kanamycin, 100 μg/ml oxytetracycline, or without antibiotic was measured by differential pulsed voltammetry (DPV) and electrochemical impedance spectroscopy (EIS) in aerobic test device with an IS-C screen printed electrode. The plots show one of three representative replicates with evidence of growth by different parameters (current ( $I$ ), potential ( $U$ ), impedance ( $Z$ ) and combined method (score)).

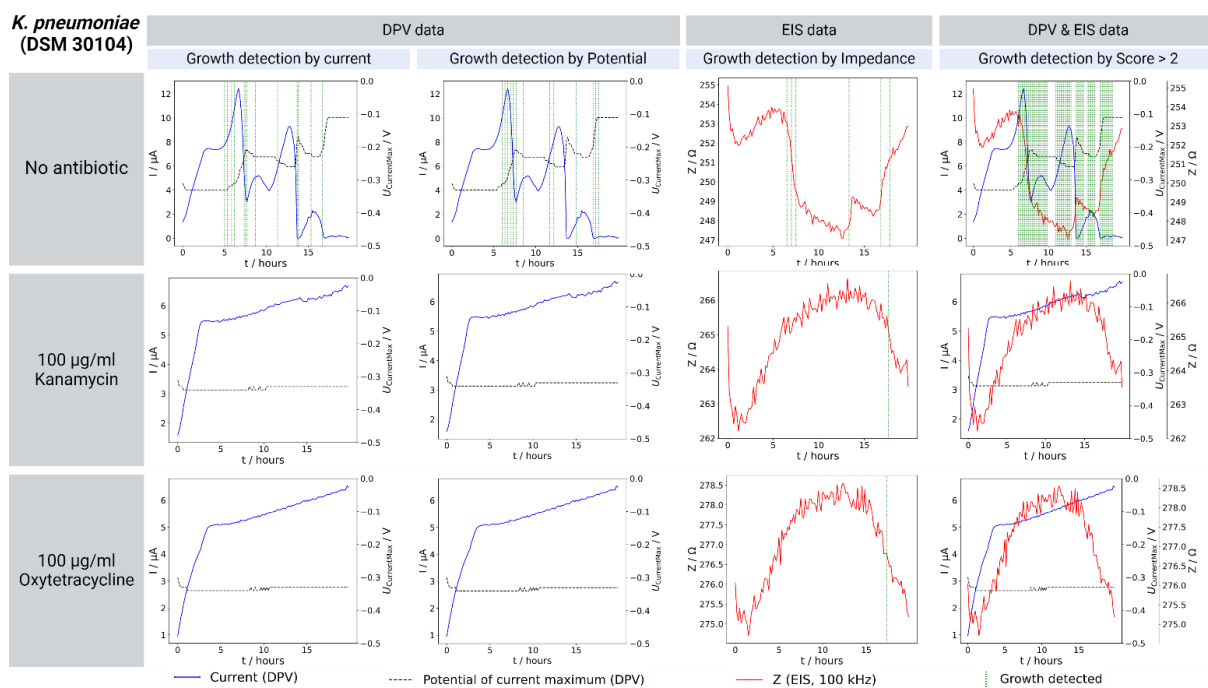


**Figure S6.** Electrochemical measurement and bioinformatics analysis for antibiotic susceptibility of *Klebsiella pneumoniae* (DSM 30104). Bacterial growth of *K. pneumoniae* with 100 μg/ml kanamycin, 100 μg/ml oxytetracycline, or without antibiotic was measured by differential pulsed voltammetry (DPV) and electrochemical impedance spectroscopy (EIS) in aerobic test device with an IS-C screen printed electrode. The plots show one of three representative replicates with evidence of growth by different parameters (current ( $I$ ), potential ( $U$ ), impedance ( $Z$ ) and combined method (score)).

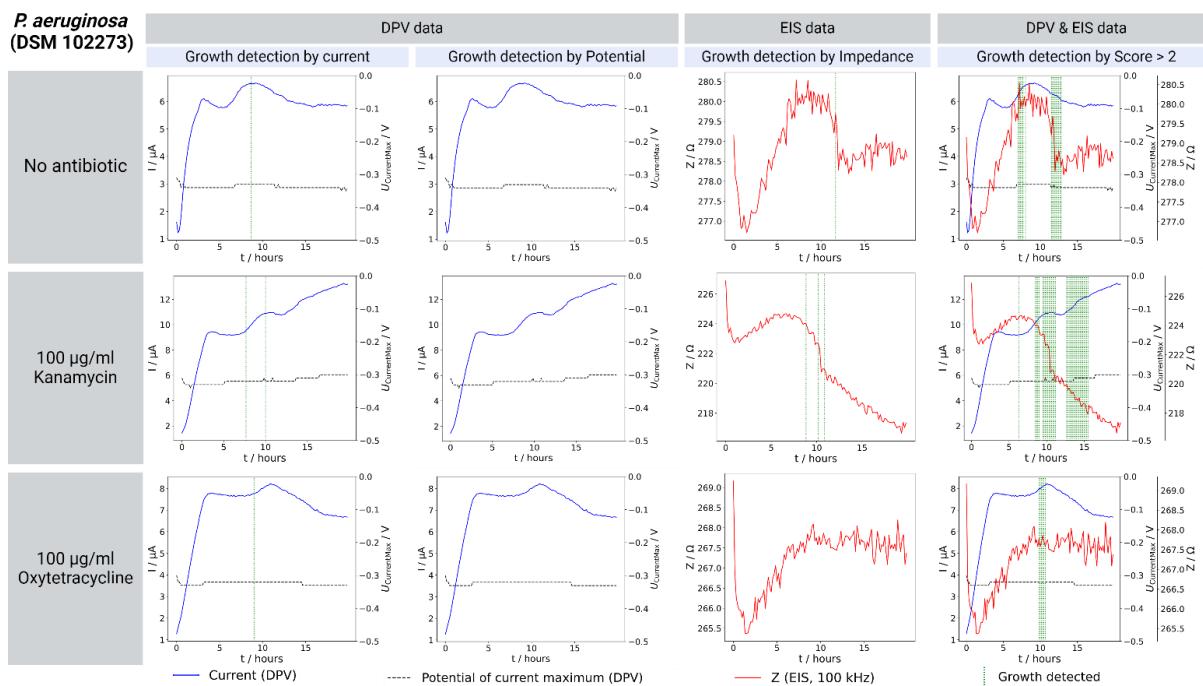


**Figure S7.** Electrochemical measurement and bioinformatics analysis for antibiotic susceptibility of *Pseudomonas aeruginosa* (DSM 102273).

Bacterial growth of *P. aeruginosa* with 100 μg/ml kanamycin, 100 μg/ml oxytetracycline, or without antibiotic was measured by differential pulsed voltammetry (DPV) and electrochemical impedance spectroscopy (EIS) in aerobic test device with an IS-C screen printed electrode. The plots show one of three representative replicates with evidence of growth by different parameters (current (*I*), potential (*U*), impedance (*Z*) and combined method (score)).

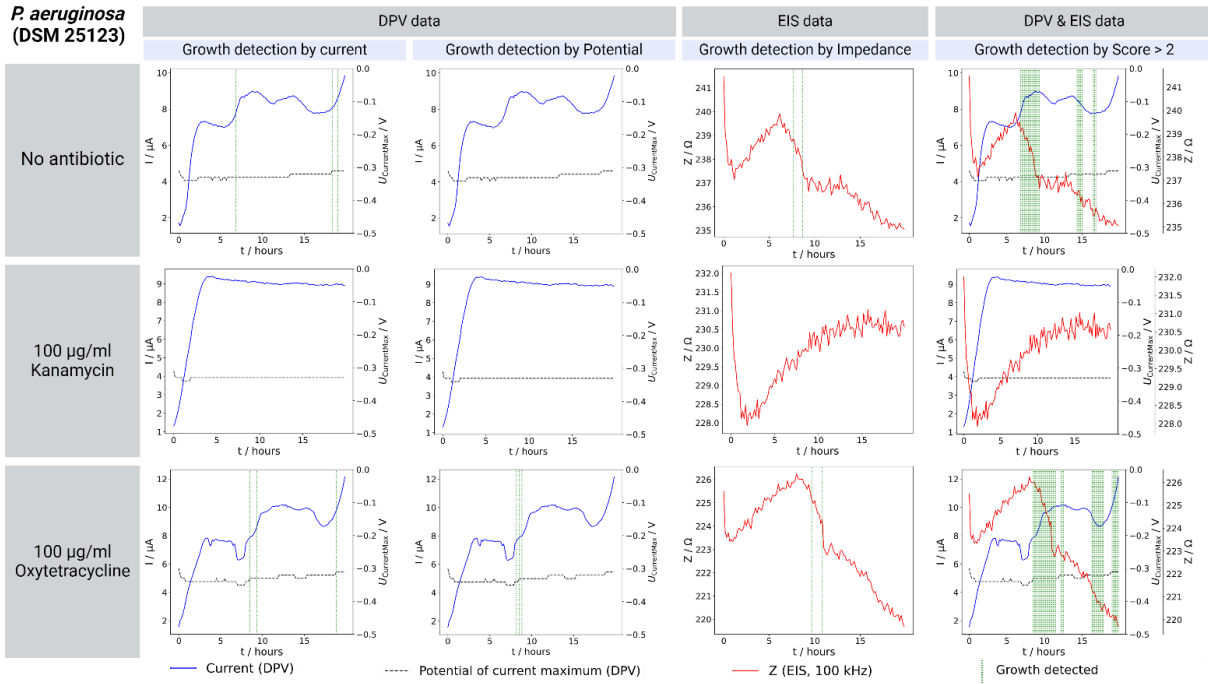


**Figure S8.** Electrochemical measurement and bioinformatics analysis for antibiotic susceptibility of *Pseudomonas aeruginosa* (DSM 25123). Bacterial growth of *P. aeruginosa* with 100 µg/ml kanamycin, 100 µg/ml oxytetracycline, or without antibiotic was measured by differential pulsed voltammetry (DPV) and electrochemical impedance spectroscopy (EIS) in aerobic test device with an IS-C screen printed electrode. The plots show one of three representative replicates with evidence of growth by different parameters (current ( $I$ ), potential ( $U$ ), impedance ( $Z$ ) and combined method (score)).

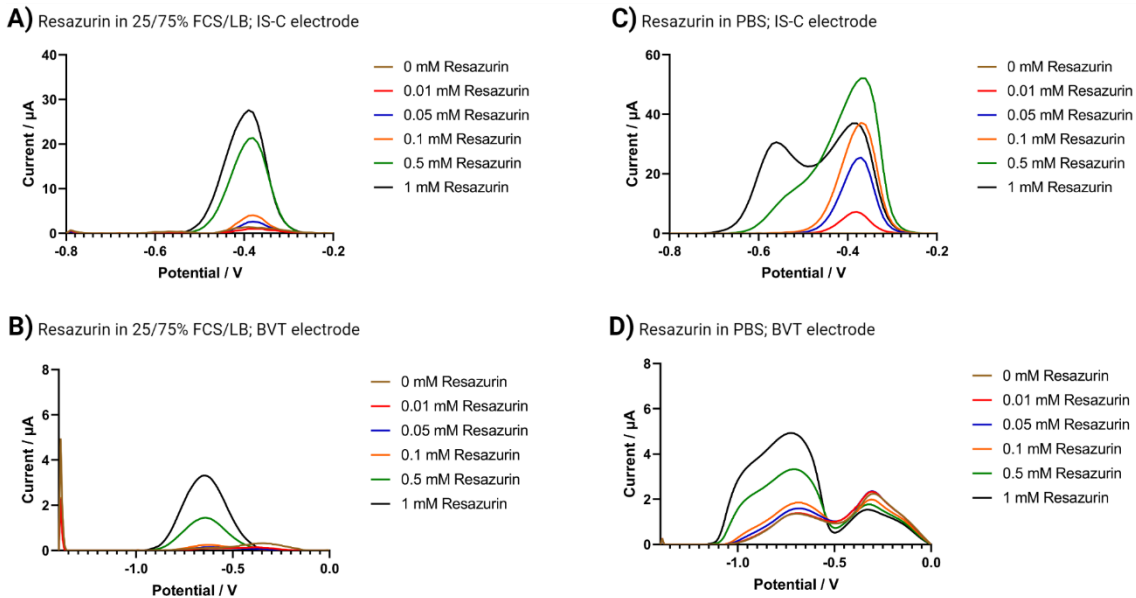


**Figure S9.** Differential pulse voltammetry (DPV) graphs of resazurin. DPV measurement of Resazurin on IS-C (graphite) and BVT (gold)

electrodes at different concentrations in 25/75% FCS/LB (A, B) or PBS (C, D). Values are shown as mean of (IS-C and BVT) 2 devices á 3 measurements.

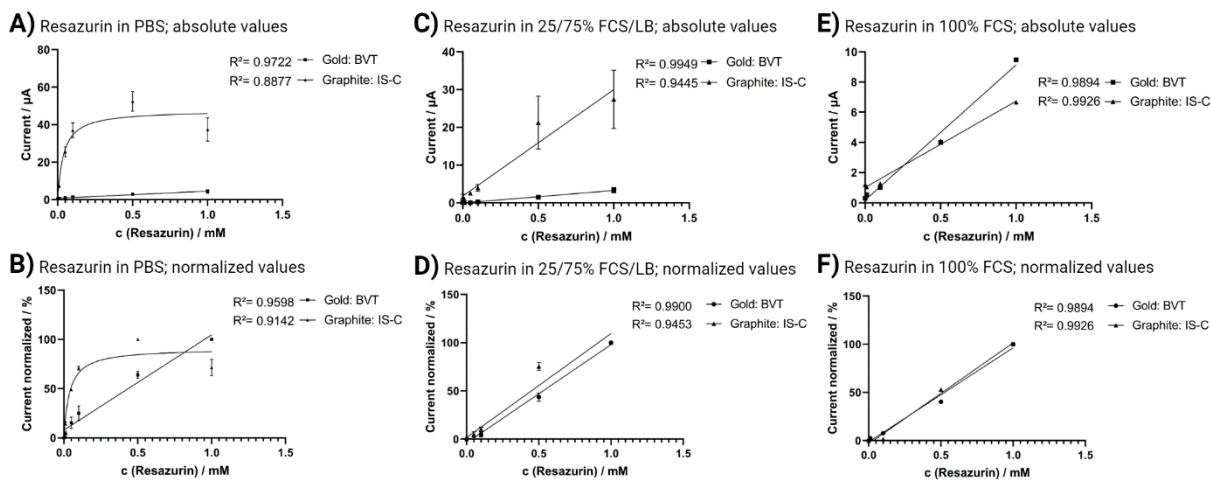


**Figure S10.** Concentration dependent signals of differential pulse voltammetry (DPV) for resazurin. Measurement of Signal on IS-C (graphite) and BVT (gold) electrodes at different concentrations in PBS (A and B), 25/75% FCS/LB (C and D) or 100% FCS (E and F). Current intensities of concentration dependent peak are shown as absolute values (A, C and E) or normalized for each electrode (B, D and F; 0 = lowest value, 100 = highest value). Values are shown as mean  $\pm$  SD of (IS C and BVT) 2 devices á 3 measurements each (100% FCS only 1 device á 1 measurement). Linear regression or non-linear regression (IS-C in PBS) were performed with GraphPad Prism 8.

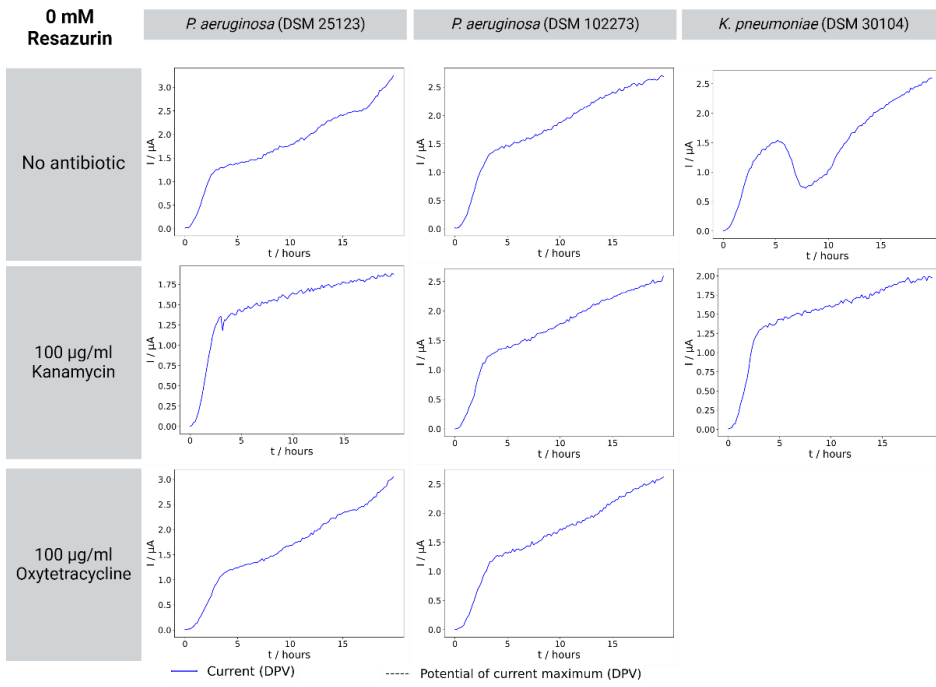


**Figure S11.** Differential pulsed voltametry (DPV) measurement without Resazurin. Current intensity ( $I$ ) measured by DPV at  $-0.3$  V for *P. aeruginosa* (DSM 25123), *P. aeruginosa* (DSM 102273) and *K. pneumoniae* (DSM 30104) without the supplementation of Resazurin. Bacterial strains were treated with 100  $\mu\text{g/ml}$  kanamycin, 100  $\mu\text{g/ml}$  oxytetracycline, or without antibiotic in an aerobic test device with an IS-C screen printed electrode.

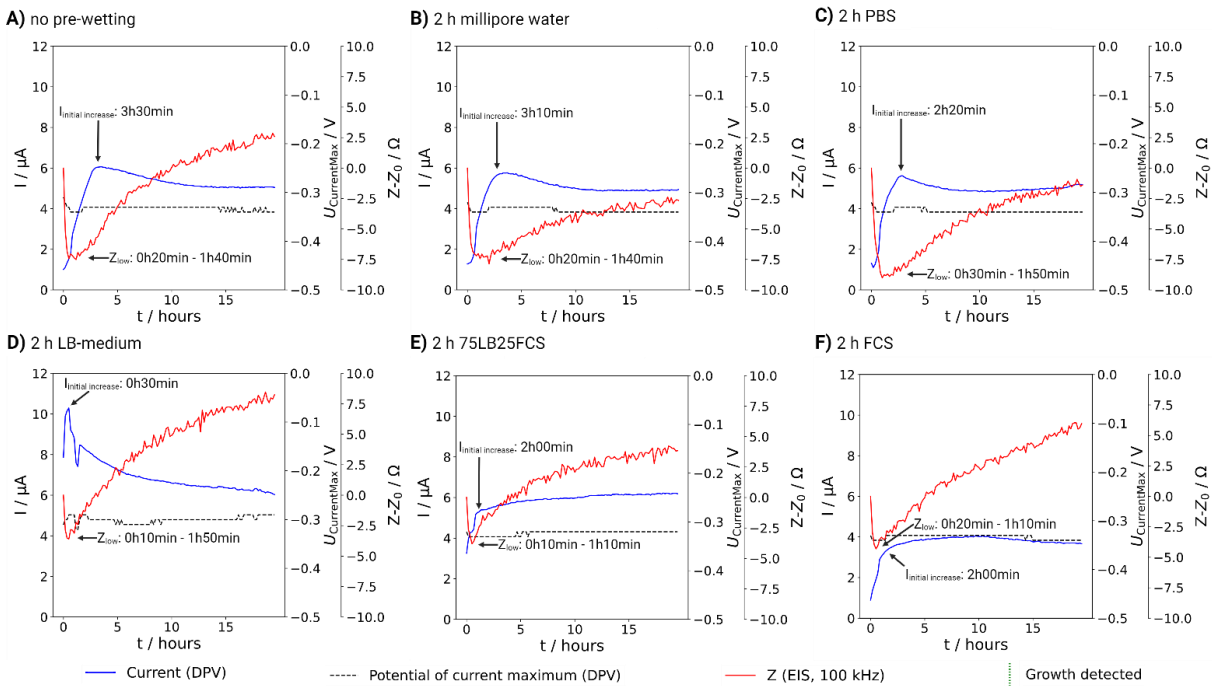
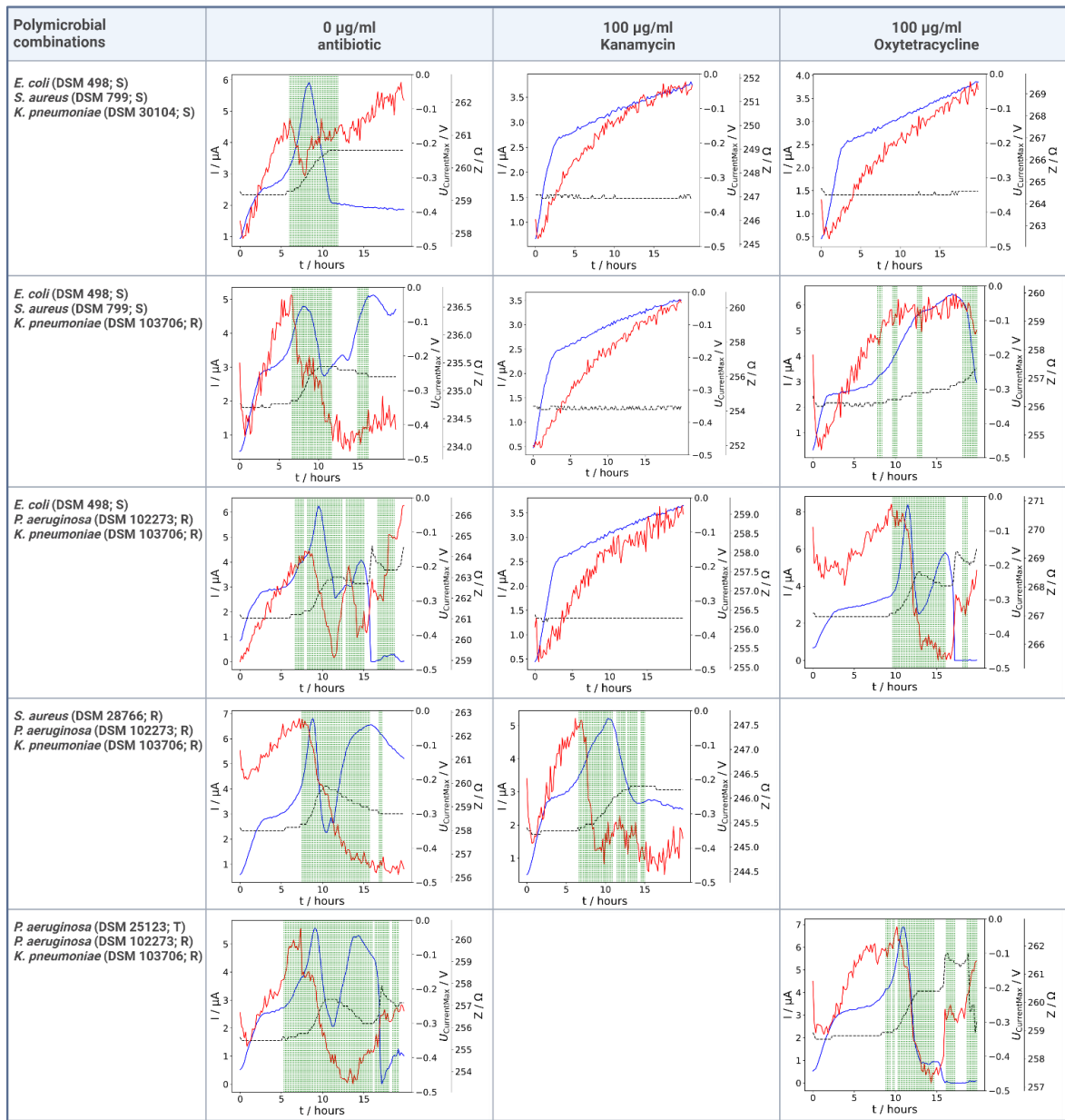


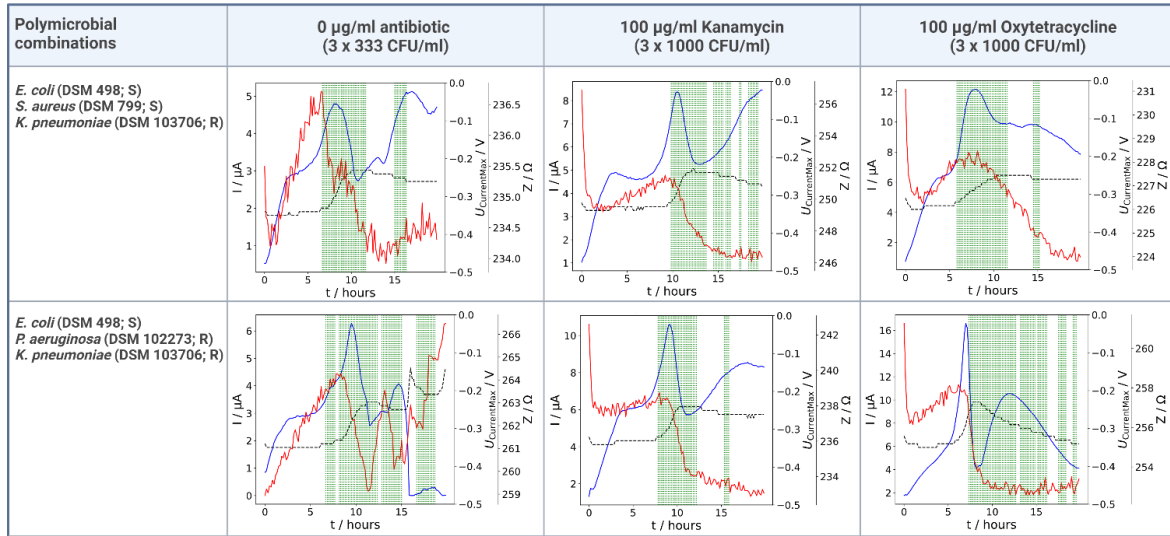
**Figure S12.** Influence of pre-treatment of the electrodes on the time to reach equilibrium. Aerobic one-chamber devices ( $n = 1$ ) were pre-incubated

2 h with A) none, B) millipore water, C) PBS, D) LB-medium, E) 75% LB 25% FCS or F) 100% FCS prior to loading with 25/75% FCS/LB containing 0.2 mM Resazurin (t = 0 h). Time for initial increase of current ( $I_{initial\ increase}$ ) and time for initial low of impedance ( $Z_{low}$ ) indicated with arrows for each pre-treatment.



S: Sensitive R: Resistant T: High tolerance

**Figure S13.** Evaluation of artificial polymicrobial infections in human plasma by the combined method in the 3D printed prototype. Measurements ( $n = 1$ ) were performed for combinations of three strains randomly selected from the available pathogens used in this study to match samples from 3 sensitive (S) to 3 resistant (R) strains for both antibiotics.

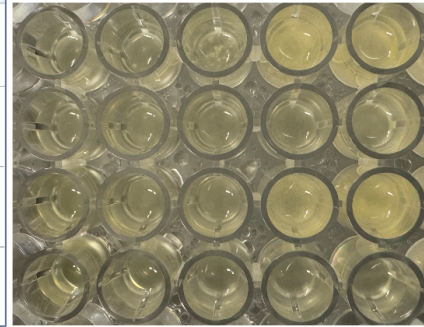


S: Sensitive R: Resistant

**Figure S14.** Evaluation of artificial polymicrobial infections in human plasma by the combined method in the 3D printed prototype. Measurements ( $n = 1$ ) were performed for combinations of three strains according to Figure S13. Initial bacteria concentration of treated samples were tested with 1000 CFU/ml per strain to match non-polymicrobial AST experiments.

A) Broth microdilution

Concentration antibiotic	100 µg/ml	10 µg/ml	1 µg/ml	0.1 µg/ml	0.01 µg/ml
<i>S. aureus</i> (DSM 799) Kanamycin	✓	✓	✓	✗	✗
<i>K. pneumoniae</i> (DSM 30104) Kanamycin	✓	✓	✓	✓	✓
<i>S. aureus</i> (DSM 799) Oxytetracycline	✓	✓	✓	✗	✗
<i>K. pneumoniae</i> (DSM 30104) Oxytetracycline	✓	✓	✓	✓	✓



✓ Sensitive / no growth observed ✗ Resistant / growth observed

B) MIC by 3D printed prototype

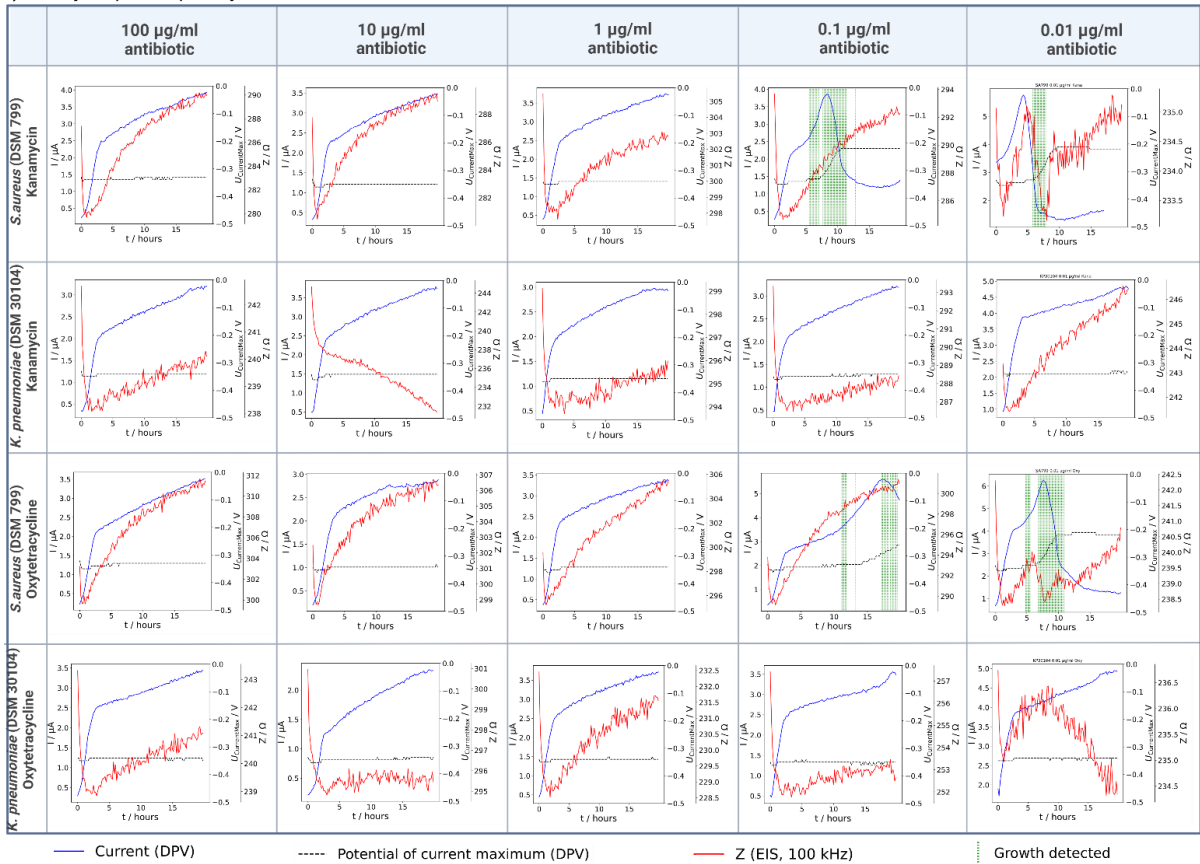


**Figure S15.** Minimum inhibitory concentration (MIC) measurement by A) broth microdilution and B) 3D printed prototype. Measurements ( $n = 1$ ) were performed for 2 sensitive strains, *S. aureus* (DSM 799) and *K. pneumoniae* (DSM 30104), with different concentrations of kanamycin and oxytetracycline. Detection of growth for the electrochemical AST was performed with the combined method.

**References**

- [1] B. Kowalska-Krochmal, R. Dudek-Wicher, *Pathogens* **2021**, *10*, 165.
- [2] International Standard. ISO 20776-1, *Susceptibility Testing of Infectious Agents and Evaluation of Performance of Antimicrobial Susceptibility Test Devices. Part 1, Broth Micro-Dilution Reference Method for Testing the in Vitro Activity of Antimicrobial Agents against Rapidly Growing Aerobic Bacteria Involved in Infectious Diseases*, British Standards Institution, London, **2020**.
- [3] H. A. Crosby, J. Kwiecinski, A. R. Horswill, in *Analytical and Bioanalytical Chemistry*, **2016**, pp. 1–41.
- [4] A. E. Deller, B. M. Hryniewicz, C. Pesqueira, R. P. Horta, B. J. G. Da Silva, S. Weheabby, A. Al-Hamry, O. Kanoun, M. Vidotti, *Polymers* **2023**, *15*, 739.
- [5] Ø. Ø. Dalheim, S. Steen, *Journal of Ocean Engineering and Science* **2020**, *5*, 333.
- [6] I. Galani, E. Xirouchaki, K. Kanellakopoulou, G. Petrikkos, H. Giamarellou, *Clinical Microbiology and Infection* **2002**, *8*, 579.

## **A.2 Supporting Material for Chapter 3.2**

### **A.2.1 Supporting Material: Methacryloyl-GlcNAc Derivatives Copolymerized with Dimethacrylamide as a Novel Antibacterial and Biocompatible Coating**



Supplementary Material

## Methacryloyl-GlcNAc Derivatives Copolymerized with Dimethacrylamide as a Novel Antibacterial and Biocompatible Coating

Max Borgolte <sup>1,2</sup>, Oliver Riestler <sup>1,3,4</sup>, Tereza Kacerova <sup>5,6</sup>, Simone Rentschler <sup>1,3</sup>, Magnus S. Schmidt <sup>1</sup>, Susanne Jacksch <sup>1</sup>, Markus Egert <sup>1</sup>, Stefan Laufer <sup>3,4</sup>, René Csuk <sup>2</sup> and Hans-Peter Deigner <sup>1,4,7,\*</sup>

- <sup>1</sup> Institute of Precision Medicine, Furtwangen University, Jakob-Kienzle Str. 17, 78054 Villingen-Schwenningen, Germany; Max.Borgolte@hs-furtwangen.de (M.B.); Oliver.Riestler@hs-furtwangen.de (O.R.); S.Rentschler@hs-furtwangen.de (S.R.); Magnus.Schmidt@hs-furtwangen.de (M.S.S.); Susanne.Jacksch@hs-furtwangen.de (S.J.); Markus.Egert@hs-furtwangen.de (M.E.)
  - <sup>2</sup> Department of Organic Chemistry, Martin-Luther University Halle-Wittenberg, Kurt-Mothes-Str. 2, 06120 Halle/Saale, Germany; Rene.csuk@chemie.uni-halle.de
  - <sup>3</sup> Department of Pharmaceutical and Medicinal Chemistry, Institute of Pharmaceutical Sciences, Eberhard Karls University Tuebingen, Auf der Morgenstelle 8, 72076 Tuebingen, Germany; Stefan.laufer@uni-tuebingen.de
  - <sup>4</sup> Faculty of Science, Eberhard Karls University Tuebingen, Auf der Morgenstelle 8, 72076 Tuebingen, Germany
  - <sup>5</sup> Department of Chemistry, Czech University of Life Sciences, Kamýcká 129, 16500 Prague, Czech Republic; tereza.kacerova.18@ucl.ac.uk
  - <sup>6</sup> Department of Chemistry, University College London, London WC1H 0AJ, UK
  - <sup>7</sup> EXIM Department, Fraunhofer Institute IZI (Leipzig), Schillingallee 68, 18057 Rostock, Germany
- \* Correspondence: dei@hs-furtwangen.de

**Citation:** Borgolte, M.; Riestler, O.; Kacerova, T.; Rentschler, S.; Schmidt, M.S.; Jacksch, S.; Egert, M.; Laufer, S.; Csuk, R.; Deigner, H.-P. Methacryloyl-GlcNAc Derivatives Copolymerized with Dimethacrylamide as a Novel Antibacterial and Biocompatible Coating. *Pharmaceutics* **2021**, *13*, 1647. <https://doi.org/10.3390/pharmaceutics13101647>

Academic Editors: Ewa Kłodzińska, Marek Konop

Received: 3 August 2021

Accepted: 2 October 2021

Published: 9 October 2021

**Publisher's Note:** MDPI stays neutral with regard to jurisdictional claims in published maps and institutional affiliations.



**Copyright:** © 2021 by the authors. Licensee MDPI, Basel, Switzerland. This article is an open access article distributed under the terms and conditions of the Creative Commons Attribution (CC BY) license (<http://creativecommons.org/licenses/by/4.0/>).

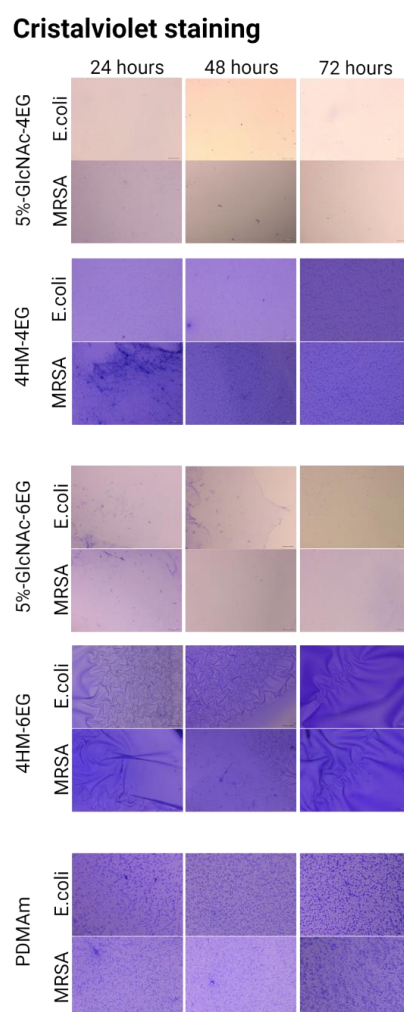


**Figure S1.** Brightfield images after crystal violet staining of biofilm formation on polymer coatings. PDMAm corresponds to the unmodified acrylate coating. Images were taken with 100× magnification using the microscope Observer.Z1 (Zeiss, Germany) after 24, 48 and 72 h of cultivation. Scale bar measures 0.1 mm.

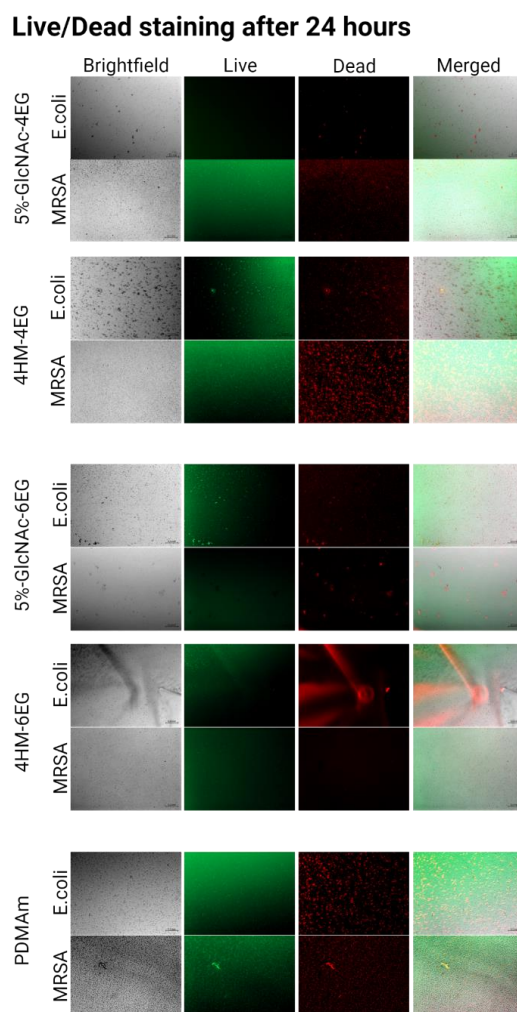


**Figure S2.** Fluorescent images after Live/Dead staining of *E. coli* and MRSA in the high-nutrition environment after 24 h of cultivation. PDMAM corresponds to the unmodified acrylate coating. Images were taken with 100× magnification using the microscope Observer.Z1 (Zeiss, Germany). Scale bar measures 0.1 mm.

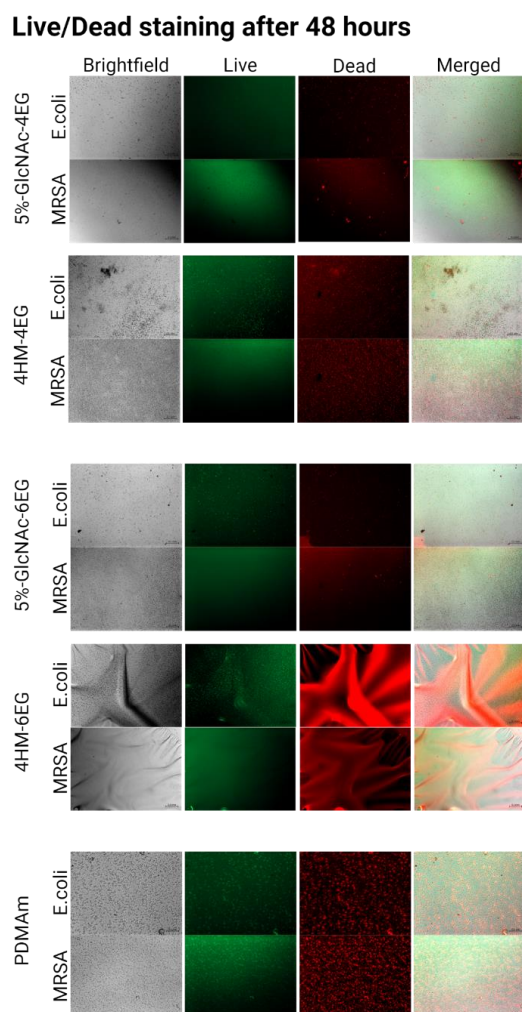


**Figure S3.** Fluorescent images after Live/Dead staining of *E. coli* and MRSA in the high-nutrition environment after 48 hours of cultivation. PDMAM corresponds to the unmodified acrylate coating. Images were taken with 100x magnification using the microscope Observer.Z1 (Zeiss, Germany). Scale bar measures 0.1 mm.

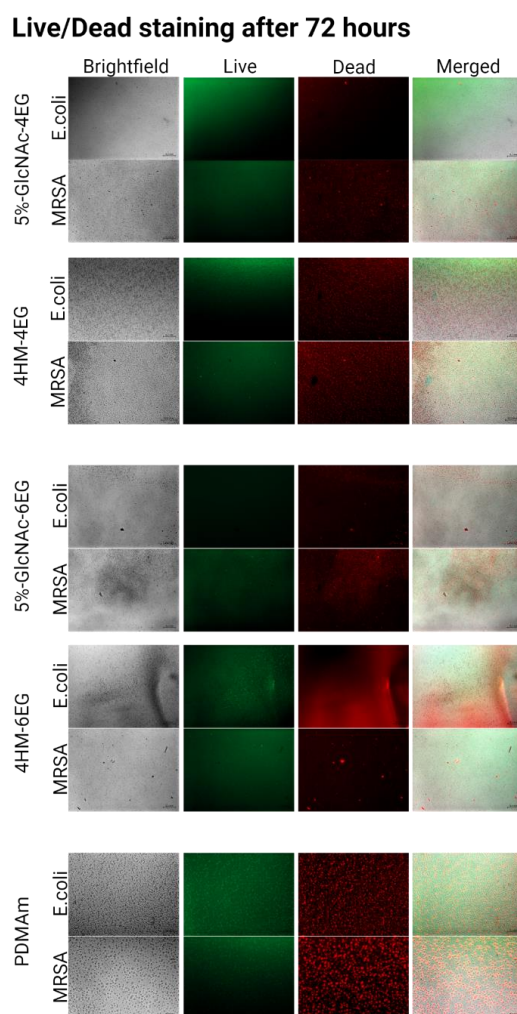


**Figure S4.** Fluorescent images after Live/Dead staining of *E. coli* and MRSA in the high-nutrition environment after 72 h of cultivation. PDMAM corresponds to the unmodified acrylate coating. Images were taken with 100× magnification using the microscope Observer.Z1 (Zeiss, Germany). Scale bar measures 0.1 mm.

**A.2.2 Supporting Material: Synthesis of a biocompatible benzophenone-substituted chitosan hydrogel as novel coating for PEEK with extraordinary strong antibacterial and anti-biofilm properties**

## Supporting Information

# Synthesis of a biocompatible benzophenone-substituted chitosan hydrogel as novel coating for PEEK with extraordinary strong antibacterial and anti-biofilm properties

Max Borgolte<sup>1,2</sup>, Oliver Riestler<sup>1,3</sup>, Isabel Quint<sup>1,3</sup>, Felix Blendinger<sup>4,5</sup>, Volker Bucher<sup>4</sup>, Stefan Laufer<sup>3,6</sup>,

René Csuk<sup>2</sup>, Luca Scotti<sup>7</sup> and Hans-Peter Deigner\*<sup>1,8,9</sup>

<sup>1</sup> Institute of Precision Medicine, Furtwangen University, Jakob-Kienzle Str. 17, 78054 Villingen-Schwenningen, Germany

<sup>2</sup> Martin-Luther University Halle-Wittenberg, Organic Chemistry, Kurt-Mothes-Str. 2, 06120, Halle, Saale, Germany

<sup>3</sup> Institute of Pharmaceutical Sciences, Department of Pharmacy and Biochemistry, Eberhard-Karls-University Tuebingen, Auf der Morgenstelle 8, Tuebingen, 72076, Germany

<sup>4</sup> Institute for Microsystems Technology (iMST), Furtwangen University, Neckartal 142, 78628 Rottweil, Germany

<sup>5</sup> Institute for Applied Physics, Eberhard Karls University Tuebingen, Auf der Morgenstelle 8, 72076 Tuebingen, Germany

<sup>6</sup> Tuebingen Center for Academic Drug Discovery & Development (TüCAD2), 72076 Tuebingen, Germany

<sup>7</sup> Department of Medical, Oral and Biotechnological Sciences, University "G. d'Annunzio" of Chieti-Pescara, Via dei Vestini, 66100 Chieti, Italy

<sup>8</sup> Faculty of Science, Eberhard Karls University Tuebingen, Auf der Morgenstelle 8, 72076 Tuebingen, Germany

<sup>9</sup> EXIM Department, Fraunhofer Institute IZI (Leipzig), Schillingallee 68, 18057 Rostock, Germany

\* Correspondence: dei@hs-furtwangen.de

**Abstract:** Chitosan derivatives substituted with benzophenone groups that can be cross-linked by ultraviolet light were synthesized as coatings for PEEK substrates used in the construction of lumbar cages. The IC<sub>50</sub> values of the benzophenone-modified chitosan polymers in solution before crosslinking were in the same range as those reported for native chitosan. The resulting hydrogel surface after crosslinking exhibited excellent antimicrobial properties and was highly effective (up to 5 log-fold) against clinically relevant strains of methicillin-resistant *S. aureus* and *E. coli*. As a result, the coated surface also significantly reduced biofilm formation. The coatings show good biocompatibility with numerous cell lines as well as low levels of cytotoxicity (ISO 10993-5) and pyrogenicity (ISO 10993-11). The coatings also exhibited strong antioxidant properties toward formed hydroxyl radicals in an in-vitro Fenton reaction. Overall, substitution of chitosan with benzophenone residues is an interesting and important approach to the functionalization of materials used for medical implants that are prone to microbial contamination and mechanical failure. Biocompatible antimicrobial coatings might also be employed in photopatterning methods used in the design of medical devices.

### Table of Contents

1.	Synthesis .....	2
1.1	Calibration curve of 4-benzoyl-benzoic acid in EtOH .....	2
2.	Surface characterization.....	3
2.1	XPS surface characterization .....	3
2.2	SEM-EDS surface characterization .....	4
3.	Surface topology .....	5
3.1	Microscopic images (200 x magnification) of the coatings .....	5
4.	Microbiology.....	6
4.1	Antibacterial assay for the evaluation of coatings .....	6
4.2	Bacteriostatic Assay.....	7

## 1. Synthesis

### 1.1 Calibration curve of 4-benzoyl-benzoic acid in EtOH

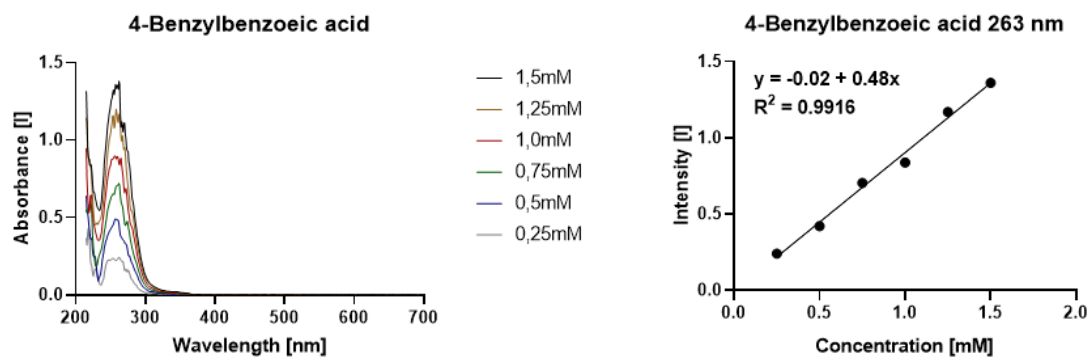


**Figure S1.** Full spectrum (left) and calibration curve with corresponding formula calculated with maxima at 263 nm of 4-benzoyl-benzoic acid in EtOH, used for calculation of the degree of substitution of the benzophenone-chitosan derivatives.

## 2. Surface characterization

### 2.1 XPS surface characterization

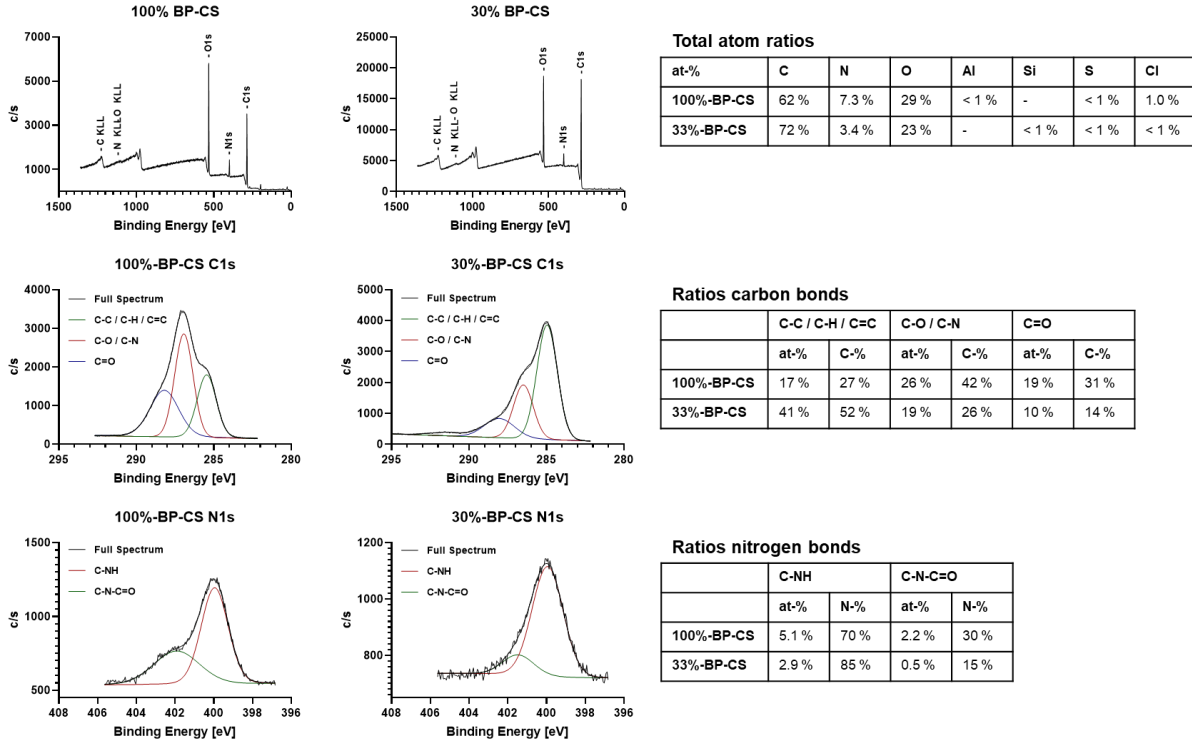
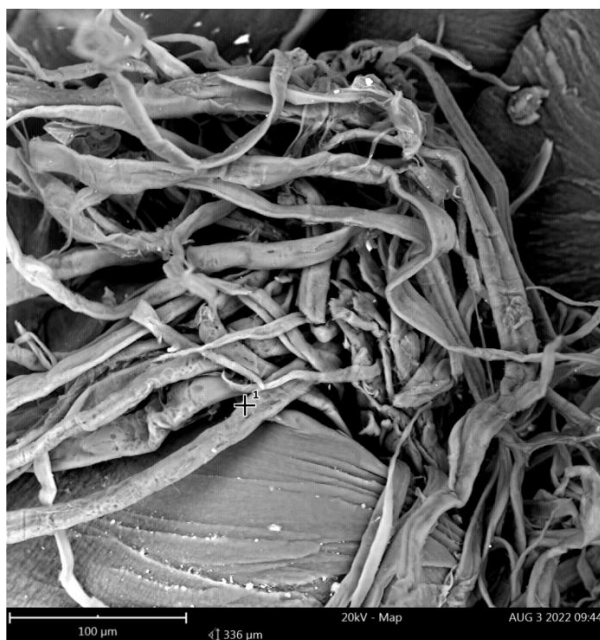


Figure S2. XPS spectra of 100%-BP-CS and 33%-BP-CS coating, together with calculated ratios of the atoms in the coating.

## 2.2 SEM-EDS surface characterization



Element	Atomic conc.	Weight conc.	Oxide Symbol	Stoich wt conc.
O	58.54 %	64.38 %		
C	31.75 %	26.21 %		
N	9.64 %	9.28 %		
Si	0.06 %	0.12 %	SiO <sub>2</sub>	0.74 %

Figure S3. SEM-EDS surface characterization of the 100%-BP-CS coating and the corresponding atomic concentrations. Area of measurement is marked in the SEM image.

### 3. Surface topology

#### 3.1 Microscopic images (200 x magnification) of the coatings

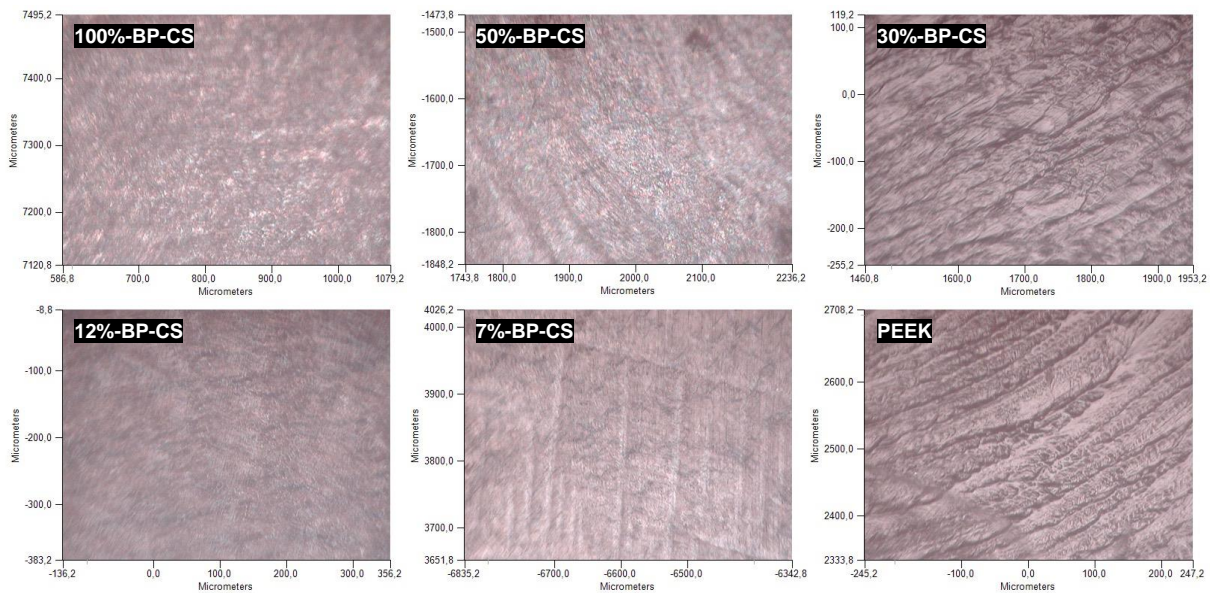


**Figure S4.** Microscopic images of the coatings, taken with 200x magnification using the PerkinElmer IR Microscope. The shown areas were used for IR measurements of the coating.

## 4. Microbiology

### 4.1 Antibacterial assay for the evaluation of coatings

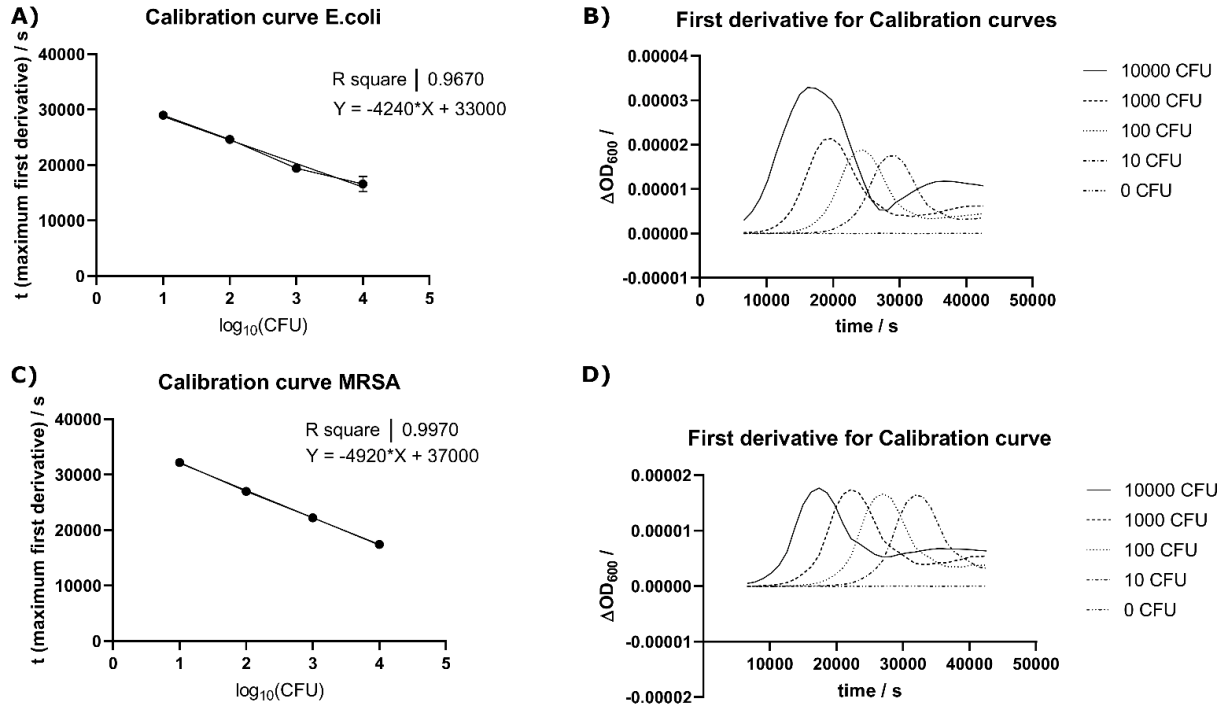


**Figure S5.** Calibration curves of *Escherichia coli* (A) and *Staphylococcus aureus* (C) for the correlation between the logarithmic colony forming units (CFU) and the time needed to reach the growth curve's maximum of the first derivative. The calculated first derivatives for *Escherichia coli* (B) and *Staphylococcus aureus* (D).

## 4.2 Bacteriostatic Assay

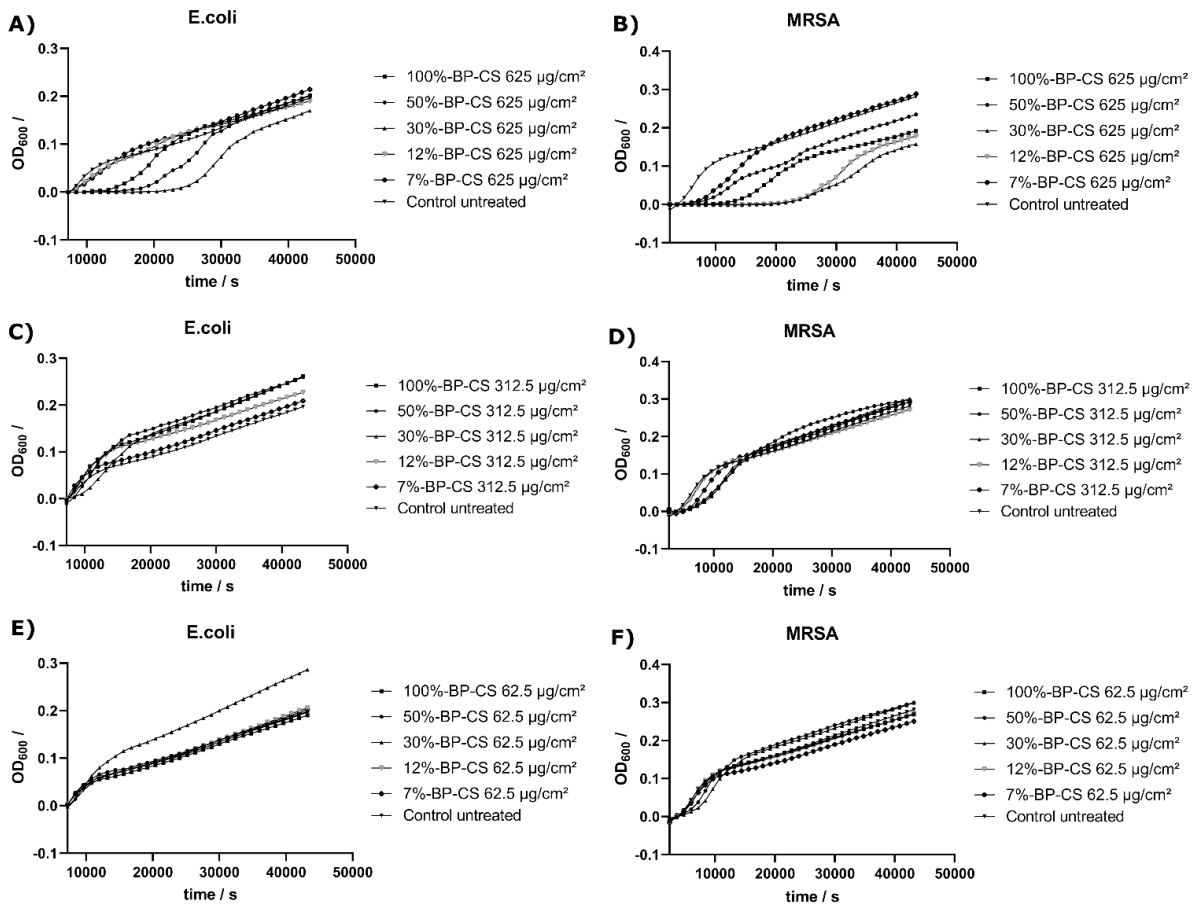


**Figure S6.** Growth curves of alive bacteria after 24 h incubation in direct contact with polymer coatings. Three different concentrations were used in the casting process: 625 µg/cm<sup>2</sup> (A, B), 312.5 µg/cm<sup>2</sup> (C, D) and 62.5 µg/cm<sup>2</sup> (E, F). They were tested with bacterial solution of *Staphylococcus aureus* (B, D, F) and *Escherichia coli* (A, C, E).

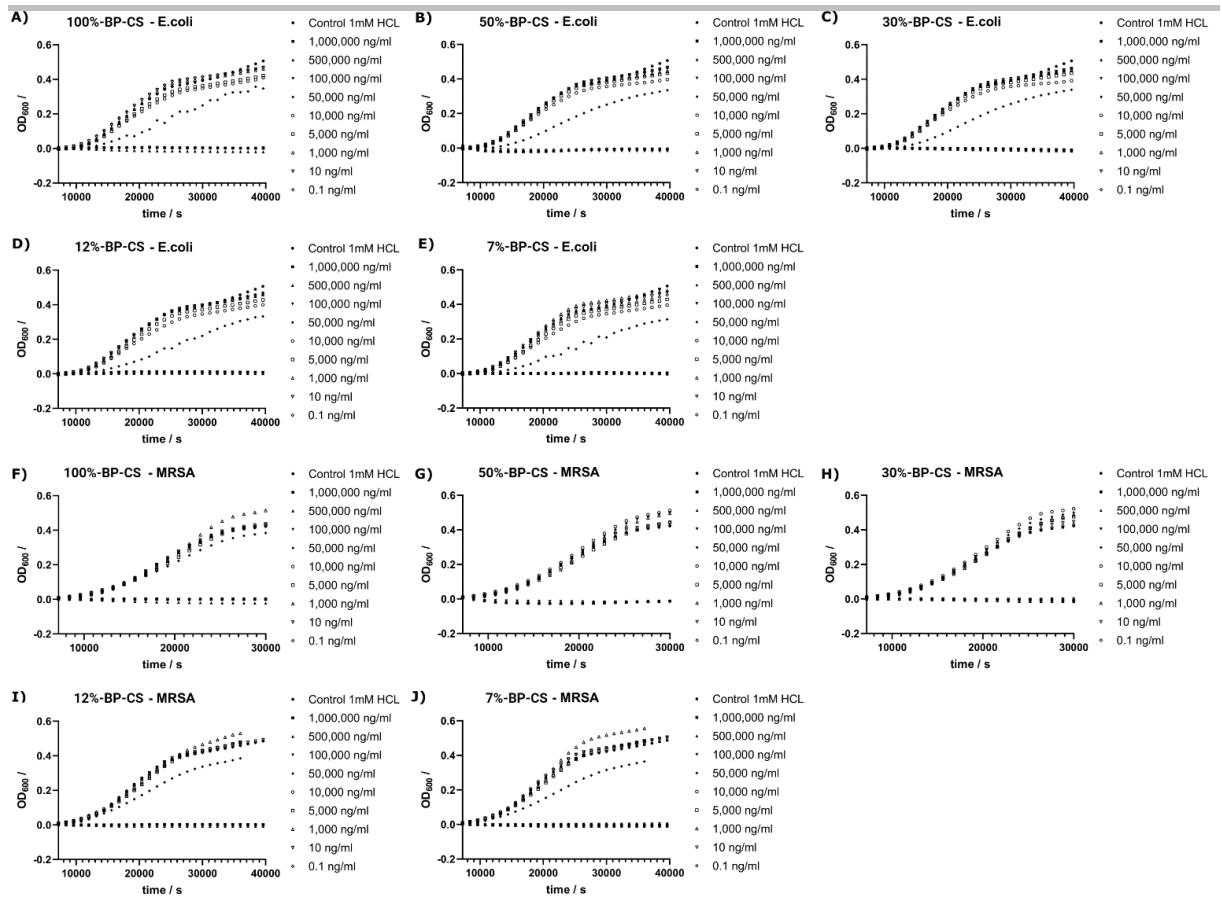


**Figure S7.** Growth curves of *Escherichia coli* (A - E) and *Staphylococcus aureus* (F - J) treated with various concentrations of the chitosan derivatives solubilized in 1 mM HCl.

## **A.3 Supporting Material for Chapter 3.3**

### **A.3.1 Supporting Material: Synergy of R-(–)carvone and cyclohexenone-based carbasugar precursors with antibiotics to enhance antibiotic potency and inhibit biofilm formation**

Supporting information:

## Synergy of R-(-)Carvone and Cyclohexenone-based Carbasugar Precursors with Antibiotics to Enhance Antibiotic Potency and Inhibit Biofilm Formation.

Oliver Riester <sup>1,2</sup>, Pia Burkhardtmaier <sup>1</sup>, Yuna Gurung <sup>1</sup>, Stefan Laufer <sup>2,3</sup>, Hans-Peter Deigner <sup>1,4,5,#</sup>, Magnus S. Schmidt <sup>1,\*,#</sup>

<sup>1</sup> Institute of Precision Medicine, Furtwangen University, Jakob-Kienzle-Strasse 17, Villingen-Schwenningen, 78054, Germany

<sup>2</sup> Institute of Pharmaceutical Sciences, Department of Pharmacy and Biochemistry, Eberhard-Karls-University Tuebingen, Auf der Morgenstelle 8, Tuebingen, 72076, Germany

<sup>3</sup> Tuebingen Center for Academic Drug Discovery & Development (TüCAD2), 72076 Tuebingen, Germany

<sup>4</sup> Faculty of Science, Eberhard-Karls-University Tuebingen, Auf der Morgenstelle 8, Tuebingen, 72076, Germany

<sup>5</sup> EXIM Department, Fraunhofer Institute IZI (Leipzig), Schillingallee 68, Rostock, 18057, Germany

\* Corresponding author: [smag@hs-furtwangen.de](mailto:smag@hs-furtwangen.de)

# Both authors share senior authorship

### Table of content

<b>Biocompatibility</b> - Figure S1   Biocompatibility of the compounds <b>rac-7</b> and <b>3</b> .	S2
<b>Microbial growth</b> - Figure S2   Effects of the compounds <b>rac-7</b> and <b>3</b> on the bacterial growth	S3
<b>Biofilm</b> - Figure S3   Evaluation of biofilm formation in the presence of compounds <b>rac-7</b> and <b>3</b> .	S4
<b>NMR Spectra</b> - Figure S4   <sup>1</sup> H-NMR spectrum of compound <b>2</b> .	S5
<b>NMR Spectra</b> - Figure S5   <sup>13</sup> C-NMR spectrum of compound <b>2</b> .	S5
<b>NMR Spectra</b> - Figure S6   <sup>1</sup> H-NMR spectrum of compound <b>3</b> .	S6
<b>NMR Spectra</b> - Figure S7   <sup>13</sup> C-NMR spectrum of compound <b>3</b> .	S6
<b>NMR Spectra</b> - Figure S8   COSY spectrum of compound <b>3</b> .	S7
<b>NMR Spectra</b> - Figure S9   NOESY spectrum of compound <b>3</b> with indicated crosscoupling.	S7
<b>NMR Spectra</b> - Figure S10   <sup>1</sup> H-NMR spectrum of compound <b>6</b> .	S8
<b>NMR Spectra</b> - Figure S11   <sup>13</sup> C-NMR spectrum of compound <b>6</b> .	S8
<b>NMR Spectra</b> - Figure S12   <sup>1</sup> H-NMR spectrum of compound <b>7</b> .	S9

## Biocompatibility

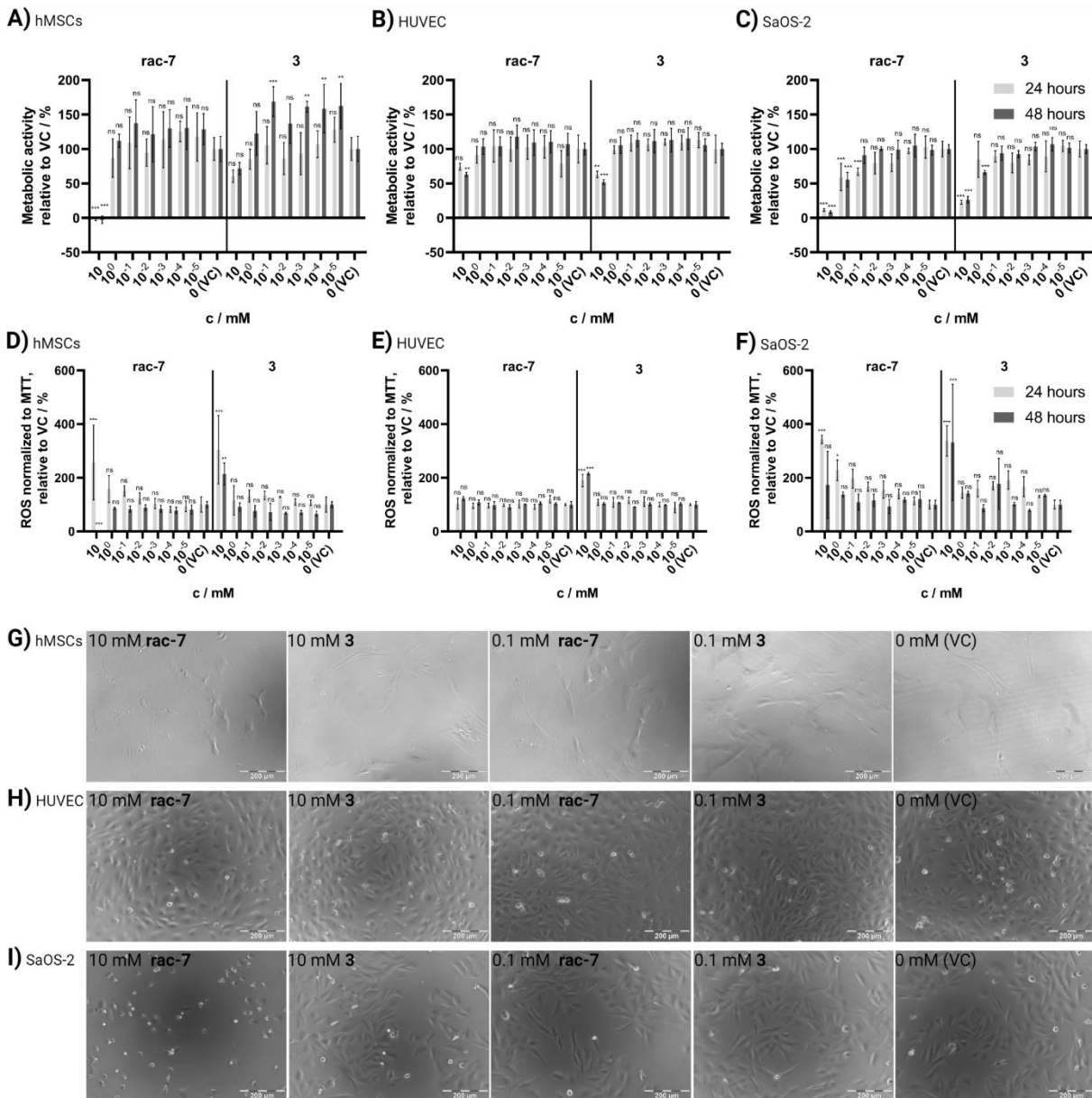


Figure S1 | Biocompatibility of the compounds *rac-7* and **3**. Human mesenchymal stem cells (hMSC), human umbilical vein endothelial cells (HUVEC) and SaOS-2 human osteogenic sarcoma cells treated for 24 and 48 hours. **A - C** Evaluation of metabolic activity at different concentrations of CSPs with MTT – assay in comparison to vehicle control (VC). **D – F** Cellular reactive oxygen species (ROS) normalized to MTT – assay and compared to VC. VC was treated with same volume of PBS without CSPs. Values are shown as mean  $\pm$  SD ( $n = 3$ ). Statistical significance was analyzed with Two-way ANOVA and Dunnett post-hoc test against respective VC (ns, not significant; \*  $p < 0.05$ ; \*\*  $p < 0.01$ ; \*\*\*  $p < 0.001$ ). **G – I** Representative microscopic images of hMSCs, HUVECs and SaOS-2 cells treated with compounds *rac-7* or **3**. Scale bar measures 200  $\mu\text{m}$ .

## Microbial growth

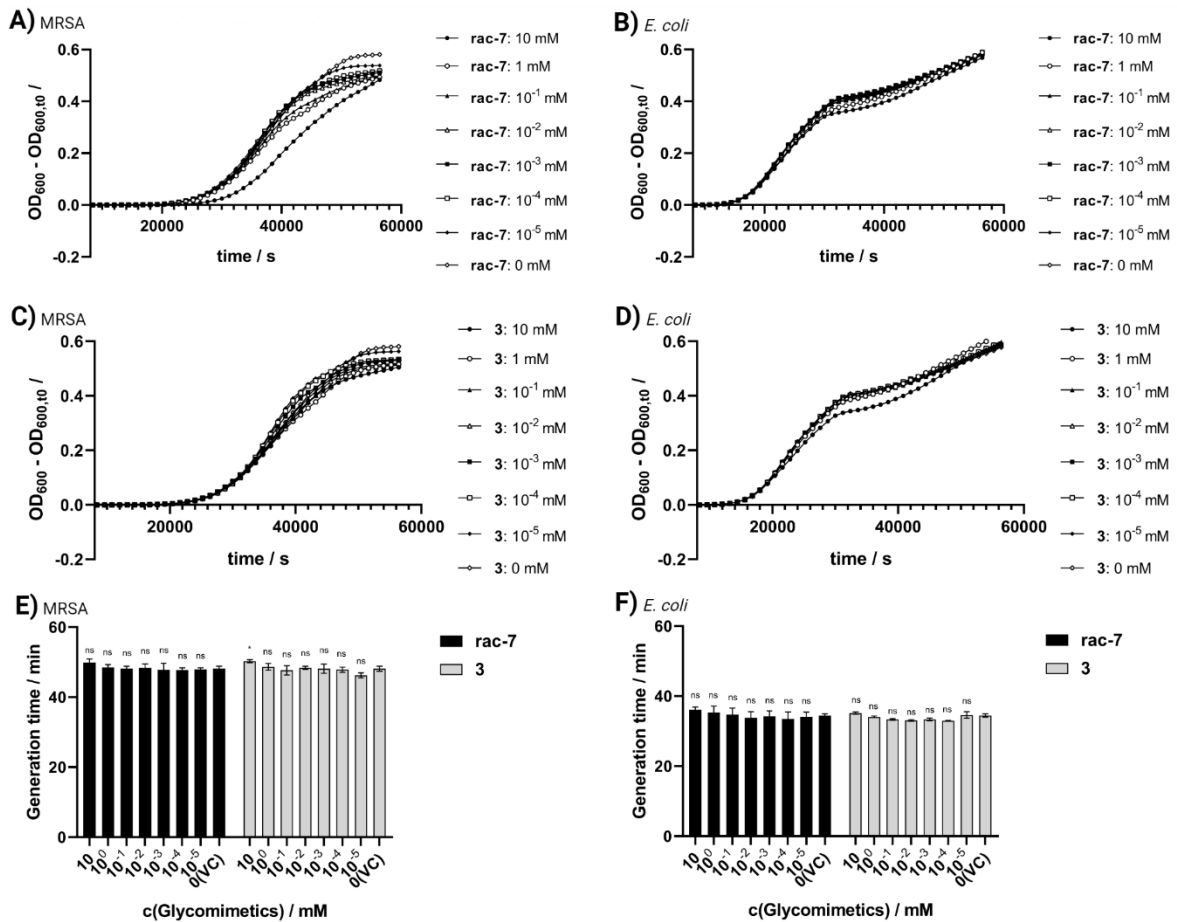


Figure S2 | Effects of the compounds **rac-7** and **3** on the bacterial growth of *Escherichia coli* (*E. coli*; **B, D, F**) and methicillin-resistant *Staphylococcus aureus* (MRSA; **A, C, E**). Measured optical density at 600 nm ( $OD_{600}$ ) showing the growth curves treated with several concentrations of the carbasugar precursors (CSPs) **rac-7** (**A, B**) and **3** (**C, D**) in LB medium. Concentration-dependent influence of CSPs on the generation time of *E. coli* (**F**) and MRSA (**E**) in LB medium (additional concentrations to Figure 3). Values are shown as mean (**A - D**:  $n = 3$ ) or mean  $\pm$  SD (**E, F**:  $n = 3$ ). Statistical significance was analyzed with Two-way ANOVA and Dunnett post-hoc test against respective vehicle control (VC) (ns, not significant; \*  $p < 0.05$ ; \*\*  $p < 0.01$ ; \*\*\*  $p < 0.001$ ).

## Biofilm

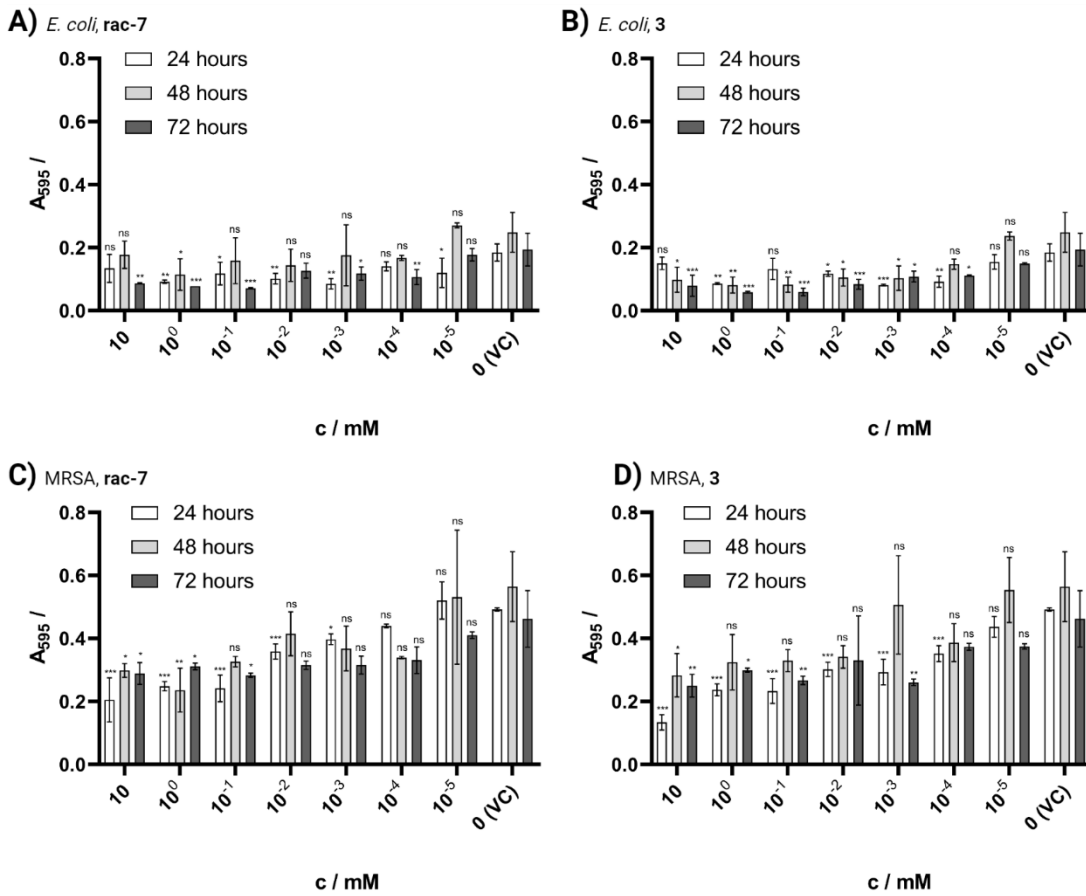
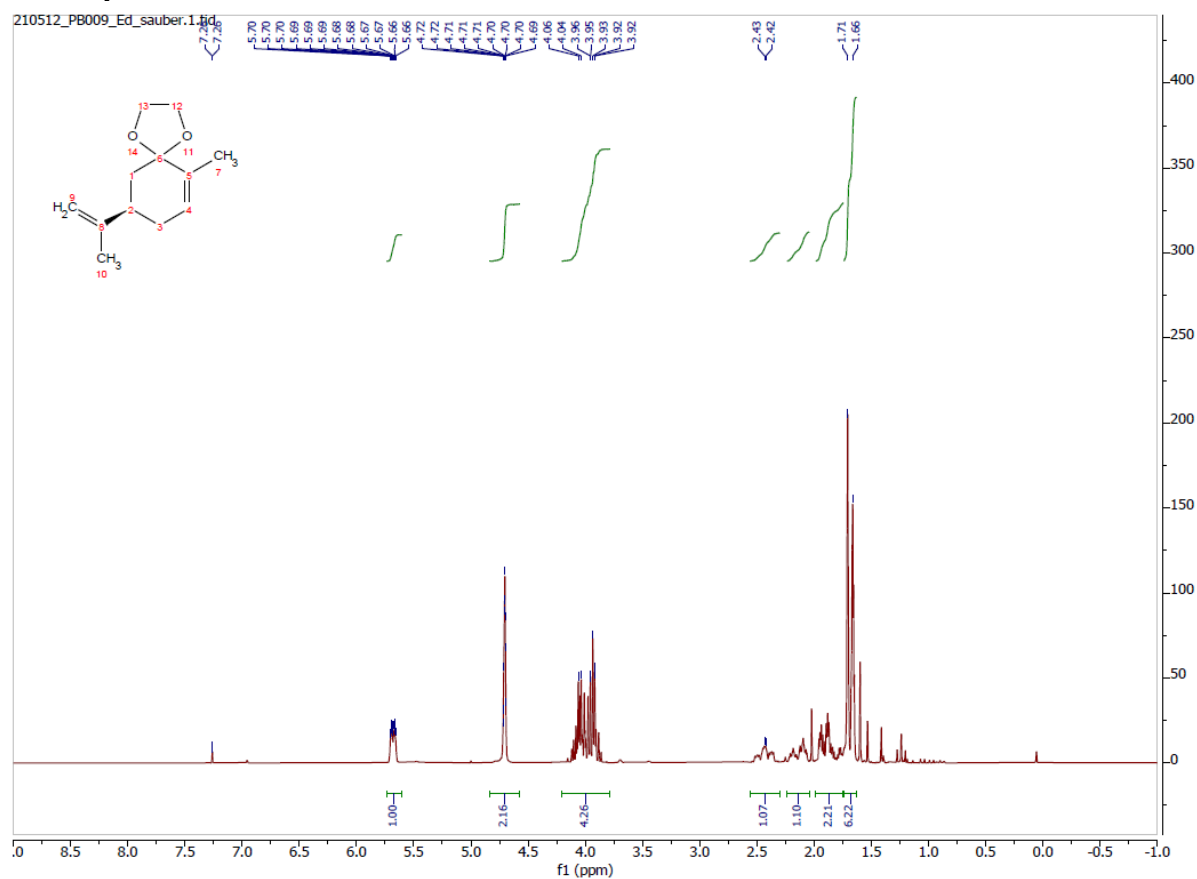
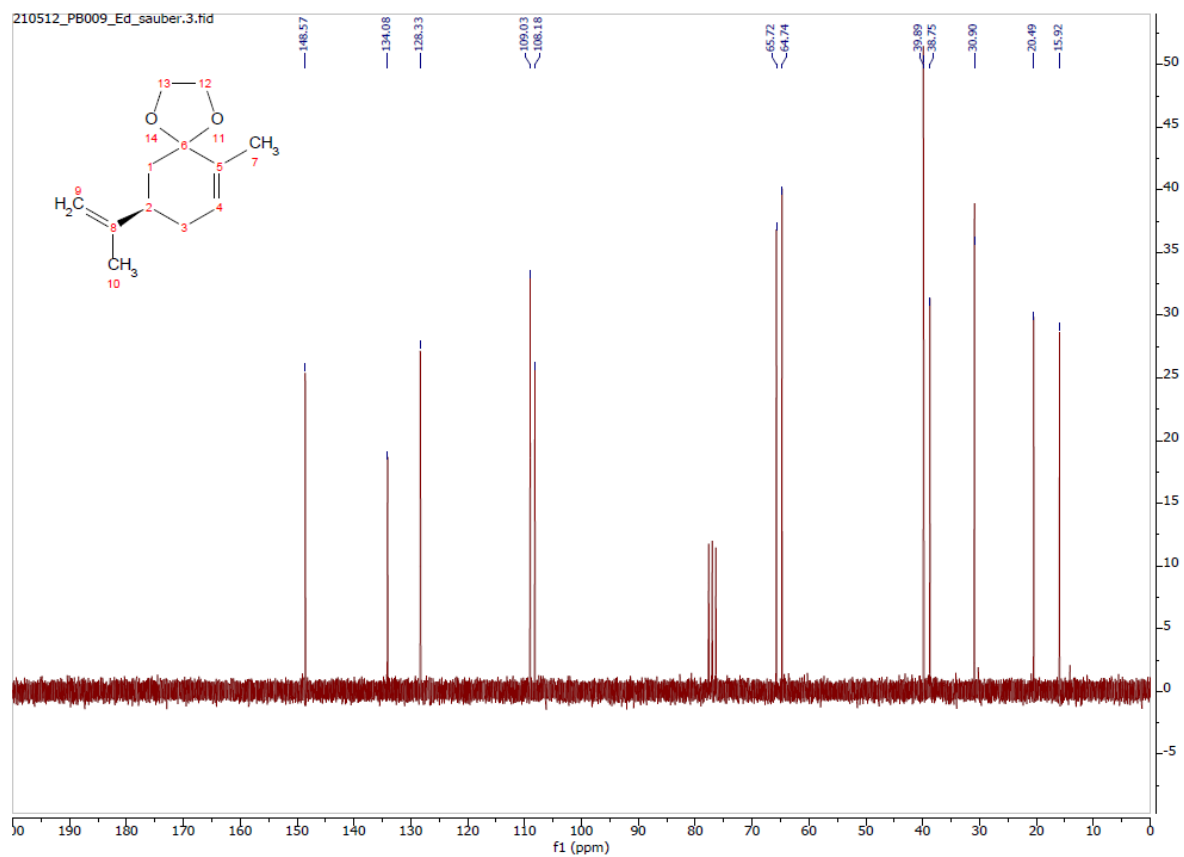
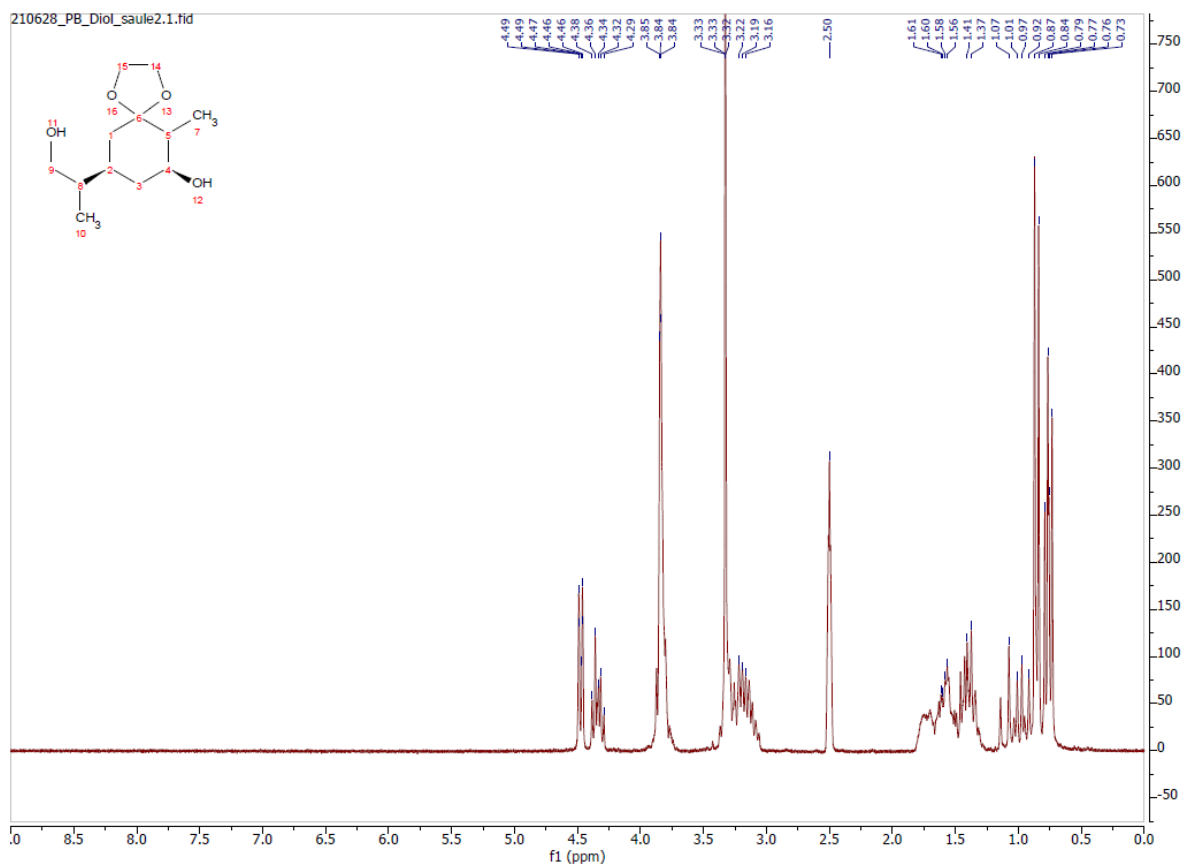
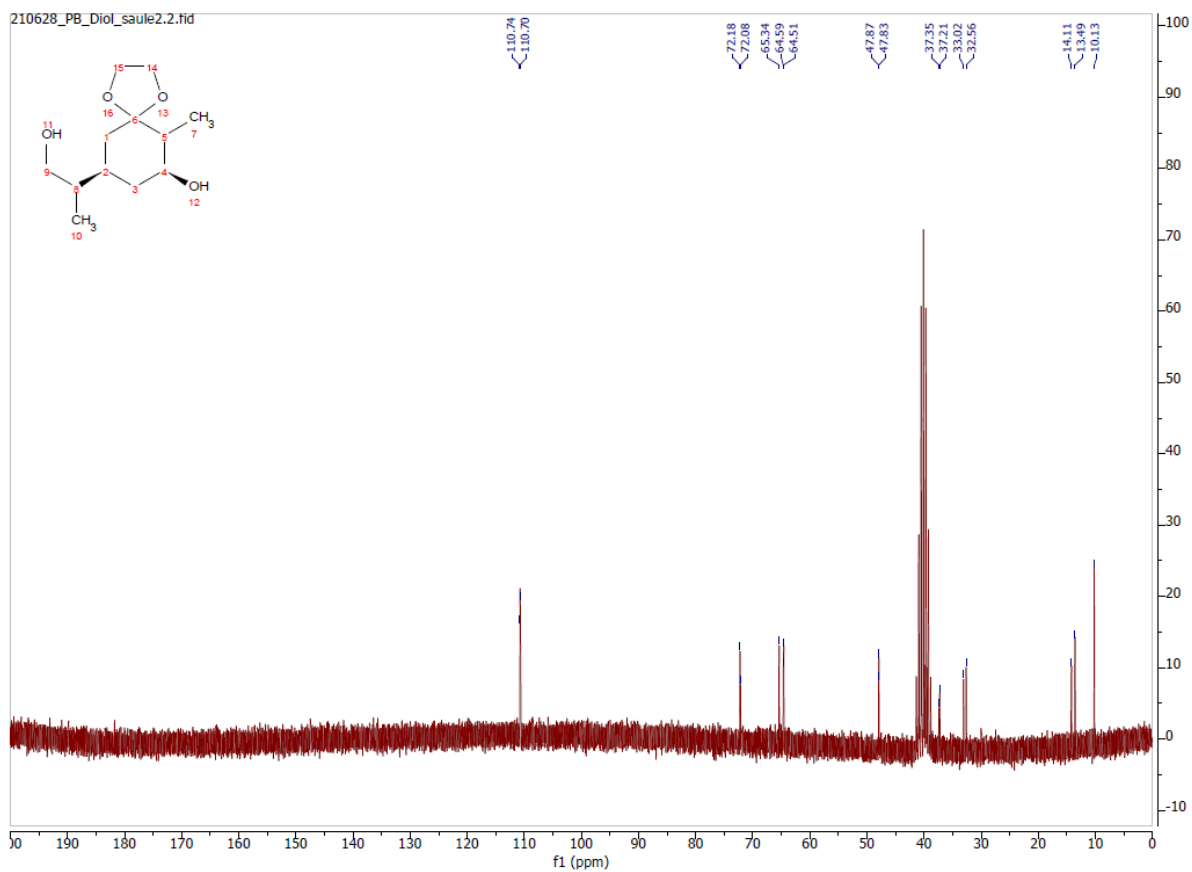


Figure S3 | Evaluation of biofilm formation in the presence of compounds **rac-7** and **3**. Biofilm formation of *Escherichia coli* (*E. coli*; **A – B**) and methicillin-resistant *Staphylococcus aureus* (MRSA; **C – D**) after 24, 48 and 72 hours of incubation in the presence of 10 mM to 10 nM carbasugar precursors. Absolute values are shown as mean  $\pm$  SD ( $n = 2$ ). Statistical significance was analyzed with Two-way ANOVA and Dunnett post-hoc test against respective vehicle control (n s, not significant; \*  $p < 0.05$ ; \*\*  $p < 0.01$ ; \*\*\*  $p < 0.001$ ).

## NMR Spectra

Figure S4 |  $^1\text{H-NMR}$  spectrum of compound **2**.Figure S5 |  $^{13}\text{C-NMR}$  spectrum of compound **2**.

Figure S6 |  $^1\text{H}$ -NMR spectrum of compound 3.Figure S7 |  $^{13}\text{C}$ -NMR spectrum of compound 3.

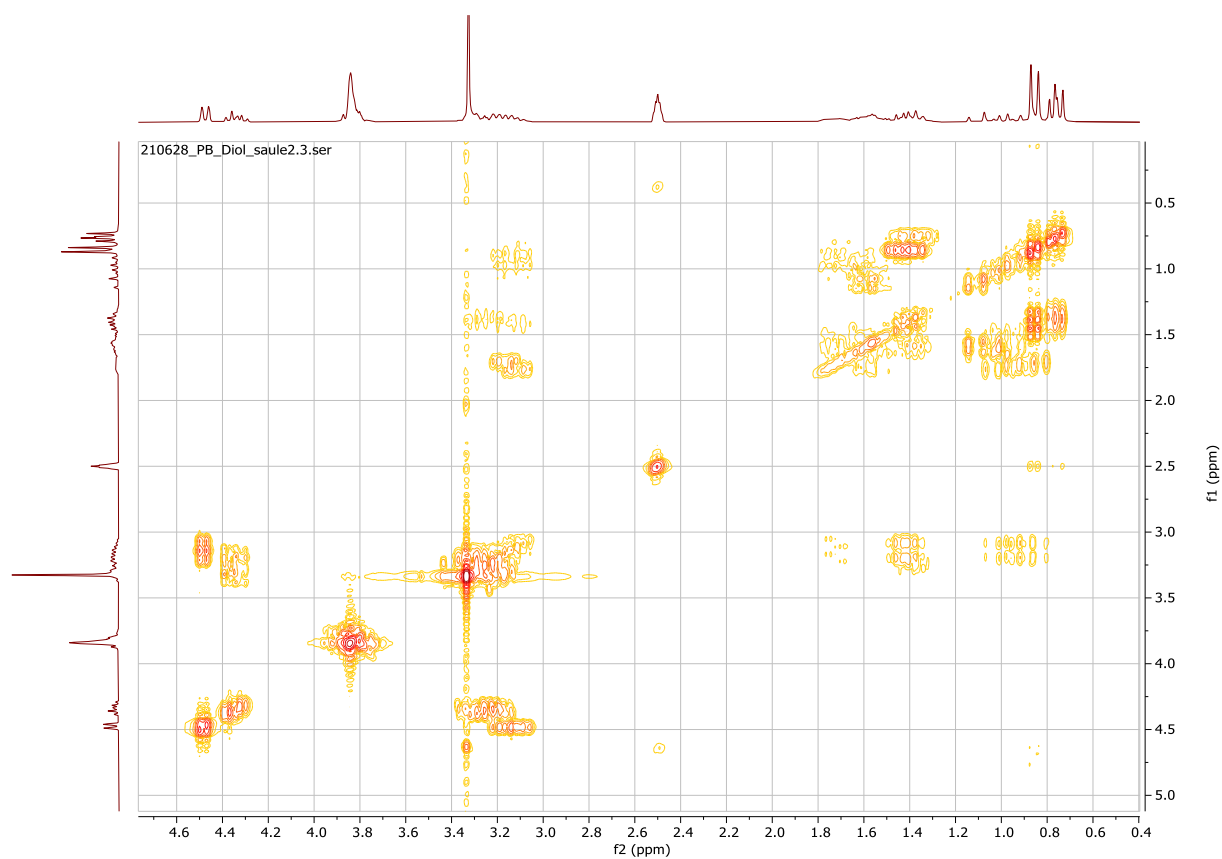


Figure S8 | COSY spectrum of compound 3.

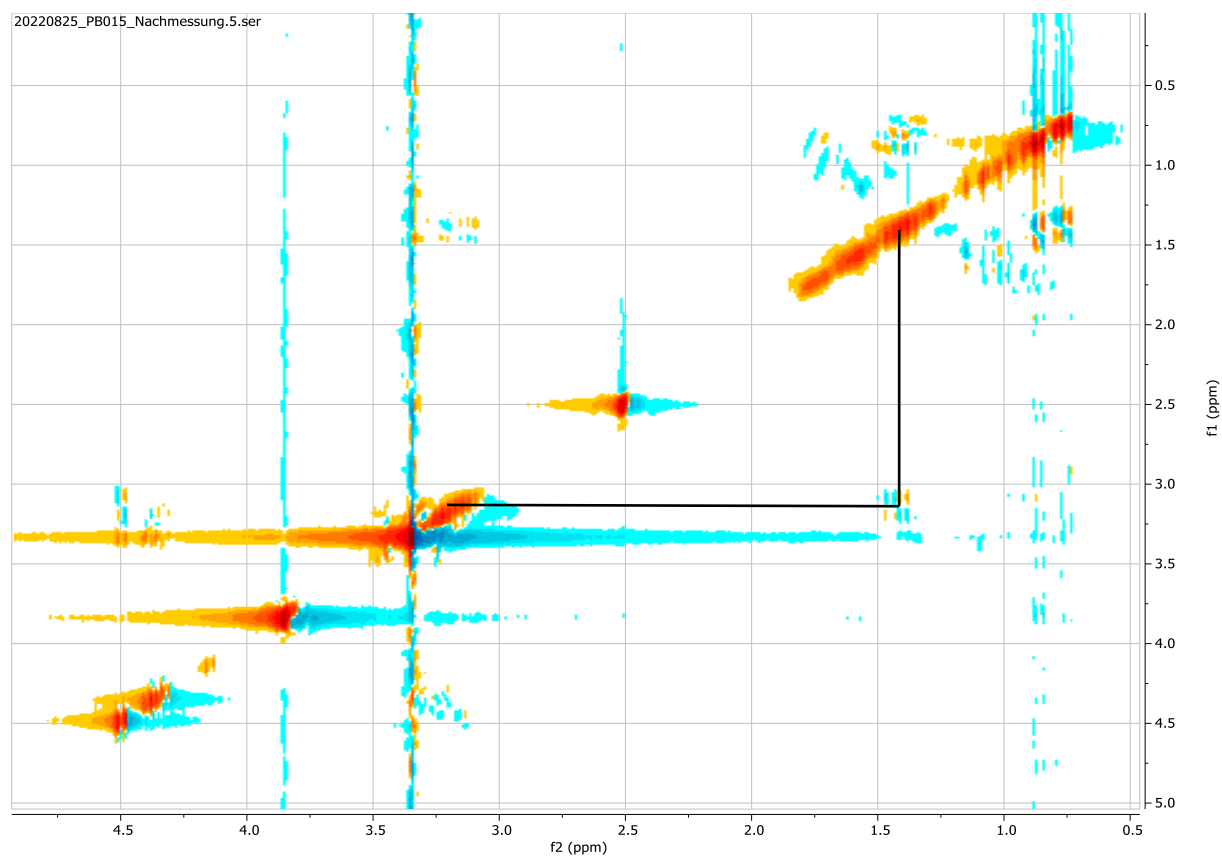
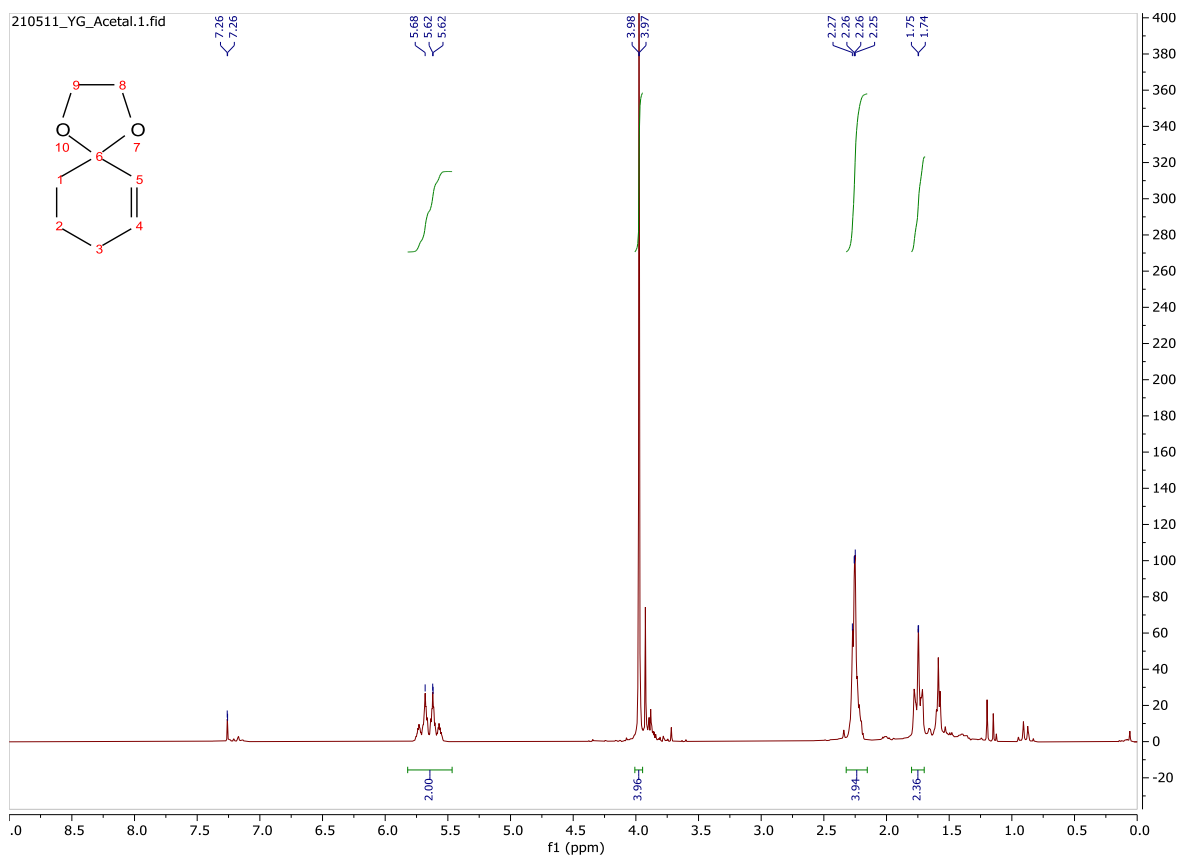
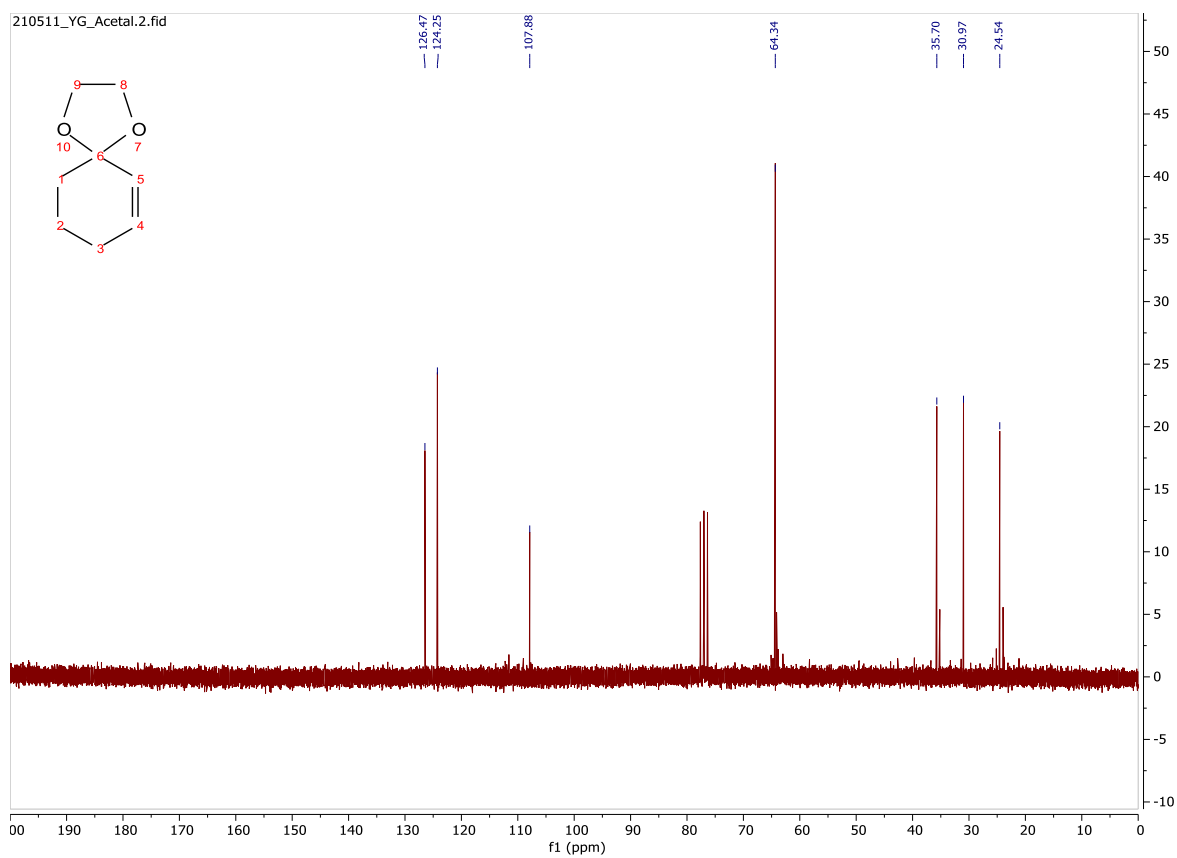
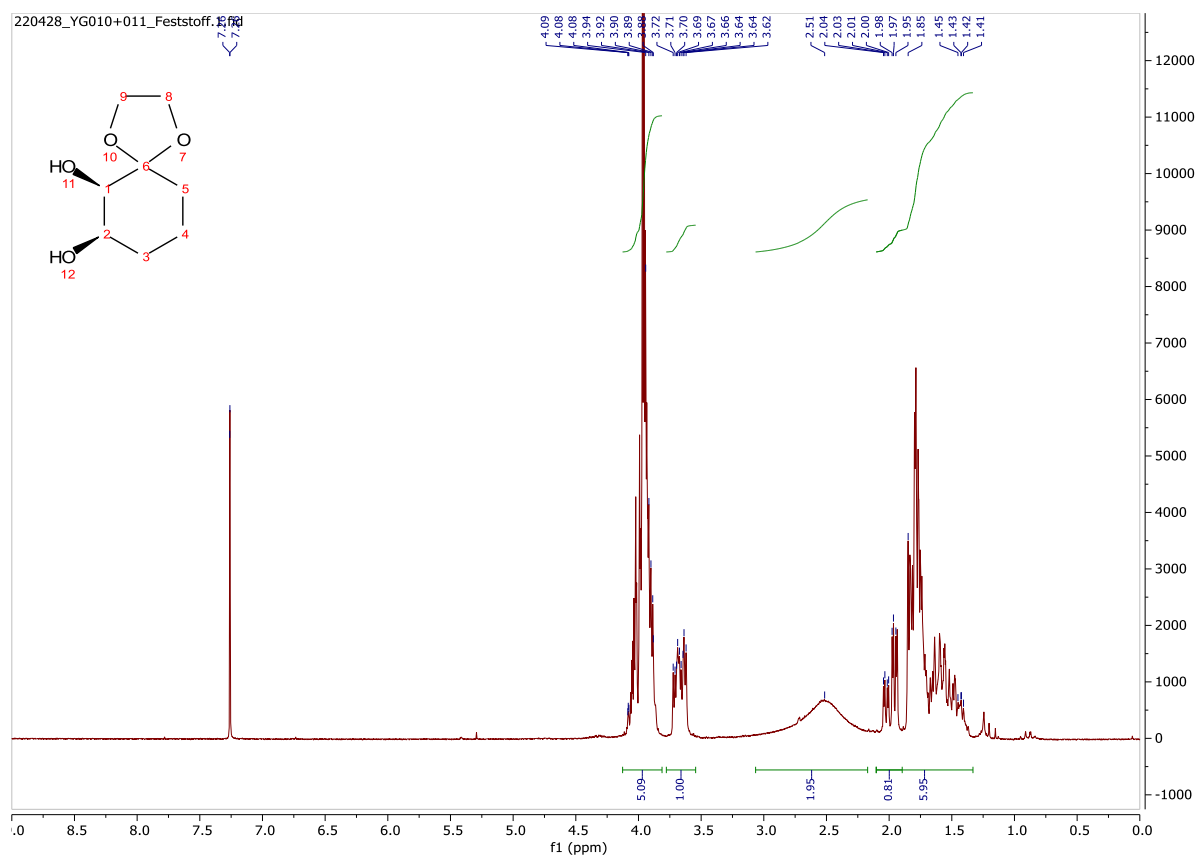


Figure S9: NOESY spectrum of compound 3 with indicated crosscoupling.

Figure S10 |  $^1\text{H}$ -NMR spectrum of compound 6.Figure S11 |  $^{13}\text{C}$ -NMR spectrum of compound 6.

Figure S12 |  $^1\text{H-NMR}$  spectrum of compound 7.